UNIVERSITÉ DU QUÉBEC À RIMOUSKI

MÉLANGE TURBULENT DANS L'ESTUAIRE MARITIME DU SAINT-LAURENT

Thèse présentée

dans le cadre du programme de doctorat en océanographie

en vue de l'obtention du grade de Philosophiae Doctor

PAR

FRÉDÉRIC CYR

Juin 2014

Composition du jury :

Cédric Chavanne, président du jury, Université du Québec à Rimouski

Daniel Bourgault, directeur de recherche, Université du Québec à Rimouski

Peter S. Galbraith, codirecteur de recherche, Institut Maurice-Lamontagne

Luc Rainville, examinateur externe, University of Washington

Dépôt initial le 16 décembre 2013 Dépôt final le 27 juin 2014

Flore.

Science studies what's at the edge of understanding, and what's at the edge of understanding is usually fairly simple. And it rarely reaches human affairs.

Noam Chomsky

Au moment où j'écris ces lignes, il est plus facile de poser un robot sur une comète que de faire une lutte efficace aux problèmes climatiques, environnementaux et sociaux. Vraiment, l'être humain est une drôle d'espèce...

Texel, 13 novembre 2014

REMERCIEMENTS

Petite histoire de doctorat...

Beaucoup de personnes sont passées (et restées) dans mon entourage au cours de mon doctorat. Quand je suis débarqué à l'ISMER le 3 mai 2009, James Caveen et Simon Senneville m'ont accueilli et installé dans le O-240, le siège social du LASSO [1]. Dans ce local bourré de meubles, deux étudiants étaient cachés : Pierre St-Laurent et Simon St-Onge. Ils ont su tout de suite m'intégrer. Ils étaient là aussi pour répondre à mes questions de débutant et si je les dérangeais, ça ne paraissait pas. Il y avait aussi Joanie, Virginie et Sylvain qui étaient sensés être là, mais ils n'y étaient pas souvent. Merci à eux aussi pour l'intégration.

Assez rapidement par la suite s'est enchaînée une suite de péripéties : feu à l'université, travaux de construction (qui durent encore aujourd'hui), déménagement dans un local en tapis plein de poussière, retour dans le O-240, mais sans les fenêtres, changement de mobilier, etc. À travers tout ce chamboulement, le nombre d'étudiants a explosé. J'ai donc beaucoup de personnes à remercier pour l'ambiance du labo, trop pour tous les nommer, mais je suis sûr qu'ils se reconnaissent. Je tiens à remercier spécialement Paul, qui a traversé pas mal toutes ces étapes avec moi, ainsi que Camil et Thibault, deux autres qui ont aussi vu l'évolution du LASSO. Merci aussi à ceux qui étaient là quand je suis parti : Anne-Claire, Mélany, Benoit, Elliot, Julien, Robin.

Évidemment, un énorme merci à Daniel qui, à partir de Terre-Neuve, m'a invité à faire un doctorat avec lui. Nous sommes arrivés presque en même temps à Rimouski. Bien qu'il jouait son rôle de superviseur, j'ai eu l'impression d'avoir une relation d'ami et de collaborateur avec lui, comme le démontre les nombreux projets *parascolaires* auxquels nous avons participé. Même chose pour Peter, partenaire principal de mes sorties de terrain au cours desquelles les heures en mer ont permis un brassage d'idées intéressant. Les nombreux party

1. Laboratoire d'analyse et de simulation des systèmes océaniques

et soupers avec vous deux m'ont aussi montré un autre côté de la recherche plus *détendu*. Vous m'avez aussi montré à rester sur mes gardes avec vos questions-pièges, car vous vous rappelez longtemps des mauvaises réponses ! Merci aussi au Fond québécois de recherche - Nature et technologies (FRQ-NT) qui a financé ma thèse et qui continue de me soutenir avec une bourse de post-doctorat.

Merci à Cédric Chavanne et Luc Rainville, respectivement président et examinateur externe sur le jury de thèse, ce fut un plaisir de partager de bons moments avec vous durant et après ma soutenance de thèse. Vos commentaires ont été très pertinents (et très flatteurs) et continuent de me faire réfléchir encore ajourd'hui. Ils sont aussi une motivations à continuer dans le domaine de la recherche. J'ai un merci spécial à faire à Dany Dumont et Frédéric Maps, deux jeunes chercheurs qui ont été, chacun à leur façon, une source d'inspiration pour mieux comprendre la recherche et à Joël Chassé pour avoir siégé sur mon comité de thèse. Merci aux techniciens qui m'ont aidé sur le terrain : Rémi, Bruno, Gilles et Sylvain.

En plus de ceux que j'ai cotoyés à l'université, il y a bien sûr les amis et la famille qui nous ont beaucoup aidés, Eveline et moi, dans notre tentative de concilier famille-rénovation-étude-plaisir. Notre passage à Rimouski fut tout aussi marquant au point de vue personnel. En plus des études, nous avons eu une maison centenaire à rénover et vécu l'arrivée d'une petite Flore. Merci à mes parents pour leurs nombreux coups de main et à Rose-Marie et Guillaume, nos colocs d'exception.

Finalement, merci Eveline de ne pas m'avoir largué en chemin. Je suis conscient que la vie avec moi n'est pas de tout repos, surtout quand je suis en *rush* de travail. Je n'aurais peut-être jamais réussi si tu ne m'avais pas aidé de toutes les façons dont tu l'a fais. Flore, peut-être que tu ne liras jamais ces lignes, mais sâche que ta maman a été exceptionnelle pour permettre à papa de finir son doctorat. Merci à toi aussi d'être apparue si belle et si gentille dans notre vie de fou. Merci.

RÉSUMÉ

Entre 2009 et 2012, les premières mesures directes du taux de dissipation de l'énergie cinétique turbulente dans l'estuaire maritime du Saint-Laurent (EMSL) ont été effectuées avec un profileur vertical de micro-structures. Il s'avert que le mélange dans la couche limite de fond près des bords de l'EMSL est 10 fois supérieur à celui à l'intérieur, loin des bords et quatre fois plus élevé durant le flot par rapport au jusant. Il semble aussi que le mélange à la tête du chenal Laurentien, l'extrémité en amont de l'EMSL, soit quant à lui 300 fois supérieur au mélange intérieur. Avec l'aide d'observations historiques de température et de salinité provenant de la station de monitorage Rimouski, il a été démontré que l'érosion de la couche intermédiaire froide (CIF), c.-à-d. son mélange estival, est assuré à un tiers par des processus près des bords et aux deux tiers par des processus locaux, loin des bords. Les données d'un mouillage déployé le long des bords de l'EMSL suggèrent aussi que les déplacements verticaux de la CIF le long de la topographie en pente sont forcés par des marées internes générées à la tête du chenal Laurentien. L'utilisation d'observations historiques de concentration de nitrate dans l'EMSL combinées aux observations de turbulence a permis une estimation des flux verticaux turbulents de nitrates à la tête du chenal Laurentien ainsi qu'à la station Rimouski. Les flux à la tête du chenal sont 600 fois plus élevés qu'à la station Rimouski et peuvent à eux seuls soutenir la majeure partie de la production primaire hors bloom.

Mots clés : turbulence, mélange côtier, profileur vertical de micro-structures, estuaire maritime du Saint-Laurent, couche intermédiaire froide, marées internes, flux turbulent de nitrate.

ABSTRACT

Between 2009 and 2012, the first measurements of dissipation rates of turbulent kinetic energy in the Lower St. Lawrence Estuary (LSLE) were carried out with a vertical microstructure profiler. Boundary mixing in the bottom boundary layer at a sloping boundary is 10 times higher compared to inner mixing far from boundaries and four times higher during the flood compared to the ebb. Mixing is also 300 times higher at the head of the Laurentian channel, a sill located at the upstream limit of the LSLE, compared to interior mixing. Using historical temperature and salinity observations from the monitoring station Rimouski, it is shown that boundary mixing accounts for one-third of the erosion rates (i.e., waming by mixing) of cold intermediate layer (CIL). Interior mixing, i.e., mixing far from boundaries, accounts for the remaining two-thirds. Observations from a mooring deployed over the sloping boundary suggest also that the CIL undergoes swash/backwash motions on the slope in response to a forcing by internal tides generated at the head of the Laurentian channel. The combination of turbulence measurements and historical nitrate concentration observations reveals that turbulent nitrate fluxes are 600 times higher at the head of the Laurentian channel than at the Rimouski station. Such fluxes can account for most of the post-bloom primary production in the LSLE.

Keywords : turbulence, coastal mixing, vertical microstructure profiler, Lower St. Lawrence Estuary, cold intermediate layer, internal tides, turbulent nitrate fluxes.

TABLE DES MATIÈRES

LISTE DES TABLEAUX

LISTE DES FIGURES

INTRODUCTION GÉNÉRALE

Observations *in situ* de turbulence : contexte historique et scientifique

Les mesures de la turbulence dans l'océan ont commencé dans les années 1950 à partir de profileurs horizontaux (Stewart et Grant, 1999), mais la discipline n'a vraiment connu son essort qu'à partir des travaux de Osborn (1974) et de l'apparition de sondes (*shear probes*) capables de mesurer le cisaillement à la micro-échelle, c'est-à-dire l'échelle du centimètre. Ces sondes, insensibles aux changements de température dans la colonne d'eau contrairement à leurs prédécesseurs (des anémomètres à fil chaud), ont ouvert la voie à l'utilisation de profileurs verticaux de turbulence, beaucoup plus faciles à déployer que des profileurs horizontaux (voir Lueck et al., 2002, pour une revue historique du sujet). Conforté par cette certaine démocratisation des techniques de mesure de la turbulence dans l'océan, le champ de recherche est toujours aujourd'hui en pleine ébulition.

L'intérêt grandissant pour l'étude des mécanismes responsables de la turbulence et du mélange est d'autant plus important que ceux-ci ne sont que très peu ou mal représentés dans les modèles numériques actuels (Umlauf et Burchard, 2005). Ceci s'explique par le fait que les échelles temporelles et spatiales contenant l'énergie d'où provient la turbulence sont réparties sur plusieurs ordres de grandeur. En modélisation, les dimensions des grilles de calcul et le pas de temps des modèles posent des limitations spatio-temporelles à la résolution des plus petites échelles, c'est-à-dire les échelles où cette énergie est libérée par mélange turbulent. Les modélisateurs contournent généralement ce problème en développant des paramétrisations qui servent à prendre en compte la turbulence et le mélange qui n'est pas explicitement résolu par les modèles. La stratégie à adopter pour développer de telles paramétrisations consiste à relier les processus turbulents non résolus (ex : tourbillons, ondes internes, etc.) à ceux qui le sont (ex : cisaillement des courants moyens). La mise au point de telles paramétrisations demande par contre une bonne connaissance des mécanismes qui

génèrent la turbulence.

L'intérêt pour de telles observations est d'autant plus important considérant que certains milieux comme le Saint-Laurent sont encore presque *vierges* d'observations de la turbulence. Le potentiel de collaboration avec les autres disciplines de l'océanographie est également considérable dans de telles circonstances. Parmi les types d'études possibles, notons par exemple les flux verticaux d'éléments nutritifs, d'oxygène ou autres éléments biochimiques (Lewis et al., 1986; Rippeth et al., 2009; Bourgault et al., 2011, 2012; Williams et al., 2013), les blooms phytoplanctoniques (Huisman et al., 1999; Ghosal et Mandre, 2003; Taylor et Ferrari, 2011), les couches minces phytoplanctoniques (Durham et Stocker, 2012) ou la resuspension de sédiments (Bogucki et al., 1997; Hosegood, 2004; Bourgault et al., 2014). Toutes ces études sont basées sur des observations *in situ* ou numériques du mélange turbulent.

C'est donc dans ce contexte que ce sont déroulés les travaux de doctorat, c'est-à-dire celui de l'étude d'une discipline qui jouit d'un certain engouement en océanographie étant donné que très peu de choses sont actuellement connues de la turbulence dans certains milieux. La toile de fond pour cette thèse est le golfe et l'estuaire maritime du Saint-Laurent où ont été effectuées les sorties de terrain (Figure 1). Dans les prochaines pages, nous verrons comment la turbulence participe à l'érosion de la couche intermédiaire froide du Saint-Laurent et à la remise en suspension d'éléments nutritifs dans les eaux de surface.

Mélange en milieu côtier et couches intermédiaires froides

Il est généralement admis que le vent et les marées sont les seuls mécanismes capables de fournir l'énergie de mélange nécessaire au maintient de l'équilibre dynamique de l'océan (Munk et Wunsch, 1998; Wunsch, 2000; Wunsch et Ferrari, 2004). Alors que le vent fournit l'énergie à un taux d'environ 1 TW, les marées générées par les mouvements astronomiques fournissent l'énergie à un taux de 3.7 TW et est le mécanisme le plus probable pour fournir le mélange nécessaire à l'océan profond. Bien qu'une partie de l'énergie des marées soit

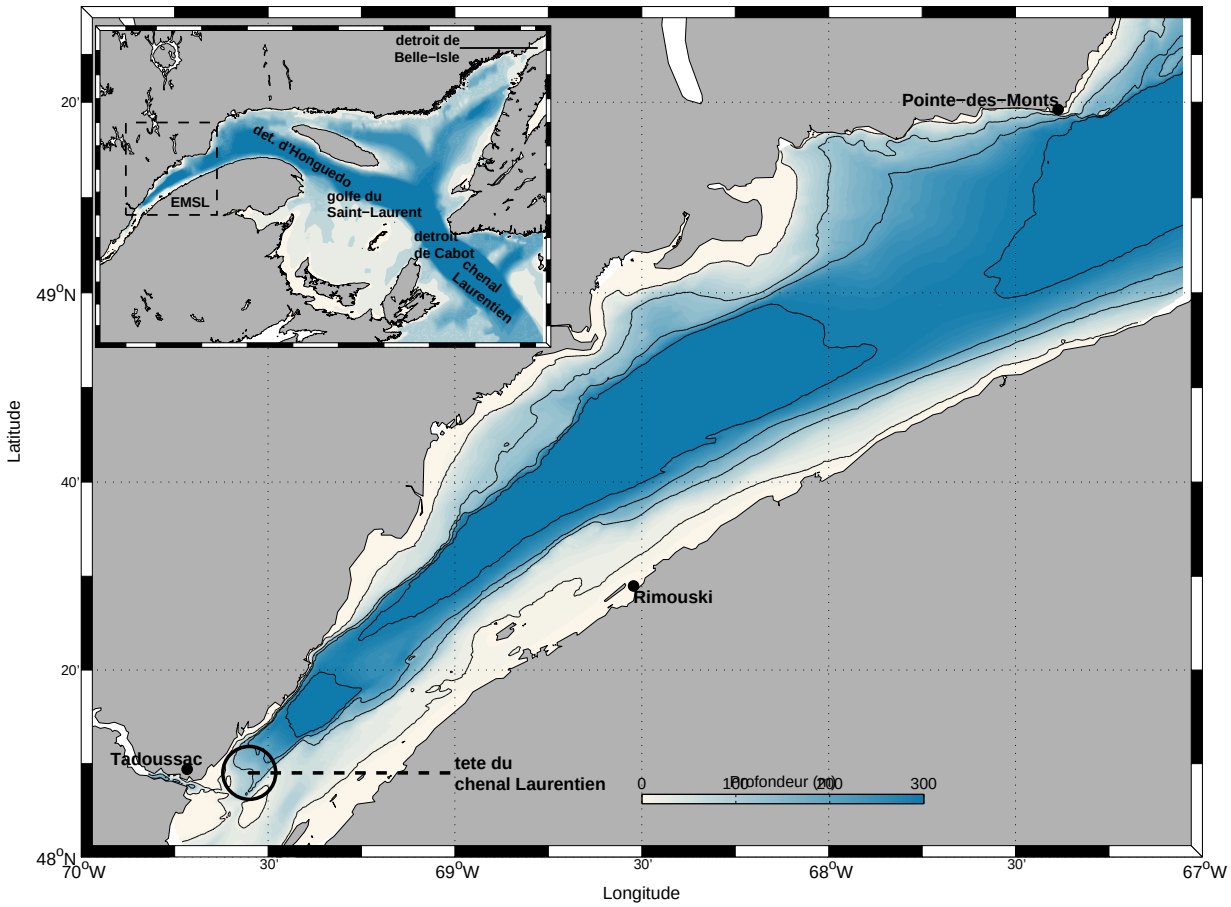

FIGURE 1: Carte bathymétrique du golfe (encadré) et de l'estuaire maritime du Saint-Laurent (EMSL). La tête du chenal Laurentien est identifiée par un encerclé.

transférée sous forme d'ondes internes pour ensuite être dissipée dans l'océan profond, la majeure partie de celle-ci (60-70%) est dissipée dans les océans côtiers étant donné leur plus faible profondeur et leur topographie complexe (Egbert et Ray, 2000; Rippeth, 2005). Malgré le fait que les océans côtiers occupent une petite fraction de la surface totale occupée par les océans (~7%), ils contrôlent entre 15-30% de la production primaire à l'échelle planétaire et jouent par le fait même un rôle majeur dans la séquestration du carbone dans les océans (20-50%) (p.-ex., Tsunogai et al., 1999; Muller-Karger, 2005; Rippeth, 2005). Quantifier les mécanismes de mélange responsables de la cascade d'énergie entre les mouvements des marées et la dissipation dans les océans côtiers est donc crucial pour notre compréhension du cycle du carbone et de ses effets sur le climat planétaire. Cette étude vise donc l'avancement des connaissances en ce qui à trait au mélange turbulent dans ces environnements dynamiques et complexes.

D'un autre point de vue, les couches intermédiaires froides (CIF) sont des structures estivales présentes dans plusieurs bassins subarctiques. On les trouve par exemple dans les mers Noire (Tuzhilkin, 2008), Baltique (Chubarenko et Demchenko, 2010), de Bering (Kostianoy et al., 2004) et d'Okhotsk (Rogachev et al., 2000), dans le golfe du Saint-Laurent (Banks, 1966) et dans l'océan Atlantique près des côtes de Terre-Neuve (Petrie et al., 1988). Ces masses d'eau sont généralement formées durant la saison hivernale en tant que couche froide mélangée de surface. La couche de surface devient une CIF lorsqu'emprisonnée entre une couche profonde d'origine océanique et une nouvelle couche mélangée de surface qui apparaît généralement au printemps suite à la fonte des glaces, à l'augmentation du débit des rivières et au réchauffement de la température de l'air. À leur formation, ces masses d'eau possèdent généralement les propriétés de la couche mélangée hivernale de surface, c'est-à-dire, sont froides et généralement riches en oxygène et en nutriments (Gilbert et Pettigrew, 1997; Gregg et Yakushev, 2005; Galbraith, 2006; Smith et al., 2006a). Par leur température, les CIFs contrôlent donc une partie importante de l'état et du climat des bassins côtiers subarctiques et leur rôle est aussi de première importance pour l'écologie marine (Ottersen et al., 2004).

Bien que quelques études traitent de la formation de ces couches, très peu d'information est disponible quant à leur évolution estivale et à la dégradation progressive de leurs propriétés (volume, minimum de température et contenu de chaleur). Dans les pages qui suivent, le terme *érosion* réfère à cette évolution par mélange de la CIF à la suite de sa regénération hivernale (qui a lieu généralement de décembre à mars). Dans les bassins où la stratification est dominée par les gradients de salinité, ces couches ont un comportement passif, c'est-à-dire qu'elles se mélangent sans affecter de façon considérable le champ de densité. Cette propriété passive nous permet d'inférer le mélange turbulent nécessaire à l'érosion observée de la CIF. La comparaison entre ce mélange inféré et celui mesuré nous permet d'en apprendre un peu plus sur la répartition spatiale de la turbulence.

Le cas du Saint-Laurent

Le golfe du Saint-Laurent est un bassin d'environ 236 000 km^2 dont fait partie l'estuaire maritime ($\sim$ 9000 km^2) qui correspond à la partie située approximativement entre Tadoussac et Pointe-des-Monts (Figure 1). Il est ouvert sur l'océan Atlantique via les détroits de Cabot et de Belle Isle, et reçoit son principal apport d'eau douce du fleuve Saint-Laurent. Sa bathymétrie est constituée, entre autres, de chenaux, dont le principal, le chenal Laurentien, s'étend sur plus de 1000 km, entre la pente continentale et sa tête près de Tadoussac (Figure 1). Ce chenal profond (>290 m) se termine alors abruptement à un seuil, où la bathymétrie remonte rapidement de 325 m à environ 50 m en moins de 15 km.

Les masses d'eau évoluent de façon similaire à celles décrites précédemment pour les régions subarctiques, c'est-à-dire, passant d'un système à deux couches pendant l'hiver à un système à trois couches pendant le reste de l'année (p. ex. Koutitonsky et Bugden, 1991). La CIF du golfe est caractérisée par des eaux avoisinant le point de congélation et des salinités de 32 – 33 psu. Pendant les mois d'été, la CIF existe dans le golfe sous une couche de surface mélangée (environ 0 – 50 m) et au dessus d'une couche plus chaude (1 à <8 °C) et plus salée

(> 33 psu) à des profondeurs supérieures à 150 m. Le renouvellement de la CIF s'effectue au cours de l'hiver alors que la couche mélangée de surface s'approfondie suite au refroidissement de l'air, au mélange induit par les tempêtes de vent et, en moindre importance, suite au rejet de saumure lié à la formation de glace de mer (Galbraith, 2006; Smith et al., 2006a).

La CIF n'est toutefois pas seulement formée localement sur l'ensemble du golfe, puisqu'une portion de celle-ci, variable d'une année à l'autre, provient d'une intrusion d'eau du plateau du Labrador via le détroit de Belle Isle (e.g., Lauzier et Bailey, 1957; Banks, 1966; Petrie et al., 1988; Galbraith, 2006; Smith et al., 2006a). De plus, pour la portion du golfe correspondant à peu près à l'estuaire maritime, la trop grande stratification liée à la décharge d'eau douce du fleuve empêche la formation de la CIF (Ingram, 1979b; Galbraith, 2006; Smith et al., 2006b). La CIF qui s'y trouve provient donc de l'advection vers l'amont de la CIF formée dans le reste du golfe. La présence de la CIF, en plus d'affecter la distribution de température de la colonne d'eau, influence la circulation et le climat dans le golfe du Saint-Laurent (Saucier et al., 2003). Son rôle et sa variabilité interannuelle est aussi de première importance pour des espèces visées par les pêches commerciales telles que le crabe des neiges ou la morue atlantique (Lovrich et al., 1995; Dionne et al., 2003; Tamdrari et al., 2012).

Bien que la CIF soit très fréquemment mentionnée dans la littérature sur le Saint-Laurent (voir Gilbert et Pettigrew, 1997; Smith et al., 2006a, pour un survol historique), sa définition varie d'un auteur à l'autre. Par exemple, Lauzier et Bailey (1957) ont utilisé l'isotherme $T = 0\,^{\circ}\mathrm{C}$ comme la limite supérieure de température pour la CIF. D'autres auteurs ont préféré des définitions différentes, comme par exemple $T < 1.5\,^{\circ}\mathrm{C}$ (Banks, 1966; Bugden et al., 1982), $T < 3\,^{\circ}\mathrm{C}$ (Gilbert et Pettigrew, 1997; Smith, 2005) ou plus récemment $T < 1\,^{\circ}\mathrm{C}$ (p.-ex. Galbraith et al., 2013). Comme la recherche présentée s'intéresse à la CIF durant les mois d'avril à novembre, cette dernière définition a été retenue puisque l'isotherme $T = 1\,^{\circ}\mathrm{C}$ est approximativement le minimum de température restant à la fin de notre période d'étude, c'est-à-dire, lorsque la CIF disparait lors de sa fusion avec la couche hivernale de surface.

Forcées par les apports d'eau douce du fleuve et des différentes rivières, les masses

d'eau évoluent dans le golfe suivant une circulation de type estuarienne le long du chenal Laurentien, alors que la couche de surface s'écoule généralement vers l'océan et les couches profondes remontent graduellement le golfe jusqu'à l'estuaire (Koutitonsky et Bugden, 1991). Étant donné cette circulation, la couche intermédiaire froide termine son parcours vers l'amont à la tête du chenal Laurentien où elle est extraite vers la surface grâce au vigoureux mélange vertical qui est suspecté d'être présent à ce seuil (p. ex. Ingram, 1975, 1976, 1979b, 1983, 1985; Gratton et al., 1988; Saucier et Chassé, 2000), mais encore jamais mesuré avant ce doctorat. Les eaux profondes et riches en nutriments qui sont ainsi acheminées vers la surface sont ensuite entrainées vers l'aval par la circulation estuarienne. Cette extraction de la CIF à la tête du chenal Laurentien modifie donc de façon considérable les températures de surface le long de l'estuaire avec des effets sur le climat local. L'apport continuel de nutriments à la tête du chenal Laurentien soutient aussi une forte production primaire tout au long de l'été dans l'estuaire maritime (Levasseur et al., 1984; Therriault et Levasseur, 1985; Plourde et al., 2001).

De récentes études ont permis à la fois une meilleure compréhension des mécanismes de formation et d'évolution de la CIF durant l'hiver (Galbraith, 2006; Smith et al., 2006a,b), de même que sa réponse à la variation des forçages par le vent et par le débit du fleuve (Saucier et al., 2009). De plus, une meilleure description de sa variabilité intra-annuelle et interannuelle a été proposée (Gilbert et Pettigrew, 1997). Cette étude, utilisant 47 ans de données provenant de 5 régions du golfe (l'estuaire, le détroit de Cabot et les régions nord-est, nord-ouest et centre du golfe) consistait en une étude plus complète que celle menée par Banks (1966). Alors que celui-ci proposa que le coeur de la CIF (minimum de température rencontré à l'intérieur de celle-ci) se réchauffait à un rythme de 0.2 °C par mois entre avril et novembre, étude basée sur 10 ans de données provenant de 3 régions du golfe (centre du golfe, détroit de Cabot et détroit d'Honguedo), Gilbert et Pettigrew (1997) proposaient qu'au contraire le coeur se réchauffait de façon différente d'une région à l'autre, augmentant de 0.08 °C à 0.30 °C par mois, respectivement pour le centre du golfe et l'estuaire.

Cependant, aucune de ces études ne quantifie le mélange turbulent responsable de cette érosion. Cette quantification et l'identification des mécanismes d'érosion ainsi que leur lien avec l'environnement physique est une étape clef à la fois pour la prédiction de la variation interannuelle de la CIF et au sens plus large pour une meilleure prise en compte du mélange les modèles numériques. Ceci est doublement important pour la CIF du Saint-Laurent qu'il s'avère que la mauvaise représentation des processus de mélange turbulent pourrait être à l'origine d'erreurs dans la modélisation de la formation de la CIF dans le golfe (Smith et al., 2006a).

Problématique et objectifs de la recherche

Profitant du manque de données autour de la question des processus d'érosion, les travaux de thèse visent à mieux comprendre l'érosion de la CIF et son extraction à la tête du chenal Laurentien. Il faut comprendre ici que l'étude de la CIF est une mise en contexte plus spécifique (ou un prétexte) pour l'étude du mélange turbulent dans l'estuaire maritime du Saint-Laurent. Plus spécifiquement, les objectifs principaux de la thèse sont les suivants :

1. Identifier et quantifier les mécanismes responsables de la turbulence qui mélange la couche intermédaire froide ;
2. Quantifier le flux de nutriments qui résulte de l'extraction des couches intermédiaire et profonde à la tête du chenal Laurentien.

Ces objectifs sont traités dans ce qui suit en trois objectifs spécifiques correspondants aux trois chapitres de la thèse :

— Chapitre 1 : Quantifier l'érosion estivale moyenne de la CIF et quantifier le mélange qui s'opère dans le golfe ;

— Chapitre 2 : Étudier le comportement de la CIF près des bords de l'estuaire maritime et quantifier le mélange qui s'en suit (*Boundary mixing*) ;

— Chapitre 3 : Quantifier les flux verticaux de nitrate provenant de l'extraction des couches profondes à la tête du chenal Laurentien.

Voici les résumés des trois chapitres de la thèse :

Chapitre 1 : Interior versus boundary mixing of a cold intermediate layer

Le résultat principal de cet article publié dans *Journal of Geophysical Research* (Cyr et al., 2011), est notre capacité à déterminer l'importance relative du mélange près des bords (*boundary mixing* en anglais) sur le budget de mélange total du golfe du Saint-Laurent. Dans cette étude, nous avons tout d'abord quantifié l'érosion de la CIF à partir de profils historiques de température et de salinité. Nous avons ensuite quantifié le mélange à partir de nouveaux profils de turbulence réalisés au cours de la thèse. Nous avons déterminé qu'environ deux-tiers du mélange nécessaire à l'érosion de la CIF est assuré par la turbulence à l'intérieur du bassin, alors que le dernier tiers pourrait être assuré par des processus turbulents qui prennent place près des bords. Contrairement aux études précédentes sur le mélange en océans côtiers qui suggèrent plutôt que la turbulence intérieure est la principale source du mélange, nous avons trouvé que le mélange aux frontières est non-négligeable dans le golfe du Saint-Laurent.

Chapitre 2 : Behavior and mixing of a cold intermediate layer near a sloping boundary

Le résultat principal de cet article soumis au journal *Ocean Dynamics*, est la démonstration que le comportement de la CIF près du bord nord de l'estuaire maritime est le résultat de marées internes générées une centaine de kilomètres en amont. Ce résultat à été obtenu à partir du déploiement d'un mouillage à haute résolution spatio-temporelle près du bord nord de l'estuaire pendant trois semaines à l'automne 2011. De plus, le mélange turbulent quantifié à partir de 322 profils de turbulence révèle que les derniers 10 m de la colonne d'eau dissipent l'énergie cinétique turbulente à un taux de $\epsilon_{10\,\mathrm{m}} = 1.6 \times 10^{-7}\,\mathrm{W\,kg^{-1}}$, soit un ordre de grandeur plus élevé que dans l'intérieur de l'estuaire, loin des bords. Les observations suggèrent

aussi que la dissipation durant le flot est quatre fois plus grande que durant le jusant. Les contraintes sur le fond, les instabilités de cisaillement et les ondes internes sont considérés comme mécanismes de mélange.

Chapitre 3 : Turbulent nitrate fluxes at the head of the Laurentian channel

Dans cet article soumis à *Journal of Geophysical Research*, nous avons quantifié les flux verticaux de nitrate à la tête du chenal Laurentien, lieu reconnu dans le Saint-Laurent pour le vigoureux mélange turbulent qui s'y trouve. Ces flux ont été calculés à partir de profils historiques de concentration de nitrate et de nouveaux profils de turbulence issus d'une campagne de terrain effectuée en 2009. Les flux verticaux ont été comparés pour deux stations, soit la limite en amont du chenal Laurentien (la tête du chenal ou station 25) et la station Rimouski (station 23) située environ 100 km en aval. Les diffusivités turbulentes ainsi que les flux de nitrate à la base de la couche du surface sont respectivement $\overline{K}_{\text{st. 25}} = 4.5(1.1, 13) \times 10^{-2}\,\text{m}^2\,\text{s}^{-1}$, $\overline{K}_{\text{st. 23}} = 4.4(2.3, 7.6) \times 10^{-5}\,\text{m}^2\,\text{s}^{-1}$, $\overline{F}_{\text{st. 25}} = 120(23, 400)\,\text{mmol}\,\text{m}^{-2}\,\text{d}^{-1}$ et $\overline{F}_{\text{st. 23}} = 0.21(0.12, 0.33)\,\text{mmol}\,\text{m}^{-2}\,\text{d}^{-1}$. Les nombres entre parenthèse indiquant les limites de l'intervalle de confiance à 95% sur la moyenne. Les observations suggèrent que la combinaison entre déplacements verticaux des isopycnes et fort mélange dans les premiers 60 m de la colonne d'eau est la clé permettant de soutenir les importants flux à la station 25 (deux à trois ordres de grandeur plus élevé que ceux de la station 23). Un calcul d'ordre de grandeur suggère aussi que bien que ce flux pourrait soutenir la majeure partie du bloom phytoplanctonique printannier et la production estivale post-bloom dans l'estuaire maritime. Ce calcul suggère aussi que la majorité des nitrates refaisant surface sont consommés dans l'estuaire maritime du Saint-Laurent au lieu d'être exportés dans le golfe.

ARTICLE I

INTERIOR VERSUS BOUNDARY MIXING OF A COLD INTERMEDIATE LAYER

1.1 Abstract

The relative importance of interior versus boundary mixing is examined for the erosion of the cold intermediate layer (CIL) of the Gulf of St. Lawrence. Based on 18 years of historical temperature profiles, the seasonal erosion of the core temperature, thickness and heat content of the CIL are, respectively, $\dot{T}_{\min} = 0.24 \pm 0.04\,^{\circ}\mathrm{C\,mo^{-1}}$, $\dot{d}_{\min} = -11 \pm 2\,\mathrm{m\,mo^{-1}}$ and $\dot{H} = 0.59 \pm 0.09\,\mathrm{MJ\,m^{-3}\,mo^{-1}}$. These erosion rates are remarkably well reproduced with a one-dimensional vertical diffusion model fed with turbulent diffusivities inferred from 892 microstructure casts. This suggests that the CIL is principally eroded by vertical diffusion processes. The CIL erosion is best reproduced by mean turbulent kinetic energy dissipation rate and eddy diffusivity coefficient of $\epsilon \simeq 2 \times 10^{-8}\,\mathrm{W\,kg^{-1}}$ and $K \simeq 4 \times 10^{-5}\,\mathrm{m^2\,s^{-1}}$, respectively. It is also suggested that while boundary mixing may be significant it may not dominate CIL erosion. Interior mixing alone accounts for about 70% of this diffusivity with the remainder being attributed to boundary mixing. The latter result is in accordance with recent studies that suggest that boundary mixing is not the principal mixing agent in coastal seas.

1.2 Introduction

Cold intermediate layers (CILs) are common summer features of many subarctic coastal seas. Such water masses are found for example in the Black Sea (Tuzhilkin, 2008), the Baltic Sea (Chubarenko and Demchenko, 2010), the Bering Sea (Kostianoy et al., 2004) the Sea of Okhotsk (Rogachev et al., 2000), the Gulf of St. Lawrence (Banks, 1966) and can also be found in coastal oceans (Petrie et al., 1988). At formation, CILs may represent up to 45% of the total water volume of those systems (e.g., Galbraith, 2006) and therefore largely control the state and climate of subarctic coastal systems as well as the marine ecology (Ottersen et al., 2004).

The characteristics of CILs are principally governed by the properties of the surface mixed layer formed during the previous winter (Gilbert and Pettigrew, 1997; Gregg and Yakushev, 2005; Galbraith, 2006; Smith et al., 2006a). The CIL is formed when this surface mixed layer becomes insulated from the atmosphere by near-surface stratification caused by sea-ice melt, heat fluxes and increased runoff at the onset of spring. Other mechanisms such as horizontal/intra-layer convection may also contribute to CIL formation (Chubarenko and Demchenko, 2010).

Most previous studies on CILs have focused on formation mechanisms but there is little published information about the summer deterioration of their properties by mixing processes, later recalled as *erosion*. One particularity of CILs is that since they lie at intermediate depths, away from surface and bottom boundary layers, one may hypothesize that their erosion is principally governed by interior mixing processes. However, CILs also intersect the sloping bottom around lateral boundaries where turbulent processes may be much more intense than within the interior. While the fraction of CIL volume in contact with the sloping bottom may be small the role of boundary mixing may still be important if turbulence is sufficiently large. This is analogous to the boundary mixing hypothesis proposed by Munk (1966) and Munk and Wunsch (1998) for the abyssal ocean but applied here to coastal seas. The idea

of boundary mixing has been considered for mixing in sill fjords (Stigebrandt, 1976, 1979) and estuaries (Bourgault and Kelley, 2003; Bourgault et al., 2008) with the hypothesis that breaking internal waves along sloping boundaries is the main mixing agent. It has also been proposed that boundary mixing may be the main contributor to the mixing budget of lakes (Goudsmit et al., 1997), where wind-induced seiches are the principal driving mechanism, and to that of coastal seas with virtually no tides such as the Baltic Sea (see Reissmann et al., 2009, for a review). Other studies have however concluded that mixing in coastal seas is predominantly driven by interior rather than boundary processes (e.g., MacKinnon and Gregg, 2003; Rippeth, 2005; Palmer et al., 2008).

Another interesting aspect of CILs is that they can be considered as passive tracers when the buoyancy-driven circulation of coastal seas is principally driven by salinity gradients. In this case, CILs are analogous to the yearly realization of a large-scale dye release experiment. Under this hypothesis, the CIL fills uniformly the entire sea and can only be modified, or eroded, by vertical turbulent processes.

The objectives of this study are to examine whether vertical mixing alone can explain CIL erosion rates and, if so, to determine the relative importance of boundary versus interior mixing. To reach these objectives, we examine the erosion of the CIL in the Gulf of St. Lawrence using 18 years of historical CTD data, new turbulence measurements (892 casts) collected during summers 2009-2010 and a one-dimensional heat diffusion model. The historical CTD observations are used to provide statistics on CIL erosion rates and the turbulence measurements are used to provide eddy diffusivity values used in the one-dimensional model. After assessing the model we examine the relative importance of interior versus boundary mixing by comparing the modeled CIL erosion rates with and without considering diffusivity values measured near boundaries. The results are then interpreted based on a geometric scaling from which an effective eddy diffusivity is inferred and the relative contribution of boundary versus interior CIL mixing is determined.

1.3 The Gulf of St. Lawrence

The Gulf of St. Lawrence, including the estuary, is an area of about 236 000 km^2 opened to the Atlantic Ocean through Cabot Strait and the Strait of Belle Isle (Fig. 2). The bathymetry is characterized by deep channels (> 200 m), large shelves and islands. The main channel, called the Laurentian Channel, is a submarine glacial valley that runs from Tadoussac to the continental slope, past Cabot Strait (Fig. 2). The residual circulation in this channel is estuarine-like, principally driven by the freshwater discharge of the St. Lawrence River and other surrounding rivers (e.g., Koutitonsky and Bugden, 1991). In winter, the water column exhibits a 2-layer structure with a 40-150 m thick surface mixed layer with temperature near the freezing point (Galbraith, 2006) overlying a warmer (1-6 °C) but saltier (> 33 psu) bottom layer of oceanic origin (roughly 150 m-bottom). The rest of the year, the water column is characterized with three layers with the CIL sandwiched between the warmer surface and bottom layers (Koutitonsky and Bugden, 1991).

The CIL is characterized by near-freezing temperatures (T) and salinities (S) of 32-33 psu. Although the Gulf of St. Lawrence CIL is frequently mentioned in the literature, its definition varies between authors. For instance, Lauzier and Bailey (1957) used $T \leq 0$ °C as their definition. Other authors have used other definitions such as $T \leq 1.5$ °C (Banks, 1966; Bugden et al., 1982), $T \leq 3$ °C (Gilbert and Pettigrew, 1997; Smith, 2005) or more recently $T \leq 1$ °C (Galbraith et al., 2011). Since the focus here is on the CIL erosion during ice-free months, we adopted the latter definition which approximately defines the coldest limit of what remains at the end of our study period, i.e., when the CIL is replenished the following winter.

The CIL renewal occurs in winter when the surface mixed layer deepens following a combination of cold air temperature, wind-driven mixing and, to a lesser extent, brine rejection due to sea ice formation (Galbraith, 2006). While the CIL is found throughout the Gulf, its presence at a given location may be due to horizontal advection from a remote formation

site rather than resulting from local formation. For example, the region roughly located between Tadoussac and Pointe-des-Monts is too stratified, due to important freshwater input, to allow for winter convection and CIL formation (Ingram, 1979b; Galbraith, 2006; Smith et al., 2006b).

While insights about CIL formation mechanisms were gained from previous field and modeling studies cited above, still little is known about CIL erosion mechanisms and rates. Based on 10 years of data from three regions of the Gulf (Honguedo Strait, Central Gulf and Cabot Strait), Banks (1966) found that from April to November the CIL minimum temperature ($T_{\min}$) warms, on average, by $0.2\,^{\circ}\mathrm{C\,mo^{-1}}$. Based on a similar analysis but using 47 years of data from five regions, Gilbert and Pettigrew (1997) obtained CIL erosion rates ranging from $0.08\,^{\circ}\mathrm{C\,mo^{-1}}$ for the Central Gulf to $0.30\,^{\circ}\mathrm{C\,mo^{-1}}$ for the Estuary. This study also revisits these warming rates.

1.4 Datasets and methodology

1.4.1 CTD data

The CTD dataset was collected at a station named *Rimouski* and located at 48° 40′ N 68° 35′ W, about 25 km north of the city of Rimouski (Fig. 2). Thereafter, we will refer to this station as the interior station, i.e. a station in deep water (> 300 m) away from lateral boundaries. This dataset consists of 418 casts collected by Maurice-Lamontagne Institute staff (Fisheries and Oceans Canada, DFO) between 1993 and 2010 and obtained through the DFO Oceanographic Data Management System (Fisheries and Oceans - Canada, 2011). The station is typically visited once a week during ice-free months (Plourde et al., 2008) and, for the purpose of this study, only casts sampled between April and November have been selected. Temperature and salinity profiles were averaged into 1 m vertical bin size and all profiles of the same month have been averaged into a single monthly climatological profile (Fig. 3 and 4). The 95 % confidence intervals on the monthly averaged profiles have

been estimated by performing 500 bootstrap replicates of each monthly sampling (Efron and Gong, 1983).

Using this climatology, the depth-averaged volumetric heat content of the CIL was calculated as

$$H = \frac{1}{d}\int_{z_t}^{z_b} \rho c_p (T - T_f) dz \text{ for } T < 1\,^{\circ}C, \tag{1.1}$$

where d is the CIL thickness, z_t and z_b are, respectively, top and bottom limits of the layer, ρ is density determined from the equation of state of the seawater (Fofonoff and Millard, 1983) and $c_p = 4.00\,\mathrm{kJ\,kg^{-1}\,^{\circ}C^{-1}}$, the specific heat of sea water, is considered constant. For convenience, the heat content is calculated relative to the typical freezing point temperature of sea water $T_f = -1.8\,^{\circ}\mathrm{C}$.

1.4.2 Sea surface temperature (SST)

Since 2002, a meteorological buoy has been deployed at Rimouski station by the Maurice-Lamontagne Institute (DFO), usually from May to November when it then acquires data of various type every 15 minutes (Fisheries and Oceans - Canada, 2011). Among them, SST is measured at 0.5 m below sea surface with a SBE-37SI, a temperature sensor manufactured by Sea-Bird Electronic. In this study, SSTs are used to provide boundary conditions to a one-dimensional model of heat diffusion presented in section 1.6.

1.4.3 Turbulence measurements

Turbulence measurements were collected with two free-fall, loosely-tethered, vertical microstructure profilers (VMP500) manufactured by Rockland Scientific International (RSI). Together with standard Sea-Bird Electronic CTD sensors, the VMPs are equipped with

a micro-fluorescence/turbidity sensor, two fast-response thermistors and two airfoil shear probes which allow measurements of micro-scale vertical shear u_z'. One of the VMP also has a micro-conductivity sensor. All microstructure sensors sample at 512 Hz while the CTD samples at 64 Hz. See Bourgault et al. (2008) for more details on sensors and probes.

Our dataset consists of 73 casts from 6 sorties done in July and September 2009 and 819 casts from 26 sorties done between May and October 2010. Most of these sorties were realized opportunistically, depending on weather and boat availability, except for a 10-day survey accomplished in July 2010. Two small craft boats, each carrying a VMP, were then mobilized to carry out sampling across the channel on a section passing through the Rimouski interior station. Overall, 420 casts out of 892 were realized within 5 km of Rimouski station (Fig. 2). All together, these casts have no bias towards any phase of the M_2 tide cycle and are slightly biased toward neap tide (not shown). Uncertainties in mean quantities caused by this bias will be reflected in our analysis below through 95% confidence intervals obtained by bootstrapping. All surveys were carried out in relatively calm sea conditions. The wind speed was generally less than 20 km h^{-1} and wave heights less than 1 m.

Assuming isotropic turbulence, the dissipation rate (ϵ) of turbulent kinetic energy was calculated, using standard procedures (e.g., Lueck et al., 2002), as

$$\epsilon = \frac{15\nu}{2}\overline{\left(u_z'\right)^2}, \tag{1.2}$$

where $\nu = f(T)$ is the kinematic molecular viscosity as function of temperature and the overline indicates here a 5-m scale spatial average. The shear variance $\left(u_z'\right)^2$ was obtained by spectral integration to remove random noise. Eddy diffusivity coefficients were calculated as (Osborn, 1980)

$$K = \Gamma\frac{\epsilon}{N^2}, \tag{1.3}$$

where Γ is the dissipation flux coefficient and N is the 5-m scale background buoyancy frequency. Using $\Gamma = 0.2$, (Osborn, 1980; Moum, 1996), an upper bound for the eddy diffusivity coefficient was determined. An estimation of the 95 % confidence intervals of the mean turbulence profile was obtained by performing 500 bootstrap replicates of the sampling set.

1.5 Observations

1.5.1 CIL characteristics and variability

The CIL structure and variability for the 1993-2010 period can be qualitatively appreciated in Fig. 5. During spring, the CIL is roughly 50-100 m thick and centered around 60 m. It persists throughout summer and fall until it becomes regenerated and replenished the following winter. The temperature field within the CIL exhibits important intraseasonal variability. For example, in 2001 isotherms displacement reached 50 m and the minimum CIL temperature varied by $\sim$ 1 °C on monthly timescales. The CIL even disappeared, according to our definition, for a 2-week period at the beginning of July. A striking feature often occurs in fall (e.g., 2004, 2007 and 2009), when within about a week, the CIL suddenly plunges downward by approximately 50 m. The origin of these intraseasonal variations is unknown and will not be addressed in this study.

The evolution of monthly averaged profiles reveal that the temperature (Fig. 3) and the salinity (Fig. 4) of the surface layer increases from April to August. While the salinity of this layer continues to increase from September to November, the layer rapidly cools and deepens during the same period. Underneath the surface layer, that is under 50 m, the CIL temperature minimum increases from April to November while the salinity stays relatively constant. We interpret this as an indication that the mid-depth salinity field is approximately in steady state ($\frac{\partial S}{\partial t} \simeq 0$) during ice-free months, likely due to a balance between longitudinal advection and vertical diffusion. Unlike the salinity, no equivalent compensating source of cold water can feed the CIL once it has been replenished during winter. The CIL thus acts like a passive

tracer, being slowly mixed by vertical diffusion.

The monthly climatology of the temperature distribution within the CIL (Fig. 3) can be synthesized in a single contourplot that reveals the general characteristics of the CIL and its seasonal erosion (Fig. 6a). From April to November the CIL thickness steadily decreases while the minimum temperature increases. This erosion can be quantified by examining the evolution of the climatological minimum temperature of the CIL $T_{\min}$ (Fig. 7a), which increases linearly at a rate of $\dot{T}_{\min} = 0.24 \pm 0.04\,^{\circ}\mathrm{C\,mo^{-1}}$, as determined by performing linear best fits to the climatological timeseries. The error reported is the standard error determined by bootstrap analysis (Efron and Gong (1983)). The erosion of the CIL can also be quantified by the rate of its thickness decrease which is $\dot{d} = -11 \pm 2\,\mathrm{m\,mo^{-1}}$ (Fig. 7b). Finally, the seasonal change in CIL mean heat content is $\dot{H} = 0.59 \pm 0.09\,\mathrm{MJ\,m^{-3}\,mo^{-1}}$ (Fig. 7c). Note that the sudden fall deepening events of the CIL observed in Fig. 5 clearly show up in the monthly temperature climatology (Fig. 6a) and also in the climatological evolution of CIL core depth (Fig. 7d). The CIL also shows interannual variability of the warming rate of the CIL core (Fig. 8), reaching values as high as $\dot{T}_{\min} = 0.30\,^{\circ}\mathrm{C\,mo^{-1}}$ (1999 and 2004) and as low as $\dot{T}_{\min} = 0.15\,^{\circ}\mathrm{C\,mo^{-1}}$ (1997 and 2003). Note that years 2009 and 2010, i.e., the years that turbulence was sampled were climatologically close-to-normal (Fig. 8).

1.5.2 Turbulence

A typical VMP cast is shown in Fig. 9 providing profiles of temperature T, density ρ, microstructure shear u_z', turbulent dissipation rate ϵ and eddy diffusivity K. Turbulence within the CIL (gray intervals in Figure 9) is typically low compared to patches of much higher dissipation often found in the top 50 m or so of the water column.

Turbulence measurements collected in 2009 and 2010 are synthesized in Fig. 10. Two series of mean profiles are presented, i.e., the average of all available casts (892), including interior and boundary regions (dark gray, solid line), and the average of interior casts only

(light gray, dashed-line). Globally, highest dissipation rates and diffusivities are found in the top 20 m or so of the water column with values reaching $\epsilon \sim 10^{-6}\,\mathrm{W\,kg^{-1}}$ and $K \sim 10^{-3}\,\mathrm{m^2\,s^{-1}}$. Under 20 m, there is a decreasing trend of the dissipation and the diffusivity with depth; the increase in dissipation and diffusivity observed near 130 m likely comes from the numerous turbulence casts made on the shelf that passed through the bottom boundary layer at that depth. When considering only interior casts (420), the mean dissipation rate and diffusivity underneath the surface layer (20-180 m) are, respectively, $\overline{\epsilon}_i = 1.3\,(0.9,\ 1.7) \times 10^{-8}\,\mathrm{W\,kg^{-1}}$ and $\overline{K}_i = 2.4\,(1.5,\ 3.5) \times 10^{-5}\,\mathrm{m^2\,s^{-1}}$, where the numbers in parentheses are the bootstrap 95 % confidence intervals. When considering all available casts (892), the mean dissipation and diffusivity for the same depth range are respectively $\overline{\epsilon}_a = 1.9\,(1.3,\ 2.8) \times 10^{-8}\,\mathrm{W\,kg^{-1}}$ and $\overline{K}_a = 4.3\,(2.6,\ 6.6) \times 10^{-5}\,\mathrm{m^2\,s^{-1}}$, i.e., respectively 1.5 and 1.8 times higher than when considering only interior casts.

These diffusivities are close to an order of magnitude greater than that previously inferred by Bugden (1991) from least square fit on temperature data in the Gulf between 200-300 m and on the same order than that inferred by Ingram (1979b) near Tadoussac in the 50-100 m depth range.

1.6 Heat diffusion model

1.6.1 Model description

We now examine with a one-dimensional heat diffusion model whether the turbulence measured during calm conditions could explain the observed climatological CIL erosion rates. With this approach we neglect horizontal advection under the assumption that only vertical turbulent mixing can redistribute heat within the water column.

The model numerically solves the following equation for the temporal evolution of the water column temperature $T(z,t)$ (e.g. Kundu and Cohen, 2007)

$$\frac{\partial T}{\partial t} = \frac{\partial}{\partial z}\left(K\frac{\partial T}{\partial z}\right), \tag{1.4}$$

where K is the eddy diffusivity of heat taken here to be equivalent to the eddy diffusivity of mass as defined in Equation 1.3 (Thorpe, 2007). Eddy diffusivity is assumed to be variable with depth but constant in time, i.e, $K = K(z)$.

Equation 1.4 is solved numerically with a first-order Euler scheme on a grid size $\Delta z = 1\,\text{m}$ and using a time step $\Delta t = 100\,\text{s}$. The vertical resolution thus adequately resolve the different layers and fits the resolution of CTD bins. The time step respects the Courant-Friedrich-Levy stability condition. A no-flux boundary condition is applied at the sea bottom fixed at $z = 300\,\text{m}$. A daily climatological sea surface temperature (SST) is imposed as boundary conditions at the top of the water column. This climatology was evaluated over the period 2002-2009 using observations from the oceanographic buoys (Fisheries and Oceans - Canada, 2011) and interpolated to the model time step Δt. Equation 1.4 was initialized with the climatological temperature profile for April (Fig. 3).

Two simulations were carried out with different heat diffusivity profiles. The first simulation uses the mean interior diffusivity profile K_i, while the second uses the mean diffusivity profile of all casts collected across the channel, i.e., K_a (Fig. 10). Since no casts were done deeper than about 180 m, K_i and K_a are extended to 300 m using a constant value equal to the minimum value of the mean profile.

Note that this model is designed to examine the average seasonal evolution of the temperature structure and not a particular year. For this reason, the model is forced with quasi climatological boundary conditions. For consistency, a climatological profile of eddy diffusivity should also be used. However, such statistics are not available. We therefore work under the assumption that the turbulence measured in 2009 and 2010 are representative of long-term mean conditions. This appears to be a reasonable assumption given that years 2009-2010 were subject to close-to-normal erosion rates (Fig. 8).

1.6.2 Results

While the model has difficulties to reproduce the evolution of the surface layer above 50 m (see Doyon et al. (2000) for a similar model of the surface mixed layer) it reproduces qualitatively well the CIL from April to November (Fig. 6 and 11). Overall, the simulation using K_a better reproduces the observations except perhaps for the month of June where using K_i offers a slight improvement (Fig. 11). The better performance of the model with K_a instead of K_i is also seen when examining a space-time contour plot of $T(z,t)$ (Fig. 6).

Quantitatively, the simulation with K_a reproduces remarkably well, i.e., within the uncertainties, the CIL erosion rates (Fig. 12 and Table 1). In this case, the modeled and observed erosion rates (i.e., $\dot{T}_{\min}$, $\dot{d}$ and $\dot{H}$) agree to within 8% or better. On the other hand, using only the interior diffusivity K_i accounts for about 65% of the observed erosion rates.

1.7 Discussion

Our analysis suggests that interior diffusivity during calm wind conditions (Fig. 10) accounts for about 65% of the mid-channel CIL erosion rate (Table 1). However, the apparent missing mixing is recovered when all profiles collected throughout the section are included in the analysis. This suggests that non-local boundary mixing processes, although not dominant, may contribute significantly to mid-channel erosion.

With this in mind, we now examine the role that boundary mixing may play in eroding the CIL at mid-channel. We start by assuming that, on monthly time-scales, there is a continuous exchange of properties along isopycnals between boundaries, where the CIL intersects the sloping bottom and the interior. Inspired by Armi (1978), Garrett and Gilbert (1988),Garrett et al. (1993) and Toole et al. (1997), we estimate the effective diffusivity coefficient using the following geometric scaling

$$K_e = K_b \frac{A_b(z, h_b)}{A(z)} + \tilde{K}_i \frac{A_i(z, h_b)}{A(z)}, \tag{1.5}$$

where K_e is the effective diffusivity coefficient at depth z, while K_b and $\tilde{K}_i$ are, respectively, constant diffusivity coefficients within the bottom boundary layer and in the interior, and h_b the bottom boundary layer thickness. Similarly, $\frac{A_b}{A}$ and $\frac{A_i}{A} = 1 - \frac{A_b}{A}$ are respectively the fraction of the CIL inside and outside the bottom boundary layer of thickness h_b at depth z (Fig. 13). Note that unlike the previously cited authors, we kept in the formulation for K_e the contribution from interior mixing (i.e., the second term in Equation 1.5), since we have indications that boundary mixing is not dominant in front of interior mixing.

The thickness of the bottom boundary layer h_b was visually-inferred by inspecting the vertical structure of the dissipation rates ϵ of 150 casts that hit the bottom out of the 892 (Fig. 14). On average, these measurements show an approximate exponential growth of ϵ towards the bottom, starting at about 10 m above the bottom. Based on these measurements we set $h_b = 1 \times 10^1$ m.

Considering the climatological CIL limits from our observations (Fig. 6a) and assuming that the depth spanned by the CIL is uniform across the section, the fraction of the CIL area within the bottom boundary layer varies between 2-3% between April and October (the CIL has disappeared by November according to our climatology). In other words,

$$\overline{\left(\frac{A_b(z, h_b)}{A(z)}\right)} = \overline{\frac{1}{(z_t - z_b)} \int_{z_t}^{z_b} \frac{A_b(z, 10\,\mathrm{m})}{A(z)} \, \mathrm{d}z} \simeq 3\%,$$

where z_t and z_b are the climatological CIL limits and the overline indicates an average in time between April and October.

We extracted from our measurements the mean diffusivity that is within the bottom boundary layer ($h_b = 1 \times 10^1$ m) using casts that reached the bottom. This yielded $K_b = 3.3(2.1, 4.8) \times 10^{-4}\,\mathrm{m^2\,s^{-1}}$. Letting $\tilde{K}_i = \overline{K}_i = 2.4\,(1.5,\ 3.5) \times 10^{-5}\,\mathrm{m^2\,s^{-1}}$, i.e. the measured

interior diffusivity (Section 1.5.2), Equation 1.5 gives $K_e = 3.3 \times 10^{-5}\,\mathrm{m^2\,s^{-1}}$. This value is slightly lower, but within confidence intervals, than $\overline{K}_a = 4.3\,(2.6,\ 6.6) \times 10^{-5}\,\mathrm{m^2\,s^{-1}}$, i.e., the depth-averaged diffusivity of all profiles collected across the section (Section 1.5.2). We note also that both terms in Equation 1.5 are significant in the mixing budget, but their contribution to the effective diffusivity is not the same. Our scaling suggests that the interior mixing supplies 70% of the effective diffusivity while the boundary mixing supplies the remaining 30%. We conclude from this analysis that boundary mixing may contribute to the CIL erosion observed at mid-channel but that its role is not dominant in front of interior mixing.

To examine whether this analysis is relevant to a broader geographical context, we calculated the fraction of the volume of the CIL found within the bottom boundary layer throughout the Gulf of St. Lawrence. This calculation was done using historical CIL data for the months of August and September between 1995 and 2010 (see Galbraith et al., 2011; Tamdrari et al., 2012, for details) and assuming a 10-m thick bottom boundary layer throughout the Gulf. The result suggests that, on average, 6 ± 1% of the Gulf's CIL is within the bottom boundary layer. This fraction is about twice as large as the value inferred from our sampling section. This suggests that boundary mixing may be more important throughout the Gulf than at our sampling section off Rimouski. This possibility is highlighted when examining the area throughout the Gulf where the CIL intersects the sloping bottom (Fig. 15). On average during this period, the CIL is in contact with approximately 30% of the Gulf's seabed. Regions where the CIL reached the seabed more often are located in the Southern Gulf (Bradelle and Orphan Banks), Northeastern Gulf and the bank off of the western tip of Anticosti Island. These regions may therefore contribute substantially to CIL erosion.

1.8 Conclusion

Two goals were pursued in this study: 1) to test a model of vertical diffusion for the erosion of a CIL and; 2) to discuss the importance of boundary versus interior mixing on

this erosion. The seasonal erosion of the core temperature, thickness and heat content of the Gulf of St. Lawrence CIL off Rimouski are, respectively, $\dot{T}_{\min} = 0.24 \pm 0.04\,^{\circ}\mathrm{C\,mo^{-1}}$, $\dot{d}_{\min} = -11 \pm 2\,\mathrm{m\,mo^{-1}}$ and $\dot{H} = 0.59 \pm 0.09\,\mathrm{MJ\,m^{-3}\,mo^{-1}}$. These rates are remarkably well reproduced with a one-dimensional diffusion model fed with observed turbulent diffusivities. This suggests that the CIL is principally eroded by vertical diffusion processes. Our analysis further suggests that interior mixing processes contribute to approximately 70% to this erosion with the remaining being attributed to boundary mixing. This conclusion supports recent studies (e.g., MacKinnon and Gregg, 2003; Rippeth, 2005; Palmer et al., 2008) that also proposed that boundary mixing may not be the predominant mixing source in coastal seas. However, it would be relevant to extend this study to other regions of the Gulf where boundary mixing may be more important.

It is unclear at this point what mixing mechanisms operate either in the interior or at boundaries. Given that our analysis is based on observations collected during calm wind conditions leads us to believe that wind plays a secondary role in eroding the CIL. Internal shear associated with the internal tide that can cause up to 20 m isopycnal displacement is the most likely candidate for producing turbulence in the interior. Near sloping boundaries where the CIL intersects the bottom, internal wave breaking and bottom shear stresses are likely at work. It is not possible to conclude at this point on the modulation of the mixing with the M_2 and neap/spring tide cycles. Preliminary results (not presented) however suggest that while the neap/spring cycle has no incidence on the interior mean diffusivity, it can modulate the mean diffusivity at boundaries by up to a factor of two. However, new field experiments are required to make further progress in those directions.

1.9 Acknowledgments

This work was funded by “Le Fonds de recherche du Québec - Nature et technologies”, the Natural Sciences and Engineering Research Council of Canada, the Canada Foundation

for Innovation and Fisheries and Oceans Canada. The authors would also like to thank Pierre Joly and his collaborators for their sampling effort since 1993, now part of the Atlantic Zonal Monitoring Program, as well as the technicians and students who helped in our 2009 and 2010 summer campaigns: Bruno Cayouette, Rémi Desmarais, Gilles Desmeules, Sylvain Leblanc, Camil Hamel, Joachim Bobinet and Guillaume Turbide.

	$\dot{T}_{\min}$ (°C mo^{-1})	$\dot{d}$ (m mo^{-1})	$\dot{H}$ (MJ m^{-3} mo^{-1})
climatology of observations	0.24	-11	0.59
model, K_i	0.16	-7	0.46
model, K_a	0.22	-12	0.63

Table 1: Slopes of linear best fits for Fig. 12. The three columns are respectively the CIL core temperature warming rate, the CIL thinning rate and the rate of increase in CIL heat content. Each is calculated for the climatology of CTD observations (1993-2010), the modeled temperature diffusion using respectively the interior diffusivity profile K_i and the mean diffusivity profile from all available casts K_a.

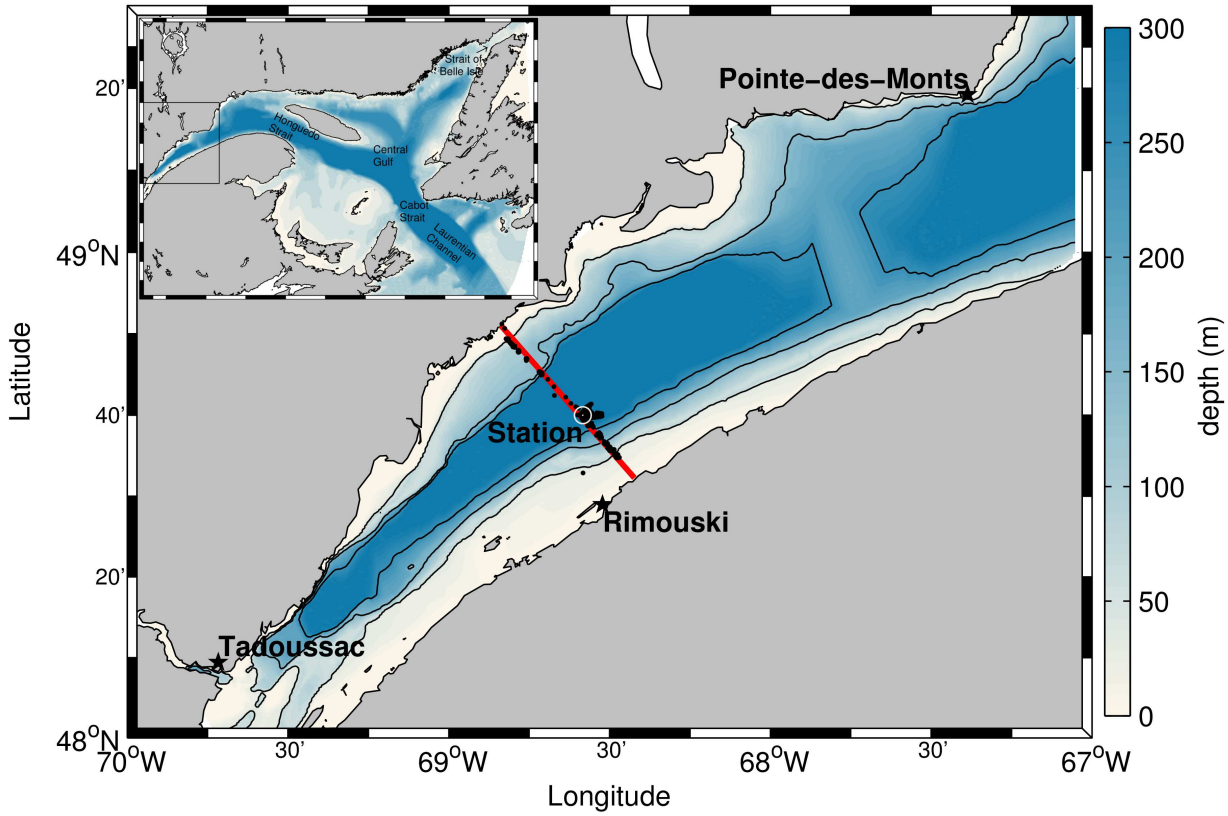

Figure 2: Location of 892 VMP casts (black dots) and bathymetric features of the St. Lawrence Estuary (main figure) and the Gulf of St. Lawrence (inset). The black contour lines are the 50, 150 and 250 m isobaths. Rimouski station is identified with a white circle superimposed over the maximum profile concentration. The red line is the section referred to in Fig. 13 and where sampling was performed during 10 days in July 2010.

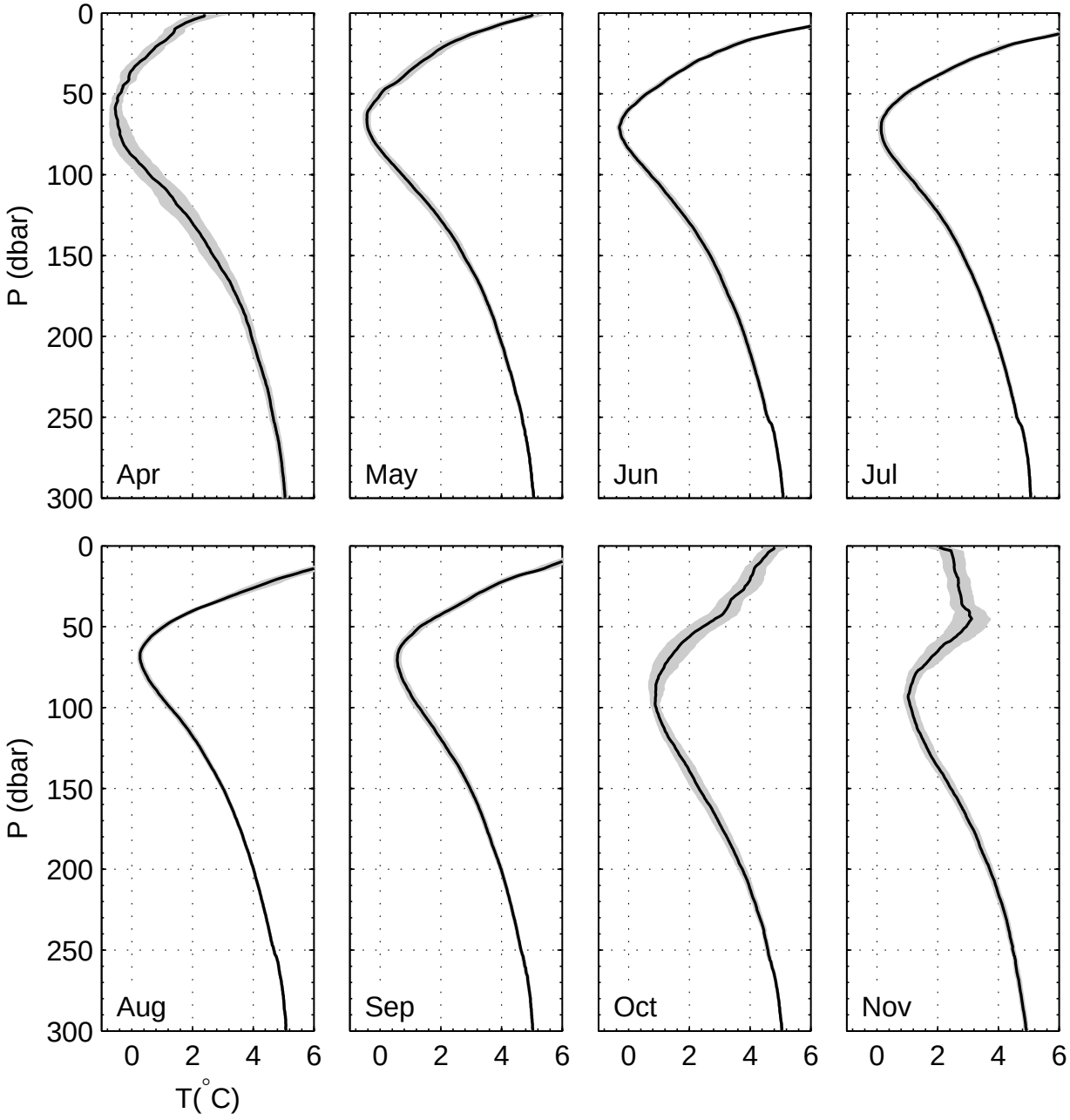

Figure 3: Monthly mean temperature profiles calculated from April to November over the period 1993-2010 from the CTD casts of Fig. 5. The gray shadings are the 95% confidence intervals

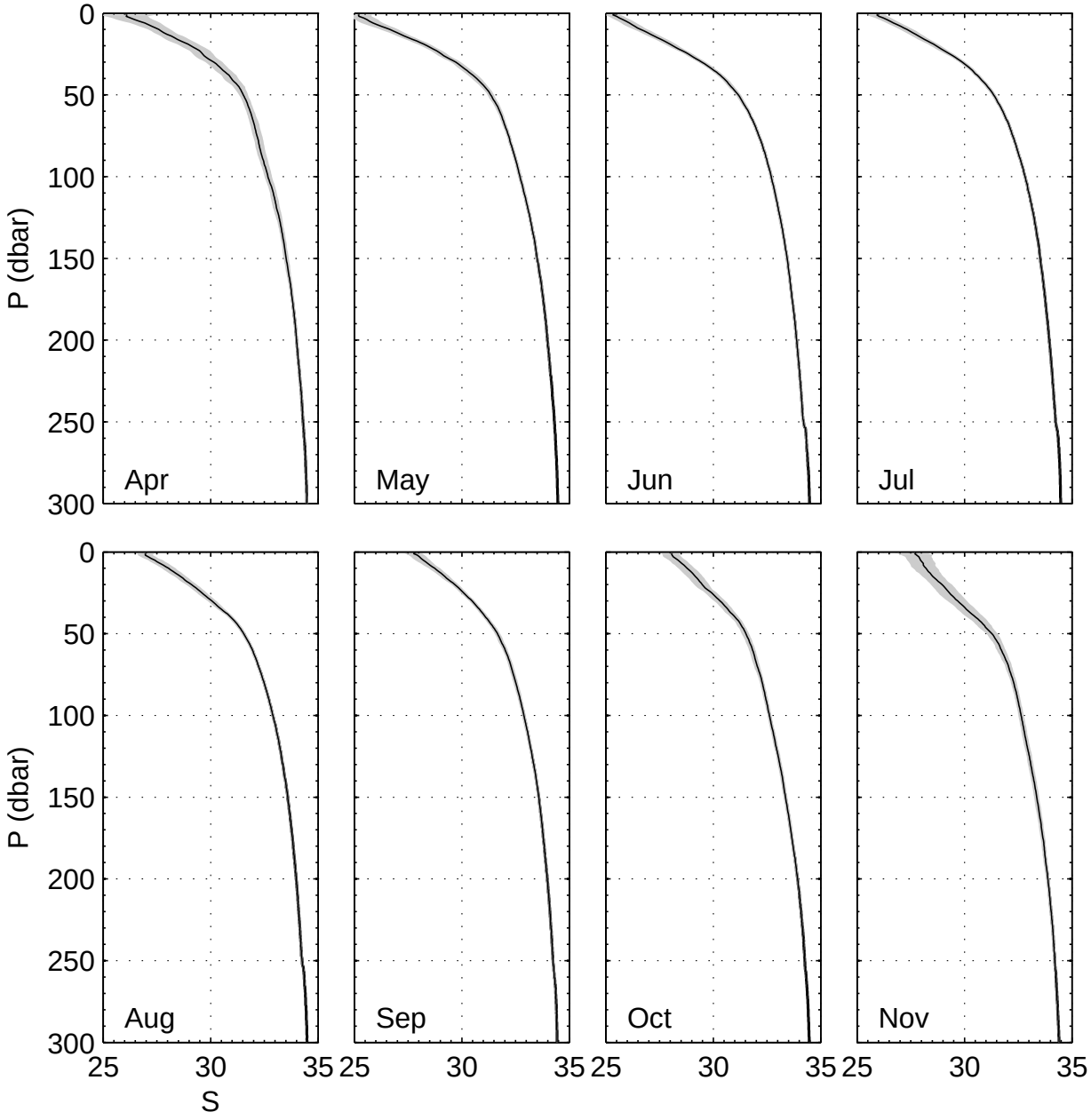

Figure 4: Monthly mean salinity profiles calculated as in Fig. 3.

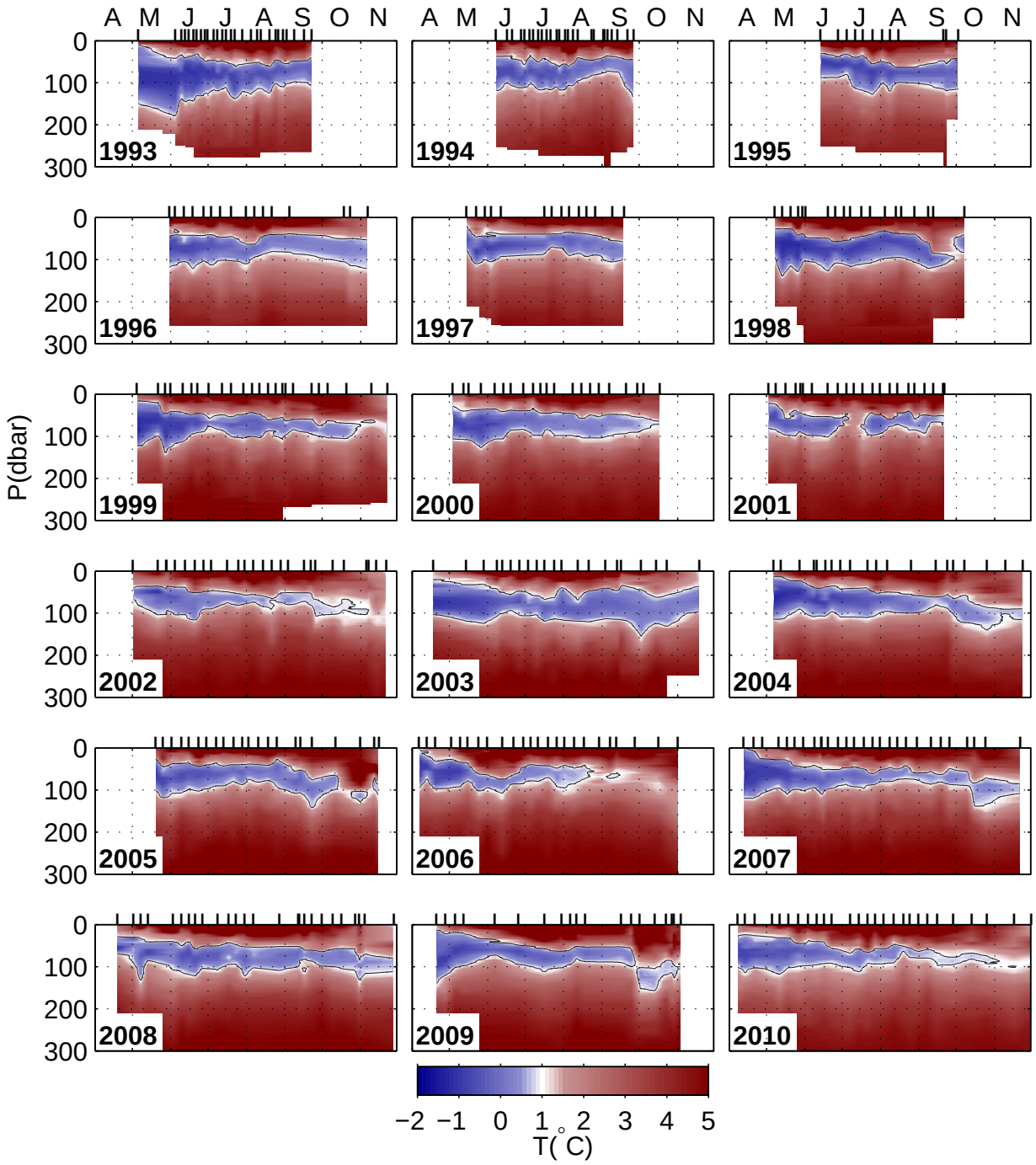

Figure 5: Evolution of temperature profiles from April to November, linearly interpolated from 418 CTD casts that are indicated by lines at the top of each panel. To focus on the CIL, the color scale is saturated at 5°C while summer surface temperature can reach more than 10°C, and 1°C isotherms are highlighted with a black contour.

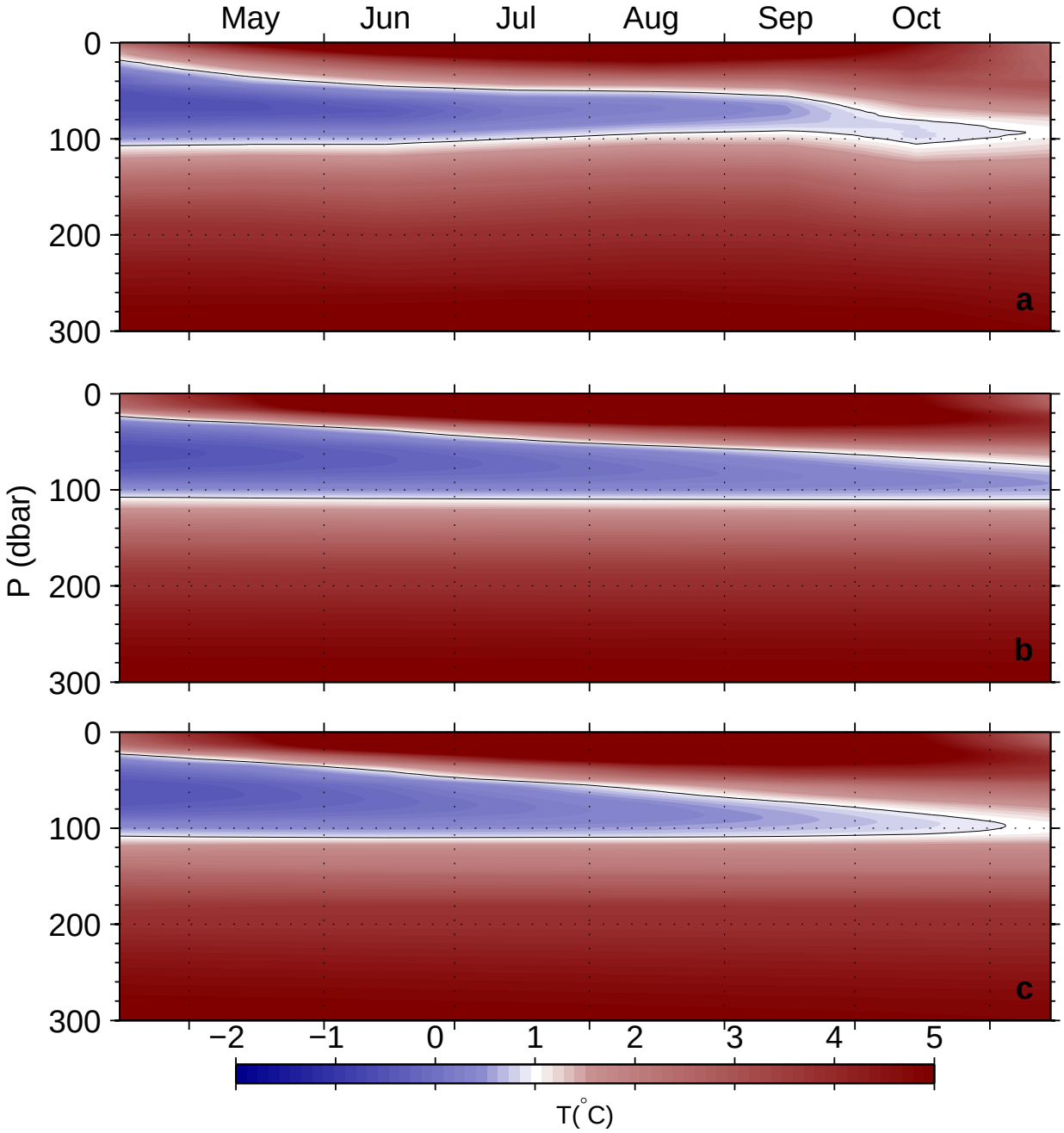

Figure 6: April to November water temperature. a) Monthly climatology over the period 1993-2010 calculated from the CTD casts of figure 5. b) Modeled evolution of temperature using the observed mean interior diffusivity profile K_i. c) Modeled evolution of temperature using the diffusivity profile from all available casts K_a. Figure properties are the same as Fig. 5.

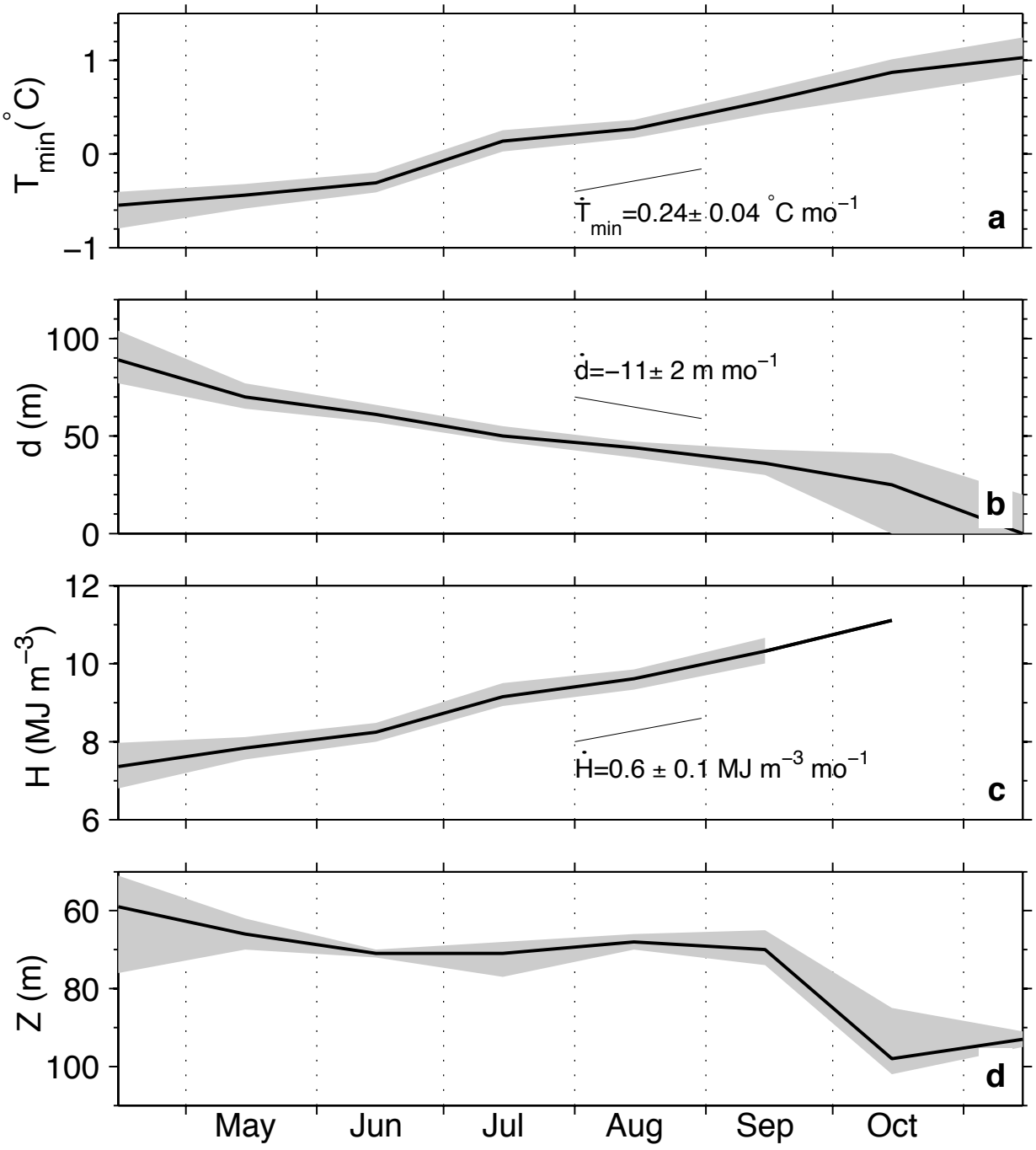

Figure 7: Evolution of CIL properties. Solid lines are monthly averages over the period 1993-2010. The shaded areas are the 95% confidence interval. a) Temperature of the CIL core. b) Thickness of the CIL. c) Heat content of the CIL. d) Depth of the CIL core. Thin short lines in the three first panels are the mean slopes (erosion rates) calculated in section 1.5.1. The mean slope is reported on panels with the 95% confidence intervals (see Table 1 for comparison with model results).

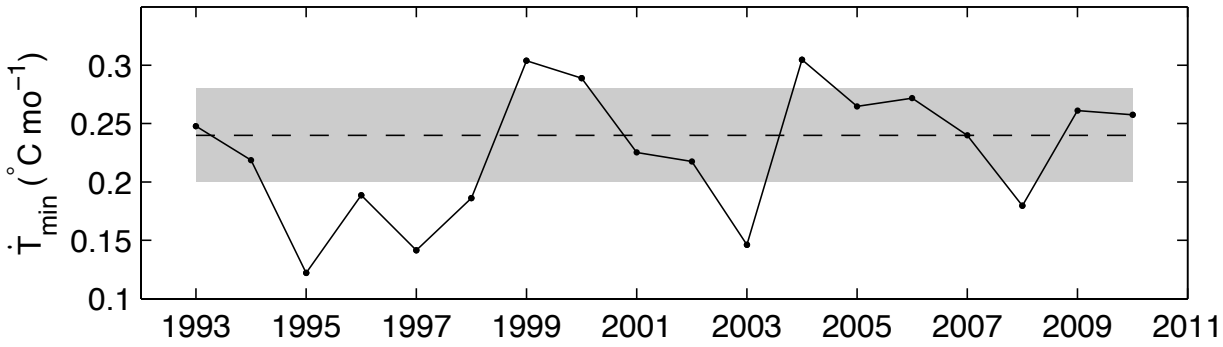

Figure 8: Interannual variability of the warming rate of the CIL core, calculated between April and November for every year over the period 1993-2010. The warming rate is defined as the slope of the best linear fit of the evolution of the CIL core temperature as shown in Fig. 7a. The dashed line is the average warming rate (0.24°C mo^{-1}) and the shaded area is the 95% confidence interval envelope (±0.04 °C mo^{-1}).

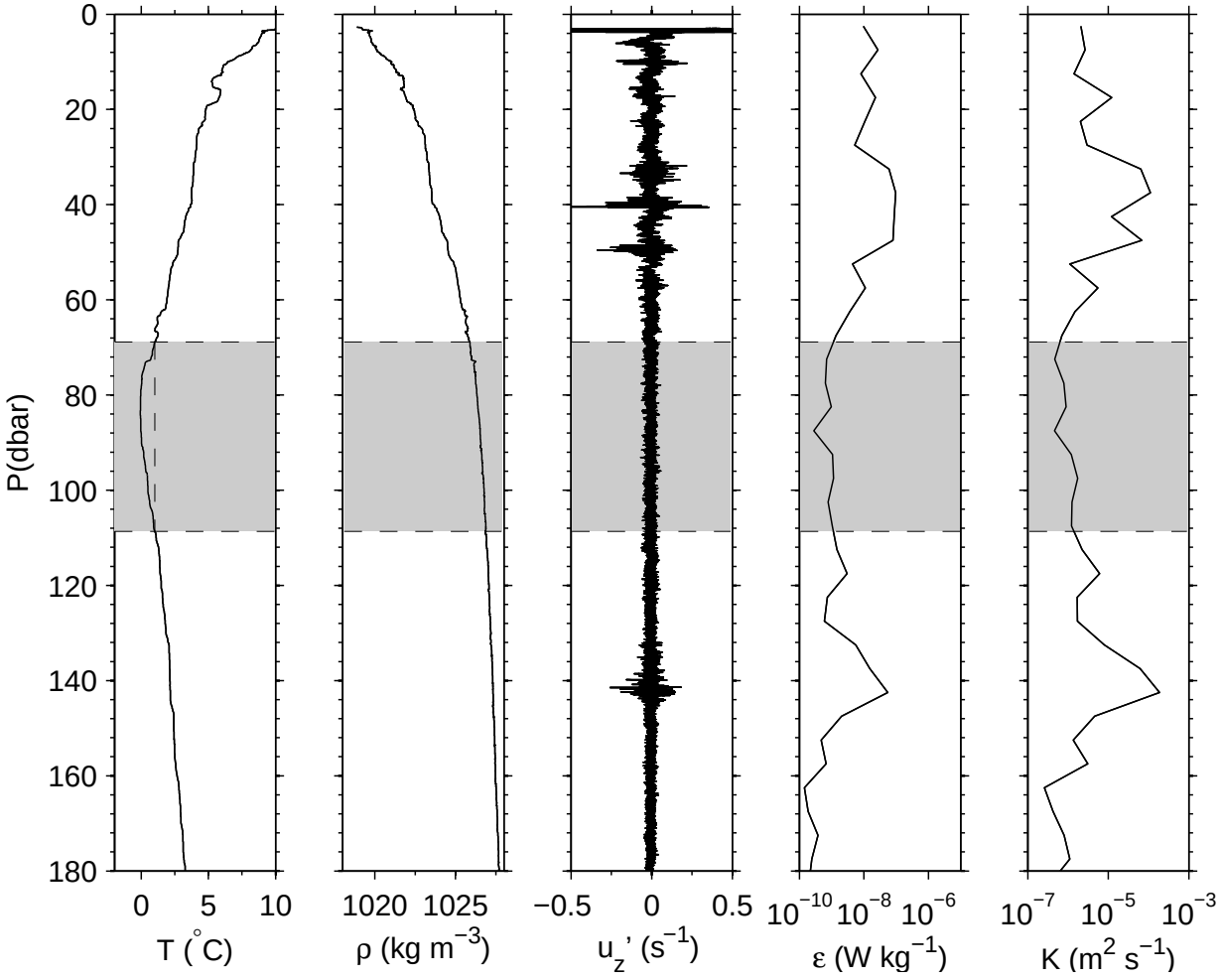

Figure 9: Typical turbulence profiler measurements, from July 21 2009. The three left-hand panels (temperature, sea water density and vertical shear) are unfiltered profiles, i.e., sampled at 64 Hz for T and ρ and 512 Hz for u_z'. The two right-hand panels are 5-m scale TKE dissipation rate, ϵ, and eddy diffusivity, K. The CIL has been highlighted in first panel and its depth is reported on all panels as shaded areas.

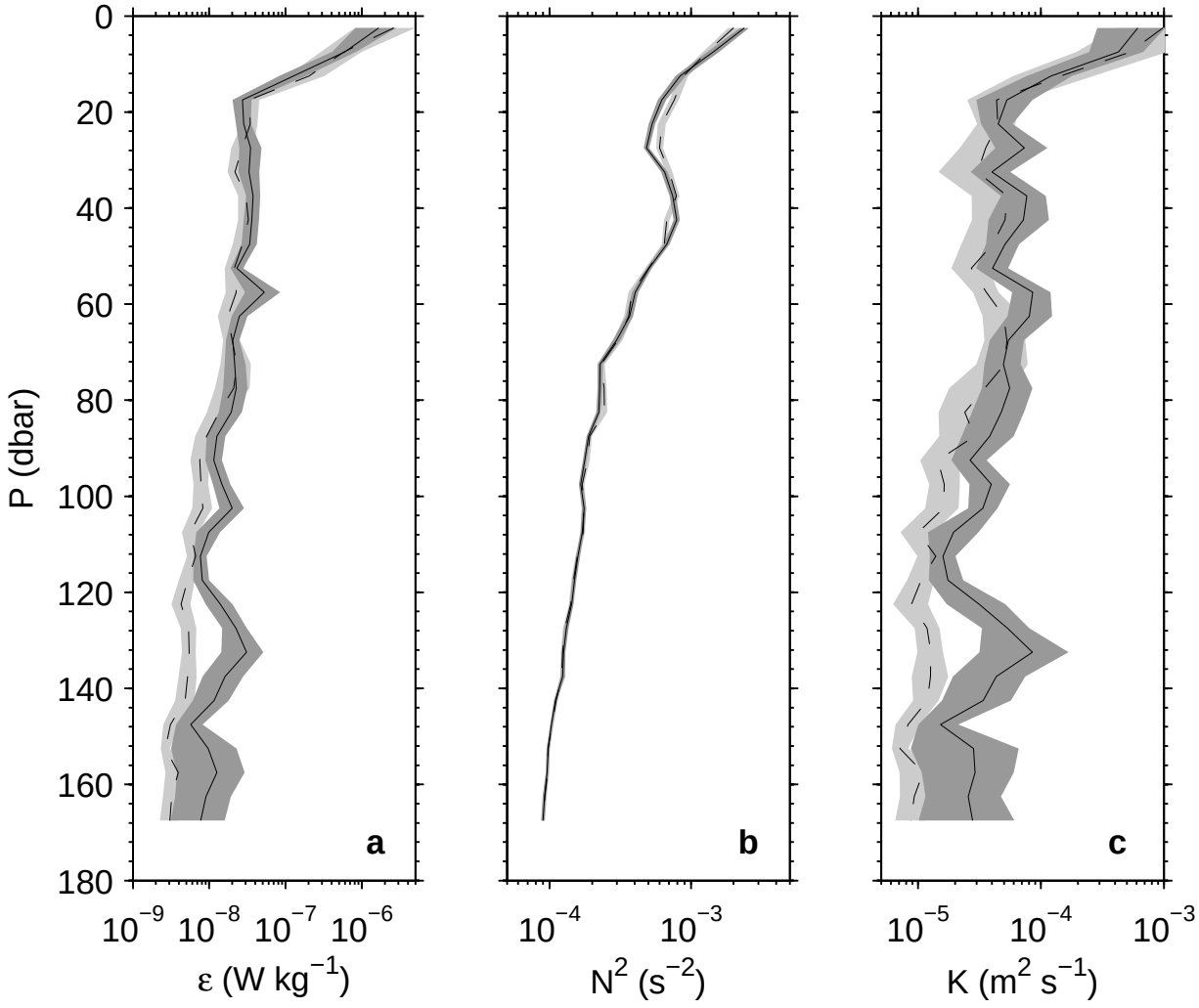

Figure 10: Mean quantities from all 892 VMP casts for 2009-2010 (dark gray, solid lines). a) Mean dissipation rate of turbulent kinetic energy. b) Mean buoyancy frequency squared. c) Mean eddy diffusivity coefficient. The gray shades indicate 95% confidence intervals. Mean quantities for casts taken at mid-channel (420) are also presented (light-gray, dashed-lines)

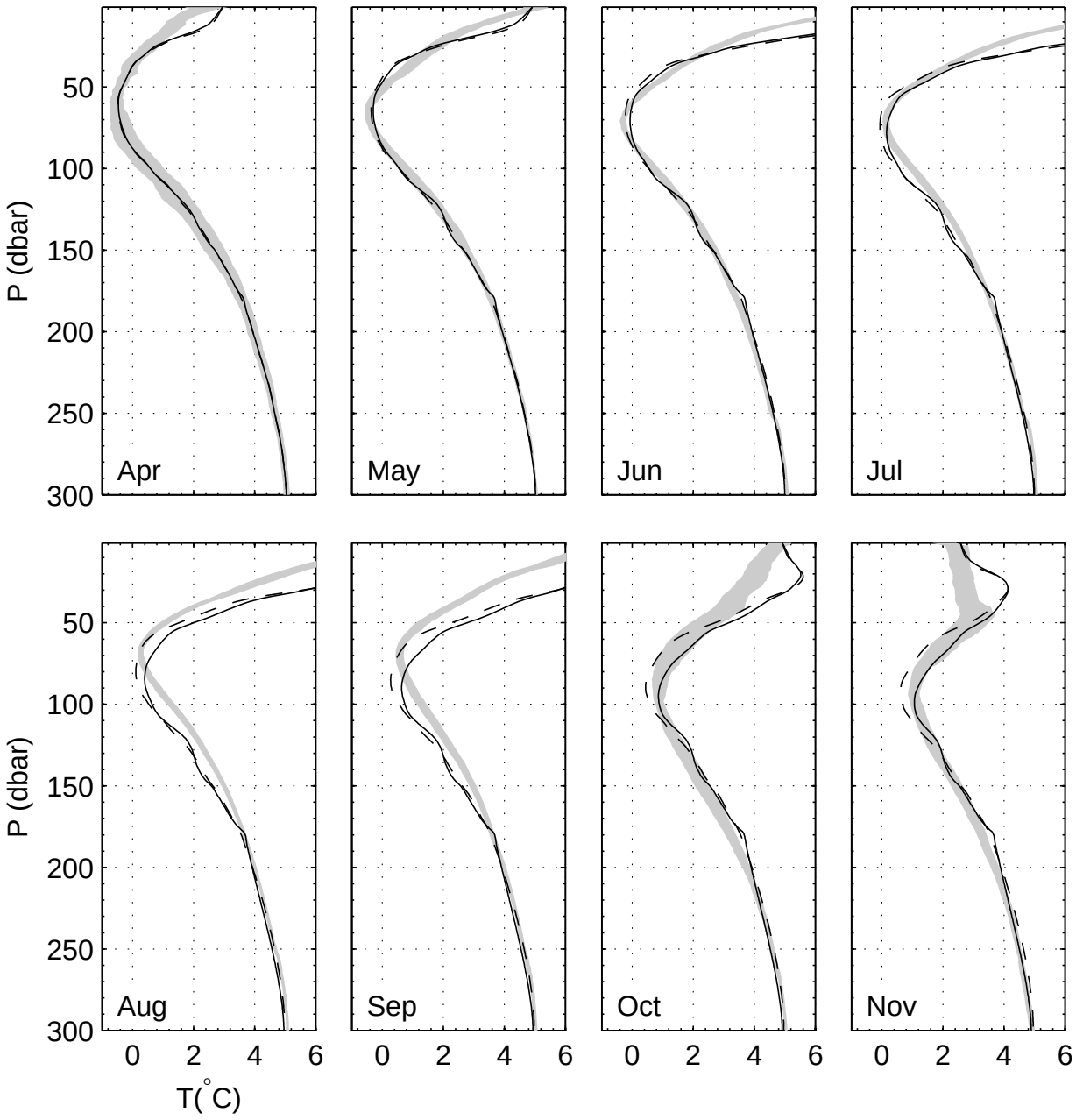

Figure 11: Details of the evolution of monthly mean temperature profiles for observations and simulations. The observed 95% confidence intervals of the observed mean temperature profile (shaded area) is compared to two simulations done with respectively the average observed diffusivity at mid-channel K_i (dashed lines) and from all available casts along the section K_a (solid lines).

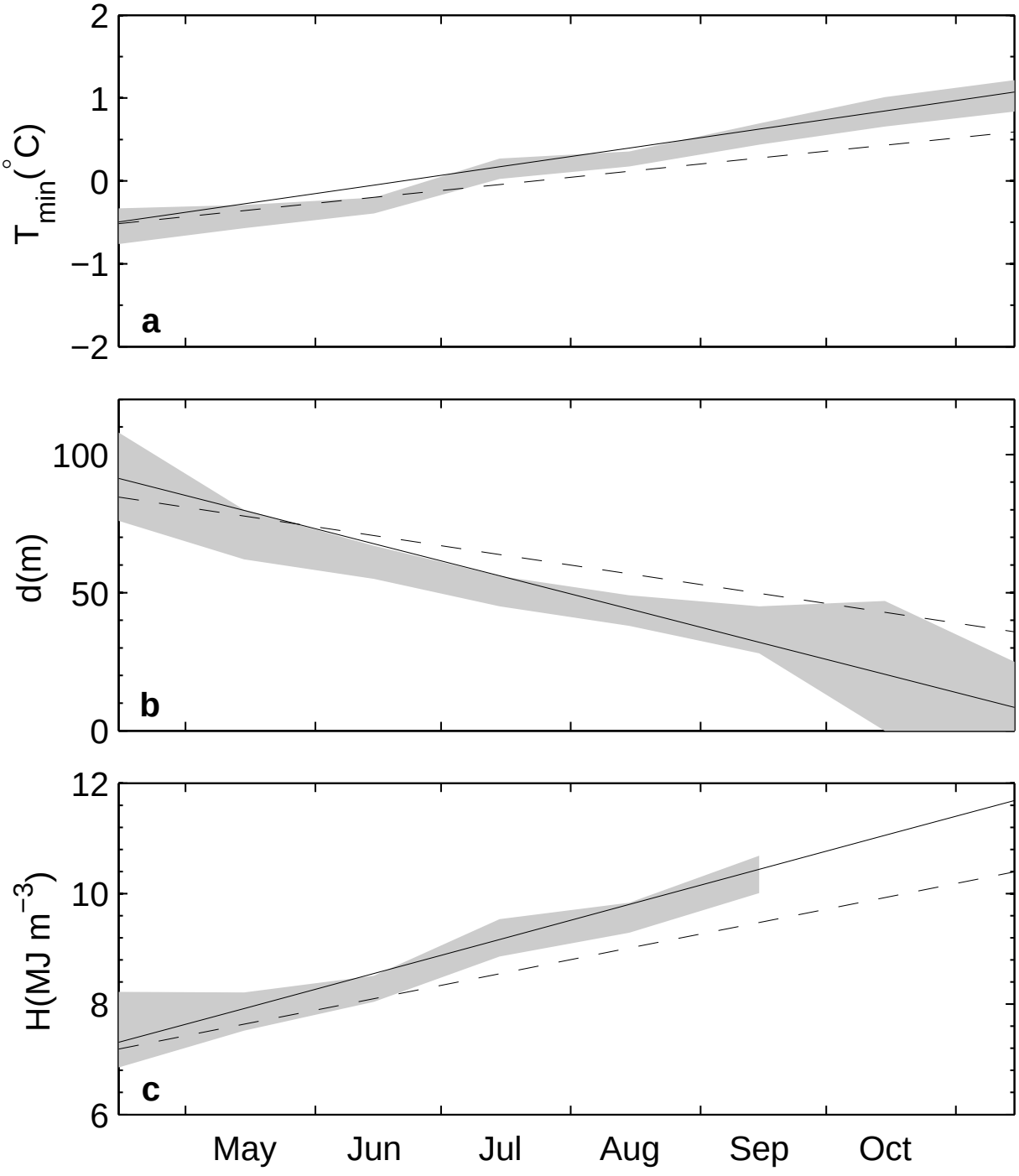

Figure 12: Comparison between observed and modeled CIL erosion rates: a) core temperature, b) thickness and c) heat content. 95% confidence interval of the observations (1993-2010) are presented, together with the linear best fits of the monthly means from the model when forced respectively with K_i (dashed lines) and K_a (solid lines). All slopes are provided in Table 1.

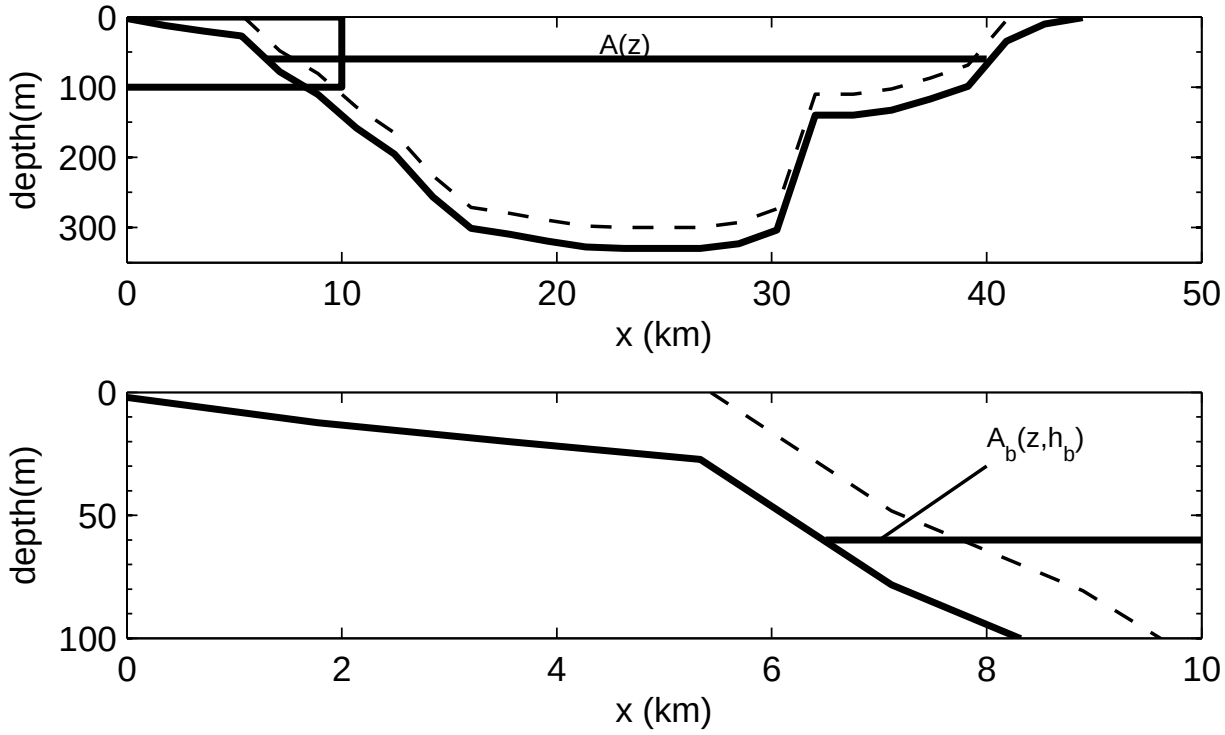

Figure 13: Details of the geometric scaling used to calculate the "apparent" eddy diffusivity (Eq. 1.5). (upper panel) Bathymetric section of the estuary at Rimouski station (see Fig. 2, red line). (lower panel) Enlargement of the rectangle in the upper panel. For both panels, x is the distance from the South shore. The dashed line corresponds to the upper limit of the bottom boundary layer of height h_b (not to scale for emphasis). $A(z)$ is the channel width at depth z and $A_b(z, h_b)$ is the width of $A(z)$ within the boundary layer.

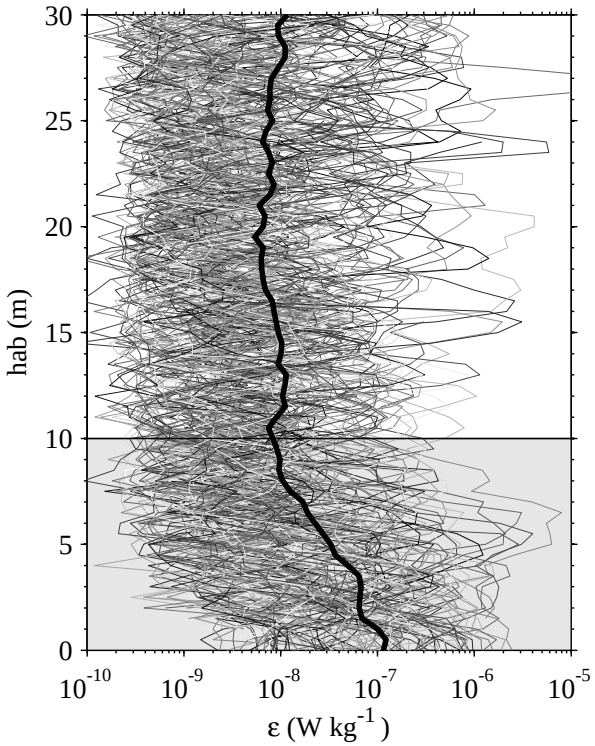

Figure 14: All dissipation rate profiles (150) that hit the bottom (gray curves) and their mean (thick black curve) . Data are presented relative to height above bottom (hab). The gray shaded area highlights the visually-inferred 10-m thick bottom boundary layer.

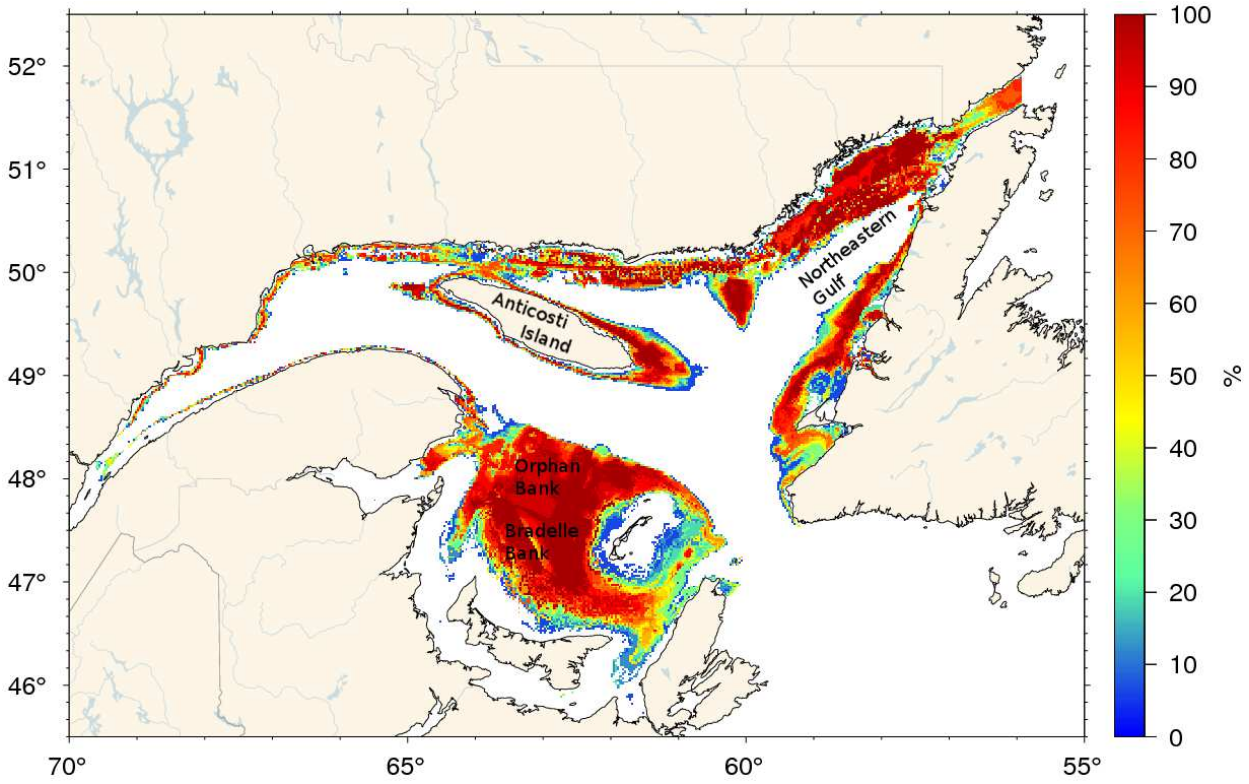

Figure 15: Occurrence of the CIL that reaches the seabed from 1995 to 2010. The white regions are where the CIL never reached the seabed.

ARTICLE II

BEHAVIOR AND MIXING OF A COLD INTERMEDIATE LAYER NEAR A SLOPING BOUNDARY

2.1 Abstract

As in many other subarctic basins, a cold intermediate layer (CIL) is found during ice-free months in the Lower St. Lawrence Estuary (LSLE), Canada. Using a high resolution mooring deployed near the northern side of the estuary, the CIL behavior above the sloping bottom is examined. Observations show successive swash/backwash of the CIL on the slope at a semi-diurnal frequency. It is shown that these upslope and downslope motions are likely be caused by internal tides in the LSLE, generated at the nearby channel head sill. Quantification of mixing from 322 turbulence casts reveals that in the bottom 10 m of the water column, the time-average dissipation rate of turbulent kinetic energy is $\epsilon_{10\,\mathrm{m}} = 1.6 \times 10^{-7}\,\mathrm{W\,kg^{-1}}$, an order of magnitude greater than what found in the interior of the basin, far from boundaries. Near bottom dissipation during the flood phase of the M_2 tide cycle (upslope flow) is about four times greater than during the ebb phase (downslope flow). Bottom shear stress, shear instabilities and internal wave scattering are considered as potential boundary mixing mechanisms. Although non-linear internal waves have also been observed, these are likely not an important mixing mechanism at the sampling site.

2.2 Introduction

In a recent study, Cyr et al. (2011) concluded that although not dominant, boundary mixing can contribute significantly to the mixing budget of the Gulf of St. Lawrence, a semi-enclosed subarctic sea located in eastern Canada. This study was carried out at the *Rimouski section*, a transect extending across the Lower St. Lawrence Estuary (LSLE), off Rimouski (Fig. 16) and was based on the analysis of hundreds of historical CTD profiles and approximately a thousand new turbulence profiles collected close to, and away from a sloping boundary. The key feature of this study was the comparison between observed vertical mixing and the mixing inferred by examining the summer erosion of the cold intermediate layer (CIL) that was assumed to act like a horizontally-uniform passive tracer. Mixing mechanisms were however not identified and no understanding was available on how the CIL actually behaves where it intersects sloping bottoms. It was suggested that bottom shear stress and internal waves may be the principal mixing agents at sloping boundaries.

The goal of the present study is therefore to examine in greater detail the behavior of the CIL and the mixing mechanisms responsible for its erosion along sloping boundaries in the Gulf of St. Lawrence. In order to achieve this goal, a field experiment was carried out in a region where the CIL intersects the sloping bottom on the northern part of the Rimouski section. We present here the results of this experiment interpreted within the context of internal tide theory.

2.2.1 The Lower St. Lawrence Estuary and internal tides

The St. Lawrence Estuary is commonly defined as the region between Québec city (the upper limit of salt intrusions) and Pointe-des-Monts, where begins the Gulf of St. Lawrence (e.g., Forrester, 1974; El-Sabh, 1979; Koutitonsky and Bugden, 1991) (Fig. 16). The estuary is generally subdivided into the Upper and Lower St. Lawrence Estuary (USLE and LSLE, respectively) by a shallow sill at the head of the Laurentian channel near Tadoussac. This

deep (>290 m) channel starts on the continental slope, runs across the Gulf and ends near Tadoussac where the total depth abruptly shallows from 325 m to about 50 m in less than 15 km.

The LSLE width varies from about 44 km at the mouth to about 13 km at the head. Because of its unusually large width for an estuary (about five times the internal Rossby radius) and because its water masses properties are similar to the Gulf of St. Lawrence, the LSLE is also commonly considered to be part of the Gulf. In winter, the major part of the Gulf of St. Lawrence is characterized by two water masses: a surface layer near the freezing point and a warmer and saltier deep layer of oceanic origin. For the rest of the year, the system is stratified into three water masses after a surface layer is formed as a result of the spring freshet and the increasing air temperature. The previous winter surface layer then becomes trapped as a CIL between two warmer layers (e.g., El-Sabh, 1979; Koutitonsky and Bugden, 1991; Galbraith, 2006; Smith et al., 2006a; Cyr et al., 2011). Once regenerated during the winter, the CIL properties are slowly eroded during summer months as a result of mixing (its core temperature warms at a rate of $\sim 0.24\,^{\circ}$C per month while its thickness decrease at a rate of ~ 11 m per month; Gilbert and Pettigrew, 1997; Cyr et al., 2011). Because of winter low surface layer salinities in the LSLE that inhibit mixing and convection, the CIL is not formed in the LSLE but is rather advected from the Gulf during the summer months as the result of the estuarine circulation (e.g., Galbraith, 2006; Smith et al., 2006a).

Numerous past studies have discussed the generation and propagation of an internal tide generated at the sill near the head of the Laurentian channel and emanating seaward out of the estuary (e.g. Forrester, 1970, 1974; Ingram, 1979a; Wang et al., 1991; Galbraith, 1992). Forrester (1974) was the first to describe the internal tide by fitting density observations to theoretical vertical modal structures in the LSLE. He found that at the M_2 frequency, the internal tide that predominantly emanates from the head is consistent with a Poincaré-type wave in the second vertical and first horizontal modes with a wavelength of about 60 km along-channel. He also found evidence of Kelvin waves at the diurnal frequency.

Wang et al. (1991) focused on the evolution of the internal tide energy field along the estuary with three moorings along the LSLE. They suggested that after its generation at the sill, the semi-diurnal internal tide propagates with decaying amplitude, typically with vertical isopycnal displacements from about 80 m at the generation site to about 30 m 140 km downstream, i.e. 40 km downstream of Rimouski section. They also suggested that higher tidal harmonics observed at all three sites (e.g., M_4 and M_6) are the result of non-linear interactions of the semi-diurnal internal tide with the sill.

2.3 Datasets and Methodology

2.3.1 Mooring data

A mooring was deployed between September 20 and October 12, 2011 on the 83 m isobath of the north shore of the estuary (N080, Fig. 16), in a region where the bottom slope is approximately constant at 3% from 40 m to 120 m. It was equipped with one Acoustic Doppler Current Profiler (RDI Workhorse ADCP, 600 kHz) at 59 m depth, looking downward to the bottom and 8 *RBR Ltd* thermistors between 30-79 m. Thermistors at 30, 40 and 50 m depth were equipped with pressure sensors (model TDR-2050), while the others (60, 65, 70, 75, 79 m) only measured temperature (model TR-1060). The mooring summary is provided in Table 2. All thermistors are expected to have a precision better than 0.01°C. Raw velocity measurements have an error (defined as the statistical standard deviation on measurements) of 8.1 cm s^{-1} on each 3 second ensemble. Currents have been rotated by $-33.5°$ to produce along-shore (u) and cross-shore (v) velocities. Velocities in the bottom 1.5 m above the sea bed have been discarded to avoid side-lobe contamination of the near bottom velocity field. Unless otherwise specified, current velocities have been smoothed using a 5 minute averaging window to reduce the error to 1.4 cm s^{-1}.

High frequency current fluctuations, presumably caused by the passage of gravitational non-linear internal waves were detected by examining vertical velocity fluctuations, from

which an activity index was calculated. The *area density energy*, in $\mathrm{J\,m^{-2}}$, was calculated following a modified version of Equation 5 in Richards et al. (2013):

$$E_a = \int_{z_1}^{z_2} \rho_0 w_{30s}^2(z,t)dz, \tag{2.1}$$

where $z_1 = 61\,\mathrm{m}$ and $z_2 = 81.5\,\mathrm{m}$, the ADCP depth range, $\rho_0 = 1025\,\mathrm{kg\,m^{-3}}$ and w_{30s} is the vertical velocity averaged in 30 s time intervals, a period that reduces the error to $2.5\,\mathrm{cm\,s^{-1}}$ while still permitting to resolve internal wave oscillatory motions (their shortest temporal period is typically 5-10 minutes).

2.3.2 Fine- and micro-structure data

Turbulence measurements were collected during summers 2009-2012 with two free-fall, loosely-tethered, vertical micro-structure profilers (VMP500) manufactured by Rockland Scientific International (RSI). Along with other sensors, these profilers are equipped with two airfoil shear probes that allow measurements of micro-scale ($\sim 1\,\mathrm{cm}$) vertical shear u_z' (see Cyr et al., 2011, for other sensors). They are also equipped with a fine-scale ($\sim 1\,\mathrm{dm}$) temperature-conductivity-depth (CTD) sensors manufactured by Sea-Bird Electronics.

A total of 1644 casts have been collected in the region. Statistics from a portion of this dataset have been published in two studies (Cyr et al., 2011; Bourgault et al., 2012). For the purpose of this study, 322 casts collected over the northern boundary of the channel during summers 2010-2012 are considered (see Fig. 16). For all these casts, the VMP hit the sloping bottom at depths varying from 20 m to 110 m (>80% in the 60-110 m range).

An Acoustic Doppler Current Profiler (RDI Workhorse ADCP 300 kHz or 600 kHz) was mounted overboard of the small craft boat used to collect the turbulence profiles, at about 1 m below the surface and looking downward. Although the vertical bin size and the ensemble length were variable between sorties, the ADCP data were averaged into 4-m bins and five

minutes time intervals during post-processing. The error for these averaged measurements is expected to equal or be less than $1.4\,\mathrm{cm\,s^{-1}}$. This allows the calculation of the mean shear ($S^2 = \overline{\left(\frac{\partial u}{\partial z}\right)^2} + \overline{\left(\frac{\partial v}{\partial z}\right)^2}$). Approximate noise level on shear measurements can be estimated using the error on measured velocities ($u' = v' = 1.4\,\mathrm{cm\,s^{-1}}$). It is expected to be on the order of $S_n^2 \sim \frac{2(u')^2+2(v')^2}{\Delta z^2} = 5 \times 10^{-5}\,\mathrm{s^{-2}}$, with $\Delta z = 4\,\mathrm{m}$, for the shear squared.

The dissipation rate (ϵ) of turbulent kinetic energy (TKE) was calculated from u_z' using standard procedures (see Cyr et al., 2011):

$$\epsilon = \frac{15\nu}{2}\overline{\left(u_z'\right)^2}, \tag{2.2}$$

where $\nu = f(T)$ is the kinematic molecular viscosity as function of temperature and the overline indicates here a vertical 1 m bin average. The shear variance $\overline{\left(u_z'\right)^2}$ was obtained by spectral integration to remove random noise.

Turbulent diffusivity was calculated from the dissipation rate and stratification as:

$$K = \frac{\Gamma\epsilon}{N^2}. \tag{2.3}$$

Here $N^2 = \frac{-g}{\rho}\frac{\partial \rho}{\partial z}$, the background buoyancy frequency squared, sorted to remove density inversions and averaged in 1-m bins to match ϵ resolution, and Γ is an indicator of the mixing efficiency, which we will refer here as the *flux coefficient*, according to Smyth et al. (2001).

A common practice is to calculate the diffusivity using the constant flux parameter $\Gamma = 0.2$ (e.g., Osborn, 1980; Moum et al., 2002, 2004; Burchard, 2009; Holtermann et al., 2012). On the other hand, Shih et al. (2005) proposed a parametrization for the mixing efficiency that depends on the turbulent activity, or the buoyancy Reynolds number ($Re_b = \frac{\epsilon}{\nu N^2}$), leading to mixing efficiency significantly lower than $\Gamma = 0.2$ when the turbulence is *fully developed* ($Re_b > 100$). This parametrization, tested by Fer and Widell (2007) and recently used by

van der Lee and Umlauf (2011) for the coastal ocean has the form:

$$\Gamma = \begin{cases} 2Re_b^{-\frac{1}{2}} & \text{if } Re_b > 100, \\ 0.2 & \text{otherwise.} \end{cases} \tag{2.4}$$

The applicability of this parametrization on microstructure observations has recently been called into question by Gregg et al. (2012) who opted for the traditional constant value until some contradictions with oceanic observations were resolved. Here we present the result of both parametrizations, although diffusivity values discussed in the text have been calculated using $\Gamma = 0.2$, consistent with previous studies in this area (Cyr et al., 2011; Bourgault et al., 2012). Averaged values for turbulent variables presented in this study (N^2, S^2, ϵ, K and E_a), were calculated assuming log-normal distributions (Baker and Gibson, 1987).

2.3.3 Phase averaging

Hourly tide levels were obtained using the *xtide* software (*www.flaterco.com/xtide*) for the city of Rimouski. These predictions are based on harmonic analyzes and do not take into account storm surges or other local effects. Over the three-week mooring deployment, the predicted and measured times of high and low tides were off by two minutes at most (not shown).

Some temperature and currents data presented in this study are plotted relative to the M_2 tide cycle. To do so, the closest high tide was first identified for each measurement (cast or mooring profile). Then, the M_2 period (12.42 hours) was split into 13 classes relative to the time of the closest high tide ($t = [-6, -5, -4, ..., 4, 5, 6]$ h) and the mean value or profile for each class was calculated. Positive and negatives classes correspond respectively to ebb and flood phases of the tidal cycle.

2.3.4 Revisiting the Forrester internal tide model

Forrester (1974) described the semi-diurnal internal tide in the LSLE as being mainly a progressive Poincaré-type wave in the second vertical mode and first horizontal mode (see summary description in Sec. 2.2.1). As shown in Forrester (1974), vertical mode-1 is not allowed in the LSLE because the channel width at the generation site is too narrow. For comparison with mooring observations, we now revisit its analytic model for the propagation of internal waves for an idealized infinite rectangular channel in the x-direction, with depth $H = 300\,\text{m}$ and width $W = 36\,\text{km}$. Note that unlike the work of Forrester (1974) where the channel width was set to 25 km, we chose $W = 36\,\text{km}$ to better match the width of the Rimouski section. This channel width includes the sloping boundary where the mooring is located, but excludes shallower shelves with depth <40 m on each side of the channel.

Vertical displacement η and velocities u and v for a Poincaré wave of vertical mode-n and horizontal mode-m are given by (see Forrester, 1974, Eq. 6):

$$\begin{aligned}
\eta(x,y,z,t) &= \left(\sin\lambda y - \frac{\sigma\lambda}{\kappa f}\cos\lambda y\right)\eta_0(z)\cos(\sigma t - \kappa x)\\
u(x,y,z,t) &= \left(\frac{\sigma}{\kappa}\sin\lambda y - \frac{\lambda}{f}\left(\frac{\sigma^2 - f^2}{\kappa^2+\lambda^2}\right)\cos\lambda y\right)\frac{d\eta_0(z)}{dz}\cos(\sigma t - \kappa x)\\
v(x,y,z,t) &= \left(\frac{f^2\kappa^2 + \sigma^2\lambda^2}{f\kappa(\kappa^2+\lambda^2)}\sin\lambda y\right)\frac{d\eta_0(z)}{dz}\sin(\sigma t - \kappa x).
\end{aligned} \tag{2.5}$$

Here, σ is the frequency of the wave, taken as the M_2 frequency ($\sigma = 1.4053\times10^{-4}\ \text{s}^{-1}$) and f is the Coriolis parameter. Note that contrary to the model of Forrester (1974), our x-axis is defined positive downstream, consistent with coordinate system of Figure 16. The z-axis is positive downward and $y = 0$ corresponds to the southern boundary of the rectangular channel. Wavenumbers κ and λ, respectively in the x- and y-directions are related through the dispersion relation of Poincaré waves:

$$\sigma^2 = f^2 + c_n^2(\kappa_{nm}^2 + \lambda_m^2), \tag{2.6}$$

where c_n is the mode-dependent phase velocity of the wave that will be determined later. Equation 2.6 indicates that a necessary condition for Poincaré waves to exist is that $\sigma > f$. Because the wave is bound by side walls in the y-direction, $\lambda_m = m\frac{\pi}{W}$ for the m^{th} horizontal mode of oscillation.

In order to use equations 2.5, the modal vertical displacement structure $\eta_0(z)$ is needed. To do this, we followed Forrester (1974) and considered an idealized horizontally-uniform background density stratification given by an exponential profile of the form:

$$\rho = \rho_r e^{\left(\frac{d}{z+h}\right)}. \tag{2.7}$$

Here, $\rho_r = 1027.5\,\mathrm{kg\,m^{-3}}$, $d = -0.0924\,\mathrm{m}$ and $h = 15.4\,\mathrm{m}$ and represent a best fit to 198 CTD casts obtained at proximity of the mooring during the deployment period. For all the 1-m bins considered in the observed mean profile, the relative error with the fit is at most 0.03%.

As shown by Forrester (1974), such analytic density profile allows the following vertical structure for isopycnal displacement:

$$\eta_0(z) = \eta_n(z+h)^{1/2} \sin\left[\left(\frac{-gd}{c_n^2} - \frac{1}{4}\right)^{1/2} \ln(z+h) + \theta_n\right], \tag{2.8}$$

where $\eta_n = 1\,\mathrm{m}$ is an arbitrary scaling factor chosen to approximately match the observed isotherms displacements, and c_n and θ_n are discrete constants that can be determined from Eq. 2.8 given the vertical mode number and the boundary conditions $\eta_0(z = 0) = 0$ and $\eta_0(z = H) = 0$.

Note that it is also possible to find the vertical modal structure η_0 by numerically solving

the Poincaré waves eigenvalue problem (e.g., Gill, 1982), but in this case, a full-depth (i.e. 300 m) density profile would be needed. Here, the exponential coefficients were obtained by least square minimization of profiles not deeper than $\sim$ 110 m, but the analytical expression was extended to 300 m, the depth of the channel for this model. Since the stratification evolves seasonally and spatially in the LSLE, this choice was the best trade-off to obtain a full depth profile that best matches the surface stratification at our sampling site. The use of a mean profile from the center of the channel during the time of our experiment would have lead to a node position for vertical displacement at 71 m instead of 54 m which would not compare favorably with our observations. It must be kept in mind that this is an indication that one of our hypothesis is not satisfied, i.e., that the density background is horizontally homogeneous.

Given the vertical displacement η at any location and time, the temperature field $T(x, y, z, t)$ can be estimated as

$$T(x, y, z, t) = T_0(z) - \eta \frac{dT_0}{dz}, \tag{2.9}$$

where $T_0(z)$ is the background, horizontally-uniform and time-invariant temperature profile. This background temperature profile corresponds to the mean temperature profile sampled at the proximity of the mooring during the deployment period for the 0-80 m depth range. For illustration purposes, the temperature profile was oversimplisticaly linearly interpolated below 80 m to reach 5°C at 300 m, the approximate climatological value. Since the temperature is used here as a tracer, this has no effect on the dynamics. Results from this model will be presented in Section 2.4.2.

2.4 Observations

2.4.1 Cold intermediate layer behavior at the slope

An overview of temperature and velocity fields for the mooring deployment duration is presented in Figure 17. Temperature and velocities are low-pass filtered with a cut-off period

of 25-hour to highlight sub-tidal dynamics. The CIL is defined here as water temperature below 1°C (Cyr et al., 2011) and is contoured in Figure 17b with a solid black line. The CIL exhibits large (> 10 m) vertical displacements and temperature fluctuations on weekly periods, and sometimes even disappears for a few days before reappearing later on. The origin of these fluctuations is not known and may originate from horizontal advection of CIL inhomogeneities associated with changes in low-frequency circulation as suggested by panels *c* and *d*. In the alongshore direction (panel c), the advection from the Gulf towards the estuary was variable, with a maximum inland currents of about 10 cm s^{-1} near 24 September and a maximum seaward current of about 5 cm s^{-1} near 6 October. To a lesser extent, currents were also variable in the crossshore direction (panel d), with most of the subtidal advection at this depth towards the interior of the channel, although a few pulses towards the shore are also visible. From this short mooring deployment it is difficult to conclude on these current fluctuations. Possible explanations may however include Kelvin or other topographic waves generated seaward that can travel on this side of the channel. Such waves have already been observed in the LSLE with periods of about 5-8 days for the lowest modes (Lie and El-Sabh, 1983; Mertz and Gratton, 1990).

To focus on tidal oscillations of the CIL, Figure 18 presents a snapshot of a timeseries encompassing about 6 semi-diurnal (M_2) tidal cycles. Isotherms exhibit large oscillations at this frequency with displacements reaching up to 40 m. Pockets of warm water, up to 2°C anomalies, also appear semi-diurnally and alternatively below and above the CIL. While the warm anomalies seen above the CIL may have arisen from vertical isotherm heaving, the source of the near-bottom anomalies must come either from longitudinal (along-shore) or lateral (across-shore) advection. It will be shown in Section 3.2 that this signal may be partly explained by an internal tide that causes periodic swash/backwash flow of warm, sub-CIL water on the slope.

This semi-diurnal pattern is now examined using the whole dataset averaged relative to the M_2 tide cycle (Fig. 19). In the along-shore direction (19b), the currents near the bottom

reverse earlier than those above, near $t \sim$ 0h at the bottom compared to $t \sim$ 1.5h at 20 m *hab*. Baroclinic forcing induced by internal tides may be responsible for such lag. The mean velocity profile in this direction exhibits a log-type profile, typical of a flow above a rigid bottom, with about 5 cm s^{-1} in the upstream direction at 20 m, decreasing towards 0 cm s^{-1} at the bottom. In the cross-shore direction (Fig. 19c), upslope currents occur during the flood and the in the early ebb for flow above 15 m *hab*. Again, on an average M_2 cycle, it is possible to see that the upslope flow arises in successive pulses as shown preceedingly in Figure 18. The mean velocity profile of the flow over the mooring duration is toward the south shore (downslope) at about 1 cm s^{-1}. The CIL also disappears during an average M_2 cycle. This can also be seen in Figure 18 when the CIL thickness decreases and sometimes disappears. The reason for this behavior will be examined in the next subsection.

Spectral analysis reveals that although most of the variance in temperature and along- and cross-shore velocities is at the M_2 frequency, higher harmonics are also present in all fields (Fig. 20ab). To distinguish between currents in the bottom boundary layer and above (BBL thickness is estimated to be about 10 m thick later in the study, e.g., Fig. 24), the spectral analyses have been performed for different depth ranges (0-10 m and 10-20 m *hab*). For both depth ranges, the M_2 variance level largely dominates the along-shore velocities spectra (black curves), generally by two orders of magnitude above the second most important harmonic (M_4). The cross-shore velocities spectra (blue curves) are however only slightly dominated by M_2. For example, the variance level in near bottom cross-shore velocities (20a, blue line) is nearly as high at M_6 than at M_2 (about a two-fold change) and variance at M_8 is nearly as high as at M_4. For the 10-20 m depth range, variance level at M_4, M_6 and M_8 are almost equal and less than an order of magnitude lower than M_2 (20b, blue line). This reveals that the higher harmonics are relatively more important for v compared to u, consistent with the observation of successive pulses in the cross-shore velocities discussed above and visible in Figures 18c and 19c

It is not surprising that u spectra are dominated by M_2 considering the importance of the

barotropic semi-diurnal tide for the LSLE (Godin, 1979; El-Sabh, 1979; Saucier and Chassé, 2000). The fact that the energy of higher harmonics is different between u and v raises the hypothesis that forcings responsible for the along- and cross-shore motions at our sampling site may be different. Other than the barotropic tides, one mechanism that could drive motions at tidal frequencies are internal tides. Their role as the main driver for cross-shore velocities inducing vertical motions over the sloping boundary will now be addressed.

2.4.2 A model for the propagation of internal tides

The mooring deployed on the north shore of the LSLE shows, at a semi-diurnal time period and at higher frequencies, successive upslope and downslope movements, associated with cross-shore velocities. The barotropic radius of deformation ($R = \frac{\sqrt{gH}}{f} \sim 500\,\mathrm{km}$, using $H = 300\,\mathrm{m}$, the channel depth, g the gravitational acceleration and f the Coriolis parameter) is many times larger than the channel width ($W \sim 36\,\mathrm{km}$). This implies that the cross-shore velocities cannot be generated by a geostrophic adjustment of the barotropic tide entering the channel. This demonstration have also been done by Forrester (1970). In some circumstances, however, the interaction of the barotropic tidal wave with coastlines irregularities can lead to barotropic Poincaré waves which have cross-shore velocities (Taylor, 1921).

To examine whether internal tides can explain the observed velocity and temperature fields, we revisit the study of Forrester (1974) (see model description in Sec. 2.3.4). This simplified model provides a framework from which the observed currents and temperature signals can be interpreted. For the purpose of this study, we limit our analysis to the cross-section corresponding to the Rimouski section. Since the solution is periodic, we assume $x = 0$ at the Rimouski section.

Figure 21 shows that in the cross-channel direction this model results in a standing wave (vertical mode-2) inducing upslope and downslope movements near the boundaries. At

the position of the mooring (see white circles in Fig. 21), such a wave would generate the currents and isotherm displacements shown in Figure 22. Comparison between Figure 22 and the first three panels of Figure 19 shows qualitative similarities for T and v. Modeled along-shore velocities u are weaker and not in phase with those observed (note the different colorscale used), but this is expected since observed along-shore velocities are dominated by the barotropic tide. Although this calculation relies on somewhat unrealistic assumptions (the channel shape is not rectangular and the stratification changes laterally and longitudinally in the LSLE), the agreement between predicted and observed across-shore velocity amplitudes and patterns supports the idea that these are at least partly due to the transverse component of the Poincaré internal tide. This model also suggests that the observed disappearance of the CIL on an average M_2 cycle (Fig. 19) is the result of the vertical structure of the internal tide as suggested by the pinching of the CIL at the vertical node in Figure 22. The interaction of the internal tide currents with the sloping boundary may also affect the temperature evolution and may explain why the CIL often disappears, e.g., advected away from the mooring.

Only internal tides at M_2 frequency were modeled here, although M_4, M_6 and M_8 harmonics are also observed in cross-shore velocities (Fig. 20ab). These may be responsible for pulses in cross-shore velocities of Figure 18c and 19c. Wang et al. (1991) suggested that during its propagation towards the Gulf, the energy of the semi-diurnal internal tide rapidly decays and the relative importance of the higher harmonics becomes greater, leading to variance levels at M_4, M_6 and M_8 nearly as high as at M_2 in the cross-shore direction. The physical motivation for this affirmation is however still to be determined. Higher harmonics in the along-shore direction are also present, but less important compared to the variance at M_2 frequency that probably reflects the importance of the semi-diurnal barotropic tide in the LSLE.

2.4.3 Mean turbulent quantities

The near bottom water column undergoes along- and cross-slope motions at a semi-diurnal frequency, with superimposed higher harmonics as summarized in Figure 19. In such flows above a rigid surface, bottom friction reduces the velocity near the seafloor, inducing a shear in the water column. This shear (S^2) is captured by the mooring and, as expected, it is higher within the 10-m thick bottom layer, with intensification roughly at the end of both the flood and the ebb (Fig. 19). Spectral analysis of the shear at two different depth ranges shows that it is modulated by various tidal harmonics (Fig. 20). Between 10-20 m *hab*, the total shear (S^2, magenta) is M_2-dominated, with a major contribution from along-shore shear (S_u^2, black). Higher harmonics are also present in the total shear, but the cross-shore component of the shear (S_v^2, blue) dominates the signal at M_4, M_6 and M_8. Shear variance is greater for 0-10 m compared to 10-20 m, although variance in current velocities are similar for both depth ranges (Fig. 20ab). Contribution to the shear by the along-shore component of the velocity (S_u^2) is dominant over S_v^2 in the 0-10 m range, with S_u^2 variance at M_2 and M_4 being the most important harmonics.

An example of near bottom dissipation sampled by the VMP is shown in Figure 23a, representing about 7 hours of consecutive sampling, i.e., our longest timeseries near the mooring location. Each of the casts realized on this occasion hit the bottom at depths varying between 74 and 91 m. Since the boat was slowly drifting towards shallower water, it was repositioned near 16:13 UTC. Figure 23 also presents the buoyancy frequency squared (N^2), averaged in 4-m bins to match the shear vertical resolution computed from the outboard ADCP (S^2). The latter was 1-hour filtered and combined to the buoyancy frequency to compute gradient Richardson number ($R_i = \frac{\overline{N^2}}{\overline{S^2}}$) that is presented here as $\tanh(R_i)$ to better highlight regions below the threshold $R_i = \frac{1}{4}$ (orange-red colors) where shear instabilities are expected to occur (Miles, 1961). This is useful to better visualize unstable regions since $\tanh(R_i) \simeq R_i$ for $R_i < 0.5$ and $\tanh(R_{i|_{R_i \to +\infty}}) = 1$.

The dissipation is generally patchy. High turbulence level can be found near the surface, but we limit our analysis to the turbulence below the pycnocline which is located above $\sim$ 20 m depth according to Figure 23b. A notable feature is the high dissipation rate found near the seabed between 13:00-15:00, a period corresponding to the end of the flood (high tide at 14:31 UTC). This period correspond to high shear and low R_i near the seabed. Note that the bottom boundary layer is always stratified ($N^2 > 10^{-5}\,\mathrm{s}^{-2}$). Further from the bottom, turbulent layers a few meters thick that can last for hours are found. These are generally aligned with bands of high shear and low R_i. This possible relation between shear, stratification and dissipation is examined in Section 2.5.3.

We summarized all similar sorties in Figure 24, where 322 VMP casts and corresponding (simultaneous) velocity and shear profiles from the outboard ADCP are presented. Highest shear (24b, black curves) is found in the bottom 10 m of the water column and corresponds to a rapid decrease in the mean velocity $U = \sqrt{u^2 + v^2}$ (24a). On the other hand, the stratification N^2 (24b, gray curves) decreases steadily from about 50 m to the bottom, except in the bottom 5 m where it slightly increases. R_i decreases quasi-linearly from about 50 m to 10 m *hab* (24c). Between 10 m and 5 m, R_i decreases more rapidly driven by the increasing shear and falls below the threshold $R_i = \frac{1}{4}$ (vertical dashed line). In the bottom 5 m, R_i remains almost constant and below the threshold.

The dissipation rate of TKE (ϵ) presented in Figure 24d (black lines) increases toward the bottom of the water column. Flood and ebb averaged profiles are more or less the same until below 10 m *hab* where $\overline{\epsilon}_{\mathrm{flood}}$ ($2.8(1.9, 3.9)\times10^{-7}\,\mathrm{W\,kg^{-1}}$) exceeds $\overline{\epsilon}_{\mathrm{ebb}}$ ($0.72(0.53, 0.98)\times10^{-7}\,\mathrm{W\,kg^{-1}}$) by about a four-fold change on average. Here numbers in parentheses are the bootstrapped 95% confidence interval on the mean value and overlines refer to a vertical average of the mean profile in the 0-10 m *hab* depth range. On average, the enhanced dissipation near the seabed during the flood is consistent with the snapshot presented in Figure 23. The average dissipation rate in the bottom 10 m over all times is $\overline{\epsilon}_{10\,\mathrm{m}} = 1.6(1.2, 2.0)\times10^{-7}\,\mathrm{W\,kg^{-1}}$, an order of magnitude greater than that measured in the interior (far from the boundaries) and

reported in Cyr et al. (2011).

Mean diffusivity profiles are calculated here using both constant ($\Gamma = 0.2$, black lines) and variable (Eq. 2.4, gray lines) mixing efficiencies. Using $\Gamma = 0.2$, mean diffusivity in the bottom 10 m *hab* gives $\overline{K}_{\text{flood}} = 11(6.7, 18) \times 10^{-4}\,\text{m}^2\,\text{s}^{-1}$, $\overline{K}_{\text{ebb}} = 2.5(1.6, 3.8) \times 10^{-4}\,\text{m}^2\,\text{s}^{-1}$ and $\overline{K}_{10\,\text{m}} = 6.0(4.1, 8.5) \times 10^{-4}\,\text{m}^2\,\text{s}^{-1}$. The diffusivity $\overline{K}_{10\,\text{m}}$ is about 5 times higher than the mean diffusivity in the bottom 10 m presented in Bourgault et al. (2012), calculated from a subset of this dataset. The reason for this difference is the use of a trimmed mean on diffusivity in Bourgault et al. (2012). When using the same statistics the averaged diffusivity is the same, within uncertainties. Note that using the Shih et al. (2005) parametrization for the last 10 m would give $\overline{K}_{\text{Shih}} = 6.5(5.6, 7.6) \times 10^{-5}\,\text{m}^2\,\text{s}^{-1}$, i.e., nearly an order of magnitude lower than when using $\Gamma = 0.2$. This value is however inconsistent with the near bottom diffusivities inferred by inverse modeling in this area (Cyr et al., 2011).

2.4.4 High-frequency internal waves observations

Surface signature of high-frequency gravitational internal wave trains were occasionally reported during our surveys near the mooring site. Three of them were sampled by an echo-sounder deployed from the boat and the echograms suggest that turbulence is at work (Fig. 25).

For two of the three waves, where current measurements are available, we overlaid the internal wave activity calculated from equation 2.1, but using the outboard ADCP currents (panels *b* and *c*, turquoise curves). For the last wave, measurements with the VMP were also realized through the wave. This Figure indicates a correspondence between highest E_a activity and the presence of the waves, although the signal is clearly affected by the vertical motions of the profiler (see panel *c*).

For the third wave, the echogram (panel *c*) reveals that there is roughly a 10 m range between the crest and the through. Near the surface, high dissipation rates (panel *c*) and

strong shear (panel *d*) are also associated with its passage. However, strong shear is also found near the bottom and at mid-depth during and after the passage of the wave. From this sole observation and since no data is available for the period preceding the wave, it is not possible to determine whether the large shear observed was solely induced by the passage of the wave.

In order to determine the role played by such internal waves in bottom shear enhancement, we compared the mean shear averaged over the 1.5-5 m *hab* range (Fig. 26a, black curve) with the index for internal wave activity calculated with Equation 2.1 (gray curve) for the mooring duration. Note that this time, E_a is calculated from the moored ADCP and the vertical velocity signal is not affected by the presence of the profiler as in Figure 25. The threshold for IWs detection was determined as an excess of E_a above the mean value by 5 standard deviations (dashed gray line). Similarly, we defined *significant* shear enhancement by an increase of more than 5 standard deviations above the mean value, which is generally more than a 10-fold increase (black dashed line in Fig. 26a). For some periods, internal wave activity coincides with shear enhancement, but for other periods both variables seem uncorrelated. To illustrate this, we selected two periods (gray shades in Fig. 26a) where peaks in E_a and S^2 above the thresholds are more or less aligned (Fig. 26b) and where they are not (Fig. 26c). Bourgault et al. (2008) also observed similar behavior in the upper St. Lawrence Estuary, where shoaling internal waves were about half of the time associated with shear maxima and half of the time with shear minima. The explanation given was that sometimes the shear induced by the wave adds-up with the background shear for a larger total shear, while sometimes they cancel each other out. A similar explanation may also be valid for our sampling site where only a small fraction of the IWs shear increase the background shear (Fig. 26e).

Among 338 episodes of internal wave activity, 32 are associated with significant near bottom shear enhancement. Whereas IWs are mostly detected near the high tide (more than 50 % in the $t = [-3, 1]$ h range), no clear relationship shows up regarding the phase at which

they correspond to shear enhancement (Fig. 26e) .

2.5 Discussion

2.5.1 CIL behavior in response to internal tides

The study suggests that during mooring deployment the node for vertical displacement is located near 25-30 m *hab*, i.e., at CIL depth (Fig. 19). Our best fit on density profile gives a node in the solution of vertical displacement (η_0, Eq. 2.8) at $z = 54$ m, i.e., 29 m *hab* at mooring site, thus supporting the idea that the pinching of the isotherms at this depth is the reason why the CIL disappears at some phases of the M_2 tide cycle.

Our study also highlights that this node position is highly variable depending on near surface stratification. Using the density profile measured at the basin interior instead of near the boundary to compute the second vertical modal structure would displace the node down by nearly 20 m (see Section 2.3.4). With such horizontally inhomogeneous stratification, internal tides generated at the head of the Laurentian channel are thus spatially modulated during their propagation out of the estuary. This changing vertical structure thus makes any generalization concerning their behavior (node position, current amplitudes, etc.) difficult and caution should be taken in interpreting these results.

Cross-shore currents are also associated to internal tides (Fig. 21). In our model, however, they do not interact with the real topography. In the real case of a sloping boundary, these currents could generate upslope and downslope currents. This may explain the asymmetry (maximum displacement not in phase at each depth) that exists in Figure 19a compared to Figure 22a. Although u and v velocities are nearly in phase (upslope flow during the flood), this is fortuitous since internal tides have a wavelength in the propagation direction many times smaller than the barotropic tides. Depending on the distance from the generation site, the current reversals of internal tides does not necessarily occur in phase with the reversal of

barotropic tide that generates it. At the mooring site, the lag between barotropic high tide and cross-shore current reversal (driven by internal tides) is about 1.5 h (Fig. 19), about equivalent to the phase shift applied in Figure 22 for better visual comparison ($\phi = \frac{\pi}{4} \sim 1.5$ h for the M_2 period).

Internal tides in the LSLE thus impact, at semi-diurnal and higher frequencies, the velocity, salinity, temperature and other physico-chemical property distribution. In preparation to field programs, care should be taken to not under-sample in time the water column properties that are subject to large variations due to such isopycnals heaving. For example, a CIL index (Galbraith, 2006), based on the cold water volume, is used in annual reports on the physical oceanographic conditions of the Gulf of St. Lawrence (e.g. Galbraith et al., 2012). When based on a single profile, estimates that use the CIL thickness may be not representative of the mean conditions, depending on which phase of the isotherms heaving it has been realized.

2.5.2 Boundary mixing in the LSLE

From about 150 casts that reached the bottom (not necessarily above the sloping bottom), Cyr et al. (2011) reported near bottom diffusivity to be $K_b = 3.3(2.1, 4.8) \times 10^{-4}\,m^2\,s^{-1}$. With such a diffusivity, boundary mixing was estimated to account for about one third of the mixing budget in the LSLE. When analyzed in terms of dissipation, this corresponds to $\epsilon_b = 1.2(1.0, 1.4) \times 10^{-7}\,W\,kg^{-1}$ (values not reported in Cyr et al. (2011)). In the present study, a more extensive sampling above the sloping bottom reveals that the average dissipation and diffusivity in the bottom 10 m are $\overline{\epsilon}_{10\,m} = 1.6(1.2, 2.0) \times 10^{-7}\,W\,kg^{-1}$ and $\overline{K}_{10\,m} = 6.0(4.1, 8.5) \times 10^{-4}\,m^2\,s^{-1}$ (Section 2.4.3), thus higher than the results of Cyr et al. (2011).

The study thus supports the findings of Cyr et al. (2011) that boundary mixing is significant at the scale of the LSLE and possibly the Gulf of St. Lawrence. Using a scaling for the effective diffusivity at the basin scale (K_e, Cyr et al., 2011, Eq. 5) with updates from this

study, we suggest $K_e = 4.1 \times 10^{-5}\,m^2\,s^{-1}$ and reassess that boundary mixing can account for about 30-40% of this value.

Mean profiles reported in Figure 24 are also informative of the nature of turbulent processes encountered in the LSLE. For certain shallow highly stratified or partially mixed estuaries, one may expect that most of the dissipation is determined by bottom stress and stress in the pycnocline (e.g. Geyer and Smith, 1987; Geyer et al., 2000, 2010). In these estuaries, the stratification varies within a broad range of values between ebb and flood conditions with often very weak stratification during strongest tidal flow (e.g. Nepf and Geyer, 1996; Peters, 1997; Geyer et al., 2000; Kay, 2003). The LSLE does not behave such as these estuaries since even in the near bottom part of the water column the stratification profile remains nearly constant between the ebb and the flood (Fig. 24b). Although near bottom ϵ is modulated by the semi-diurnal tide cycle (by a four-fold change, section 2.4.3), the difference between flood and ebb mean stratification profile at each depth is less than 1%. In fact, with a mean stratification near $N \sim 10^{-2}\,s^{-1}$ and dissipation rate in the $\epsilon \sim [10^{-8}, 10^{-7}]\,W\,kg^{-1}$ range, turbulence in the LSLE falls within the continental shelf turbulence definition, following the classification of oceanic and estuarine turbulence by Geyer et al. (2008) (see their Figure 1). Mixing mechanisms likely to be encountered in the LSLE are thus those usually present at the continental slope, including shear instabilities of various origin, bottom friction and internal wave induced mixing.

2.5.3 Boundary mixing mechanisms and forcings

Our observations suggest that bottom and interior mixing processes are at work at our sampling location. The former is suggested by the high dissipation rates found near the bottom, while the latter is suggested by the higher shear and dissipation bands found in the interior of the water column (Figs. 23 and 24). These two regions will be discussed next in an attempt to identify mixing mechanisms at work and their origin (forcings).

In this area subject to intense tidal currents, mixing by *bottom shear stress* resulting from the friction of the flow over the bottom may be expected to occur. For an unstratified flow, the dissipation driven by bottom friction should follow a log-law scaling, commonly referred to as the *law of the wall*: $\tilde{\epsilon} = \frac{u_*^3}{\kappa z}$. Here $\kappa = 0.41$ is the von Kármán constant, z the distance from the bottom and $u_* = \sqrt{C_d} U_\mathrm{b}$ the temporally variable friction velocity, that depends on a constant drag coefficient (C_d) and the near bottom velocity U_b (see Walter et al., 2012, for example).

Since this theory is suitable for unstratified water, we first identified near bottom profiles where buoyancy effects were not expected to affect overturning in the bottom boundary layer (BBL). This condition is expected to hold when the Ozmidov scale ($l_o = \left(\frac{\epsilon}{N^3}\right)^{\frac{1}{2}}$, a length-scale for the size of overturns limited by stratification) is larger than the scale of the overturns limited by their distance to the bottom ($l = \kappa z$, the length-scale that appears in the law-of-the-wall). This condition can be written $l_o > \kappa z$. The result of this condition for our sampling on 22 September 2011 is highlighted by the magenta lines in Figure 23. For all our dataset, the portions of the BBL identified this way were never thicker than 6 m *hab*, and only 9% of the bins below this depth satisfied the condition. This signifies that the near bottom layer is generally well stratified, or at least that the turbulence is sufficiently weak to be affected by the stratification. Although less frequent, weak stratification conditions drive most of the near bottom dissipation as suggested by the difference between the thick and the thin gray lines in Figure 24d, which are respectively the average of low stratification bins and the averaged profile without them.

Moreover, the dissipation profile inferred in the bottom 6 m using the above log-law scaling (Fig. 24d, dashed gray line) is comparable, in magnitude, to the dissipation profile observed during periods of low stratification (thick-solid gray line). Here the log-law scaling was calculated using $C_d = 3 \times 10^{-3}$ (Soulsby, 1997) and $U_\mathrm{b} = U_{2\mathrm{m}}$, the velocity measured by the moored ADCP at 2 m *hab* and 15-minute filtered to reduce the error on the measurements. Note that we used $U_{2\mathrm{m}}$ rather than the commonly used velocity at 1 m *hab* to avoid the side-

lobe effects of the ADCP measurements near the seabed. The use of different drag coefficients would not significantly affect this comparison because using $C_d = [1 - 5] \times 10^{-3}$ (range of values commonly found in the literature) leads approximately to a 2-fold change on ϵ_{wall}. The two profiles above also compare favorably when looking at their averaged values, which are $\epsilon_{BBL} = 7.2 \times 10^{-7}\,\mathrm{W\,kg^{-1}}$ and $\epsilon_{wall} = 8.1 \times 10^{-7}\,\mathrm{W\,kg^{-1}}$, respectively for the low stratified BBL and inferred from the log-scaling.

However, there is a caveat in that selecting only mixing events that satisfy $l_o > \kappa z$ is akin to applying a filter that can pick up cases of strong dissipation *or* weak stratification. Events with dissipation lower than that expected from the law of the wall may be filtered out, artificially creating a good fit between observed dissipation rates and those expected from the law of the wall. A visual inspection of the distribution of both stratification and dissipation rates indicated that this filtering selected a combination of both high dissipation and low stratification, mitigating this effect. Still, the analysis shows that dissipation rates within a maximum of 6 m *hab* are at least consistent with the law of the wall for 9% of all observations.

The fact that the dissipation inferred from near bottom velocities scales relatively well with the measured dissipation when the stratification is low suggests that most of the dissipation in the bottom 6 m of the water column are driven by bottom shear stress. Within this depth range, S^2 and N^2 (and thus Ri) are approximately constant between flood and ebb, implying that shear instabilities cannot account for the difference between $\epsilon_{\mathrm{flood}}$ and ϵ_{ebb}. In the same depth range, the mean velocity profile is however shifted towards greater values during the flood compared to the ebb, implying greater kinetic energy input to be dissipated by bottom friction. Because shear in the along-shore direction largely dominates the shear spectrum in the 0-10 m *hab* depth range (Fig. 20), we may hypothesize that the barotropic tidal currents are the main drivers for bottom shear stress mixing, although internal tides also generate near bottom shear. Conditions favorable to bottom shear stress only occur in about 9% of our sampling, the rest of the time the turbulence generated by bottom friction is likely suppressed by

the stratification as suggested by the lower dissipation when ignoring low stratified bins (thin gray line in Figure 24d). Non-linear internal waves (IWs) were also occasionally detected at the sampling site, but observations reveal that only about 10% of them were accompanied with significant bottom shear enhancement. This study thus suggests that the role of IWs in bottom shear stress mixing is small at our sampling site.

In counter part, other mechanisms besides bottom stress must explain the approximately exponential increase of the dissipation from about 25 to 5 m *hab* (Fig. 24d). Such an increase, combined with the fact that the BBL is mostly stratified, suggests internal waves scattering (or bottom wave generation) as a possible mixing mechanism responsible for this near bottom mixing enhancement (Garrett et al., 1993; Toole et al., 1994; Slinn and Riley, 1996; St. Laurent, 2002). This mechanism was also recently summarized by Gregg et al. (2012) for mixing above a continental slope.

The localized bands of enhanced turbulence presented in Fig. 23 generally correspond to bands of lower Richardson number, suggesting that shear instabilities are at work in the interior of the water column. Low Richardson numbers generally present near the bottom (Figs. 23 and 24) also suggest that shear instabilities may be expected below $\sim$ 10 m *hab*, but their effect should not dominate over bottom stress mixing that explains most of the ϵ increase in this depth range (see text above). To examine a possible systematic relation between stratification, shear and dissipation, we plotted 4-m resolution bin of ϵ in function of N^2 and S^2 in a manner similar to MacKinnon and Gregg (2003) and van der Lee and Umlauf (2011) (Fig. 27a). For this exercise, we ignored bins satisfying $l_o > \kappa z$. Results suggest that higher dissipation rates occur as critical Richardson numbers ($R_i = \frac{1}{4}$, solid line) are approached or exceeded. Except for this, no general patterns are easily discernible, and observation comparisons with both the Gregg-Henyey (Gregg, 1989, hereafter GH) and the MacKinnon and Gregg (2003), hereafter MG parametrizations are visually poor (Figures 27b and c). The equations for these two parametrizations are respectively:

$$\epsilon_{\mathrm{GH}} = 1.8\times10^{-6}\left[f\cosh^{-1}\left(\frac{N_0}{f}\right)\right]\left(\frac{S^4}{S^4_{\mathrm{GM}}}\right)\left(\frac{N^2}{N_0^2}\right), \tag{2.10}$$

and

$$\epsilon_{\mathrm{MG}} = \epsilon_0\left(\frac{N}{N_0}\right)\left(\frac{S}{S_0}\right). \tag{2.11}$$

Here, f is the Coriolis frequency, $N_0 = S_0 = 3\,\mathrm{cph}$ (MacKinnon and Gregg, 2003) and $S^4_{\mathrm{GM}} = 1.66\times10^{-10}\left(\frac{N^2}{N_0^2}\right)^2$. We also impose $\epsilon_0 = 5.1\times10^{-9}\,\mathrm{W\,kg^{-1}}$ in the MG parametrization, chosen so that the parametrization average matches the observations average.

In an attempt to isolate whether the stratification or the shear has a dominant effect on the dissipation, our observations (Fig. 27a) are now presented in terms of N^2 and S^2 only (Fig. 27d-e, shaded areas). This corresponds to vertical and horizontal averages of panel *a*. The flat shaded area in panel *d* suggests that there is no link between stratification and dissipation. In counterpart, panel *e* suggests that the dissipation has a tendency to increase with increasing shear. Doing the same averaging for the two parametrizations reveals that the MG parametrization captures relatively well this dissipation increase with shear. Note that the decreasing dissipation at the maximum shear may be caused by outliers since the number of bins where it happens is very low.

The Gregg-Henyey parametrization was developed for thermocline mixing in the deep ocean and overestimates the dependency of the dissipation on the shear by many orders of magnitude and is not suited for the coastal ocean. The MG parametrization was developed for this reason and is always closer to our observations compared to the GH parametrization. The reason why no dependency between the dissipation and the stratification is observed is unknown at this point. It may be due to the nearby presence of a sloping boundary that may continuously help the restratification through secondary circulation after mixing operates (Phillips et al., 1986; Garrett, 1990, 2001; Moum et al., 2002).

Overall, the dependence between shear and dissipation suggests that shear instabilities are responsible for most of the dissipation out of the near bottom region where $l_o > \kappa z$ is satisfied. Forcings driving the shear are difficult to isolate, but for the 10-20 m *hab* range, spectral analysis suggests that the shear is at least partly sustained by tidal harmonics in the along-shore direction at M_2, with significant contribution from the across-shore direction at M_4, M_6 and M_8 (Fig. 20). Since our study suggests that across-shore velocities are mostly due to internal tides, these are in part responsible for shear instabilities within the water column. As suggested earlier, internal wave scattering or reflecting on the bottom may also contribute to the dissipation increase as the bottom is approached. The mechanisms by which these waves dissipate their energy can be either by breaking or by locally generating shear instabilities.

2.6 Conclusion

In a recent study, Cyr et al. (2011) concluded that although not dominant, boundary mixing can contribute significantly to the erosion of the Gulf of St. Lawrence CIL. In the conclusion of that study, questions were raised concerning possible boundary mixing mechanisms. This partly motivated the deployment of the mooring at station N080, i.e. where the CIL intersects the sloping bottom. Mooring observations were completed with 322 VMP turbulence profiles down to the bottom, over the sea floor.

CIL behavior at the slope has been depicted as alternating swash/backwash of the layer on the sloping boundary at a semi-diurnal frequency, with superimposed higher harmonics. The CIL also thickens and shrinks (and sometimes disappears at mooring location) at semi-diurnal and higher frequencies. This behavior is part of the 3-dimensional structure of internal tides generated at the head of the Laurentian channel and propagating out of the estuary. To date, studies focusing on internal tides in the LSLE are limited to scarce observations and idealized models, and the region still lacks a detailed description of the propagation of these

tides. This description is however difficult because of the complex bathymetry and changing water stratification properties along the channel.

Observations suggest that near bottom turbulence increase is driven by bottom shear stress in the bottom ~6 m *hab*. Bottom friction of the strong barotropic tidal currents may be responsible for this stress. When currents are maximum, i.e. during the flood, the dissipation rates of TKE are approximately 4 times higher than during the ebb. However such strong turbulence occurs in about 9% of our profiles and corresponds to periods when the maximum size of overturns in the BBL are not controlled by the stratification. Below about 25 m *hab*, the dissipation also increases albeit to a lesser extent as the bottom is approached. Internal wave scattering may be responsible for this increase. A systematic relation between shear and dissipation shows that shear instabilities of various origins may drive a significant part of the mixing above the BBL.

Finally, this study supports the findings of Cyr et al. (2011) that boundary mixing, although not dominant, can account for a significant part of the mixing budget of the LSLE and possibly the Gulf of St. Lawrence. Turbulent dissipation of TKE at the sloping boundary is about an order of magnitude greater than in the interior (far from boundary) and can explain about 30-40% of the total mixing budget.

2.7 Acknowledgments

This work was funded by “Le Fonds de recherche du Québec - Nature et technologies”, the Natural Sciences and Engineering Research Council of Canada, the Canada Foundation for Innovation and Fisheries and Oceans Canada and is a contribution to the scientific program of Québec-Océan. The authors would like to thank Rémi Desmarais and Paul Nicot who were frequent crew members during our summer sampling campaigns and an anonymous Reviewer who provided valuable comments to improve this manuscript.

	N080
total depth (m)	83
ADCP depth (frequency, orientation)	59 (600 kHz, down)
ADCP range (m)	61-bottom
ADCP sampling freq. (Hz)	$\frac{1}{3}$
thermistors depth (m)	30, 40, 50, 60, 65, 70, 75, 80
thermistor sampling freq. (Hz)	0.2, 0.2, 0.2, 0.1, 0.1, 0.1, 0.1, 0.1

Table 2: Mooring information

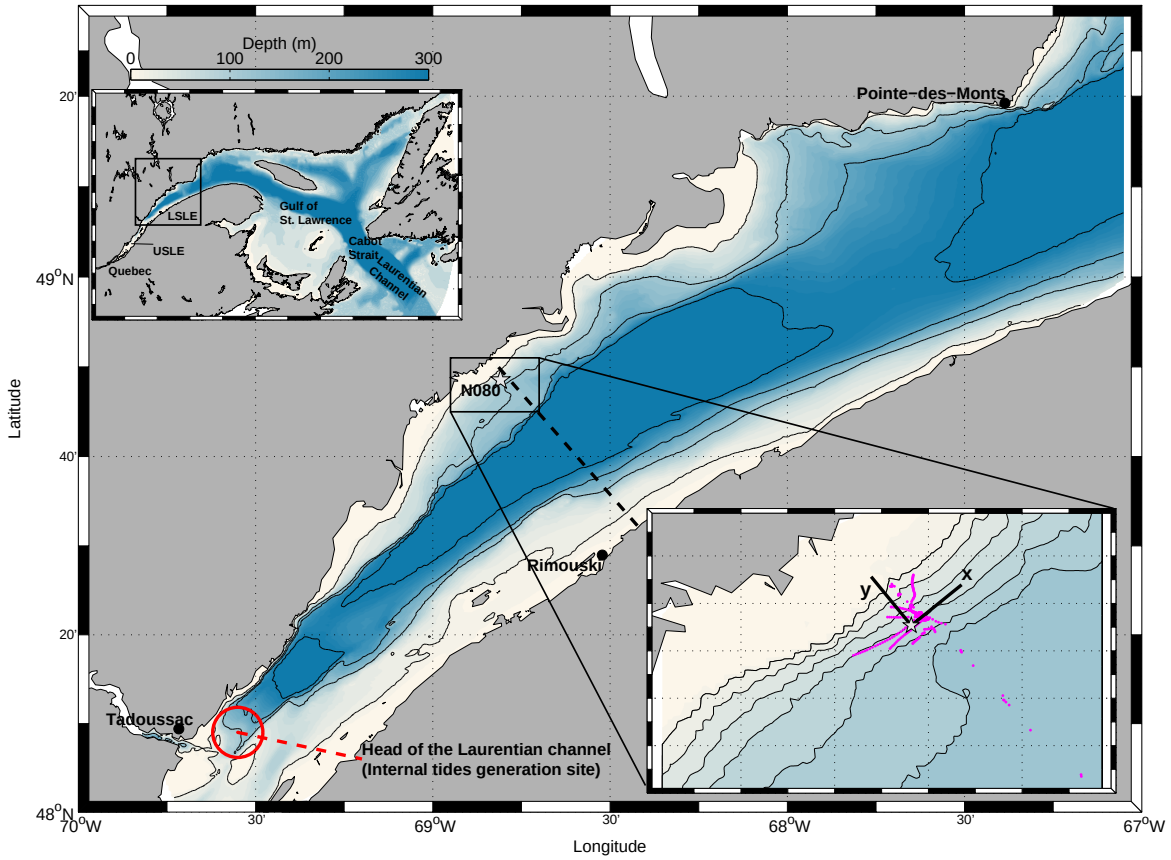

Figure 16: Bathymetry of the Gulf of St. Lawrence (upper inset) and the Upper (USLE) and Lower St. Lawrence Estuary (LSLE). The square box in the upper inset correspond to the LSLE where the study was realized (main figure). Isobaths 20, 120, 200 and 300 m have been added. The dashed line is the Rimouski section across the estuary. Second inset shows details of the study area on the northern portion of the transect, between isobaths 20-120 m (shown with 20 m intervals). Positions of mooring N080 (white star) and of the 322 VMP profiles used in this study (purple dots) are also presented.

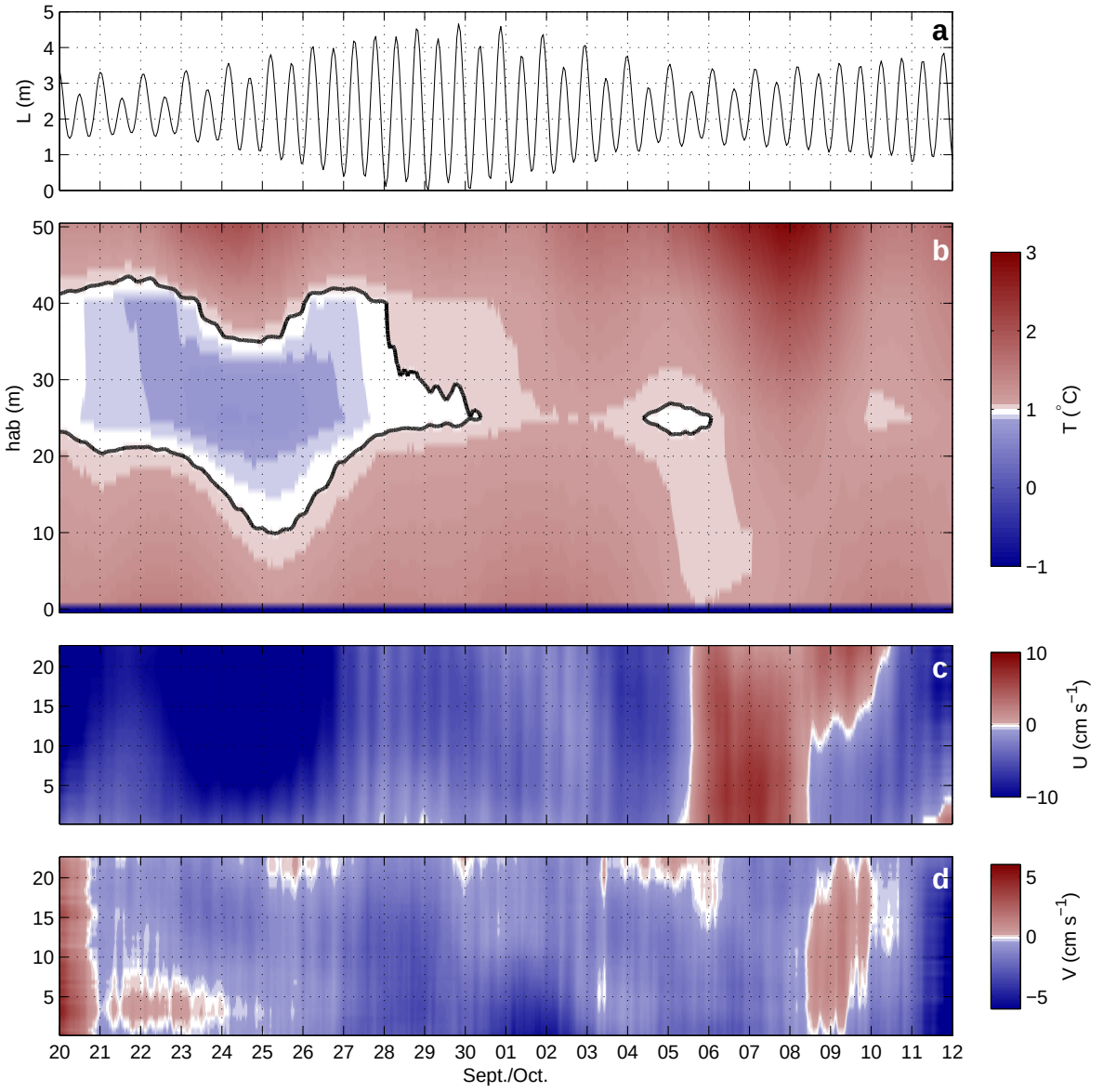

Figure 17: Temperature and currents measured for the duration of the mooring deployment. (a) Predicted tide water level at Rimouski (L). (b) Evolution of the temperature field for this period as measured by the thermistor chain. Temperature was linearly interpolated between thermistors and a 25-hour low-pass filter has been applied. Solid lines are $T = 1°C$ contours. (c-d) Respectively the along- and cross-shore velocities measured by the ADCP over the slope. A 25-hour low-pass filter has been applied on both current components. The vertical axis for the three last panels is the height above bottom (*hab*).

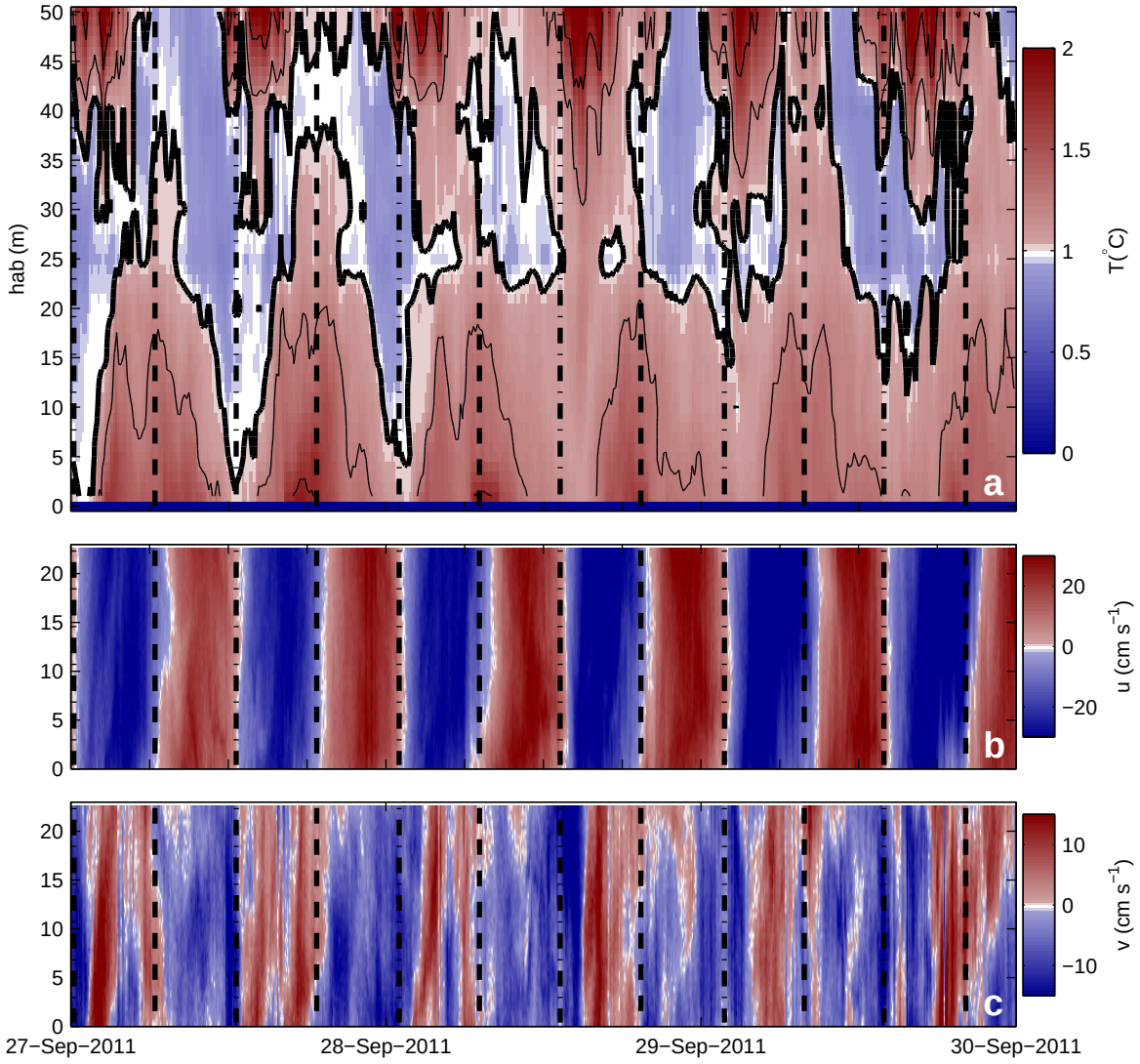

Figure 18: Example of a timeseries from the mooring for temperature (T), along- and cross-shore velocities for a three-day period, 27-30 September 2011. The temperatures are 10-minute averaged and linearly interpolated between each thermistors, while the velocities are 10-minute averaged and raw in the vertical (0.5 m). Thick solid lines in (a) are $T = 1$°C contours while thin lines are $T = 1.25$ and 1.75°C. High tides (dashed lines) and low tides (dashed-dot lines) are also identified in all panels for reference.

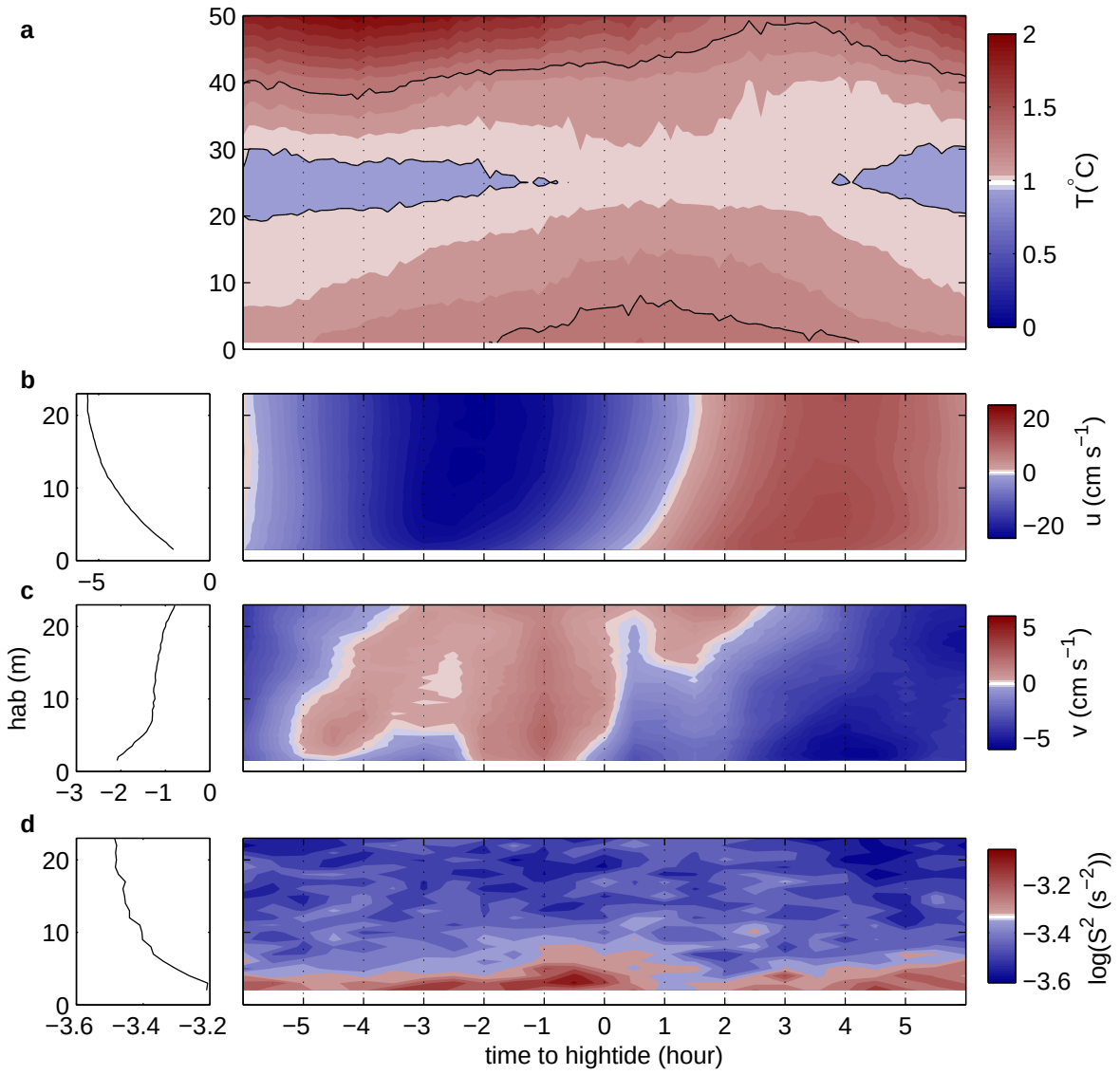

Figure 19: Mooring conditions relative to the M_2 tide cycle. All fields have been averaged in 15-minute classes relative to the high tide. The vertical axis is the height above bottom (*hab*). (a) Temperature field, with isotherms 1°C and 1.3°C (black lines) added for visual reference. (b) and (c), along- and cross-shore velocities, with 0.5 m vertical bins. (d) Base-10 log of the mean shear S^2. Note that panel *a* spans 50 m on the vertical while others span only 25 m. Left side panels in *bcd* are the time-averaged profiles.

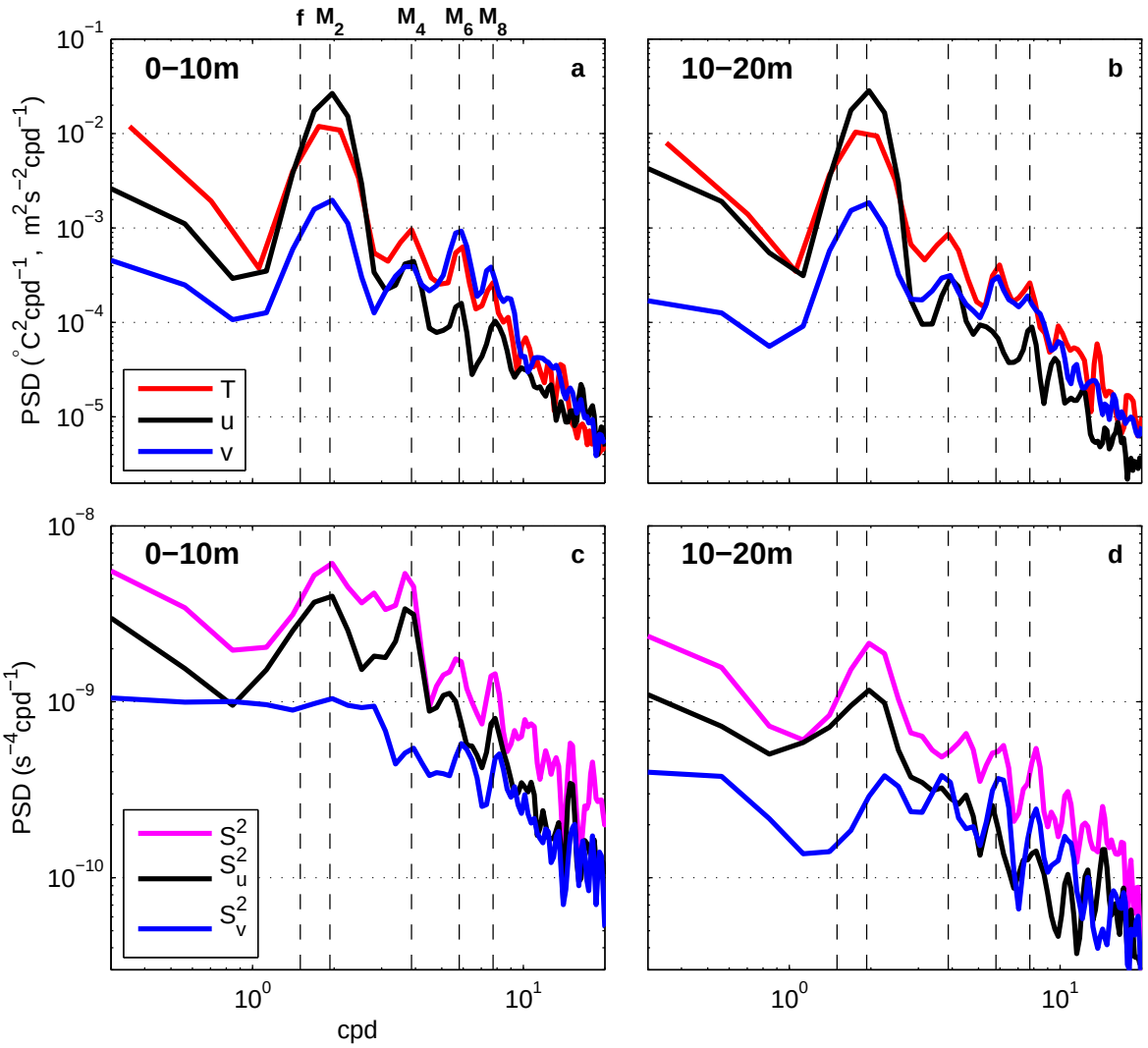

Figure 20: Power spectrum density (PSD) for temperature, cross-shore (u) and along-shore (v) velocities, vertically-averaged over the depth range 0-10 m (a) and 10-20 m (b) above the seabed. (c-d) Power spectrum density for the total shear (S^2), along-shore ($S_u^2 = \left(\frac{\partial u}{\partial z}\right)^2$) and cross-shore shear ($S_v^2 = \left(\frac{\partial v}{\partial z}\right)^2$) for the same depth ranges. The frequency is in *cycle per day* (cpd). Tidal Harmonics M_2, M_4 ,M_6 and M_8 have been added for reference (vertical dashed lines). The choice of the window used for PSD calculations (Hanning window of ~2.2 days) makes the inertial frequency f hard to distinguish from M_2

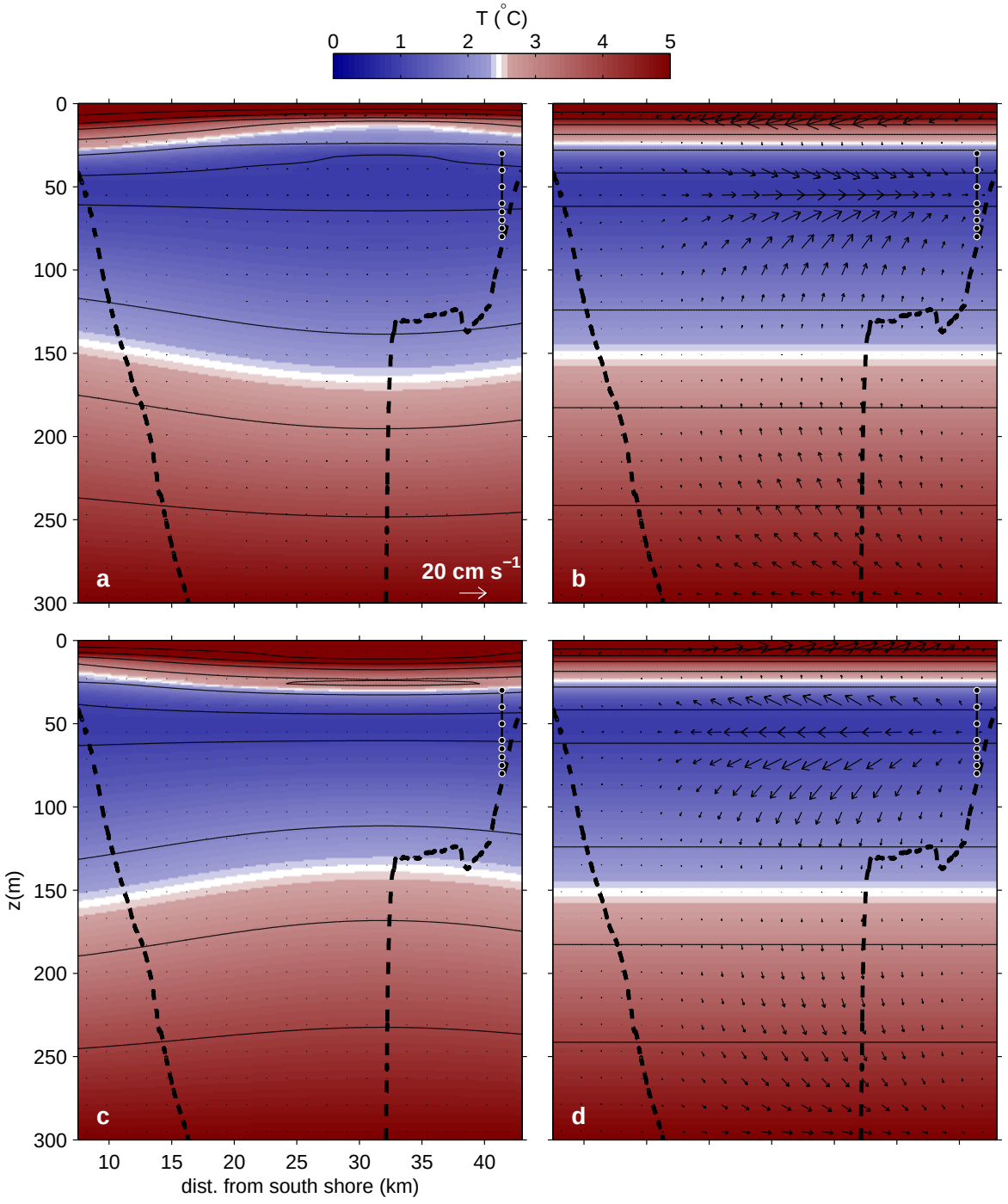

Figure 21: Predicted isotherms displacements for a mode-2 Poincaré internal tide (Eq. 2.9) at 4 different phases of the M_2 tide cycle, i.e., $\phi = 0$, $\frac{\pi}{2}$, π and $\frac{3\pi}{2}$ respectively (see Fig. 22). Velocity vectors for the cross-section are also added for reference (v and w from Eq. 2.5). Vectors are scaled according to figure horizontal and vertical axes. (a,c) maximum displacement, minimum velocity. (b,d) minimum displacement, maximum velocity. The bottom topography of the Rimouski section (dashed lines) with the position of the mooring N080 (vertical line with circles representing thermistors) are also added. The x-axis is the distance from the south shore near the city of Rimouski.

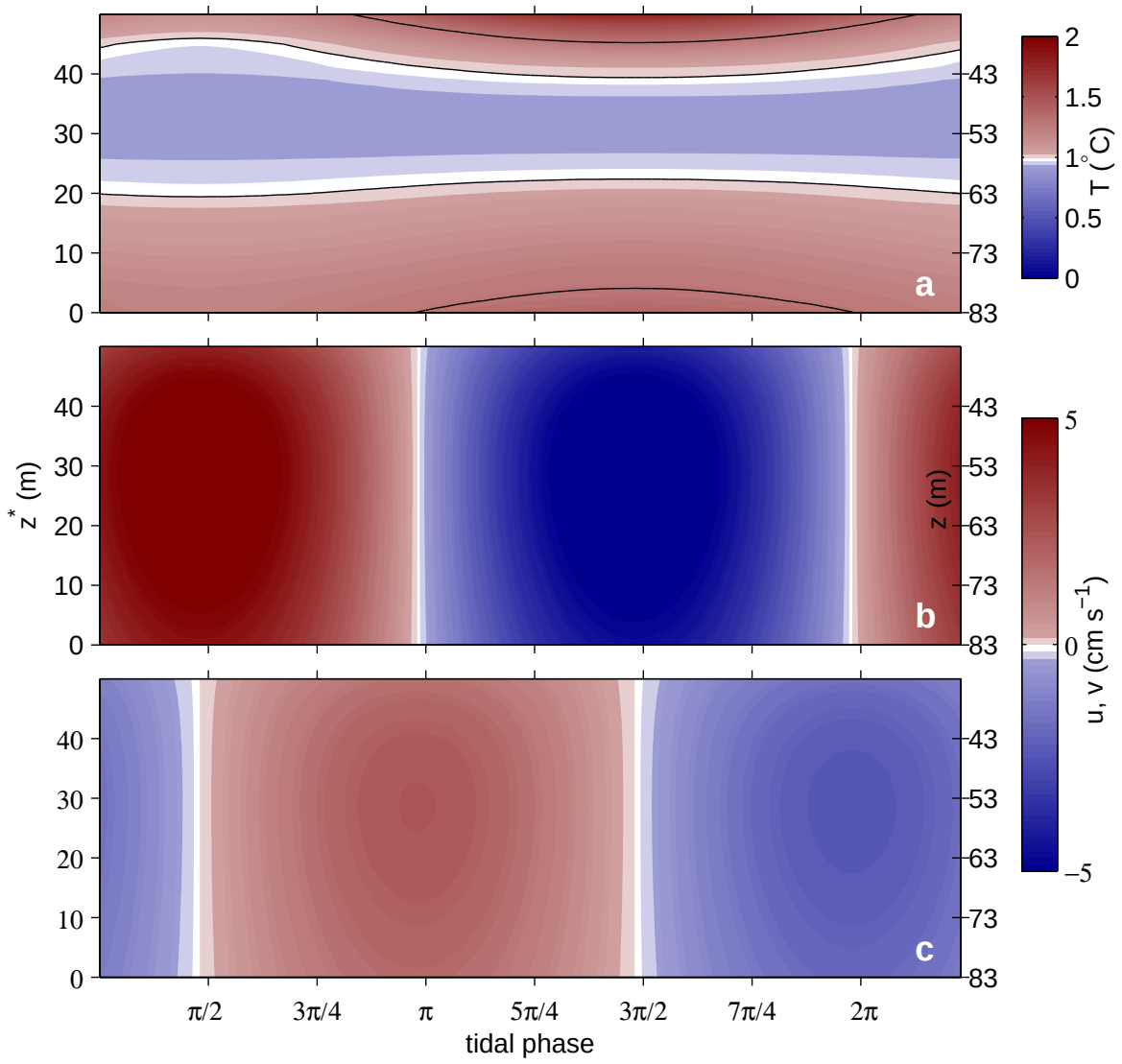

Figure 22: Predicted temperature (T), along- (u) and cross-shore (v) velocities evolution during a M_2 tide cycle for an idealized mode-2 Poincaré internal tide (Equations 2.5 and 2.9) for approximate mooring location ($y = 33.9$ km) and its depth span. For better comparison with Figure 19, the left-hand side vertical axis is $z* = z_0 - z$, where $z_0 = 83$ m is the total depth at mooring location. The horizontal axis also starts at $\phi = \frac{\pi}{4}$ instead $\phi = 0$ for the same reason. The water column depth z is provided as the right-hand vertical axis of the figure. Isotherms $T = 1°$C and $T = 1.3°$C have also been added in panel a (black lines).

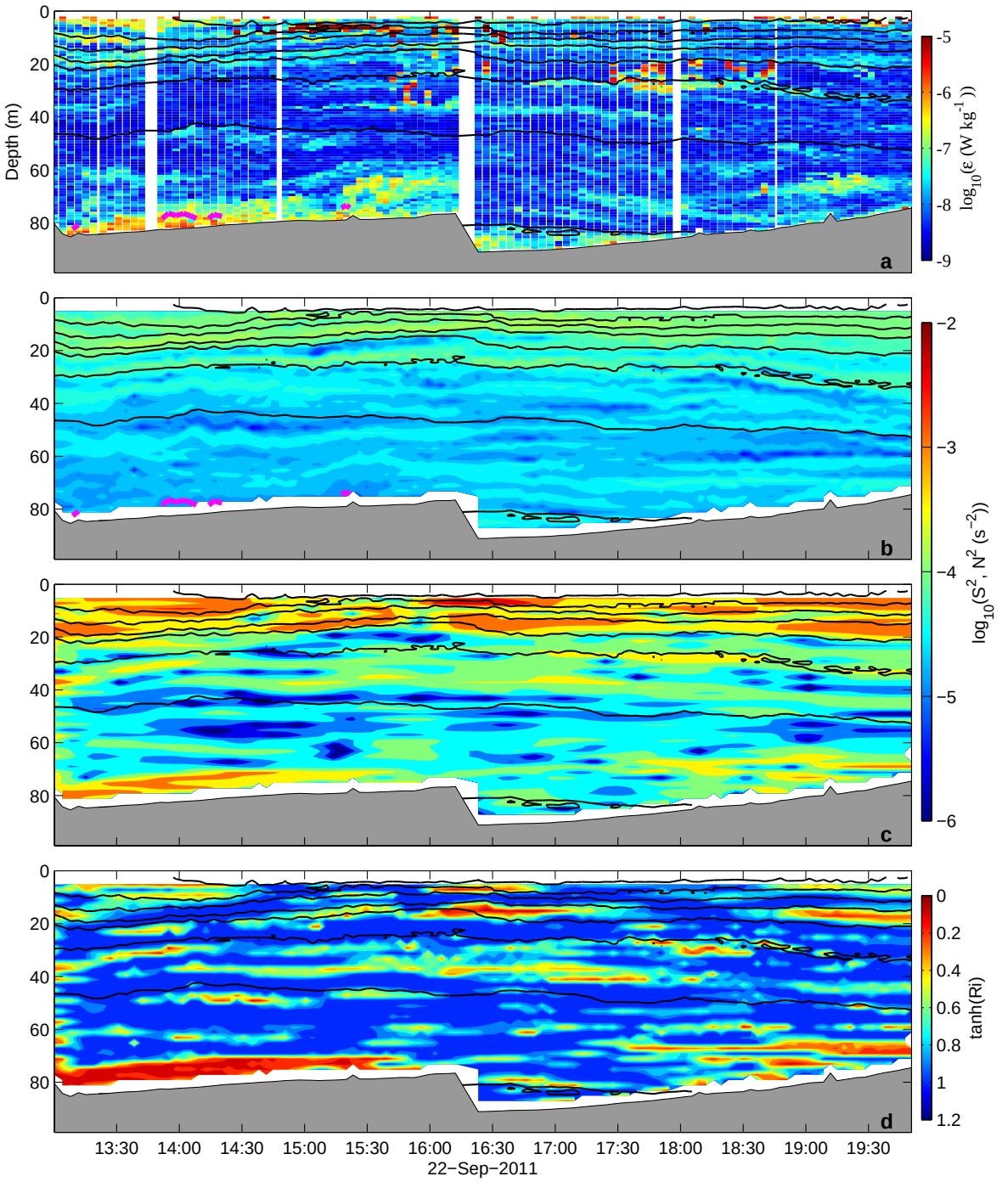

Figure 23: Turbulence versus water column stability parameters as a function of time and depth (m) in the proximity of the mooring on September 22, 2011, measured from a drifting boat (repositioned at 16:13). (a) Dissipation rate of turbulent kinetic energy (ϵ). (b) Background buoyancy frequency squared in 4-m bins (N^2). (c) Background shear squared in 4-m bins (S^2). (d) 4-m scale Richardson number (R_i). Black lines in all panels indicate isopycnals. Magenta lines in panels *a* and *b* indicate regions near the bottom where $l_o > \kappa z$ (see Section 2.5.3).

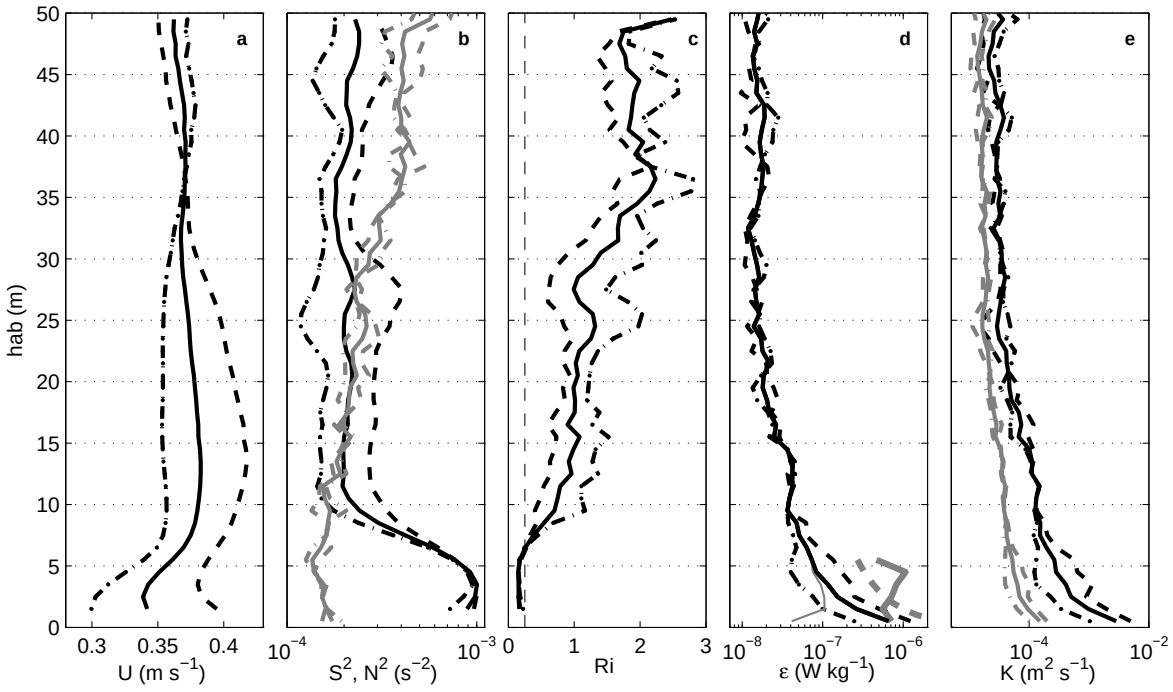

Figure 24: Averaged quantities of our 322 VMP casts (solid lines). Averaged profiles when considering only flood (dashed) and ebb (dot-dashed) are also presented. (a) Velocity profiles $U = \sqrt{u^2 + v^2}$ from the ADCP deployed outboard, corresponding to VMP casts. (b) Shear (S^2, black lines) calculated with velocity profiles from outboard ADCP, and stratification (N^2, gray lines) from VMP casts. (c) Richardson number ($Ri = \frac{N^2}{S^2}$) calculated from the ratio of mean profiles of panel *b*. (d) Dissipation rate of TKE when using all available bins (thick black lines) and bins when the size of overturns is limited by the stratification, e.g., when $l_o < \kappa z$ (thin gray line). Also on this panel, the dissipation when the size of overturns is not limited by the stratification ($l_o > \kappa z$, thick gray line) and the dissipation inferred from near bottom velocities using the log-law scaling presented in section 2.5.3 ($\tilde{\epsilon} = \frac{u_*^3}{\kappa z}$, dashed-gray line). (e) Turbulent diffusivity calculated using a constant ($\Gamma = 0.2$, black lines) and variable (Eq. 2.4, gray lines) flux parameter. Except U, averaged profiles are calculated assuming log-normal distribution.

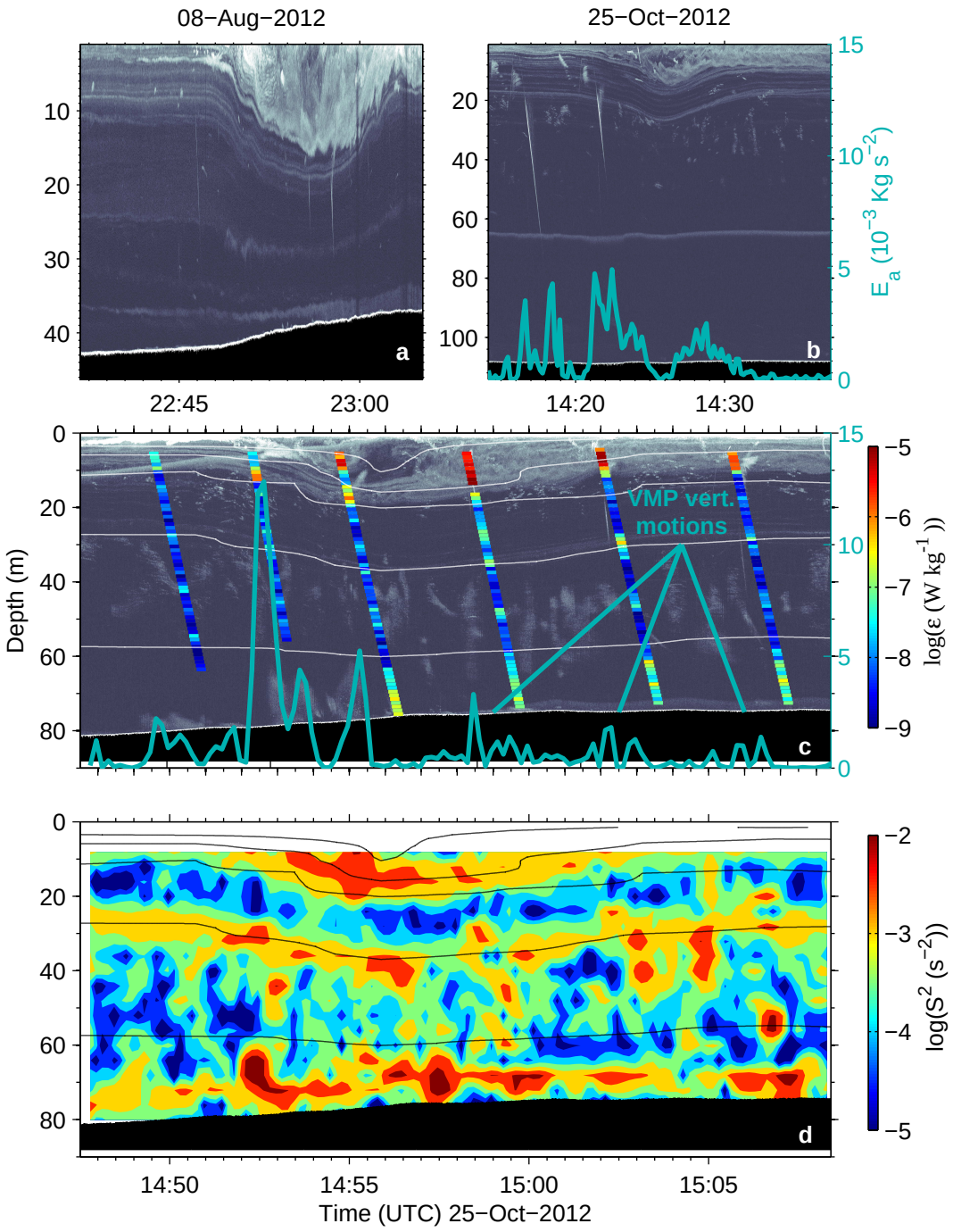

Figure 25: Non-linear solitary waves observed with an echo-sounder. (a) Echogram at 120 kHz of the first wave (8 August 2012). (b) Echogram at 120 kHz of the second wave (25 October 2012). (c) Echogram at 120 kHz of the third wave (25 October 2012), with dissipation rate of TKE (ϵ) superimposed. (d) Mean shear measured from the outboard ADCP during the passage of the third wave. Isopycnals (1022, 1023, 1024, 1025, 1026 kg m^{-3}) have been added on panels *c* and *d*, measured with the CTD on the VMP. Turquoise curves in panels *b* and *c* are the internal wave activity E_a calculated from equation 2.1. Evidence that the vertical motions of the profiler are picked up by the outboard ADCP and interfere with the internal wave activity index is also illustrated in panel *c*.

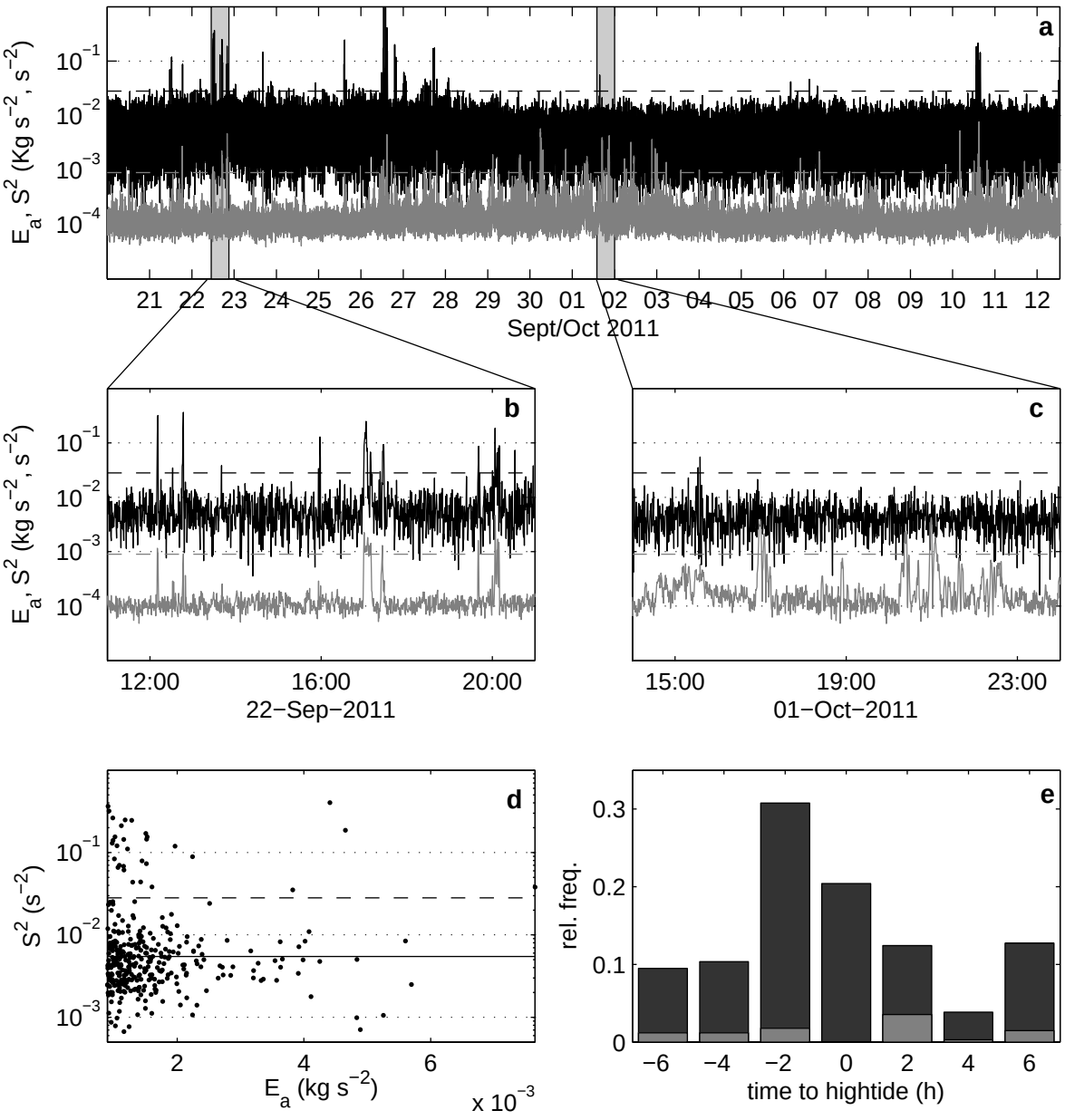

Figure 26: (a) Comparison between the area density energy (E_a, Eq.2.1, gray) and the mooring shear S^2 (black). Dashed lines correspond to 5 standard deviation above the mean value. Gray shades correspond to enlargement of panels (b) and (c). (d) Scatter plot of E_a versus S^2 for 338 internal waves (IWs) detected in (a). The solid line is the mean shear value for the mooring deployment and the dashed line represents 5 standard deviations above the mean value. (e) Histogram of the relative distribution of the 338 detected IWs relative to the M_2 tide cycle (dark gray). The fraction of IWs that induce significant shear enhancement is also added (light gray).

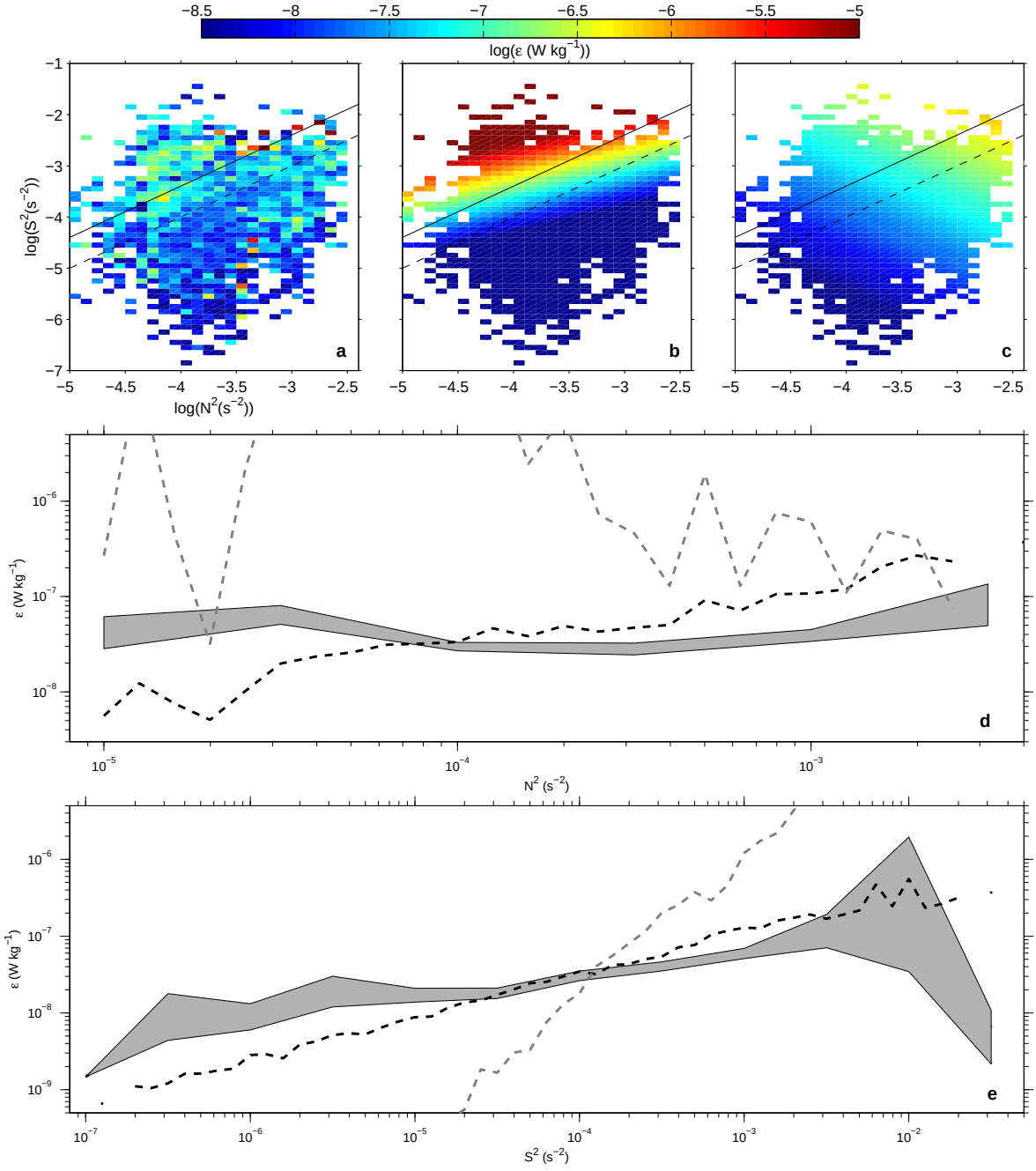

Figure 27: Dissipation rates of turbulent kinetic energy in function of the buoyancy frequency squared (N^2) and the shear squared (S^2). (a) Observations from all 322 profiles with bins satisfying $l_o > \kappa z$ removed. The solid and dashed lines are respectively $R_i = 1$ and $R_i = \frac{1}{4}$. (b) Same as a, for the Gregg-Henyey scaling ϵ_{GH} (Eq. 2.10). Note that to keep a single colorbar, panel b is saturated since ϵ_{GH} values range between $[10^{-13} - 10^{-3}]\,\mathrm{W\,kg^{-1}}$. (c) Same as a, for MacKinnon and Gregg (2003) scaling ϵ_{MG} (Eq. 2.11). (d-e) Respectively the vertical and horizontal averages of the three panels above to highlight the effect of the buoyancy frequency and the shear on dissipation. The shaded area is the bootstrapped 95% confidence interval on observations while the dashed-gray and the dashed-black lines are the average of panel b and c respectively.

ARTICLE III

TURBULENT NITRATE FLUXES IN A LARGE-SCALE ESTUARY

3.1 Abstract

Turbulent vertical nitrate fluxes are calculated using new turbulent microstructure observations in the Lower St. Lawrence Estuary (LSLE), Canada. Two stations were compared: the head of the Laurentian Channel (st. 25), where intense mixing occurs on the shallow sill that marks the upstream limit of the LSLE, and another station located about 100 km downstream (st. 23), more representative of the LSLE mean mixing conditions. Mean Turbulent diffusivities and nitrate fluxes at the base of the surface layer for both stations were respectively (with the 95% confidence interval): $\overline{K}_{25} = 4.5(1.1, 13) \times 10^{-2}\,\mathrm{m^2\,s^{-1}}$, $\overline{K}_{23} = 4.4(2.3, 7.6)\times 10^{-5}\,\mathrm{m^2\,s^{-1}}$, $\overline{F}_{25} = 120(23, 400)\,\mathrm{mmol\,m^{-2}\,d^{-1}}$ and $\overline{F}_{23} = 0.21(0.12, 0.33)\,\mathrm{mmol\,m^{-2}\,d^{-1}}$. Observations suggest that the interplay between large isopleth heaving near the sill and strong turbulence is the key mechanism to sustain such high turbulent nitrate fluxes at station 25 (two to three orders of magnitude more than those at station 23). Calculations also suggest that these large fluxes can sustain *new* primary production rates of $4.3(0.8, 14)\,\mathrm{g\,C\,m^{-2}\,mo^{-1}}$ over the *whole* LSLE, approximately enough to account for the phytoplankton bloom and post-bloom production. Surfacing nitrates are also believed to be consumed within the LSLE, not leaving much to be exported to the nearby Gulf of St. Lawrence.

3.2 Introduction

Nutrient cycling in the global ocean controls the primary production through nutrients availability in the euphotic zone. By fixing atmospheric carbon during photosynthesis, phytoplankton growth also plays an important role in regulating anthropogenic CO_2 concentrations in the atmosphere (e.g., Tsunogai et al., 1999; Thomas et al., 2004; Arrigo, 2005). Nutrient and carbon cycles are therefore closely related and their understanding is crucial for modeling Earth's future climate.

The coastal oceans have a key role in these cycles' dynamics because they act as buffering zones between the continents, from where they receive large amounts of nutrients and organic matter from land drainage, and the deep ocean, with which they exchange nutrients, particles and energy. Because of this buffering effect, they are among the most physically and biogeochemically active regions of the oceans (Gattuso et al., 1998; Borges, 2005). Although they occupy a small fraction of the ocean surface ($\sim 7\%$), they sustain about 15-30% of the primary production and contribute to 20-50% of the carbon sequestration in the oceans (Wollast, 1998; Tsunogai et al., 1999; Thomas et al., 2004; Muller-Karger, 2005). Moreover, the coastal ocean is where about two-third of the tidal power is dissipated (Egbert and Ray, 2000). The mixing that ensues from this dissipation affects the magitude of the oceanic carbon uptake, because new primary production sustained by diapycnal nutrient fluxes is much more efficient for sequestrating carbon than the regenerated production resulting from nutrient recycling (Falkowski, 2000; Richardson et al., 2000; Sharples et al., 2001b; Allen et al., 2004; Rippeth, 2005; Rippeth et al., 2009). The aim of this study is thus to explore turbulent diapycnal nutrient fluxes in a region of the world where strong turbulence is believed to sustain high (nearly as high as spring bloom level) primary production rates throughout the summer: the Lower St. Lawrence Estuary located in the Gulf of St. Lawrence, Canada (Fig. 28).

The Gulf of St. Lawrence (GSL, Fig. 28, inset) is a coastal sea where strong tidal mixing

occurs. According to Egbert and Ray (2000), the GSL and the Bay of Fundy basins together occupy the 10th rank among the world coastal seas and shelves for their tidal dissipation level. The GSL is also a biologically-rich area hosting many commercially-important fish and crustacean species. With landings of about $3-4\times10^5$ tons a year, it sustained about 20% of the eastern Canadian fisheries prior to the mid-90's ground fish decline (Chadwick and Sinclair, 1991; de Lafontaine et al., 1991). Historical research on nutrient dynamics and primary and secondary production is thus considerable in the GSL, although major features are still not fully understood today such as the nutrient supply to the system by vertical mixing.

The surface nutrient distribution was studied during the *International Biological Program* (Steven, 1971, 1974). A major result of this program is that nutrient supply to the euphotic zone of the GSL was coming from upwelling within the Lower St. Lawrence Estuary (LSLE, Fig. 28, main panel), a large-scale (the width is many times the internal Rossby radius) estuary generally considered part of the GSL. The nutrient supply to the GSL by the LSLE was referred by Steven (1971) as the *nutrient pump*. Further studies suggested that within the LSLE, most of the nutrient surfacing from deeper layers occur at a localized area at the head of the Laurentian Channel (HLC) near Tadoussac (Ingram, 1975; Greisman and Ingram, 1977; Ingram, 1979b, 1983).

The Laurentian Channel is a long (>1000 km) and deep (>290 m) submarine valley that originates on the continental slope, runs across the Gulf and ends near Tadoussac where the total depth abruptly shallows from 325 m to about 50 m in less than 15 km (Fig. 28). It is also where the Saguenay River waters meet the outflow from the St. Lawrence River. It has been suggested that intense vertical mixing occurs at this sill, but direct measurements of turbulence have never been realized. Many qualifiers have been given to this active mixing *hotspot*: upwelling, tidal upwelling, tidal mixing, tidal front, hydraulic jump, isopycnal shoaling, internal tide mixing, etc. (Forrester, 1974; Ingram, 1975, 1976, 1979b, 1983, 1985; Gratton et al., 1988; Saucier and Chassé, 2000; Ménard, 2009). Because of this ambiguity, it has long been a wish that mixing at the HLC be examined more thoroughly (Ingram, 1975;

Gratton et al., 1988; Koutitonsky and Bugden, 1991).

For most of the year, three water layers are present in the LSLE/GSL system and these circulate with estuarine-like dynamics along the Laurentian Channel (e.g. Koutitonsky and Bugden, 1991; Saucier and Chassé, 2000; Saucier et al., 2009). The surface layer (upper 30-50 m) is generally fresher in the LSLE compared to the GSL because of high freshwater input from the St. Lawrence and Saguenay rivers. Freshwater input also drives the Gaspé Current, a strong surface coastal jet current that contributes to most of the LSLE output to the Gulf (Tang, 1980; Benoit et al., 1985; Koutitonsky and Bugden, 1991). The bottom layer (roughly below 150-200 m) is composed of salty nutrient-rich waters of Atlantic origin. In between these two layers, the cold intermediate layer (CIL) is a remnant of the previous winter Gulf surface layer that became trapped as a CIL between two warmer layers at the onset of spring (Banks, 1966; El-Sabh, 1979; Koutitonsky and Bugden, 1991; Gilbert and Pettigrew, 1997; Galbraith, 2006; Smith et al., 2006a). Waters below the CIL temperature minimum, which lies roughly at a depth of 60-100 m, have high and almost constant nutrient concentrations (Steven, 1974). The weak turbulent mixing likely limits vertical exchanges of nutrient between deep and surface layer since the low turbulent ventilation below the CIL is also responsible for the hypoxic conditions found in the deep LSLE Gilbert et al. (2005); Bourgault et al. (2012).

While the spring bloom that occurs in the Gulf leaves the surface layer generally nutrient-depleted, the nutrient concentrations in the LSLE surface waters remain high (Steven, 1971, 1974). This is because both the intermediate and the bottom layers are thought to be partly extracted (resurfacing) by vertical mixing at the HLC Ingram (1979b, 1983). About 75% of the surface nutrients found in the LSLE may therefore originate from the CIL because of this resurfacing mechanism (Greisman and Ingram, 1977; Savenkoff et al., 2001), confirming the importance of the vertical nutrient fluxes compared to the advection from the St. Lawrence River. These vertical nutrient fluxes at the HLC sustain a high primary productivity in the LSLE, with daily production rates during the summer nearly equivalent to those

during the spring bloom (Levasseur et al., 1984; Therriault and Levasseur, 1985; Plourde and Runge, 1993; Plourde et al., 2001). This high primary productivity sustains high levels of secondary production that is then exported to the Gulf, mostly via the Gaspé Current (Fortier et al., 1992; Plourde and Runge, 1993). Recently, Ouellet et al. (2013) also suggested that the LSLE has an important role for the development and growth of the GSL capelin population, which itself is important for biomass transfer to upper trophic levels. Nutrient pumping at the HLC is thus likely a keystone for food web dynamics, not only for the LSLE but also for the Gulf.

In contrast to previous studies which indirectly inferred vertical nutrient fluxes at the HLC (Greisman and Ingram, 1977; Savenkoff et al., 2001), this study presents direct measurements of turbulence profiles from which vertical nutrient fluxes are derived. The study focuses mainly on nitrate plus nitrite (NO_3+NO_2) fluxes since dissolved nitrogen is thought to be the limiting nutrient in the system (Steven, 1974; Levasseur and Therriault, 1987). Comparison will also be made between observed mixing and fluxes at the HLC and at another station located about 100 km downstream.

3.3 Methodology

3.3.1 Nutrient concentration data

Nutrient concentrations were obtained from the Ocean Data Management System public database (Fisheries and Oceans - Canada, 2013). All water bottle measurements of NO_3 + NO_2 (nitrate plus nitrite) concentrations available for the period 2000-2012 and between April and November are considered. These measurements are also accompanied with other physical measurements such as temperature and salinity. Except for station 23, these measurements are located within a square box of side roughly the width of the Laurentian Channel and centered on oceanographic stations 16-25 (Fig. 28). These stations were selected since they have been routinely visited for multidisciplinary studies in the GSL (e.g., Benoit et al.,

2006; Lehmann et al., 2009). Since station 23 has been visited quasi-weekly from May to November by scientists from the Maurice Lamontagne Institute as part of a monitoring program (Plourde et al., 2008), these measurements were selected. All other measurements were grouped per station, regardless of the time of the year they were taken. This method is similar to that of Bourgault et al. (2012), except a box of $20 \times 20\,\mathrm{km}^2$ is considered here for station 25 instead of $10 \times 10\,\mathrm{km}^2$. On average, 145 profiles were extracted per station. Station 20 contains the highest number of casts ($n = 348$) closely followed by station 23 ($n = 267$), while station 25 contains the least number ($n = 27$).

Since nitrate plus nitrite concentration measurements are from various investigators, different titrating methods were used (Clesceri et al., 1989; Grasshoff et al., 1999; Mitchell et al., 2002). To the best of our knowledge, they were all measured with autoanalyzers, whether of type Alpkem, Technicon II or Bran-Luebbe 3. For the remainder of the article, we will refer to NO_3 + NO_2 concentrations as *nitrate* concentration. This approximation is justified since for more than 95% of the water samples, NO_2 concentration represents less than 7% of the total NO_3 + NO_2 concentration.

Another survey conducted 13-hour sampling, e.g. covering the semi-diurnal tidal period, on both September 23 and 29 2012 from the R/V Coriolis II in proximity to station 25 (see white star on Fig. 28). During station occupation, conductivity-temperature-depth (CTD) casts were realized nearly every hour with a Sea-Bird SBE 9. Every three hours, Niskin bottle samples were taken for nutrient concentration analyses. An echosounder (Simrad EK-60) and a 150 kHz Acoustic Doppler Current Profiler (RDI-ADCP) were also sampling the water column during this survey.

3.3.2 Turbulence data

Turbulence measurements were collected with a free falling, loosely tethered Vertical Microstructure Profiler (VMP500) from Rockland Scientific International (RSI), deployed

from a small craft boat. This profiler is equipped with Sea-Bird Electronic sensors for fine scale ($\sim 10^{-1}$ m) measurements of pressure, temperature T and practical salinity. Salinity measurements presented in this study have been converted to absolute salinity S_A ($\mathrm{g\,kg^{-1}}$) (McDougall and Barker, 2011). Among with other microscale ($\sim 10^{-2}$ m) sensors, the VMP is equipped with two airfoil shear probes (SPM-38 from RSI) that allow measurements of the microscale vertical shear ($\frac{\partial u'}{\partial z}$).

A total of 817 turbulence profiles were collected at Station 23 during summers 2009-2012. Most have already been used in two previous studies (Cyr et al., 2011; Bourgault et al., 2012). As they were collected from a small craft boat, they were realized in relatively calm sea conditions. The maximum depth of VMP casts at this station varied between 180 m and 325 m (bottom depth).

Our team also collected 207 turbulence profiles at the HLC near station 25 between 29 September and 2 October 2009 (red dots on Figure 28), a period corresponding to a neap-tide phase of the fortnightly tide cycle (smallest high tide on September 27). To avoid snagging the profiler on the rocky bottom, profiles at the HLC were performed as close as possible to the seabed (our target was to reach within 2-5 m of the seabed) without intentionally hitting it. These observations were also carried out under relatively calm sea conditions (the wind generally did not exceed $20\,\mathrm{km\,h^{-1}}$ except for September 30 where it reached $40\,\mathrm{km\,h^{-1}}$ for an hour at the nearest meteorological station on *Ile Rouge*). During the VMP sampling at the HLC, a 600 kHz RDI-ADCP was deployed on the side of the boat at a depth of about 1 m below the surface. The vertical resolution was 0.5 m and ensembles of 35 pings were averaged every 10 s. This allowed current measurements (U, V) from which the vertical shear ($S^2 = \overline{\left(\frac{\partial U}{\partial z}\right)^2} + \overline{\left(\frac{\partial V}{\partial z}\right)^2}$, in $\mathrm{s^{-2}}$) was calculated.

Turbulence data reduction for both stations was achieved using a procedure similar to that described in previous studies in the LSLE (e.g., Cyr et al., 2011; Bourgault et al., 2012) and briefly summarized here. Dissipation rates of turbulent kinetic energy (ϵ, in $\mathrm{W\,kg^{-1}}$) were calculated by (e.g., Lueck et al., 2002; Sundfjord et al., 2007; Rippeth et al., 2009; Martin

et al., 2010):

$$\epsilon = \frac{15\nu}{2}\overline{\left(\frac{\partial u'}{\partial z}\right)^2}, \tag{3.1}$$

where $\nu = f(T)$ is the kinematic molecular viscosity (in $m^2\,s^{-1}$) as function of temperature and the overline indicates here a vertical 1-m bin averages. The shear variance $\overline{\left(\frac{\partial u'}{\partial z}\right)^2}$ was obtained by spectral integration with care taken to exclude, when necessary, high wavenumber instrumental noise.

Turbulent diffusivities (K, in $m^2\,s^{-1}$) were calculated from the dissipation rates and stratification as:

$$K = \frac{\Gamma\epsilon}{N^2}, \tag{3.2}$$

with $\Gamma = 0.2$, the flux parameter, taken here constant (Osborn, 1980; Moum et al., 2002, 2004; Burchard, 2009; Rippeth et al., 2009; Holtermann et al., 2012). Turbulent fluxes (F) of any nutrient can be calculated by combining turbulent diffusivity profiles ($K(z)$) and vertical gradient of nutrient concentration in the following equation:

$$F(z) = -K(z)\frac{\partial C(z)}{\partial z}, \tag{3.3}$$

where $C(z)$ is represent the nutrient concentration profile. As presented further in the text, nitrate fluxes are calculated here, using the salinity profiles measured by the VMP as proxies for nitrate concentration profiles.

3.4 Observations

3.4.1 Nutrient concentration

Two examples of mean nitrate concentration profiles resulting from our analysis are given for stations 25 and 23 (Fig. 29). Note that station 25 has the fewest observations (n = 27) while there were 267 casts for the monitoring station 23. The result of the bootstrap is shown as error bars where the range is the 95% confidence interval on the mean value. For these two stations in the LSLE, nitrate concentration profiles exhibit a two-layer structure, with nearly constant lower concentrations in the top 50 m of the water column and a constant maximum value below about 200 m. Although the water column is undersampled in the transition zone between these two layers, the gradual decrease of nitrate concentration between 50 and 200 m suggests that the nitracline lies in this depth range.

Binned observations for all stations were vertically and horizontally linearly interpolated between averaged values to obtain a nitrate concentration transect along the Laurentian Channel from stations 25 to 16 (Fig. 30). Highest surface nutrient concentrations are found in the LSLE (stations 25 to 21). Generally low nitrate concentrations are found in surface waters for the rest of the Gulf. Deep (>200 m) waters of the Laurentian Channel have more or less a constant nitrate concentration. There is also a subsurface minimum of nitrate concentration near $\sim$ 50 m between stations 24 and 22. This suggests that high concentration in surface waters is the result of advection of nutrient-rich waters from upstream (e.g., from station 25) rather than local vertical mixing at these stations. At station 25, however, no subsurface minimum is present, in support of the hypothesis that nutrient pumping occurs near this station. Moreover, at depths greater than 200 m, the waters of the Laurentian Channel show lower nitrate concentration between stations 24 and 25 as suggested by the deepening of the nitrate isopleths between these stations. This impoverishment in depth together with the surface enrichment suggests a vertical homogenization by turbulent diapycnal mixing. Interestingly, the average nitrate concentration integrated over the whole water column is approximately

constant along the Laurentian Channel (the vertical average only varies between 16.8 and 18.8 mmol m^{-3}, bottom panel). This suggests that the total amount of nitrate is conserved and the system is nearly in a steady state between advection of nutrient-rich slope waters at depth, vertical pumping at the HLC, surface consumption by the biology and bacterial degradation, nitrification and reduction of sinking detritus.

A look at both 13-hour timeseries near station 25 gives insights on the behaviour of the temperature, salinity and nitrate concentration at the HLC during a semi-diurnal tidal cycle (Fig. 31 and 32). Visible in temperature and salinity fields are the large vertical excursions reaching up to 60 m range in both cases. Such large vertical excursions are also visible in the nitrate timeseries of Figure 31, although the lower temporal resolution of the bottle sampling may be misleading. For example, while the temperature and salinity below 50 m plunges by nearly 60 m between 17:00 and 21:00, nitrate concentration remains constant in the interpolated field because no bottle was taken during this period. A comparison with Figure 32 suggests that nitrate isopleths should rather evolve as the temperature and salinity (see the beginning and the end of the timeseries in Fig. 32). This relationship is supported by a scatter plot of nitrate concentration versus salinity for all available measurements in the GSL/LSLE (Fig. 33). This relation is clearer for data far from the surface and the bottom, i.e. in the $S_A = [32, 34.3]$ g kg^{-1} salinity range, for which a linear relationship gives (gray line in Fig. 33a):

$$\tilde{C}_{NO_3} = aS_A + b \quad \text{in [mmol m}^{-3}\text{]}, \tag{3.4}$$

with $a = 7.35$ mmol m^{-3} kg g^{-1} and $b = -227$ mmol m^{-3}. The salinity range for the validity of this relation was chosen from visual inspection of the dataset and is a trade-off between the goodness of the fit (now with a correlation coefficient $R = 0.94$) and the desire of taking into account most of the water column. Note that this relation was established for profiles taken between April and November, but the inclusion of winter months does not significantly

change the coefficients a and b. Near the surface, advection of nitrate-rich water patches (due to nitrate surfacing or land drainage) may explain why *low* salinities ($S_A < 32\,\mathrm{g\,kg^{-1}}$) can lead either to low or high nitrate concentrations. At salinities greater than $34.3\,\mathrm{g\,kg^{-1}}$ (i.e. near the bottom), nitrate concentrations have a small tendency to decrease as the salinity increase. The reason for this behaviour is unknown, but might be related to nitrate consumption by benthic organisms.

The relationship established in Equation 3.4 is used to estimate nitrate concentration profiles from VMP casts. Examples of inferred nitrate concentration profiles from salinity are presented in Figure 33b for two profiles from the same semi-diurnal tidal cycle, one taken just downstream from the sill (thick lines) and one taken on the shallow portion above the sill (thin lines). Comparison between both salinity profiles (black curves) suggests that the profile over the sill is more or less a compression of the profile taken seaward because of the advection of the water column over the sill. This translates in the nitrate concentration profiles (cyan curves) by changing the depth range for which the relation is valid. For the profile downstream from the sill, the relation fails above 60 m while above the sill, the relation is valid from the bottom (35 m) to about 15 m. The mean nitrate concentration profiles approximated from the VMP sampling at both Stations 25 and 23 are given in Figure 29 (gray shades).

Internal tides can generate large vertical excursions at tidal frequencies such as those observed in Figure 31 and 32 and these are known to be generated at the HLC because of the interaction of the semi-diurnal tidal currents with the sill (e.g., Forrester, 1970, 1974; Ingram, 1979a; Wang et al., 1991; Galbraith, 1992). At this frequency, the internal tide that predominantly emanates from the head is consistent with a Poincaré-type wave in the second vertical mode and first horizontal mode with a wavelength of about 35-60 km along-channel (Forrester, 1974; Galbraith, 1992). Evidence that the vertical excursions observed for T, S_A and nitrate concentration in Figures 31 and 32 are the result of an internal tide is suggested by what resembles a pinching and spreading of the isopleths at a node located at a depth of

about 20-30 m, typical of a vertical mode-2. The clearest illustration of such behavior is in the upper panel of Figure 31, where the pinching of the isotherms is centered at about 14:00 and the spreading is maximum at about 19:00. These occur respectively near the high and low tide in Tadoussac (high tide at 13:03 and low tide at 19:03). Surface signature of what can be considered as upward advection of cold intermediate water occurs when isotherms over the node are rising towards the surface at low tide. Nitrate concentrations are also maximum in surface water near low tide, likely the result of the same mechanism.

In the salinity field, fresher waters are found in the top $\sim$ 10 m of the water column at low tide. This is contrary to what would be expected since saltier water should follow the surfacing of colder and nitrate-rich water. An increase in the freshwater release from the St. Lawrence and the Saguenay rivers when the barotropic tidal pressure is minimum (i.e., at low tide) may explain this different behavior as suggested by previous studies (e.g., Drainville, 1968; Saucier and Chassé, 2000). In other words, the salt input to the surface water by the vertical mode-2 internal tide is hidden under a more important freshwater release.

3.4.2 Turbulence observations and nitrate fluxes

A timeseries of VMP sampling reveals that very high dissipation rates of turbulent kinetic energy occur above the sill (Fig. 34a). As a comparison, mixing at a sloping boundary about 100 km seaward from the sill rarely exceeded $\epsilon = 10^{-5}\,\mathrm{W\,kg^{-1}}$ while above the sill it often exceeds $\epsilon = 10^{-4}\,\mathrm{W\,kg^{-1}}$. Note that this figure is presented relative to the time of the profiles rather than the along-shore distance. In fact the tidal currents reversed when the boat was nearly above the shallowest portion of the sill ($\sim$18:45) and the timeseries from 17:00 to 20:30 is more or less a back and forth displacement above the sill (see the inset for profile positions).

Away from the sill (i.e., before 16:30), dissipation rates are relatively low with some higher patches near the surface and the seabed. As the sill is approached, isopycnals rose by

more than 20 m above the first peak (at ~17:00) and plunged behind it. This corresponds to high dissipation rates on the lee side of this peak. These vertical displacements are also visible in the temperature timeseries (Fig. 34b). The CIL (black lines) that lies at a depth of about 90-100 m before 14:00 is pushed over the sill (20-40 m) at about 19:00. Isopycnals are also compressed on each other generating sharp interfaces where, as we will see later, turbulence by shear instabilities likely take place (panel *a*). On the shallowest portion of the sill (i.e., after 17:30), most of the water column is highly turbulent. A lens of lighter fluid appeared at the surface at about 17:45, a period that roughly corresponds to the high tide. At this time, we visually observed a well-defined front at the surface. A very strong pycnocline also appears in the data at this time at about 10 m depth, separating two relatively well mixed water masses. Strongest mixing occurred in the upper layer. Visual surface signature of ascending and descending motions were also visible from the boat at ~20:00 and 20:30. These correspond to steep isopycnals for some part of the water column (Fig. 34a), indicating that vigorous mixing was at work. Vertical *drops* at depths between 10-30 m in the temperature panel (34b) starting at about 17:30 also suggest either high frequency internal waves or vigorous mixing in the upper part of the water column.

The relationship established in Equation 3.4 was used to infer, for each VMP cast, a corresponding nitrate profile approximation ($\tilde{C}_{NO_3}$). Nitrate concentration obtained were then combined to the diffusivity profiles to calculate the instantaneous flux using Equation 3.3 with $F = F_{NO_3}(z)$ and $C = \tilde{C}_{NO_3}$. These are calculated in mmol m^{-2} s^{-1} but expressed further in the text in mmol m^{-2} d^{-1}.

Figure 35 shows nitrate fluxes and nitrate concentrations measured from salinity over the sill. Strong turbulence generally results in high nitrate fluxes ($10^2 - 10^3$ mmol m^{-2} d^{-1}, panel *a*). This figure also illustrates how advection brings deeper nutrient rich waters over the sill where they can mix. Nitrate isopleths are also closer to each other over the sill (see also discussion around Fig. 33b), generating sharper gradient likely enhancing the flux. As we will see later in the discussion, the interplay between strong turbulence and the advection of

deeper nutrient-rich water above the sill is the key to sustain the high nutrient fluxes observed here.

Although mixing mechanisms are hard to isolate from this timeseries, observations from the 29 September 2012 13-hour survey illustrate one turbulent mechanism leading to high nutrient fluxes at the HLC (Fig. 36). This echogram, combined with currents, density and nitrate observations, shows how Kelvin-Helmholtz instabilities develop at early flood tide (14:35 - 14:40) as a result of a shear layer centered at about 60 m. A quick look at the Richardson number ($Ri = \frac{N^2}{S^2}$), an index of the water column stability relative to turbulent shear instabilities suggests that the shear is sufficiently strong to dynamically destabilize the stratification (Ri<0.25). Here ρ is the density of sea water in kg m^{-3} measured by the CTD and sorted for inversions, $g = 9.8\,\mathrm{m\,s^{-2}}$ is the gravitational acceleration and $\overline{\rho}$ the mean density of seawater averaged over 1-m size vertical bins. These conditions lead to the development of 30-m thick billows, that stir about a quarter of the total water column. These billows eventually break into turbulent mixing and produce important salt, heat and nutrient fluxes.

Unfortunately, we do not have concomitant turbulent observations with this echogram. We can nevertheless provide an order of magnitude estimate of the associated diffusivity and nutrient flux from the vertical scale $H \sim 10^1$ m of the billows and the measured buoyancy frequency $N \sim 10^{-2}\,\mathrm{s^{-1}}$, estimated from the density profile around the shear layer in Figure 36. An order of magnitude calculation suggests a diffusivity of order $K \sim \Gamma N H^2 \sim 10^{-1} \times 10^{-2}\,\mathrm{s^{-1}} \times 10^2\,\mathrm{m^2} \sim 10^{-1}\,\mathrm{m^2\,s^{-1}}$. The associated nutrient flux using $\frac{\partial C_{\mathrm{NO_3}}}{\partial z} \sim 10^{-1}\,\mathrm{mmol\,m^{-4}}$ then suggests $F \sim -K\frac{\partial C_{\mathrm{NO_3}}}{\partial z} \sim 10^{-2}\,\mathrm{mmol\,m^{-2}\,s^{-1}}$. This is a high flux (equivalent in other units to $\sim 10^3\,\mathrm{mmol\,m^{-2}\,d^{-1}}$) representative of an episodic but very energetic event.

An example of such episodic events observed during our surveys with the turbulence profiler is provided in Figure 37. This figure is a subset of data from Figure 34 corresponding to the upper 35 m of the water column, between about 17:00 and 20:30. Strong shear layers (upper panel) generally correspond to regions of high dissipation (middle panel), delimited from the regions of lower dissipation by strong density gradients. Between 18:00 and 18:15,

what resembles Kelvin-Helmholtz billows are visible in the ADCP echogram. Although these billows are smaller than those presented in Figure 36, VMP casts through them suggest that the nitrate fluxes involved just below these instabilities are of the same order of magnitude, i.e., $F_{NO_3} \sim 10^3$ mmol m^{-2} d^{-1} (bottom panel).

To obtain longer-term averaged quantities we compute averaged profiles for N^2, ϵ, K and F_{NO_3} from our 207 casts at the HLC near station 25 and from our 817 casts at Station 23 (Fig. 38). The envelope of these profiles is the bootstrapped 95% confidence interval on the average, calculated assuming log-normal distribution of the turbulent variables Baker and Gibson (1987). For the remaining of the study, we refer to the VMP sampling at the HLC also as *Station 25*, although most of the sampling is outside the square box of this station (see red dots in Figure 28).

The buoyancy frequency squared (N^2) is nearly the same between stations 25 and 23, except for the top 25 m, where it is higher at station 25. The dissipation rates (ϵ) and the diffusivity (K) are higher at station 25 than station 23 for most of the depth span. The difference is particularly important in the top 60 m of the water column where the diffusivity at station 25 is nearly constant with values near $K \sim 10^{-2}$ m^2 s^{-1}. For the 25-50 m depth range, a range justified further in the text, $\overline{K}_{25} = 4.5(1.1, 13) \times 10^{-2}$ m^2 s^{-1} and $\overline{K}_{23} = 4.4(2.3, 7.6) \times 10^{-5}$ m^2 s^{-1}, about three orders of magnitude lower. Here numbers in parentheses represent the bootstrapped 95% confidence interval on the averaged value.

Mean turbulent nitrate fluxes (F_{NO_3}) are also presented in Figure 38. Missing data at the top of the mean profiles represent the portion of the water column where salinities of $S_A = 32$ g kg^{-1} or greater are never encountered (e.g., above ~37 m at Station 23 and above ~12 m at Station 25). Fluxes at station 25 are higher than at station 23 for most of the water column, often by orders of magnitude. Since Figure 29a suggests that the nitrate-depleted layer roughly correspond to the top 50 m of the water column, we calculated the mean flux between 25-50 m as a measure of replenishment of the surface layer. This depth range is above the nitracline (estimated to lie between 50-200 m in Section 3.4.1), but encompasses

the limit often considered between the surface and the cold intermediate layer (e.g., Sinclair et al., 1976; Therriault and Levasseur, 1985; Plourde and Runge, 1993; Savenkoff et al., 2001; Plourde and Therriault, 2004). This interval has been chosen also to represent the flux within the euphotic zone that has its lower limit at a depth of 10-20 in the LSLE (Therriault and Levasseur, 1985; Vézina, 1994; Sime-Ngando et al., 1995). The mean fluxes in the 25-50 m depth range, expressed with two significant figures, are $\overline{F}_{25} = 120(23, 400)\,\mathrm{mmol\,m^{-2}\,d^{-1}}$ and $\overline{F}_{23} = 0.21(0.12, 0.33)\,\mathrm{mmol\,m^{-2}\,d^{-1}}$, respectively for stations 25 and 23.

At the transition depth between the bottom layer and the CIL the fluxes averaged over the 100-150 m depth ranges are respectively $\overline{F}_{25} = 4.2(0.4, 17)\,\mathrm{mmol\,m^{-2}\,d^{-1}}$ and $\overline{F}_{23} = 0.15(0.10, 0.24)\,\mathrm{mmol\,m^{-2}\,d^{-1}}$. Note that for fluxes calculations at station 23, the diffusivity profiles used are from the station itself, i.e. far from boundaries. As suggested by Cyr et al. (2011), the fluxes reported for this station could be increased by 60% to account for boundary mixing processes.

It is also worth noting that the survey at the HLC was realized in neap tide conditions. Historical observations in the LSLE however suggest that nutrient enrichment of the surface waters is more efficient in spring tide conditions (Ingram, 1975; Sinclair, 1978; Demers et al., 1986). This also point out that our estimated flux at the HLC may be a conservative estimate. The fortnightly modulation of mixing is also suggested by looking at bottom and surface temperatures near Tadoussac in 2009 (Fig. 39). Because of a more efficient mixing with the cold intermediate layer, surface waters (magenta line) are always colder in spring tide period (gray vertical bands in panel *b*) compared to neap tide. The temperature difference between surface and bottom water above the sill (37 m depth, black line) is also always smaller in spring tide conditions, possibly because of a better homogenization of the water column by mixing in these conditions. The fortnightly difference of mixing in the LSLE was quantified by Saucier and Chassé (2000) in a numerical experiment, where they found that the buoyancy fluxes in the LSLE in spring tide are more than the double those in neap tide. If the two-fold change in buoyancy fluxes between neap and spring tides reported by Saucier and Chassé

(2000) translates to the same difference in nitrate fluxes, total nitrate input to the LSLE may be raised by a factor 1.5.

3.5 Discussion

3.5.1 The nutrient pump mechanism

Our observations suggest that shear instabilities are one of the mixing mechanisms at work at the HLC. Figure 36 is a good example of such large instabilities driven by sheared currents that can lead to significant nitrate fluxes with overturns as large as 30 m. These instabilities are likely driven by a complex mixture of tidal currents funneled onto the sill, together with frontal activity resulting from the confluence of different water masses (Figs. 34 and 36). Internal tides also can generate turbulence by inducing shear in horizontal currents during the vertical displacements of the waves. Bottom friction is another mechanism present at the HLC, as suggested by the high shear and dissipation rates found in the near bottom region of Figure 37.

However, other sill processes are also likely to be encountered here such as lee waves, hydraulic jumps, non-linear internal waves, vortical structures, etc. (as documented in other similar coastal systems, e.g., Farmer and Armi, 1999; Nash and Moum, 2001; Klymak and Gregg, 2001; Armi and Farmer, 2002; Cummins et al., 2003; Klymak and Gregg, 2004). Observational evidence of lee waves have already been reported to occur in this area downstream of the sill as a result of ebb currents (see Saucier and Chassé, 2000, their Figure 15). Although mixing through such mechanisms may have been sampled during our campaign (see for example isopycnals rising over the sill at 17:00 in Figure 34 that may suggest hydraulic control), our limited observations likely do not give the complete portrait of turbulence generation at this sill. Although the study would benefit from new turbulence measurements in the area, one conclusion of this short survey is that mixing is high in the upper $\sim$ 60 m of the water column. Far from the HLC, it is however below this depth that the nitrate concentration starts

to increase (see for example the mean nitrate profile at station 23, Fig. 29). Without nitrate input closer to the top layer, mixing would thus not sustain high levels of surface water nitrate enrichment.

In counterpart, some of the mixing mechanisms described above imply large vertical displacements of the nitrate isopleths. The large vertical displacements driven by the barotropic tide forced onto the sill (which further generates internal tides, Figures 31 and 32) would not enrich the surface layer with nutrient if no mixing was taking place. Isopleths would instead go up and back down without modifying the mean state. The interplay between vertical displacements and mixing is thus required to sustain the *nutrient pump* since one mechanism alone is not sufficient to account for such high nutrient fluxes in surface waters. The role of intense vertical mixing near the surface as a necessary condition for nutrient enrichment was hypothesized by Ingram (1975) and Therriault and Lacroix (1976) who suggested that vertical displacement of deeper water over the sill by the barotropic tide was not sufficient for the reason mentioned above. Interestingly, without direct turbulence measurements, Therriault and Lacroix (1976) had also hypothesized that the top ~50 m was undergoing intense vertical mixing by building a stratification index based on the vertical gradient of density at the HLC.

As it was shown previously, a node in vertical displacement is present at a depth of about 20-30 m. Observations suggest that the surface nutrient enrichment by the internal tides occurs in two steps (see sketch in Figure 40). During the pinching of the isopycnals by the internal tide at the node depth, nitrate isopleths from below 60 m rise, enter the zone of vigorous turbulence and enrich the subsurface layer (panel *a*). When isopycnals diverge, newly enriched waters near the node depth are pushed to the surface by the wave where further mixing ensues (panel *b*). Near station 25, this occurs at low tide, consistent with Figures 31 and 32 and with previous observations of Therriault and Lacroix (1976).

It is suggested in Section 3.4.2 that the calculated nitrate turbulent fluxes at station 25 ($23 - 400\,\mathrm{mmol\,m^{-2}\,d^{-1}}$) may be conservative estimates. Yet, they are among the highest

reported in the literature. Of the data compiled in Table 3, only the Mauritanian upwelling region has turbulent nitrate fluxes in the same range with $\overline{F} = 120\,\mathrm{mmol\,m^{-2}\,d^{-1}}$. The other regions with the closest fluxes values are the Oregon and the New Zealand Shelves with $\overline{F} \sim 10\,\mathrm{mmol\,m^{-2}\,d^{-1}}$. This supports the efficiency of the pumping mechanism described above.

3.5.2 Contributions to the GSL nutrient budget

Sinclair et al. (1976) suggested that nutrient cycling in the LSLE/GSL system was not as hypothesized by Steven (1971), i.e., that the LSLE was acting as a nutrient supplier to the GSL. They rather suggested that the surface estuarine transport of nutrients from the LSLE accounted for less than 1% of the nutrient supply to the GSL and that its effect was geographically limited to the western portion of the Gulf. On the other hand, Savenkoff et al. (2001) (from their Figures 6 and 10) calculated by inverse modeling that the nutrient supply to the GSL by the LSLE could reach 40%.

In order to calculate the amount of nitrates brought to the surface during summer months, a surface area representative of the flux at the head of the Laurentian Channel must be calculated. A look at the 25-year Sea surface temperature (SST) climatology in the LSLE for the months of May to October, suggests that a cold SST anomaly emanates from the HLC near station 25 (Fig. 41). These data where obtained from the Maurice Lamontagne Remote Sensing Laboratory for the period 1985-2010 and generously given by P. Larouche. Since surfacing of deeper nutrient-rich waters should be accompanied by cold water (see for example Figures 31 and 32), we can therefore assume that the region where nitrate are brought to the surface at the HLC coincides with the coldest part of the SST anomaly. Three contours ($T = 5.35, 5.55$ and $5.65°\mathrm{C}$, thick black lines in Figure 41) were delimited to represent the area where the fluxes can be hypothesized to occur. They have been chosen to represent 5%, 10% and 15% of the coldest pixels within the blue box of Figure 41 (calculated from the cumulative density function of temperature pixel in the inset Figure). These threshold give

estimated areas of 73, 161 and 230 km^2, respectively. These areas is also visually similar to the *shoaling area* suggested by the numerical work in Lavoie et al. (2000) (their Figure 7). We can therefore assume that $A \sim 10^2\,km^2$ is an order of magnitude for the surfacing area representative of the nitrate flux at the HLC. Figure 41 also suggests that surfacing nutrients at the HLC are mostly advected seaward as a part of the estuarine circulation, preferably following the southern coast of the LSLE (see also Gratton et al., 1988, for a study on surface cold anomalies).

From May to November (i.e., 150 days), the observed fluxes of $120(23, 400)\,mmol\,m^{-2}\,d^{-1}$ calculated through this surface would lead to an upward pumping of $25(5, 84) \times 10^3$ tons of nitrate in the surface waters of the LSLE. This amount of nitrate is comparable (within uncertainties) to the estimated seaward nutrient transport of 20×10^3 tons of nitrate over the top 50 m, calculated by Sinclair et al. (1976) for the same period at the Rimouski section, a transect across the LSLE passing through station 23. These authors however pointed out that such a seaward flux was insufficient to sustain the primary production in the Gulf of St. Lawrence.

Another study from inverse modeling suggests a mean seaward flux out of the LSLE of $460\,mol\,N\,s^{-1}$ over the top 30 m, equivalent to 83×10^3 tons of nitrate if integrated from May to September, i.e. about equivalent to our upper bound value (Savenkoff et al., 2001, from their Figure 6). Note that this amount of nitrates is *in excess* of what consumed in the LSLE. The vertical flux integrated over the entire LSLE given by this inverse model is $685\,mol\,N\,s^{-1}$ (Savenkoff et al., 2001, their Figure 10). To better compare with this estimate, we should also take into account the vertical fluxes at Station 23, because although they are weaker than at Station 25 by two to three orders of magnitude ($\overline{F}_{23} = 0.21(0.12, 0.33)\,mmol\,m^{-2}\,d^{-1}$), they are representative of a much wider surface area (LSLE surface is $\sim 9000\,km^2$). If we assume that fluxes at Station 23 are distributed over this surface, and that fluxes at station 25 are distributed over $10^2\,km^2$, the total vertical flux over the whole LSLE, expressed in the same units as Savenkoff et al. (2001), vary between $39 - 500\,mol\,N\,s^{-1}$, i.e., smaller than the model

result.

Whether this is an overestimation of the vertical nutrient pumping by the model or whether our results presented here are underestimates is not clear. Additional nitrate sources by the rivers on the north shore of the LSLE may partly account for this difference since they are not considered in the study of Savenkoff et al. (2001), and the inverse model may compensate for missing sources by increasing the vertical pumping. Too high local nitrate consumption in the LSLE or too high nutrient export to the GSL in the model may also cause such overestimation. However, in a *best case* scenario, i.e. by considering the largest surface for the shoaling area (e.g., 230 km^2) and by increasing higher bounds of $\overline{F}_{25}$ and $\overline{F}_{23}$ by a factor 1.5 and 1.6 respectively (to account for neap-to-spring modulation at HLC and boundary mixing effect in the LSLE), the maximum vertical fluxes would be $\sim 1600\,mol\,N\,s^{-1}$, enough to account for Savenkoff et al. (2001) results ($685\,mol\,N\,s^{-1}$).

3.5.3 Nutrient pumping in sustaining primary production in the LSLE

In an attempt to estimate the LSLE primary production that could be sustained by nitrate fluxes at the HLC, let's assume that the nitrate brought to the surface water of the HLC (over $\sim 10^2\,km^2$) during a period of one month (30 days) is uniformly distributed over the whole LSLE (9000 km^2). The resulting *apparent* nitrate flux for the LSLE is: $F_a = 120(23,400)\,mmol\,m^{-2}\,d^{-1} \times 30\,d \times \frac{10^2\,km^2}{9000 km^2} = 40(8,130)\,mmol\,m^{-2}\,mo^{-1}$. Given a Redfield et al. (1963) uptake ratio by weight of C : N = 7.7 (see also Levasseur and Therriault, 1987; Levasseur et al., 1992), this suggests that the nitrate fluxes at the HLC could sustain a new production of about $4.3(0.8,14)\,g\,C\,m^{-2}\,mo^{-1}$ over the whole LSLE. Taking into account the regenerated production by assuming *f*-ratios ranging between 0.3-0.8 (Vézina, 1994; Tremblay et al., 2000), our observations suggest that a total primary production of about $1 - 48\,g\,C\,m^{-2}\,mo^{-1}$ can be sustained in the LSLE by the vertical nitrate fluxes at the HLC alone.

Estimates of the primary production averaged over the whole LSLE are given by Therriault and Levasseur (1985) and range between $28 - 44\,\mathrm{g\,C\,m^{-2}\,mo^{-1}}$ during the June-July bloom and from $0.3 - 17\,\mathrm{g\,C\,m^{-2}\,mo^{-1}}$ for the rest of the year. This suggests that nitrate fluxes at the HLC can sustain the majority of the bloom and post-bloom primary production in the LSLE. The fact that winter mixing is not responsible for the spring bloom in the LSLE is not surprising since the winter convection is known to be weak in this area due to the important freshwater content in the estuary (Galbraith, 2006; Smith et al., 2006a). These results also suggest that the nutrient fluxes at the HLC are responsible for the high primary production rates found throughout the summer in the LSLE.

Using more recent observations from the monitoring program at station 23, the mean primary production for years 2000 to 2003 between May and August (thus including the bloom), varied between $45 - 75\,\mathrm{g\,C\,m^{-2}\,mo^{-1}}$ and even reached $150\,\mathrm{g\,C\,m^{-2}\,mo^{-1}}$ in 1999 (Starr et al., 2004, inferred from their Figure 6). Although these numbers are higher than those presented above, they may however not be representative of the whole LSLE since production is spatially heterogeneous and station 23 is located in the most productive area (Therriault and Levasseur, 1985). These budgets however reveal that nitrates pumped at the HLC are almost entirely consumed in the LSLE, not leaving much for exportation in the Gulf. This is also suggested by the rapid decrease of nitrate concentration in the surface waters between the LSLE and the GSL (Fig. 30). This conclusion also supports the hypothesis that the LSLE exports mostly primary and secondary production to the Gulf rather than nutrients (Sinclair et al., 1976; Fortier et al., 1992; Plourde and Runge, 1993).

It must be noted however that the calculation above is based on vertical fluxes derived from measurements in neap tide period and are likely a lower bound estimate. Again, the total nitrate input to the LSLE, and thus the new primary production may be raised by a factor 1.5 to account for the fortnightly difference (see Section 3.4.2). This must be however taken with care and fortnightly changes of nitrate fluxes should be studied more closely. Finaly, if fluxes at station 23 are also taken into account for the total vertical fluxes, this would lead

to an additional flux of $6.3(3.6, 9.9)\,\mathrm{mmol\,m^{-2}\,mo^{-1}}$. This means that turbulent diffusivity in the LSLE, far from the HLC, can only sustain a relatively small fraction of the new primary production ($\sim 3 - 58\%$), equivalent to $0.7(0.4, 1.1)\,\mathrm{g\,C\,m^{-2}\,mo^{-1}}$.

3.6 Conclusion

In a desire to constrain the nutrients cycle and therefore the primary productivity budget in the LSLE/GSL system, nutrient fluxes resulting from strong interaction of the tides with a sill located the upstream limit of the LSLE (the head of the Laurentian Channel) were calculated. Although a better characterization of the mixing processes at the HLC is still required, the mechanics of the pump could be understood as a combination between large isopleth heaving over the sill and high dissipation rates in the top 60 m of the water column. Mechanisms leading to the strong dissipation are likely a mixture of shear instabilities, hydraulic controls and water masses convergence driven by internal and barotropic tidal currents funneled on a rough topography.

Calculations of vertical turbulent nitrate fluxes at the head of the Laurentian Channel allow us to put together pieces of the LSLE/GSL nutrient dynamics puzzle that can be summarized as follows. The so-called *nutrient pump* should be better seen as the nutrient supply to the LSLE by the HLC rather than nutrient supply to the GSL by the LSLE as it was first suggested by Steven (1971). Results from this study support the idea that high vertical nutrient fluxes at the HLC can sustain a large fraction of the bloom and post-bloom new production (i.e., the nitrate-based primary production) in the LSLE. This suggests that the nutrients are consumed locally (in the LSLE), leaving few for export to the GSL. The nutrient pump can however have indirect effects on the Gulf by feeding secondary and tertiary producers that can be exported out of the LSLE, mostly via the Gaspé Current.

The role of the LSLE in vertical fluxes of particulate carbon, and thus carbon sequestration is indeed still an open question. With data from the GSL only, Rivkin et al. (1996) con-

cluded that unlike other systems, the gulf export approximately the same amount of carbon to the bottom no matter whether the surface waters are undergoing bloom or non-bloom conditions. Since the composition of the export is changing from more chlorophyllous material in bloom compared to more fecal pellets in non-bloom conditions, it may well be that the LSLE is a source of biogenic carbon for the GSL throughout the summer. In other words, high primary productivity rates, sustained by high nutrient input in the LSLE, occur during the whole summer in the LSLE and may feed higher trophic levels that are rapidly exported to the GSL. Such an increase of secondary or tertiary producers may lead to high non-chlorophyllous particulate carbon sinking rates. New information on nutrient fluxes in the LSLE presented here may be used to test this hypothesis in future studies.

3.7 Acknowledgments

This work was funded by “Le Fonds de recherche du Québec - Nature et technologies”, the Natural Sciences and Engineering Research Council of Canada, the Canada Foundation for Innovation and Fisheries and Oceans Canada and is a contribution to the scientific program of Québec-Océan. The authors would like to thank Pierre Larouche for providing Sea Surface Temperature datasets and Cédric Chavanne and Luc Rainville for the careful reading and the helpful comments provided. Thank you also to Remi Desmarais and Paul Nicot who were frequent crew members during our summer sampling campaigns.

Reference	Region	$\overline{F}$ (mmol m^{-1} d^{-1})
Martin et al. (2010)	Porcupine Abyssal Plain	0.09
Horne et al. (1996)	Georges Bank	0.047-0.18
Lewis et al. (1986)	Subtropical North Atlantic	0.14
Law (2003)	Antarctic Circumpolar Current	0.17
Bourgault et al. (2011)	Amundsen Gulf	0.5
Carr et al. (1995)	Equatorial Pacific	0.1-1
Sundfjord et al. (2007)	Barents Sea	0.1-2
Rippeth et al. (2009)	Irish Sea	1.5
Law et al. (2001)	Northern North Atlantic	1.8
Sharples et al. (2007)	Celtic Sea Shelf Edge	1.3-3.5
Hales et al. (2009)	New England Shelf Break	0.8-5
Hales et al. (2005)	Oregon Shelf	O(10^1)
Sharples et al. (2001a)	New Zealand Shelf	12
This study	**Lower St. Lawrence Estuary**	**23-400**
Schafstall et al. (2010)	Mauritanian Upwelling Region	120

Table 3: Turbulent nitrate fluxes in the World Ocean from previous studies (adapted from Bourgault et al., 2011). The values reported are whether the flux through the nitracline, the base of the euphotic zone or the base of the mixed layer and are sorted from the lowest to the highest.

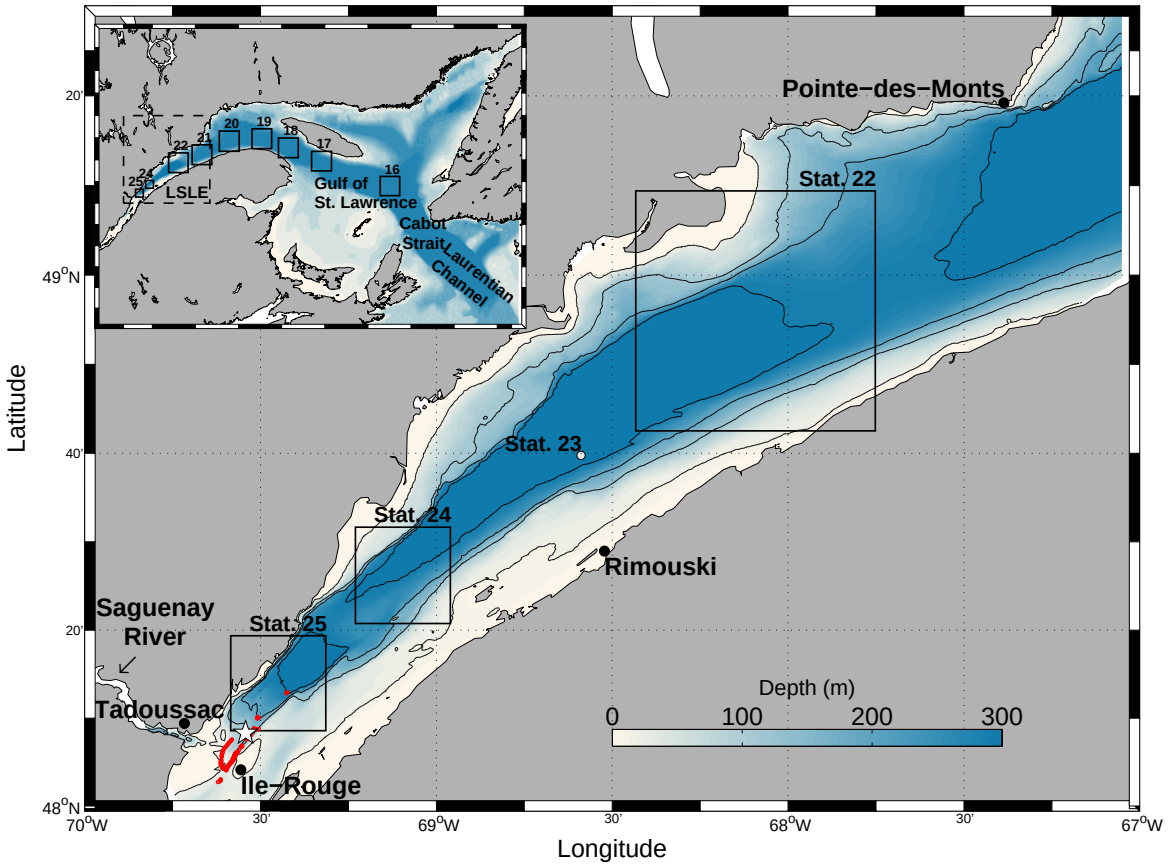

Figure 28: Map and bathymetry of the Gulf of St. Lawrence (inset) and the Lower St. Lawrence Estuary (main panel). Sampling boxes for Stations 16 to 22 and stations 24 and 25 have 50 km^2 and 20 km^2 respectively. Location of monitoring Station 23 is also shown. The fixed station occupied twice in September 2012 is represented by a white star. Sites of the turbulence profiles from the 2009 survey are identified with red dots.

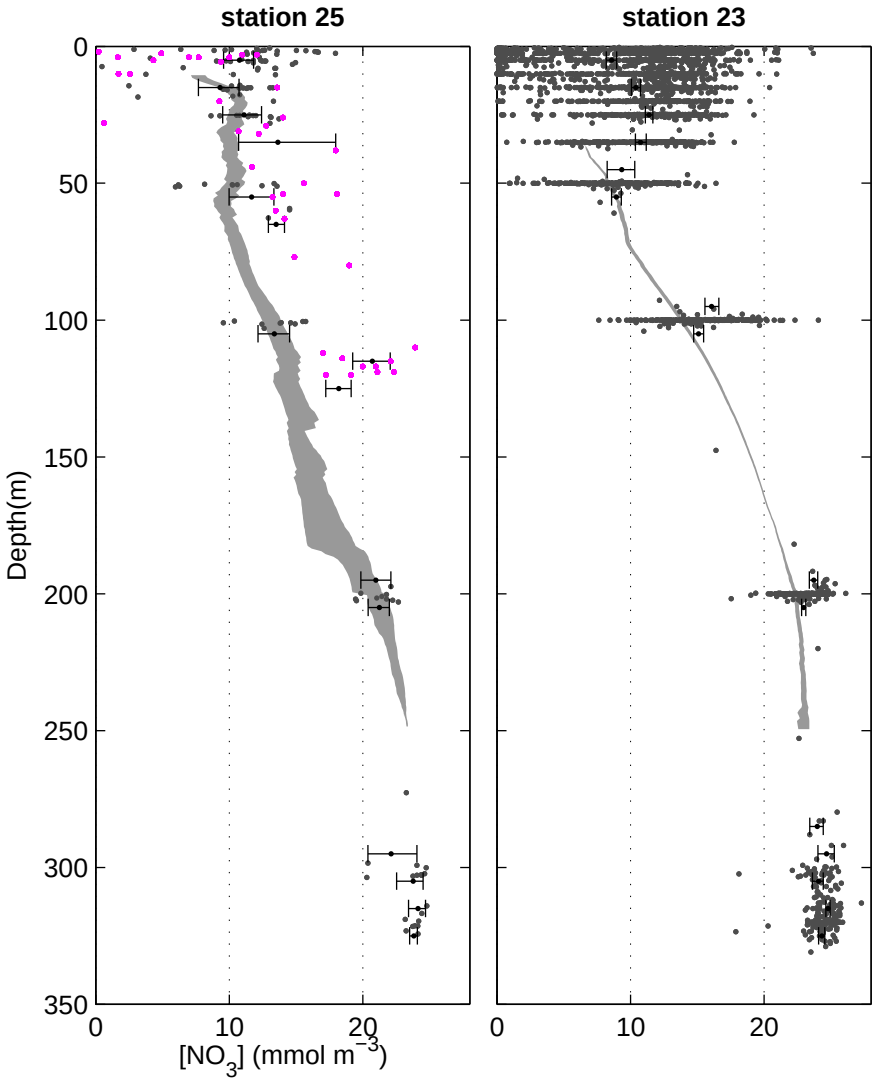

Figure 29: Nitrate concentrations for Stations 25 (left) and 23 (right). Gray dots are all available water bottle samples from 2000-2012. Purple dots on station 25 profiles are the observations from the two campaigns carried out at a fixed station in September 2012. Error bars represent the mean value and its 95% confidence interval obtained from bootstrap analysis in 10 m depth bins. Shaded profiles are fits obtained with Equation 3.4 (see section 3.3).

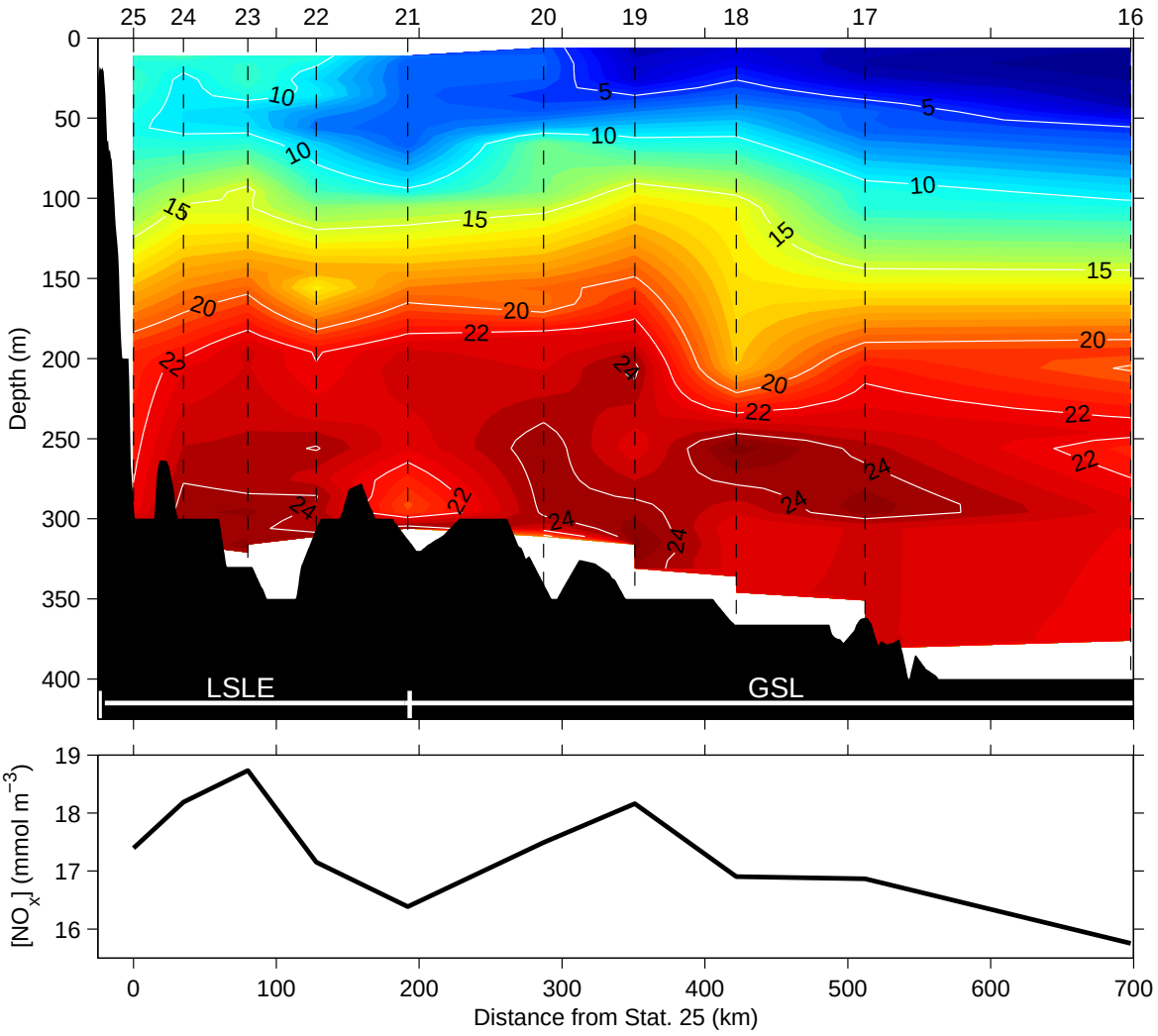

Figure 30: Nitrate concentration along the Laurentian Channel. (upper) Transect (in mmol m^3) between stations 25 to 16 identified with dashed lines (see Fig. 28). (bottom) Mean nitrate concentration for each station.

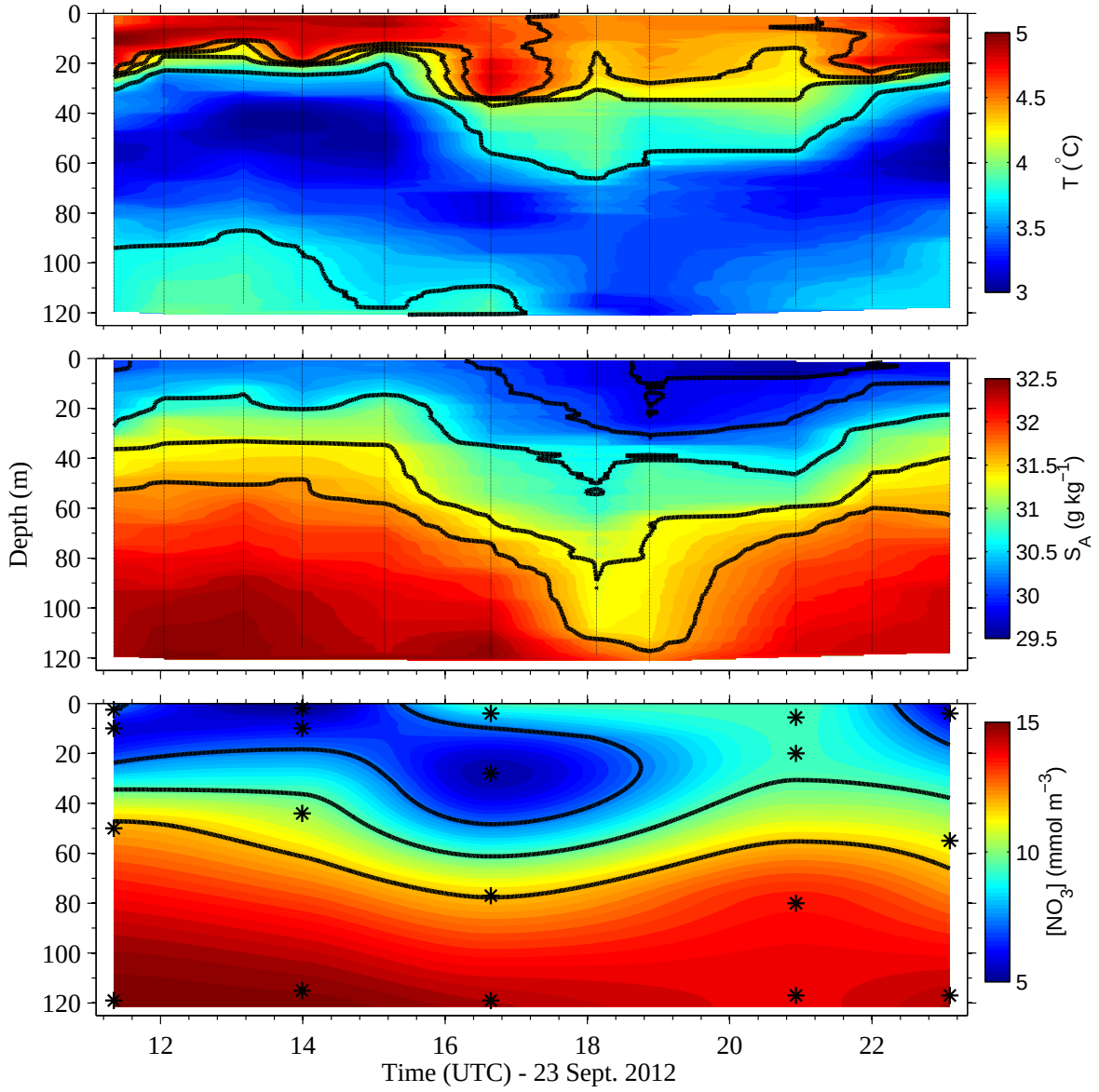

Figure 31: Semidiurnal timeseries (~13 hours) of temperature (upper panel), salinity (middle) and nitrate concentration (bottom) for a fixed station occupied on 23 September 2012 (see white star near station 25 on Fig. 28). Temperature-salinity casts are identified with dotted-lines and water sample bottles with black asterisks. The high tide was at 13:03 and the low tide at 19:03. The nearest maximum spring tide occurred on 18 September 2012.

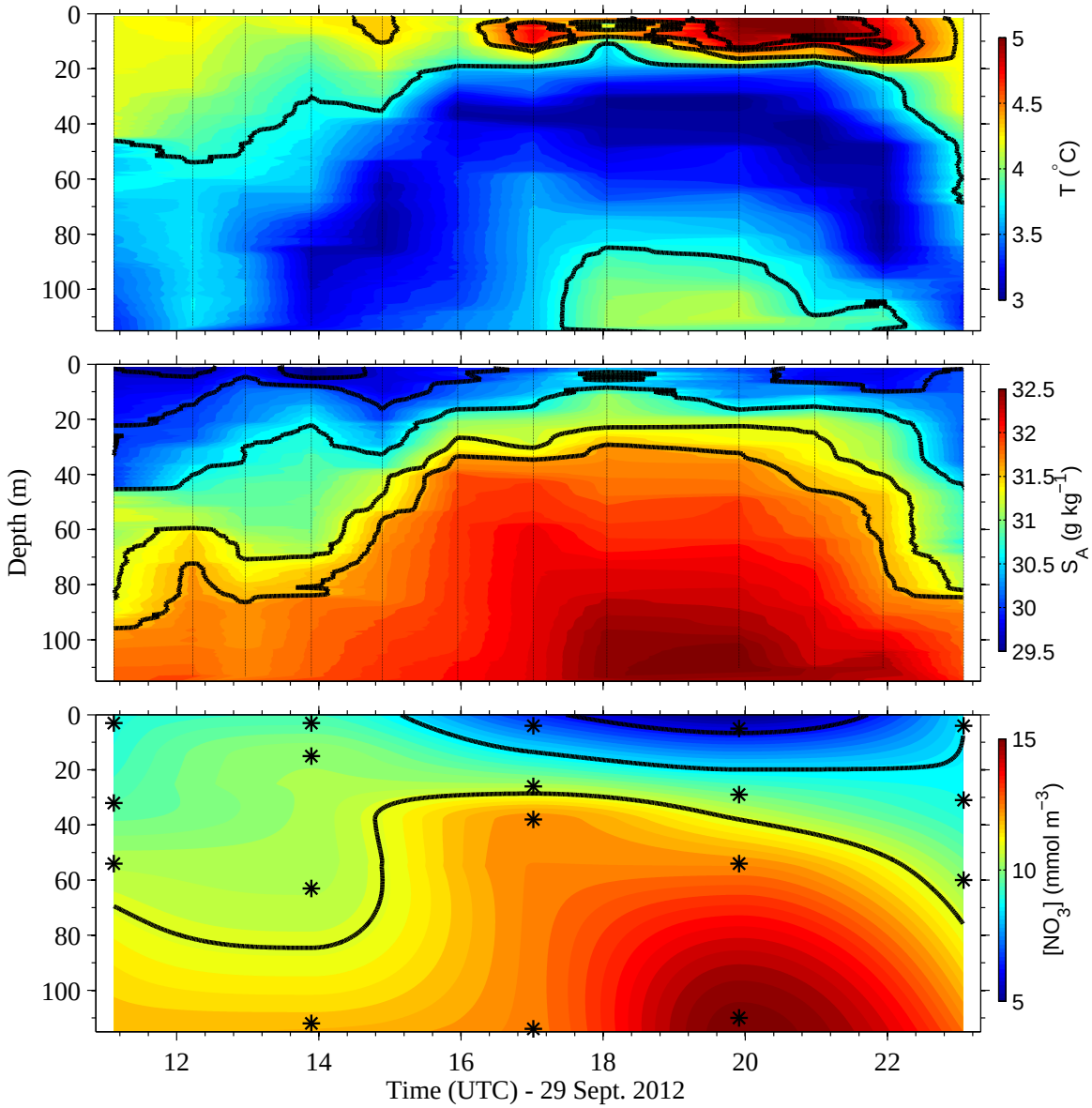

Figure 32: Similar to Figure 31, but for 29 September 2012. The high tide is at 18:59 and the low tide at 12:52. The nearest maximum spring tide is on 1 October 2012.

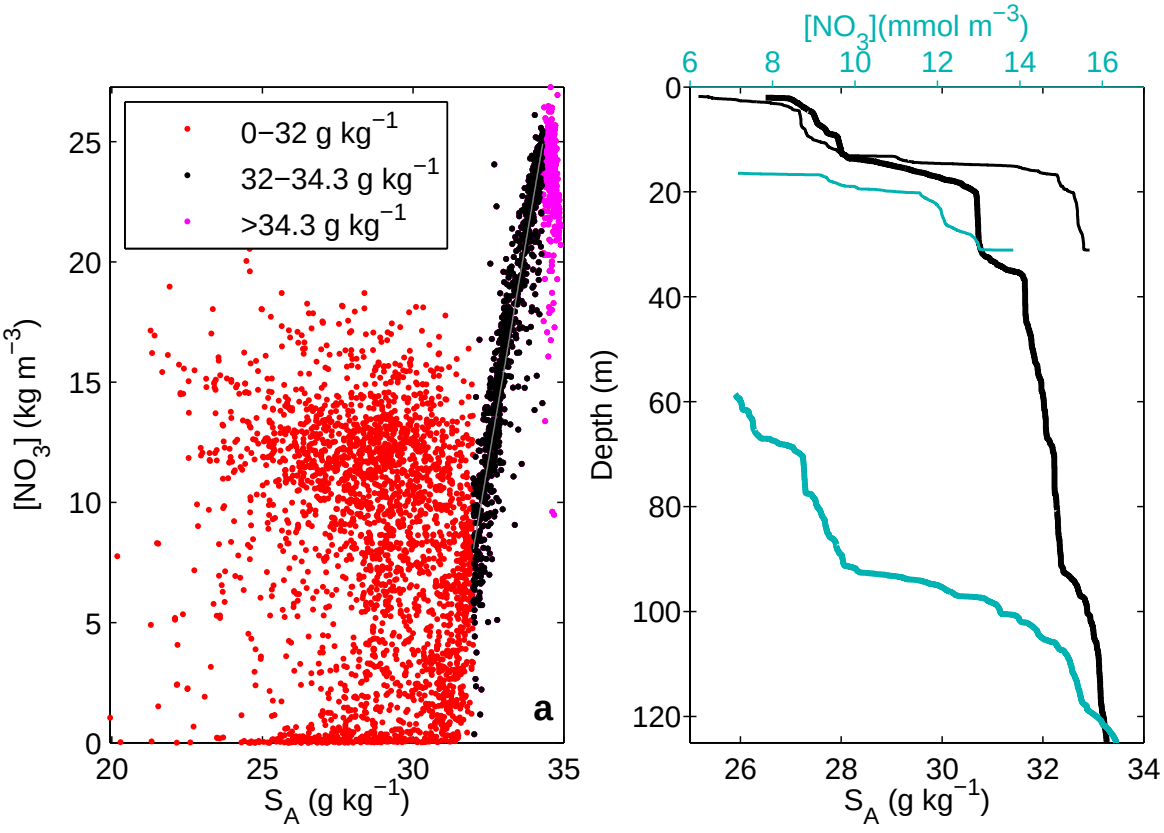

Figure 33: Nitrate concentration relationship with other physical data. (a) Scatterplot of nitrate concentration versus salinity for all 4548 measurements available from all stations. In red, measurements with salinities lower than $S_A = 32\,\mathrm{g\,kg^{-1}}$. In magenta, measurements with salinities greater than $S_A = 34.3\,\mathrm{g\,kg^{-1}}$. For the 1407 measurements with $S_A = [32, 34.3]\,\mathrm{g\,kg^{-1}}$ (black), the correlation coefficient with a linear least square fit (thin gray line) gives $R = 0.94$. (b) Salinity profiles (black) from two casts realized on 1 October 2009. In cyan, nitrate profiles inferred from Equation 3.4. The first cast was localized in the deep area seaward of the sill at 13:32 (thick lines) and the second above the sill at 18:40 (thin lines). These time references can be found on Figure 34.

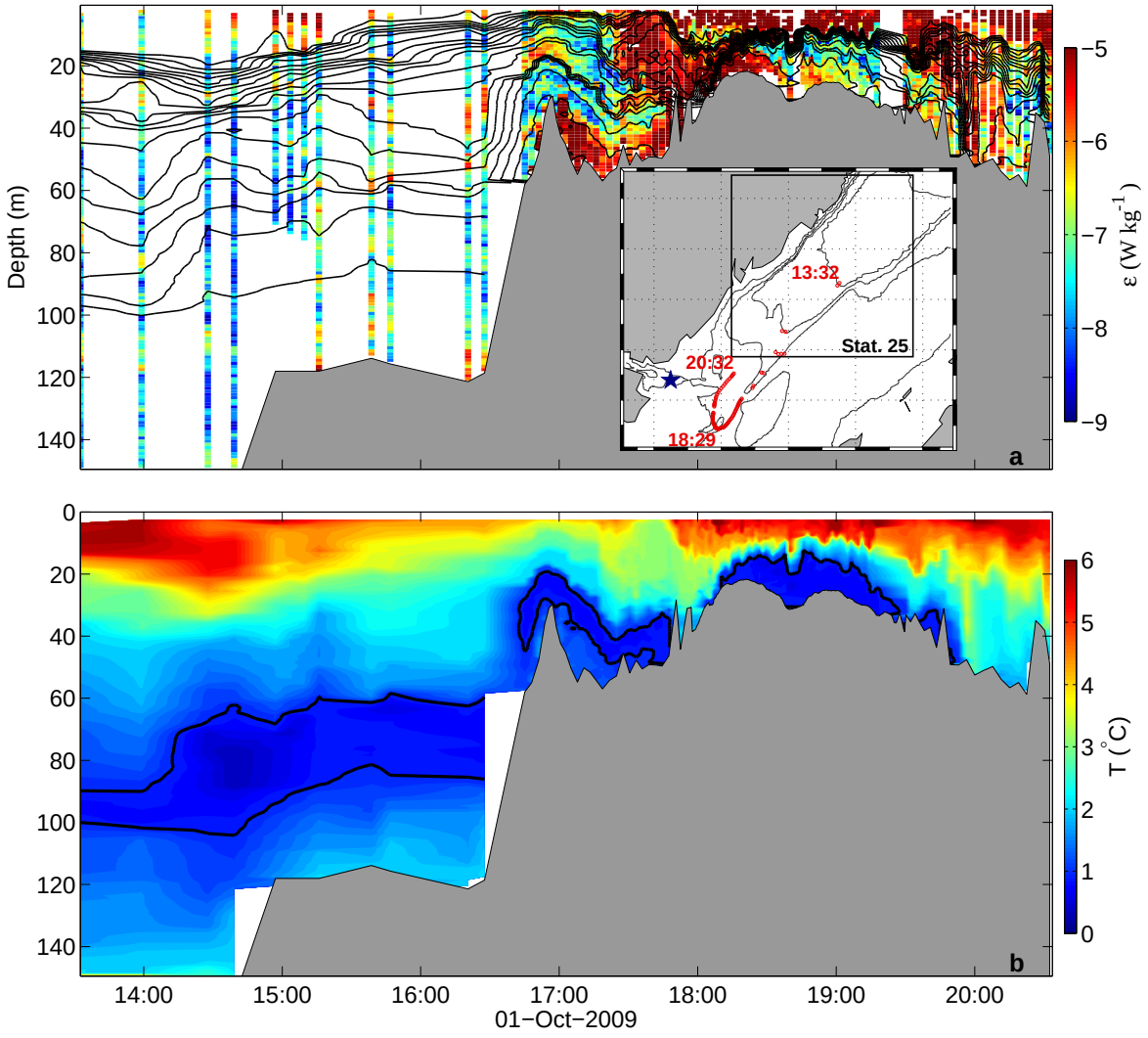

Figure 34: Example of a sampling carried out on 1 October 2009 near Station 25. (a) Dissipation rates of turbulent kinetic energy (ϵ). Isopycnals are also plotted in background for reference. Geographical position of each cast can be roughly followed with the inset Figure. The position of the two thermographs plotted in Figure 39 is also shown on the map with a blue star. (b) Temperature field linearly interpolated between casts. The thick black line is the 1 °C isotherm. Except for the shallowest portion of the sill, the gray area for both panels is the maximum depth of the casts which is our best approximation in this rapidly changing topography since casts were performed as close as possible to the seabed (see Section 3.3). On the shallowest portion of the sill, where the maximum depth is less than 35 m, the bottom is that estimated from ADCP measurements.

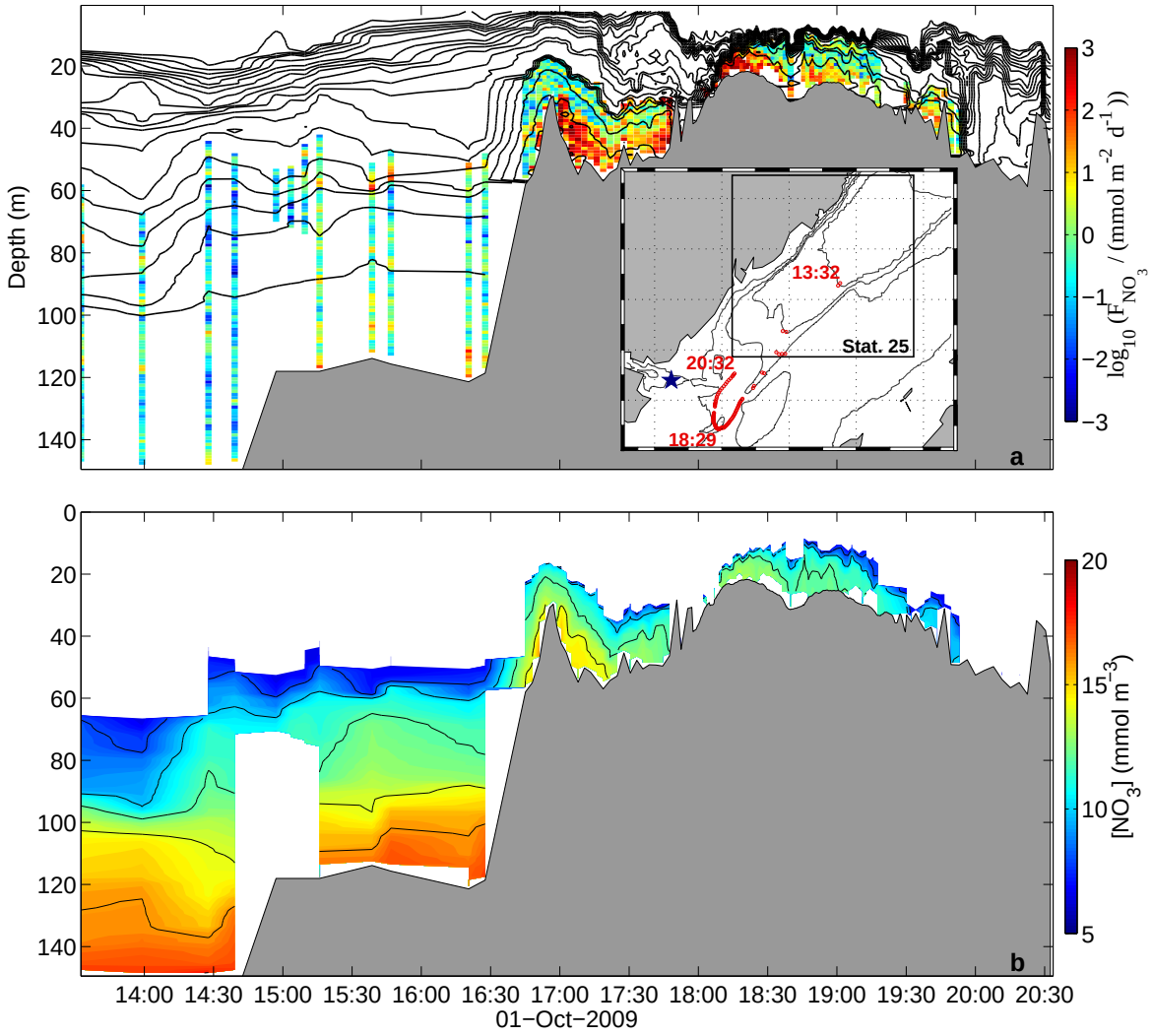

Figure 35: Same sampling as in Figure 34, but for (a) nitrate fluxes (F_{NO_3}) and (b) nitrate concentrations. For both panels, the white portion in the upper part of the figures correspond to the portion of the water column where $S_A < 32\,\mathrm{g\,kg^{-1}}$.

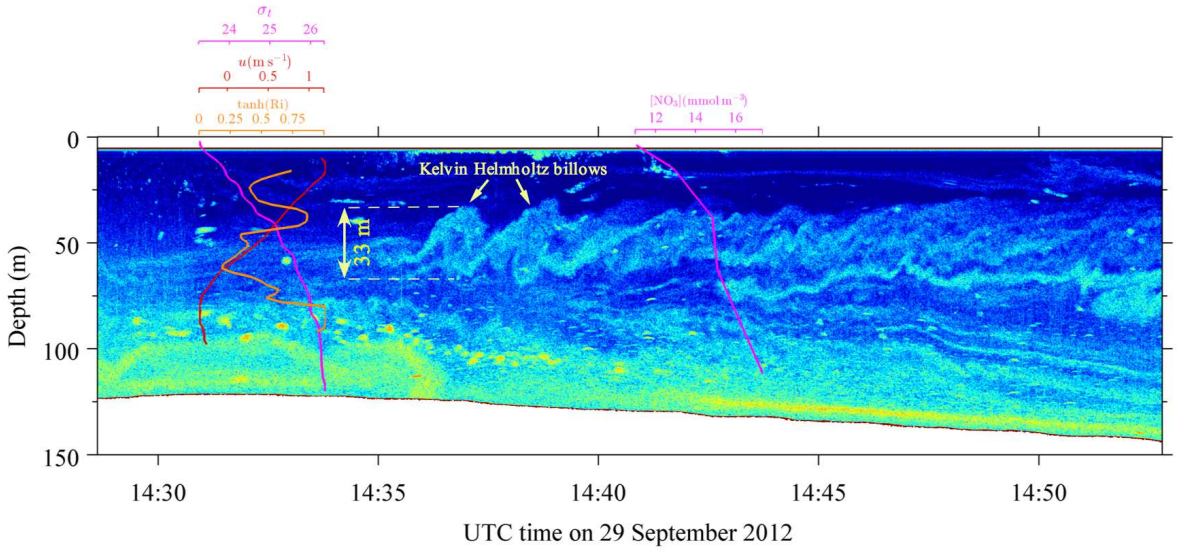

Figure 36: The nutrient pump in action. Echogram at 120 kHz from an echosounder mounted below a drifting boat on 29 September 2012 (see location on Fig. 28) shows how Kelvin-Helmholtz instabilities develop at early flood tide (14:35 - 14:40). Along-shore currents u (east and north currents rotated by 52°), density (σ_t), gradient Richardson number (Ri) and nitrate concentrations (C_{NO_3}) are also provided. Note that density and nitrate concentration profiles have been linearly interpolated to their respective time from casts outside the limits of the figure. These allow an estimation of the instantaneous vertical nitrate flux (see text).

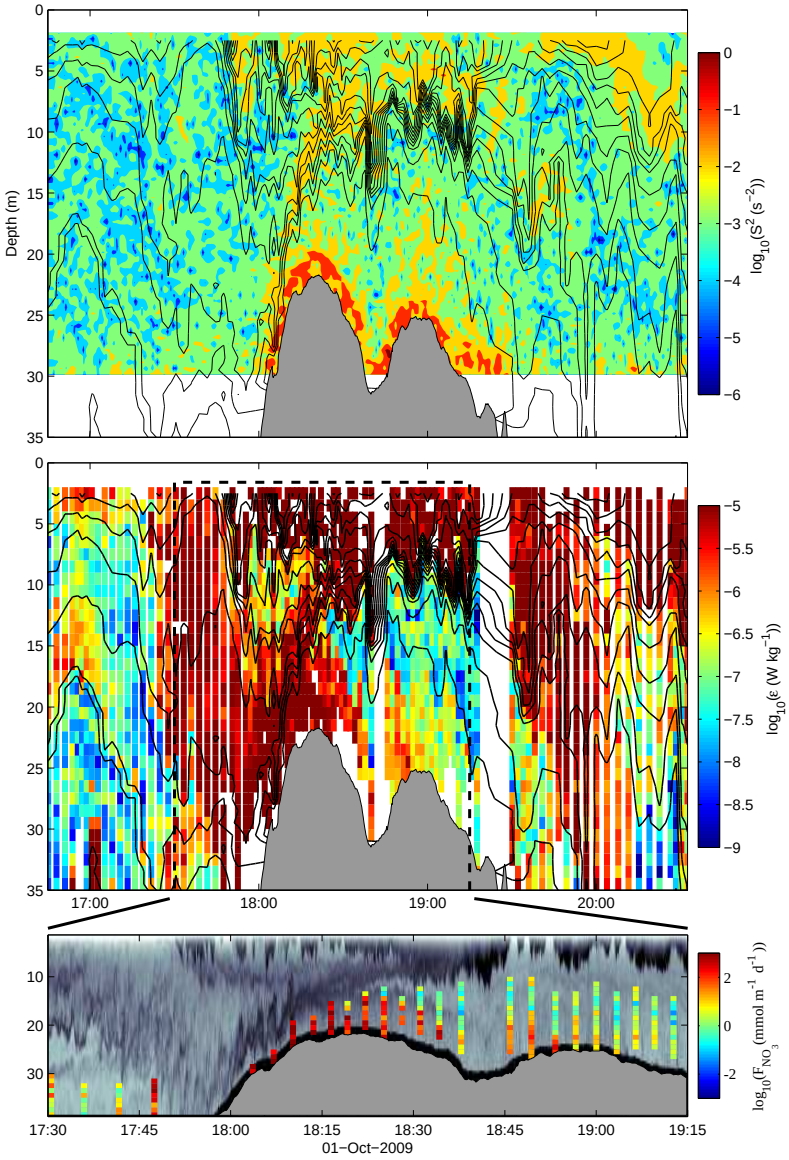

Figure 37: Close-up view of the timeseries from Figure 34. The shear (S^2) from the ADCP recorder (upper panel) and the dissipation rates of TKE (middle) are presented. The bottom panel is an enlargement of the middle panel where nitrate fluxes are presented over the ADCP echogram. Note that for a better visualization of Kelvin-Helmholtz billows (starting approximately at 18:00), the bottom panel is scaled differently from other panels and only one cast out of two is presented. Missing parts of the fluxes profiles correspond to the region where $S_A < 32\,\mathrm{g\,kg^{-1}}$.

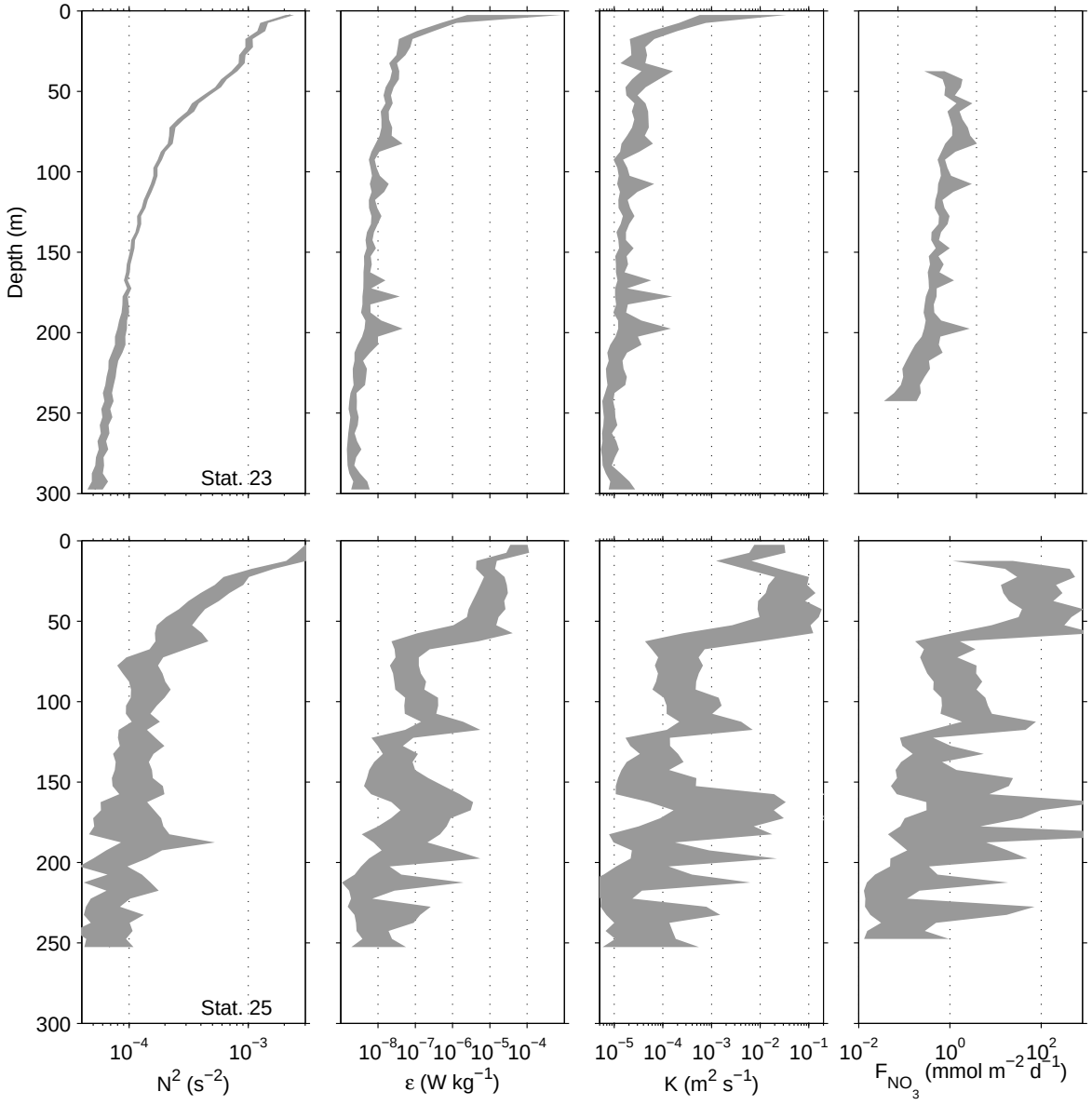

Figure 38: Buoyancy frequency squared (N^2), dissipation rate of TKE (ϵ), turbulent diffusivity (K) and turbulent nitrate flux (F_{NO_3}) for station 23 and 25, respectively. The gray intervals are the 95% confidence interval on the averaged profile.

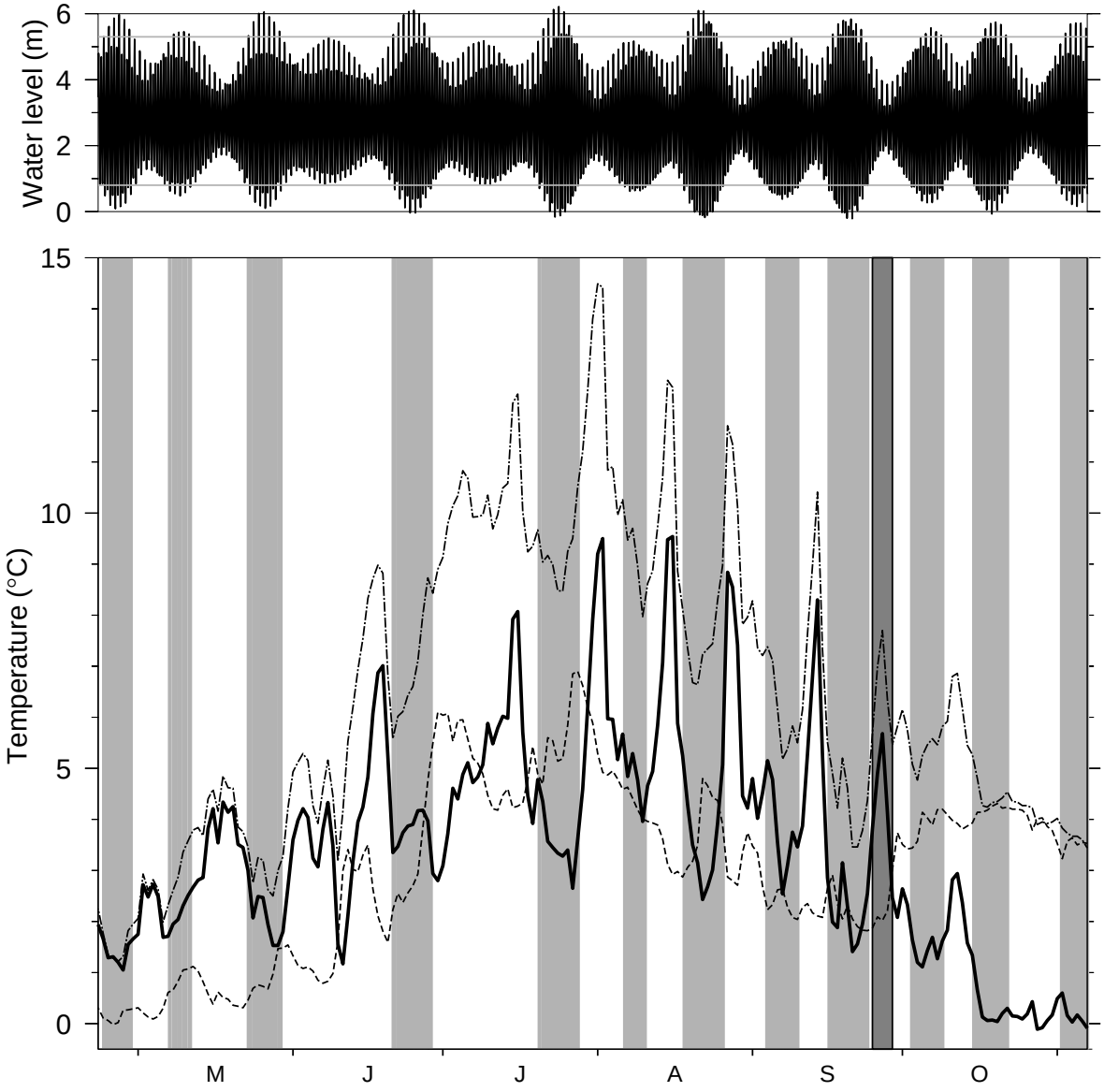

Figure 39: Spring-neap modulation of the temperature difference between the surface and bottom for thermistors deployed near Tadoussac (blue star in Fig. 34). (a) Tide level in Tadoussac. (b) Temperature evolution for 2009, 2 m below the surface (dash-got line) and near the bottom at 37 m deep (thick line). The temperature difference is also plotted in dashed. Vertical gray bands corresponds approximately to spring tides, defined here as water level above 5.3 m and below 0.8 m (thin horizontal lines in panel *a*). The period corresponding to our sampling campaign is highlighted with a darker shade.

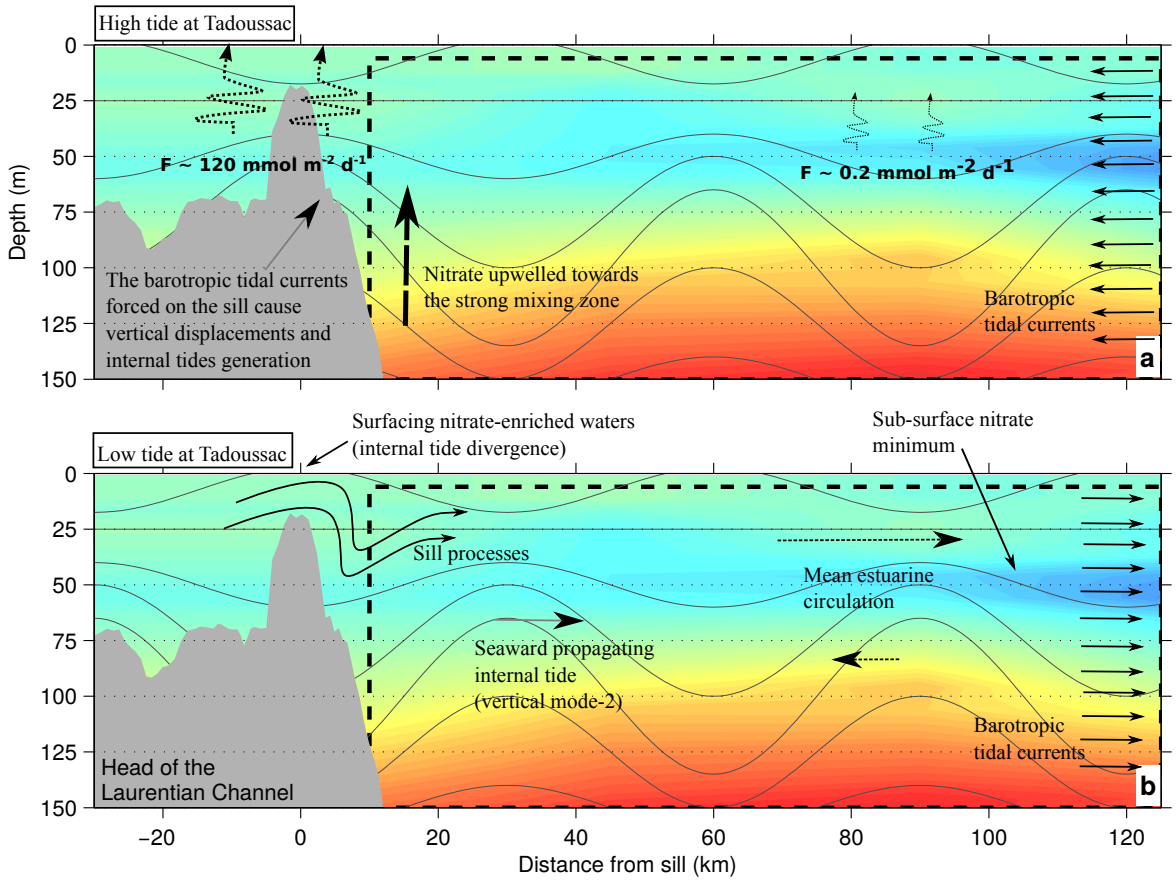

Figure 40: Sketch of some of the processes leading to nitrate fluxes in the LSLE. The color backgrounds represent nitrate concentration on an arbitrary scale, are but based on the average transect of Figure 30 (for data within the dashed rectangle). Outside the rectangle, concentration is extrapolated to the nearest value (no concentration data available from above the sill). Internal tide isopleths heaving for high (panel *a*) and low (panel *b*) tides at Tadoussac are sketched with thin gray lines for an internal tide of vertical mode-2 with a wavelength of 60 km. Turbulent sill processes are also expected to occur driven by barotropic tidal currents. The interplay between the upwelling of nitrate-rich waters by internal tides and the strong mixing near the sill leads to higher vertical nitrate fluxes (F) at the head of the Laurentian Channel compared to those at the Rimouski station (located at about 100 km downstream of the sill). Surfacing nitrate-enriched water are advected by the estuarine circulation, creating a subsurface nitrate concentration minimum further downstream (panel *b*).

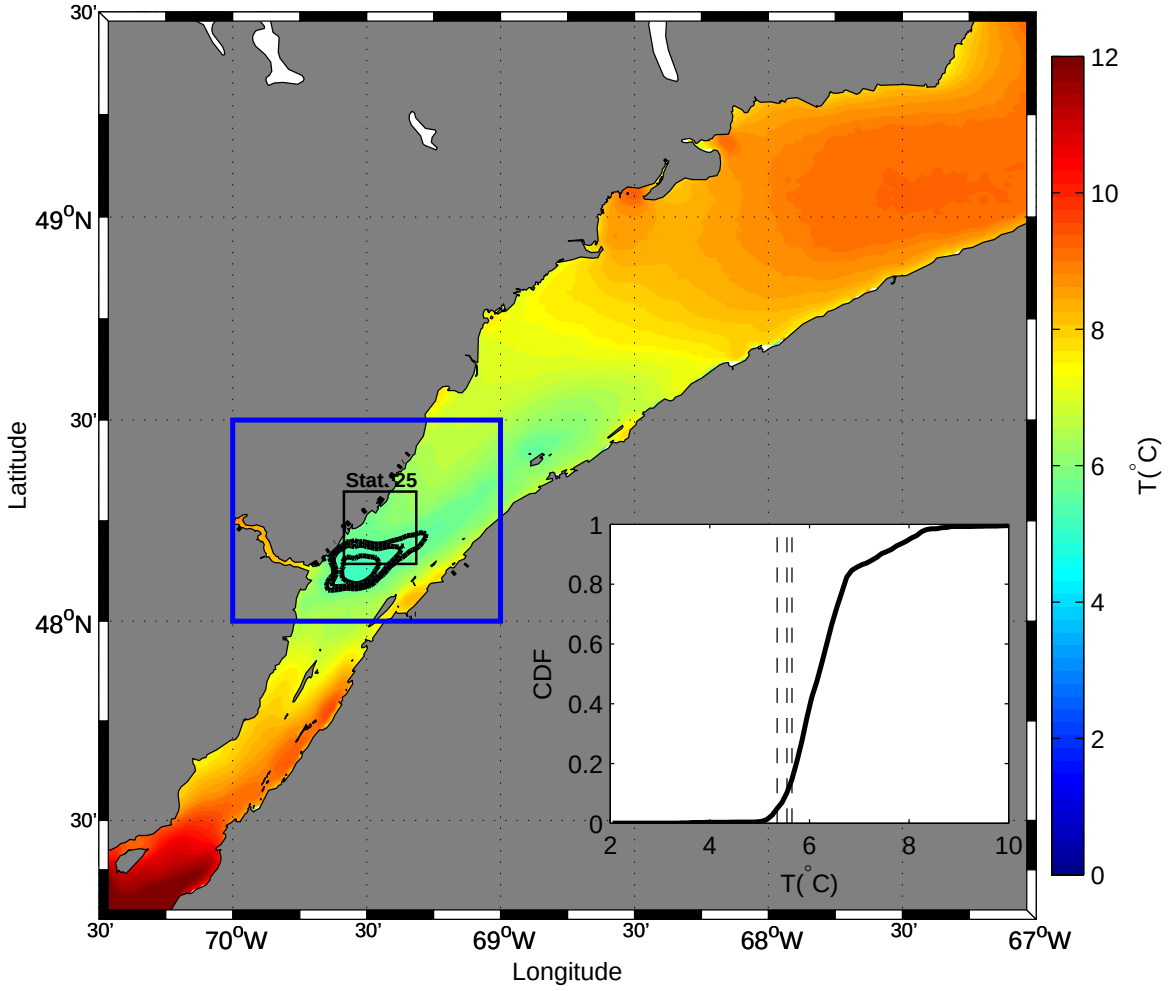

Figure 41: Averaged sea surface temperature from May to October for the 1986-2010 climatology from AVHRR remote sensing at 1.1 km resolution. Black lines correspond to temperature contours $T = 5.35, 5.55, 5.65\,^{\circ}\mathrm{C}$. These correspond to the coldest pixels (5%, 10% and 15% in the cumulative density function, inset) within the blue rectangle. Square box around Station 25 from Figure 28 is also shown for reference.

CONCLUSION GÉNÉRALE

Les trois chapitres de cette thèse font état des premières mesures de cisaillement à la micro-échelle dans l'estuaire maritime du Saint-Laurent (EMSL). Avant ce jour, seuls les travaux de Galbraith (1992) présentaient des mesures de turbulence, mais inférée à partir des inversions de densité à la fine-échelle. Bourgault et al. (2008) présentent aussi près de 200 profils de turbulence avec le même appareil que celui utilisé dans la thèse, mais ceux-ci ont été effectués en eaux moins profondes dans l'estuaire moyen, c'est-à-dire en amont de Tadoussac.

Durant les étés 2009 à 2012, un total de 1858 profils ont été effectués dans l'EMSL, excluant les centaines de profils qui n'ont pas fonctionné pour diverses raisons techniques. Pour illustrer la charge de travail, ceci représente 60 journées en mer au cours desquelles environ 235 kilomètres de cable ont été déployés manuellement dans l'eau. Si cela est possible, la figure 42 se veut un résumé de la thèse à elle seule, ou autrement dit, du *mélange turbulent dans l'estuaire maritime du Saint-Laurent*. On y trouve les chiffres importants des trois chapitres, soit les taux d'érosion de la CIF (chapitre 1), les flux turbulents de nitrate (chapitre 3) et les diffusivités turbulentes calculées à divres endroits de l'EMSL (les trois chapitres).

Retombées de la thèse

La quantification de la turbulence dans l'estuaire maritime répond tout d'abord au simple besoin du fait qu'aucune autre étude semblable n'avait été réalisée auparavant. Puisque ces données sont les premières de ce genre dans l'EMSL, différentes suites à cette thèse sont envisageables, et la porte est ouverte pour plusieurs études multidisciplinaires dans la région. Les différentes valeurs de diffusivité turbulente ou de flux de nitrate présentée à la Figure 42, sont des informations précieuses susceptibles d'être largement réutilisées et de déboucher sur d'autres études. D'ailleurs, les travaux de doctorat ont déjà permis la publication d'un article

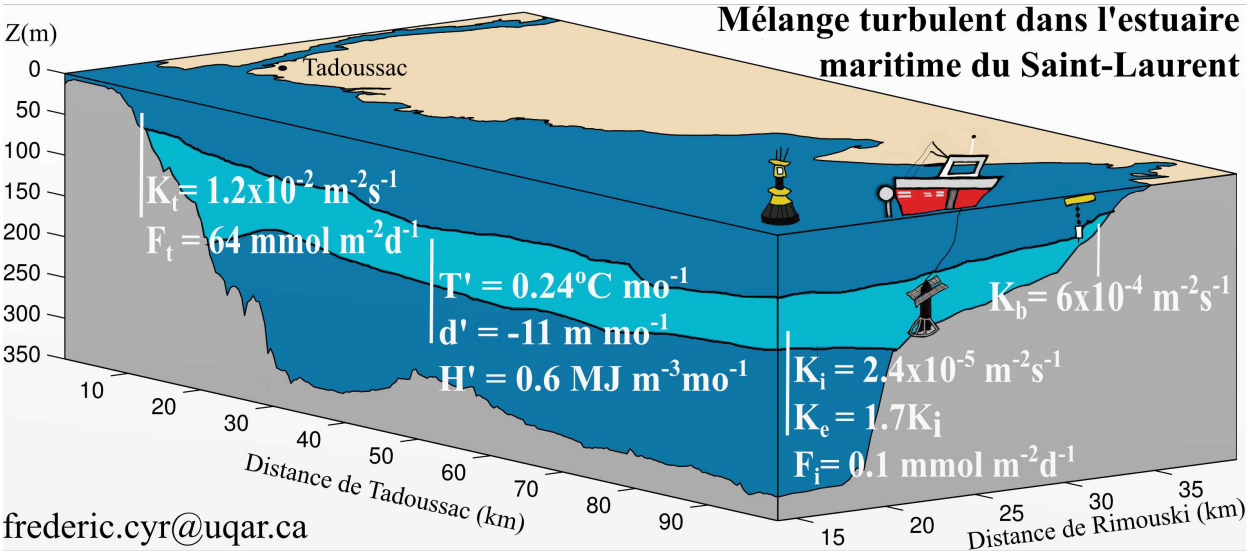

FIGURE 42: Figure récapitulative des travaux et des résultats importants de la thèse. La définition des variables ainsi que les incertitudes sur les valeurs présentées sont rapportés dans le tableau 4. Les dessins représentant l'échantillonnage (bouée IML4, bateau, VMP et mouillage) ont été effectués par Eveline Ross-phaneuf.

Taux d'érosion de la couche intermédiaire froide (CIF)*	
$T' = 0.24 \pm 0.04\,°\mathrm{C\,mo^{-1}}$	Réchauffement du coeur
$d' = 11 \pm 2\,\mathrm{m\,mo^{-1}}$	Diminution d'épaisseur
$H' = 0.59 \pm 0.09\,\mathrm{MJ\,m^2\ mo^{-1}}$	Augmentation du contenu de chaleur
Diffusivité turbulente	
$K_i = 2.4(1.5, 3.5) \times 10^{-5}\,\mathrm{m^2\,s^{-1}}$	Diffusivité interieure (dans la CIF)
$K_b = 6.0(4.1, 8.5) \times 10^{-4}\,\mathrm{m^2\,s^{-1}}$	Diffusivité aux bords (10 m près du fond)
$K_t = 1.2(0.4, 2.5) \times 10^{-2}\,\mathrm{m^2\,s^{-1}}$	Diffusivité à la tête du chenal Laurentien (25-50 m)
$K_e = 1.7K_i$	Diffusivité *effective* (effet du mélange aux bords)
Flux turbulents de nitrate	
$F_i = 0.13(0.08, 0.29)\,\mathrm{mmol\,m^2\,d^{-1}}$	Flux intérieur (à la station Rimouski, 25-50 m)
$F_t = 71(25, 140)\,\mathrm{mmol\,m^2\,d^{-1}}$	Flux à la tête du chenal Laurentien (25-50 m)

*Le symbole ± ou les nombres entre parenthèses indiquent l'intervalle de confiance 95% sur la moyenne

TABLE 4: Tableau récapitulatif des chiffres à retenir de la thèse (voir aussi la figure 42).

concernant l'hypoxie des eaux profondes de l'EMSL (Bourgault et al., 2012). De plus, les profils de diffusivité à l'intérieur et aux bords de l'EMSL, ainsi qu'à la tête du chenal Laurentien, contiennent des informations précieuses pour la validation des modèles numériques dans la région. Par exemple, le fait de savoir que la turbulence près des frontières est plus forte d'un ordre de grandeur par rapport à l'intérieur (chapitre 2) est une bonne piste pour le développement d'une paramétrisation du mélange aux frontières. Il en est de même pour la validation de l'érosion de la CIF dans les modèles. Déjà, une simple comparaison entre l'évolution observée à la station Rimouski et celle provenant du modèle régional de Saucier et al. (2003) revèle que la CIF est mal représentée par celui-ci (Figure 43). La quantification du mélange et des taux d'érosion de la CIF dans cette thèse (chapitre 1) sont des pistes à suivre pour régler ce problème.

Les travaux de thèse ont aussi redémontré que les marées internes affectent le comportement et possiblement le mélange de la CIF le long de la section Rimouski (chapitre 2). Bien peu de choses sont toutefois connues de ces marées internes et la thèse soulève plus de questions que de réponses les concernant. Quelle est l'influence du cycle vives-eaux / mortes-eaux sur la modulation de celles-ci ? Est-ce qu'il existe des régions de concentration de l'énergie des marées internes (*hotspots* pour le mélange) ? Quelle est la distribution de l'énergie des marées internes le long de l'EMSL ? etc. Ces questions pourraient être utilisées pour concevoir de futures expériences de terrain visant à y trouver réponse.

Finalement, les flux de nitrate et le calcul de la production primaire que ceux-ci peuvent soutenir (chapitre 3) est une contribution utile pour le calcul du budget de la biomasse de l'estuaire maritime. Les flux calculés peuvent aussi être utilisés pour la validation de modèles biochimiques de l'estuaire et du golfe.

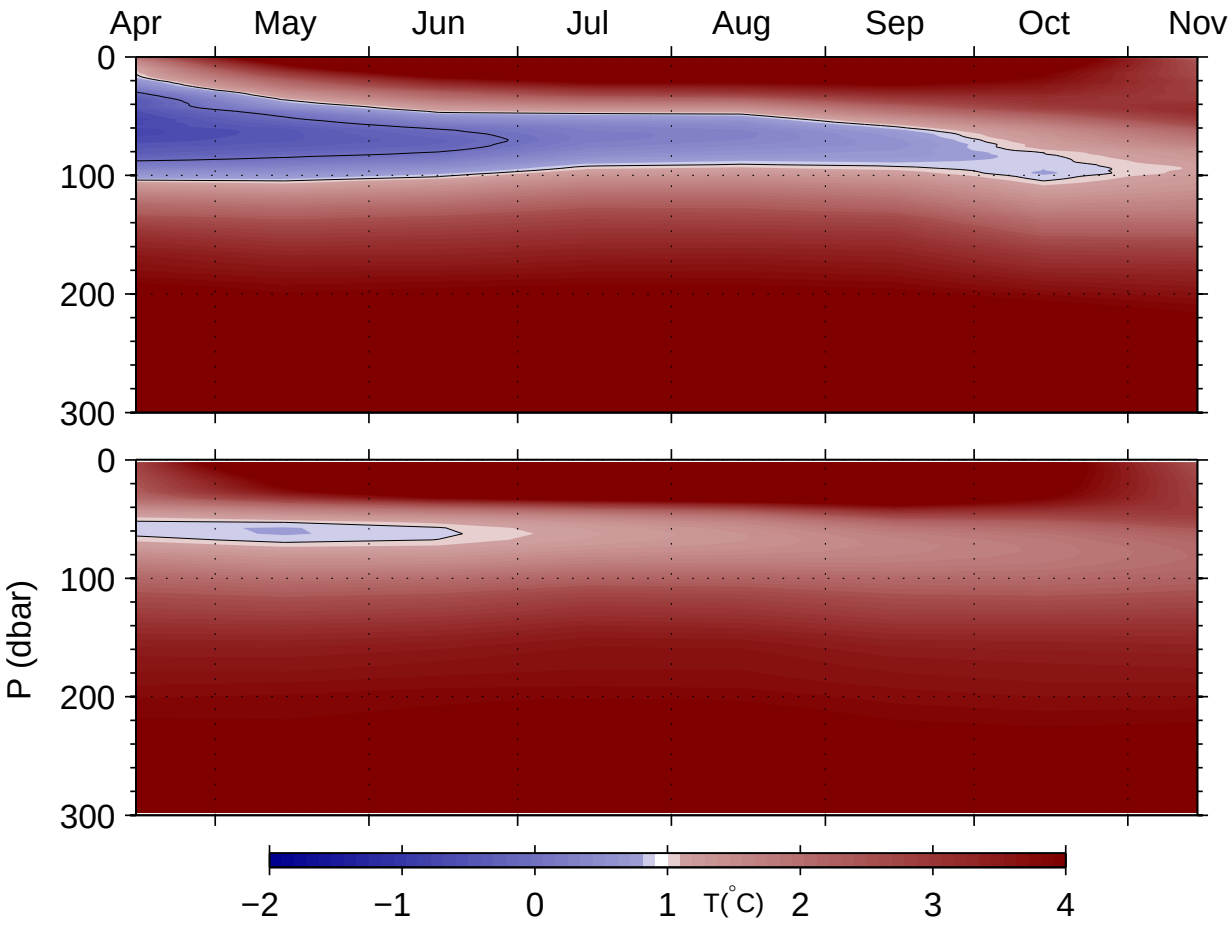

FIGURE 43: Comparaison entre observations et modèle pour l'érosion de la couche intermédiaire froide entre avril et novembre. Panneau du haut : climatologie 1993-2010 des température à la station Rimouski (adapté de Cyr et al., 2011). Panneau du bas : moyenne de l'évolution des températures modélisées par un modèle régional à 5 km de résolution (Saucier et al., 2003) entre 1997 et 2007 pour le point de grille correspondant à la station Rimouski (données fournies par Simon Senneville).

Travaux futurs

Comme nous venons de le mentionner, la thèse soulève possiblement plus de questions que de réponses concernant la dynamique de l'estuaire maritime du Saint-Laurent. Ces questions ouvrent par contre la porte à la réalisation de nouvelles études dans la région.

Dans le premier chapitre de la thèse, nous avons travaillé avec des taux d'érosion climatologiques de la CIF. Par contre, nous avons aussi montré que ceux-ci évoluent sur une base interannuelle sans pour autant tenter de trouver des explications à cette variation. Est-ce que cette variation provient d'une modulation interannuelle du mélange ? Est-ce que le débit d'eau douce des rivières ou la vigeur de la circulation estuarienne cause cette variation ? Concernant la turbulence, il serait intéressant d'utiliser les données recueillies durant la thèse à la station Rimouski afin de valider le calcul de la turbulence par la méthode des inversions de Thorpe (1977). Cette méthode utilise les inversions de densité dans les profils de densité afin d'estimer l'énergie de mélange présente dans la colonne d'eau. La validation de cette méthode nous permettrait d'utiliser par la suite les profils historiques de densité pour inférer l'évolution intra- et inter-annuelle de la turbulence.

Les résultats de la thèse suggèrent aussi que le mélange aux bords expliquer un tiers du mélange de l'EMSL, mais le mécanisme de redistribution de ce mélange vers l'intérieur est encore inconnu (chapitre 1). De plus, il est suggéré que le mélange intérieur explique les deux autres tiers du budget de mélange. Mais par quels mécanismes s'opère ce mélange loins des bords ? Quel est le rôle des marées internes (via la génération de courants cisaillés ou via les réflexions sur la surface et le fond) sur l'amplitude de ce mélange ?

Le mélange mesuré à la tête du chenal Laurentien qui a permis une estimation des flux verticaux de nitrate (chapitre 3) a été mesuré en période de mortes-eaux. Il a été cependant suggéré que le mélange en période de vives-eaux est environ deux fois supérieur à celui en mortes-eaux (Saucier et Chassé, 2000). Il serait intéressant de confirmer ceci avec des mesures de terrain et de corriger, s'il y a lieu, les flux verticaux moyens de nitrate. De

plus, notons que les quelques centaines de profils de turbulence recueillis à la tête du chenal Laurentien représentent un assez faible échantillonnage comparativement à ceux recueillis le long de la section Rimouski (près de 2000 profils). Il serait intéressant de poursuivre l'échantillonnage à la tête du chenal afin d'accroître la robustesse des statistiques concernant les flux turbulents et de mieux comprendre les mécanismes responsables du mélange turbulent.

Toutes les observations de turbulence réalisées au cours de cette thèse pourraient servir au développement de paramétrisation de la turbulence dans les modèles numériques. Un point de départ intéressant serait la comparaison entre la distribution spatiale du mélange observée et modélisée. Par exemple, les observations suggèrent un mélange 10 fois plus fort entre l'intérieur et les bords de l'EMSL et 300 fois plus fort entre l'intérieur de l'EMSL et la tête du chenal Laurentien. Qu'en est-il des modèles ? En sciences atmosphériques, certaines nouvelles paramétrisations de la turbulence dans la couche limite tiennent maintenant compte de la distribution statistique de la turbulence au lieu de seulement tenir compte des valeurs moyennes (p.-ex. Golaz et al., 2002a,b; Larson et Golaz, 2005). Les centaines de profils de turbulence récoltés aux cours des quatre étés de terrain de la thèse constituent une masse critique suffisante pour permettre, sinon le développement de telles paramétrisations, du moins une analyse poussée de la distribution statistique de la turbulence.

Finalement, des travaux de maitrise utilisant en partie des données récoltées durant la thèse est présentement en cours sur les couches minces phytoplanctoniques. Le rôle de la turbulence sur la présence ou l'évolution de ces couches pourrait également être abordée dans une étude future, étant donné que les données recueillies durant la thèse le permettent.

RÉFÉRENCES

Allen, J., Siddorn, J.R., Blackford, J.C., Gilbert, F.J., 2004. Turbulence as a control on the microbial loop in a temperate seasonally stratified marine systems model. Journal of Sea Research 52, 1–20. doi:10.1016/j.seares.2003.09.004.

Armi, L., 1978. Some evidence of boundary mixing in the deep ocean. Journal of Geophysical Research 83, 1971–1979.

Armi, L., Farmer, D.M., 2002. Stratified flow over topography : bifurcation fronts and transition to the uncontrolled state. Proceedings of the Royal Society A: Mathematical, Physical and Engineering Sciences 458, 513–538.

Arrigo, K.R., 2005. Marine microorganisms and global nutrient cycles. Nature 437, 349–356. doi:10.1038/nature04159.

Baker, M.A., Gibson, C.H., 1987. Sampling turbulence in the stratified ocean: statistical consequence of strong intermittency. Journal of Physical Oceanography 17, 1817–1838.

Banks, R.E., 1966. The cold layer in the Gulf of St. Lawrence. Journal of Geophysical Research 71, 1603–1610.

Benoit, J., El-Sabh, M.I., Tang, C.L., 1985. Structure and seasonal characteristics of the Gaspé Current. Journal of Geophysical Research 90, 3225–3236. doi:10.1029/JC090iC02p03225.

Benoit, P., Gratton, Y., Mucci, A., 2006. Modeling of dissolved oxygen levels in the bottom waters of the Lower St. Lawrence Estuary: Coupling of benthic and pelagic processes. Marine Chemistry 102, 13–32. doi:10.1016/j.marchem.2005.09.015.

Bogucki, D., Dickey, T., Redekopp, L.G., 1997. Sediment resuspension and mixing by resonantly generated internal solitary waves. Journal of Physical Oceanography 27, 1181–1196.

Borges, A.V., 2005. Do we have enough pieces of the jigsaw to integrate CO_2 fluxes in the coastal ocean? Estuaries 28, 3–27.

Bourgault, D., Cyr, F., Galbraith, P.S., Pelletier, E., 2012. Relative importance of pelagic and sediment respiration in causing hypoxia in a deep estuary. Journal of Geophysical Research 117. doi:10.1029/2012JC007902.

Bourgault, D., Hamel, C., Cyr, F., Tremblay, J.E., Galbraith, P.S., Dumont, D., Gratton, Y., 2011. Turbulent nitrate fluxes in the Amundsen Gulf during ice-covered conditions. Geophysical Research Letters 38, 2–6. doi:10.1029/2011GL047936.

Bourgault, D., Kelley, D., 2003. Wave-induced boundary mixing in a partially mixed estuary. Journal of Marine Research 61, 553–576.

Bourgault, D., Kelley, D.E., Galbraith, P.S., 2008. Turbulence and boluses on an internal beach. Journal of Marine Research 66, 563–588. doi:10.1357/002224008787536835.

Bourgault, D., Morsilli, M., Richards, C., Neumeier, U., Kelley, D., 2014. Sediment resuspension and nepheloid layers induced by long internal solitary waves shoaling orthogonally on uniform slopes. Continental Shelf Research 72, 21–33. doi:10.1016/j.csr.2013.10.019.

Bugden, G.L., 1991. Changes in the temperature salinity characteristics of the deeper waters of the Gulf of St. Lawrence, in: Therriault, J.C. (Ed.), The Gulf of St. Lawrence: small ocean or big estuary?. Canadian Special Publication of Fisheries and Aquatic Sciences 113. volume 113, pp. 139–147.

Bugden, G.L., Hargrave, B.T., Sinclair, M., Tang, C.L., Therriault, J.C., Yeats, P.A., 1982. Changes in the temperature-salinity characteristics of the deeper waters of the Gulf of St. Lawrence over the past several decades. Canadian Technical Report of Fisheries and Aquatic Sciences 1078, 89 pp.

Burchard, H., 2009. Combined effects of wind, tide, and horizontal density gradients on stratification in estuaries and coastal seas. Journal of Physical Oceanography 39, 2117–2136. doi:10.1175/2009JPO4142.1.

Carr, M.E., Lewis, M.R., Kelley, D.E., Jones, B., 1995. A physical estimate of new production in the equatorial Pacific along 150°W. Limnology and Oceanography 40, 138–147.

Chadwick, M., Sinclair, A., 1991. Fisheries production in the Gulf of St. Lawrence, in: Therriault, J.C. (Ed.), The Gulf of St. Lawrence: small ocean or big estuary?. Canadian Special Publication of Fisheries and Aquatic Sciences. volume 113, pp. 125–136.

Chubarenko, I., Demchenko, N., 2010. On contribution of horizontal and intra-layer convection to the formation of the Baltic Sea cold intermediate layer. Ocean Science 6, 285–299. doi:10.5194/os-6-285-2010.

Clesceri, L.S., Greenberg, A.E., Eaton, A.D., 1989. Standard methods for the examination of wastewater. 20th ed., APHA American Public Health Association, Washington D.C.

Cummins, P.F., Vagle, S., Armi, L., Farmer, D.M., 2003. Stratified flow over topography: upstream influence and generation of nonlinear internal waves. Proceedings of the Royal Society A: Mathematical, Physical and Engineering Sciences 459, 1467–1487.

Cyr, F., Bourgault, D., Galbraith, P.S., 2011. Interior versus boundary mixing of a cold intermediate layer. Journal of Geophysical Research 116, 1–12. doi:10.1029/2011JC007359.

Demers, S., Legendre, L., Therriault, J.C., 1986. Phytoplankton responses to vertical tidal mixing, in: Bowman, J., Yentsch, M., Peterson, W.T. (Eds.), Tidal mixing and plankton dynamics. Springer-Verlag, Berlin Heidelberg, pp. 1–40.

Dionne, M., Sainte-Marie, B., Bourget, E., Gilbert, D., 2003. Distribution and habitat selection of early benthic stages of snow crab *Chionoecetes opilio*. Marine Ecology Progress Series 259, 117–128. doi:10.3354/meps259117.

Doyon, P., Klein, B., Ingram, R.G., Legendre, L., Tremblay, D., Therriault, J.C., 2000. Influence of wind mixing and upper-layer stratification on phytoplankton biomass in the Gulf of St . Lawrence. Deep Sea Research Part II: Topical Studies in Oceanography 47, 415–433.

Drainville, G., 1968. Le Fjord du Saguenay: 1. Contribution à l'océanographie. Le Naturaliste Canadien 95, 809–853.

Durham, W.M., Stocker, R., 2012. Thin phytoplankton layers: Characteristics, mechanisms, and consequences. Annual Review of Marine Science 4, 177–207. doi:10.1146/annurev-marine-120710-100957.

Efron, B., Gong, G., 1983. A leisurely look at the bootstrap, the jackknife, and cross-validation. The American Statistician 37, 36–48.

Egbert, G., Ray, R., 2000. Significant dissipation of tidal energy in the deep ocean inferred from satellite altimeter data. Nature 405, 775–778.

El-Sabh, M.I., 1979. The Lower St. Lawrence Estuary as a physical oceanographic system. Le Naturaliste Canadien 106, 55–73.

Emery, W.J., Thomson, R.E., 2001. Data analysis methods in physical oceanography. Elsevier Science.

Falkowski, P., 2000. The Global Carbon Cycle: A Test of Our Knowledge of Earth as a System. Science 290, 291–296. doi:10.1126/science.290.5490.291.

Farmer, D., Armi, L., 1999. The generation and trapping of solitary waves over topography. Science 283, 188–190.

Fer, I., Widell, K., 2007. Early spring turbulent mixing in an ice-covered Arctic fjord during transition to melting. Continental Shelf Research 27, 1980–1999. doi:10.1016/j.csr.2007.04.003.

Fisheries and Oceans - Canada, 2011. Oceanaographic Data Management System. Address: Maurice Lamontagne Institute Mont-Joli (Quebec), Canada. http://www.osl.gc.ca/sgdo (consulted on 10 January 2011).

Fisheries and Oceans - Canada, 2013. Oceanographic Data Management System, Maurice Lamontagne Institute Mont-Joli (Quebec), Canada. Address: http://www.osl.gc.ca/sgdo (consulted on 16 August 2013).

Fofonoff, P., Millard, R.C.J., 1983. Algorithms for computation of fundamental properties of seawater. Unesco Technical Papers in Marine Science 44, 53 pp.

Forrester, W.D., 1970. Geostrophic approximation in the St. Lawrence Estuary. Tellus XXII, 53–65.

Forrester, W.D., 1974. Internal tides in the St. Lawrence Estuary. Journal of Marine Research 32, 55–66.

Fortier, L., Levasseur, M.E., Drolet, R., Therriault, J.C., 1992. Export production and the distribution of fish larvae and their prey in a coastal jet frontal region. Marine Ecology Progress Series 85, 203–218. doi:10.3354/meps085203.

Galbraith, P.S., 1992. Relating overturns to mixing and buoyancy flux. Ph.D. thesis. Dalhousie University.

Galbraith, P.S., 2006. Winter water masses in the Gulf of St. Lawrence. Journal of Geophysical Research 111. doi:10.1029/2005JC003159.

Galbraith, P.S., Chassé, J., Denis, G., Larouche, P., Brickman, D., Pettigrew, B., Devine, L., Gosselin, A., Pettipas, R.G., Lafleur, C., 2011. Physical oceanographic conditions in the Gulf of St. Lawrence in 2010. DFO Canadian Science Advisory Secretariat 2011/045, iv + 82 p.

Galbraith, P.S., Chassé, J., Gilbert, D., Larouche, P., Brickman, D., Pettigrew, B., Devine, L., Gosselin, A., Pettipas, R.G., Lafleur, C., 2012. Physical Oceanographic Conditions in the Gulf of St. Lawrence in 2011. DFO Canadian Science Advisory Secretariat 2012/023, iii + 85 p.

Galbraith, P.S., Chassé, J., Larouche, P., Gilbert, D., Brickman, D., Pettigrew, B., Devine, L., Lafleur, C., 2013. Physical oceanographic conditions in the Gulf of St. Lawrence in 2012. DFO Canadian Science Advisory Secretariat 2013/026, v + 89 p.

Gargett, A.E., Osborn, T.R., Nasmyth, P.W., 1984. Local isotropy and the decay of turbulence in a stratified fluid. Journal of Fluid Mechanics 144, 231–280.

Garrett, C., 1990. The role of secondary circulation in boundary mixing. Journal of Geophysical Research 95, 3181–3188. doi:10.1029/JC095iC03p03181.

Garrett, C., 2001. An isopycnal view of near-boundary mixing and associated flows. Journal of Physical Oceanography 31, 138–142.

Garrett, C., Gilbert, D., 1988. Estimates of vertical mixing by internal waves reflected off a sloping bottom, in: Nihoul, J C J and Jamart, B.M. (Ed.), Small-Scale Turbulence and Mixing in the Ocean - Proceedings of the 19th International Liege Colloquium on Ocean Hydrodynamics. Elsevier, New York, pp. 405–424.

Garrett, C., MacCready, P., Rhines, P., 1993. Boundary mixing and arrested Ekman layers: Rotating stratified flow near a sloping boundary. Annual Review of Fluid Mechanics 25, 291–323. doi:10.1146/annurev.fl.25.010193.001451.

Gattuso, J.P., Frankignoulle, M., Wollast, R., 1998. Carbon and carbonate metabolism in coastal aquatic ecosystem. Annual Review of Ecology, Evolution and Systematics 29, 405–434.

Geyer, W.R., Lavery, A.C., Scully, M.E., Trowbridge, J.H., 2010. Mixing by shear instability at high Reynolds number. Geophysical Research Letters 37, L22607. doi:10.1029/2010GL045272.

Geyer, W.R., Scully, M.E., Ralston, D.K., 2008. Quantifying vertical mixing in estuaries. Environmental Fluid Mechanics 8, 495–509. doi:10.1007/s10652-008-9107-2.

Geyer, W.R., Smith, J.D., 1987. Shear instability in a highly stratified estuary. Journal of Physical Oceanography 17, 1668–1679.

Geyer, W.R., Trowbridge, J.H., Bowen, M.M., 2000. The dynamics of a partially mixed estuary. Journal of Physical Oceanography 30, 2035–2048.

Ghosal, S., Mandre, S., 2003. A simple model illustrating the role of turbulence on phytoplankton blooms. Journal of Mathematical Bioleogy 46, 333–46. doi:10.1007/s00285-002-0184-4.

Gilbert, D., Pettigrew, B., 1997. Interannual variability (1948–1994) of the CIL core temperature in the Gulf of St. Lawrence. Canadian Journal of Fisheries and Aquatic Sciences 54, 57–67. doi:10.1139/cjfas-54-S1-57.

Gilbert, D., Sundby, B., Gobeil, C., Mucci, A., Tremblay, G.H., 2005. A seventy-two-year record of diminishing deep-water oxygen in the St. Lawrence estuary: The northwest Atlantic connection. Limnology and Oceanography 50, 1654–1666. doi:10.4319/lo.2005.50.5.1654.

Gill, A.E., 1982. Atmosphere-Ocean Dynamics. volume 30 of *International Geophysics Series*. Academic Press, London.

Godin, G., 1979. La marée dans le golfe et l'estuaire du Saint-Laurent. Le Naturaliste Canadien 106, 105–121.

Golaz, J.C., Larson, V.E., Cotton, W.R., 2002a. A PDF-based model for boundary layer clouds. Part I: Method and model description. Journal of the Atmospheric Sciences 59, 3540–3551.

Golaz, J.C., Larson, V.E., Cotton, W.R., 2002b. A PDF-based model for boundary layer clouds. Part II: Model results. Journal of the Atmospheric Sciences 59, 3552–3571.

Goudsmit, G., Peeters, F., Gloor, M., Wüest, A., 1997. Boundary versus internal diapycnal mixing in stratified natural waters. Journal of Geophysical Research 102, 27903–27914.

Grasshoff, K., Ehrhardt, M., Kremling, K., 1999. Methods of seawater analysis. 3rd ed., Wiley - VCH, New York.

Gratton, Y., Mertz, G., Gagné, J.A., 1988. Satellite observations of tidal upwelling and mixing in the St. Lawrence Estuary. Journal of Geophysical Research 93, 6947–6954.

Gregg, M., Alford, M., Kontoyiannis, H., Zervakis, V., Winkel, D., 2012. Mixing over the steep side of the Cycladic Plateau in the Aegean Sea. Journal of Marine Systems 89, 30–47. doi:10.1016/j.jmarsys.2011.07.009.

Gregg, M.C., 1989. Scaling turbulent dissipation in the thermocline. Journal of Geophysical Research 94, 9686. doi:10.1029/JC094iC07p09686.

Gregg, M.C., Yakushev, E., 2005. Surface ventilation of the Black Sea's cold intermediate layer in the middle of the western gyre. Geophysical Research Letters 32, 1–4. doi:10.1029/2004GL021580.

Greisman, P., Ingram, R.G., 1977. Nutrient distribution in the St. Lawrence Estuary. Journal of Fisheries Research Board of Canada 34, 2117–2123.

Hales, B., Moum, J.N., Covert, P., Perlin, A., 2005. Irreversible nitrate fluxes due to turbulent mixing in a coastal upwelling system. Journal of Geophysical Research 110. doi:10.1029/2004JC002685.

Hales, B., Vaillancourt, R.D., Prieto, L., Marra, J., Houghton, R., Hebert, D., 2009. High-resolution surveys of the biogeochemistry of the New England shelf-break front during Summer, 2002. Journal of Marine Systems 78, 426–441. doi:10.1016/j.jmarsys.2008.11.024.

Hinze, J.O., 1959. Turbulence: an introduction to its mechanism and theory. McGraw Hill, New York, NY.

Hinze, J.O., 1975. Turbulence. McGraw Hill, New York, NY.

Holtermann, P.L., Umlauf, L., Tanhua, T., Schmale, O., Rehder, G., Waniek, J.J., 2012. The Baltic Sea tracer release experiment: 1. Mixing rates. Journal of Geophysical Research 117. doi:10.1029/2011JC007445.

Horne, E.P., Loder, J.W., Naime, C.E., Oakey, N.S., 1996. Turbulence dissipation rates and nitrate supply in the upper water column on Georges Bank. Deep Sea Research Part II: Topical Studies in Oceanography 43, 1683–1712. doi:10.1016/S0967-0645(96)00037-9.

Hosegood, P., 2004. Solibore-induced sediment resuspension in the Faeroe-Shetland Channel. Geophysical Research Letters 31, 2–5. doi:10.1029/2004GL019544.

Huisman, J., van Oostveen, P., Weissing, F.J., 1999. Species dynamics in phytoplankton blooms: incomplete mixing and competition for light. The American Naturalist 154, 46–68.

Ingram, R.G., 1975. Influence of tidal-induced vertical mixing on primary productivity in the St. Lawrence Estuary, in: Nihoul, J.C.J. (Ed.), Mémoires de la Société Royale des Sciences de Liège, University of Liege, Liege. pp. 59–74.

Ingram, R.G., 1976. Characteristics of a tide-induced estuarine front. Journal of Geophysical Research 81, 1951–1959.

Ingram, R.G., 1979a. Internal wave observation off Isle Verte. Journal of Marine Research 36, 715–724.

Ingram, R.G., 1979b. Water mass modification in the St. Lawrence Estuary. Le Naturaliste Canadien 106, 45–54.

Ingram, R.G., 1983. Vertical mixing at the head of the Laurentian Channel. Estuarine, Coastal and Shelf Science 16, 333–338.

Ingram, R.G., 1985. Frontal characteristics at the head of the Laurentian Channel. Le Naturaliste Canadien 112, 31–38.

Kay, D.J., 2003. Interfacial mixing in a highly stratified estuary 1. Characteristics of mixing. Journal of Geophysical Research 108, 3072. doi:10.1029/2000JC000252.

Klymak, J.M., Gregg, M.C., 2001. Three-dimensional nature of flow near a sill. Journal of Geophysical Research 106, 22295–22311.

Klymak, J.M., Gregg, M.C., 2004. Tidally generated turbulence over the Knight Inlet sill. Journal of Physical Oceanography 34, 1135–1151.

Kolmogorov, A.N., 1941. The local structure of turbulence in incompressible viscous fluid for very large Reynolds numbers. Doklady AN SSSR 30, 299–303.

Kostianoy, A.G., Nihoul, J.C.J., Rodionov, V.B., 2004. Physical oceanography of frontal zones in the subarctic seas. volume 71 of *Elsevier Oceanography Series*. Elsevier, Amsterdam.

Koutitonsky, V.G., Bugden, G.L., 1991. The physical oceanography of the Gulf of St. Lawrence: a review with emphasis on the synoptic variability of the motion, in: Therriault, J.C. (Ed.), The Gulf of St. Lawrence: small ocean or big estuary?. Canadian Special Publication of Fisheries and Aquatic Sciences. volume 113, pp. 57–90.

Kundu, P.K., Cohen, I.M., 2007. Fluid Mechanics. Fourth ed., Academic Press, New York.

de Lafontaine, Y., Demers, S., Runge, J., 1991. Pelagic food web interactions and productivity in the Gulf of St. Lawrence: a perspective, in: Therriault, J.C. (Ed.), The Gulf of St. Lawrence: small ocean or big estuary?. Canadian Special Publication of Fisheries and Aquatic Sciences. volume 113, pp. 99–123.

Lamb, H., 1895. Hydrodynamics. Cambridge University Press, London.

Larson, V.E., Golaz, J.C., 2005. Using probability density functions to derive consistent closure relationships among higher-order moments. Monthly Weather Review 133, 1023–1042.

Lauzier, L.M., Bailey, W.B., 1957. Features of the deeper waters of the Gulf of St. Lawrence. Bulletin (Fisheries Research Board of Canada) 111, 213–250.

Lavoie, D., Simard, Y., Saucier, F.J., 2000. Aggregation and dispersion of krill at channel heads and shelf edges: the dynamics in the Saguenay – St. Lawrence Marine Park. Canadian Journal of Fisheries and Aquatic Sciences 57, 1853–1869.

Law, C.S., 2003. Vertical eddy diffusion and nutrient supply to the surface mixed layer of the Antarctic Circumpolar Current. Journal of Geophysical Research 108. doi:10.1029/2002JC001604.

Law, C.S., Martin, A.P., Liddicoat, M.I., Watson, A.J., Richards, K.J., Woodward, E.M.S., 2001. A Lagrangian F_6 tracer study of an anticyclonic eddy in the North Atlantic: patch evolution, vertical mixing and nutrient supply to the mixed layer. Deep Sea Research Part II: Topical Studies in Oceanography 48, 705–724.

van der Lee, E.M., Umlauf, L., 2011. Internal wave mixing in the Baltic Sea: Near-inertial waves in the absence of tides. Journal of Geophysical Research 116, 1–16. doi:10.1029/2011JC007072.

Lehmann, M.F., Barnett, B., Ge, Y., Gilbert, D., Maranger, R.J., Mucci, A., Sundby, B., Thibodeau, B., 2009. Aerobic respiration and hypoxia in the Lower St. Lawrence Estuary: Stable isotope ratios of dissolved oxygen constrain oxygen sink partitioning. Limnology and Oceanography 54, 2157–2169.

Levasseur, M.E., Fortier, L., Therriault, J.C., Harrison, P., 1992. Phytoplankton dynamics in a coastal jet frontal region. Marine Ecology Progress Series 86, 283–295. doi:10.3354/meps086283.

Levasseur, M.E., Therriault, J.C., 1987. Phytoplankton biomass and nutrient dynamics in a tidally induced upwelling: the role of the NO_3:SiO_4 ratio. Marine Ecology Progress Series 39, 87–97.

Levasseur, M.E., Therriault, J.C., Legendre, L., 1984. Hierarchical control of phytoplankton succession by physical factors. Marine Ecology Progress Series 19, 211–222.

Lewis, M.R., Harrison, W.G., Oakey, N.S., Hebert, D., Platt, T., 1986. Vertical nitrate fluxes in the oligotrophic ocean. Science 234, 870–873. doi:10.1126/science.234.4778.870.

Lie, H.J., El-Sabh, M.I., 1983. Formation of eddies and transverse currents in a two-layer channel of variable bottom with application to the Lower St. Lawrence Estuary. Journal of Physical Oceanography 13, 1063–1075.

Lovrich, G.A., Sainte-marie, B., Smith, B.D., 1995. Depth distribution and seasonal movements of Chionoecetes opilio (Brachyura: Majidae) in Baie Sainte-Marguerite, Gulf of Saint Lawrence. Canadian Journal of Zoology 73, 1712–1726.

Lueck, R.G., Wolk, F., Yamasaki, H., 2002. Oceanic velocity microstructure measurements in the 20th century. Journal of Oceanography 58, 153–174.

MacKinnon, J.A., Gregg, M.C., 2003. Mixing on the late-summer New England shelf—solibores, shear, and stratification. Journal of Physical Oceanography 33, 1476–1492. doi:10.1175/1520-0485(2003)033<1476:MOTLNE>2.0.CO;2.

Macoun, P., Lueck, R.G., 2004. Modeling the spatial response of the airfoil shear probe using different sized probes. Journal of Atmospheric and Oceanic Technology 21, 284–297. doi:10.1175/1520-0426(2004)021<0284:MTSROT>2.0.CO;2.

Martin, A.P., Lucas, M.I., Painter, S.C., Pidcock, R., Prandke, H., Prandke, H., Stinchcombe, M.C., 2010. The supply of nutrients due to vertical turbulent mixing: A study at the Porcupine Abyssal Plain study site in the northeast Atlantic. Deep Sea Research Part II: Topical Studies in Oceanography 57, 1293–1302. doi:10.1016/j.dsr2.2010.01.006.

McDougall, T.J., Barker, P.M., 2011. Getting started with TEOS-10 and the Gibbs Seawater (GSW) Oceanographic Toolbox. May, SCOR/IAPSO WG127.

Ménard, N., 2009. La science au service de la conservation au Parc Marin Saguenay-Saint-Laurent: Comment mieux comprendre permet de mieux protéger. Revue des sciences de l'eau 22, 115–123.

Mertz, G., Gratton, Y., 1990. Topographic waves and topographically induced motions in the St. Lawrence estuary, in: El-Sabh, M.I., Silverberg, N. (Eds.), Oceanography of a large-scale estuarine system: The St. Lawrence. Springer-Verlag, New-York. volume 39, pp. 94–108.

Miles, J.W., 1961. On the stability of heterogeneous shear flows. Journal of Fluid Mechanics 10, 496–508.

Mitchell, M.R., Harrison, G., Pauley, K., Gagné, A., Maillet, G., Strain, P., 2002. Atlantic zonal monitoring program sampling protocol. Canadian Technical Report of Hydrography and Ocean Sciences 223, iv+23 pp.

Moum, J.N., 1996. Efficiency of mixing in the main thermocline. Journal of Geophysical Research 101, 12057–12069. doi:10.1029/96JC00508.

Moum, J.N., Caldwell, D.R., Nash, J.D., Gunderson, G.D., 2002. Observations of boundary mixing over the continental slope. Journal of Physical Oceanography 32, 2113–2130. doi:10.1175/1520-0485(2002)032<2113:OOBMOT>2.0.CO;2.

Moum, J.N., Perlin, A., Klymak, J.M., Levine, M.D., Boyd, T., Kosro, P., 2004. Convectively driven mixing in the bottom boundary layer. Journal of Physical Oceanography 34, 2189–2202.

Muller-Karger, F.E., 2005. The importance of continental margins in the global carbon cycle. Geophysical Research Letters 32, L01602. doi:10.1029/2004GL021346.

Munk, W., Wunsch, C., 1998. Abyssal recipes II: energetics of tidal and wind mixing. Deep-Sea Research Part I 45, 1977–2010.

Munk, W.H., 1966. Abyssal Recipes. Deep-Sea Research 13, 707–730.

Nash, J.D., Moum, J.N., 2001. Internal hydraulic flows on the continental shelf: High drag states over a small bank. Journal of Geophysical Research 106, 4593–4611.

Nasmyth, P.W., 1970. Oceanic Turbulence. Phd thesis. University of Brithish Columbia.

Nepf, H.M., Geyer, W.R., 1996. Intratidal variations in stratification and mixing in the Hudson estuary. Journal of Geophysical Research 101, 12079–12086.

Osborn, T., 1974. Vertical profiling of velocity microstructure. Journal of Physical Oceanography 4, 109–115.

Osborn, T., 1980. Estimates of the local rate of vertical diffusion from dissipation measurements. Journal of Physical Oceanography 10, 83–89.

Ottersen, G., Alheit, J., Drinkwater, K.F., Friedland, K., Hagen, E., Stenseth, N.C., 2004. The responses of fish populations to ocean climate fluctuations, in: Stenseth, N.C., Ottersen, G., Hurrel, J.W., Belgrano, A. (Eds.), Marine ecosystems and climate variation. The North Atlantic: a comparative perspective. Oxford University Press, Oxford. chapter 6, pp. 73–94.

Ouellet, P., Olga, A., Bui, V., Lavoie, D., Chassé, J., Lambert, N., Ménard, N., Sirois, P., 2013. Seasonal distribution, abundance, and growth of larval capelin (*Mallotus villosus*) and the role of the Lower St. Lawrence Estuary (Gulf of St. Lawrence, Canada) as a nursery area. Canadian Journal of Fisheries and Aquatic Sciences 70, 1–23.

Palmer, M.R., Rippeth, T.P., Simpson, J.H., 2008. An investigation of internal mixing in a seasonally stratified shelf sea. Journal of Geophysical Research 113, 1–14. doi:10.1029/2007JC004531.

Peters, H., 1997. Observations of stratified turbulent mixing in an estuary: Neap-to-spring variations during high river flow. Estuarine, Coastal and Shelf Science 45, 69–88. doi:10.1006/ecss.1996.0180.

Petrie, B., Akenhead, S.A., Lazier, S.A., Loder, J., 1988. The cold intermediate layer on the Labrador and Northeast Newfoundland Shelves, 1978–86. NAFO Science Council Studies 12, 57–69.

Phillips, O.M., Shyu, J.H., Salmun, H., 1986. An experiment on boundary mixing: mean circulation and transport rates. Journal of Fluid Mechanics 173, 473–499.

Plourde, J., Therriault, J.C., 2004. Climate variability and vertical advection of nitrates in the Gulf of St. Lawrence, Canada. Marine Ecology Progress Series 279, 33–43. doi:10.3354/meps279033.

Plourde, S., Joly, P., Runge, J.A., Zakardjian, B., Dodson, J.J., 2001. Life cycle of *Calanus finmarchicus* in the lower St. Lawrence Estuary: The imprint of circulation and late timing of the spring phytoplankton bloom. Canadian Data Report of Fisheries and Ocean Sciences 58, 647–658.

Plourde, S., Joly, P., St-Amand, L., Starr, M., 2008. La station de monitorage de Rimouski: plus de 400 visites et 18 ans de monitorage et de recherche. Atlantic Zone Monitoring Program Bulletin , 51–55.

Plourde, S., Runge, J.A., 1993. Reproduction of the planktonic copepod *Calanus finmarchicus* in the Lower St. Lawrence Estuary: relation to the cycle of phytoplankton production and evidence for a *Calanus* pump. Marine Ecology Progress Series 102, 217–227. doi:10.3354/meps102217.

Redfield, A.C., Ketchum, B.H., Richards, F.A., 1963. The influence of organisms on the composition of sea water. The Sea, vol. 2 , 26–77.

Reissmann, J.H., Burchard, H., Feistel, R., Hagen, E., Lass, H.U., Mohrholz, V., Nausch, G., Umlauf, L., Wieczorek, G., 2009. Vertical mixing in the Baltic Sea and consequences for eutrophication – A review. Progress in Oceanography 82, 47–80. doi:10.1016/j.pocean.2007.10.004.

Richards, C., Bourgault, D., Galbraith, P.S., Hay, A., Kelley, D.E., 2013. Measurements of shoaling internal waves and turbulence in an estuary. Journal of Geophysical Research 118. doi:10.1029/2012JC008154.

Richardson, K., Visse, A., Pedersen, F., 2000. Subsurface phytoplankton blooms fuel pelagic production in the. Journal of Plankton Research 22, 1663–1671.

Rippeth, T.P., 2005. Mixing in seasonally stratified shelf seas: a shifting paradigm. Philosophical Transactions of the Royal Society A: Mathematical and Physical Sciences 363, 2837–54. doi:10.1098/rsta.2005.1662.

Rippeth, T.P., Wiles, P., Palmer, M.R., Sharples, J., Tweddle, J., 2009. The diapcynal nutrient flux and shear-induced diapcynal mixing in the seasonally stratified western Irish Sea. Continental Shelf Research 29, 1580–1587. doi:10.1016/j.csr.2009.04.009.

Rivkin, R., Legendre, L., Deibel, D., Tremblay, J.E., Klein, B., Crocker, K., Roy, S., Silverberg, N., Lovejoy, C., Mesplé, F., Romero, N., Anderson, M., Matthews, P., Savenkoff, C., Vezina, A., Therriault, J.C., Wesson, J., Berube, C., Ingram, R.G., 1996. Vertical Flux of Biogenic Carbon in the Ocean: Is There Food Web Control? Science 272, 1163–1166.

Rogachev, K.A., Carmack, E.C., Salomatin, A.S., 2000. Strong tidal mixing and ventilation of cold intermediate water at Kashevarov Bank, Sea of Okhotsk. Journal of Oceanography 56, 439–447.

Saucier, F.J., Chassé, J., 2000. Tidal circulation and buoyancy effects in the St. Lawrence Estuary. Atmosphere-Ocean 38, 505–556.

Saucier, F.J., Roy, F., Gilbert, D., 2003. Modeling the formation and circulation processes of water masses and sea ice in the Gulf of St. Lawrence, Canada. Journal of Geophysical Research 108. doi:10.1029/2000JC000686.

Saucier, F.J., Roy, F., Senneville, S., Smith, G.C., Lefaivre, D., Zakardjian, B., Dumais, J.F., 2009. Modélisation de la circulation dans l'estuaire et le golfe du Saint-Laurent en réponse aux variations du débit d'eau douce et des vents. Revue des sciences de l'eau 22, 159–176. doi:10.7202/037480ar.

Savenkoff, C., Vézina, A.F., Smith, P., Han, G., 2001. Summer transports of nutrients in the Gulf of St. Lawrence estimated by inverse modelling. Estuarine, Coastal and Shelf Science 52, 565–587. doi:10.1006/ecss.2001.0774.

Schafstall, J., Dengler, M., Brandt, P., Bange, H., 2010. Tidal-induced mixing and diapycnal nutrient fluxes in the Mauritanian upwelling region. Journal of Geophysical Research 115, C10014. doi:10.1029/2009JC005940.

Sharples, J., Moore, C.M., Abraham, R., 2001a. Internal tide dissipation, mixing, and vertical nitrate flux at the shelf edge of NE New Zealand. Journal of Geophysical Research 106, 14,069–14,081.

Sharples, J., Moore, C.M., Rippeth, T.P., Holligan, P.M., Hydes, D.J., Fisher, N.R., Simpson, J.H., 2001b. Phytoplankton distribution and survival in the thermocline. Limnology and Oceanography 46, 486–496. doi:10.4319/lo.2001.46.3.0486.

Sharples, J., Tweddle, J.F., Green, J.A.M., Palmer, M.R., 2007. Spring-neap modulation of internal tide mixing and vertical nitrate fluxes at a shelf edge in summer. Limnology and Oceanography 52, 1735–1747.

Shih, L.H., Koseff, J.R., Ivey, G.N., Ferziger, J.H., 2005. Parameterization of turbulent fluxes and scales using homogeneous sheared stably stratified turbulence simulations. Journal of Fluid Mechanics 525, 193–214. doi:10.1017/S0022112004002587.

Sime-Ngando, T., Gosselin, M., Roy, S., Chanut, J.P., 1995. Significance of planktonic ciliated protozoa in the Lower St. Lawrence Estuary: comparison with bacterial, phytoplankton, and particulate organic carbon. Aquatic Microbial Ecology 9, 243–258.

Sinclair, M., 1978. Summer phytoplankton variability in the Lower St. Lawrence Estuary. Journal of Fisheries Research Board of Canada 35, 1171–1185.

Sinclair, M., El-Sabh, M.I., Brindle, J.R., 1976. Seaward nutrient transport in the Lower St. Lawrence Estuary. Journal of Fisheries Research Board of Canada 33, 1271–1277.

Slinn, D.N., Riley, J.J., 1996. Turbulent mixing in the oceanic boundary layer caused by internal wave reflection from sloping terrain. Dynamics of Atmospheres and Oceans 24, 51–62.

Smith, G.C., 2005. The Gulf of St. Lawrence in winter: tides, mixing and watermass transformation. Ph.D. thesis. McGill University.

Smith, G.C., Saucier, F.J., Straub, D., 2006a. Formation and circulation of the cold intermediate layer in the Gulf of Saint Lawrence. Journal of Geophysical Research 111. doi:10.1029/2005JC003017.

Smith, G.C., Saucier, F.J., Straub, D., 2006b. Response of the Lower St. Lawrence Estuary to external forcing in winter. Journal of Physical Oceanography 36, 1485–1501.

Smyth, W.D., Moum, J.N., Caldwell, D.R., 2001. The efficiency of mixing in turbulent patches: Inferences from direct simulations and microstructure observations. Journal of Physical Oceanography 31, 1969–1992.

Soulsby, R., 1997. Dynamics of marine sands: a manual for practical applications. Thomas Telford.

St. Laurent, L.C., 2002. Estimating tidally driven mixing in the deep ocean. Geophysical Research Letters 29, 2106. doi:10.1029/2002GL015633.

Starr, M., St-Amand, L., Devine, L., Bérard-Therriault, L., Galbraith, P.S., 2004. State of phytoplankton in the Estuary and Gulf of St. Lawrence during 2003. Canadian Science Advisory Secretariat, Fisheries and Oceans Canada 2004/123, ii + 31 pp.

Steven, D.M., 1971. International Biological Program study of the Gulf of St. Lawrence, in: Hassan, E.M. (Ed.), Proceedings of the 2nd Gulf of St. Lawrence Workshop. Bedford Institute of Oceanography, Dartmouth, N. S., pp. 146–159.

Steven, D.M., 1974. Primary and secondary production in the Gulf of St. Lawrence. report 26. McGill University, Marine Sciences Centre.

Stewart, R.W., Grant, H.L., 1999. Early measurements of turbulence in the ocean: Motives and techniques. Journal of Atmospheric and Oceanic Technology 16, 1467–1473. doi:10.1175/1520-0426(1999)016<1467:EMOTIT>2.0.CO;2.

Stigebrandt, A., 1976. Vertical diffusion driven by internal waves in a sill fjord. Journal of Physical Oceanography 6, 486–495.

Stigebrandt, A., 1979. Observational evidence for vertical diffusion driven by internal waves of tidal origin in the Oslofjord. Journal of Physical Oceanography 9, 435–441.

Sundfjord, A., Fer, I., Kasajima, Y., Svendsen, H., 2007. Observations of turbulent mixing and hydrography in the marginal ice zone of the Barents Sea. Journal of Geophysical Research 112. doi:10.1029/2006JC003524.

Tamdrari, H., Castonguay, M., Brêthes, J.C., Galbraith, P.S., Duplisea, D.E., 2012. The dispersal pattern and behaviour of Atlantic cod (*Gadus morhua*) in the northern Gulf of St. Lawrence: results from tagging experiments. Canadian Journal of Fisheries and Aquatic Sciences 69, 112–121. doi:10.1139/F2011-137.

Tang, C.L., 1980. Mixing and circulation in the northwestern Gulf of St. Lawrence: A study of a buoyancy driven current system. Journal of Geophysical Research 25, 2787–2796.

Taylor, G.I., 1921. Tidal oscillations in gulfs and rectangular basins. Proceedings of the London Mathematical Society 20, 148–181.

Taylor, G.I., 1935. Statistical theory of turbulence. Proceedings of the Royal Society A: Mathematical, Physical and Engineering Sciences 151, 421–444. doi:10.1098/rspa.1935.0158.

Taylor, G.I., 1938. The spectrum of turbulence. Proceedings of the Royal Society A 164, 476–490. doi:10.1098/rspa.1938.0032.

Taylor, J.R., Ferrari, R., 2011. Shutdown of turbulent convection as a new criterion for the onset of spring phytoplankton blooms. Limnology and Oceanography 56, 2293–2307. doi:10.4319/lo.2011.56.6.2293.

Therriault, J.C., Lacroix, G., 1976. Nutrients, chlorophyll, and internal tides in the St. Lawrence Estuary. Journal of Fisheries Research Board of Canada 33, 2747–2757.

Therriault, J.C., Levasseur, M.E., 1985. Control of phytoplankton production in the Lower St. Lawrence Estuary: Light and freshwater runoff. Le Naturaliste Canadien 112, 77–96.

Thomas, H., Bozec, Y., Elkalay, K., de Baar, H.J.W., 2004. Enhanced open ocean storage of CO_2 from shelf sea pumping. Science 304, 1005–1008. doi:10.1126/science.1095491.

Thorpe, S.A., 1977. Turbulence and mixing in a Scottish loch. Philosophical Transactions of the Royal Society A: Mathematical and Physical Sciences 286, 125–181.

Thorpe, S.A., 2005. The turbulent ocean. Cambridge University Press, New York.

Thorpe, S.A., 2007. An Introduction to Ocean Turbulence. First ed., Cambridge University Press, New York.

Toole, J., Schmitt, R., Polzin, K., Kunze, E., 1997. Near-boundary mixing above the flanks of a midlatitude seamount. Journal of Geophysical Research 102, 947–959.

Toole, J.M., Polzin, K.L., Schmitt, R.W., 1994. Estimates of diapycnal mixing in the abyssal ocean. Science 264, 1120–1123.

Tremblay, J.E., Legendre, L., Klein, B., Therriault, J.C., 2000. Size-differential uptake of nitrogen and carbon in a marginal sea (Gulf of St. Lawrence, Canada): significance of diel periodicity and urea uptake. Deep Sea Research Part II: Topical Studies in Oceanography 47, 489–518.

Tsunogai, S., Watanabe, S., Sato, T., 1999. Is there a "continental shelf pump" for the absoprtion of atmospheric CO_2. Tellus 51B, 701–712.

Tuzhilkin, V.S., 2008. Thermohaline structure of the sea, in: Kostianoy, A.G., Kosarev, A.N. (Eds.), The Black Sea Environment. Springer-Verlag, Berlin Heidelberg. volume 5Q of *The Handbook of Environmental Chemistry*, pp. 217–253. doi:10.1007/698_5_077.

Umlauf, L., Burchard, H., 2005. Second-order turbulence closure models for geophysical boundary layers. A review of recent work. Continental Shelf Research 25, 795–827. doi:10.1016/j.csr.2004.08.004.

Vézina, A.F., 1994. Mesoscale variability in nitrogen uptake rates and the f-ratio during a coastal phytoplankton bloom. Limnology and Oceanography 39, 854–868.

Walter, R.K., Woodson, C.B., Arthur, R.S., Fringer, O.B., Monismith, S.G., 2012. Nearshore internal bores and turbulent mixing in southern Monterey Bay. Journal of Geophysical Research 117, C07017. doi:10.1029/2012JC008115.

Wang, J., Ingram, R.G., Mysak, L.A., 1991. Variability of internal tides in the Laurentian Channel. Journal of Geophysical Research 96, 16859–16875. doi:10.1029/91JC01580.

Williams, C., Sharples, J., Mahaffey, C., Rippeth, T.P., 2013. Wind-driven nutrient pulses to the subsurface chlorophyll maximum in seasonally stratified shelf seas. Geophysical Research Letters 40, 1–6. doi:10.1002/2013GL058171.

Wolk, F., Yamazaki, H., Seuront, L., Lueck, R.G., 2002. A New Free-Fall Profiler for Measuring Biophysical Microstructure. Journal of Atmospheric and Oceanic Technology 19, 780–793. doi:10.1175/1520-0426(2002)019<0780:ANFFPF>2.0.CO;2.

Wollast, R., 1998. Evaluation and comparison of the global carbon cycle in the coastal zone and in the open ocean, in: Brink, K.H., Robinson, A.R. (Eds.), The Sea, vol. 10. John Wiley and Sons, Inc.. chapter 9, pp. 213–252.

Wunsch, C., 2000. Moon, tides and climate. Nature 405, 743–4. doi:10.1038/35015639.

Wunsch, C., Ferrari, R., 2004. Vertical Mixing, Energy, and the General Circulation of the Oceans. Annual Review of Fluid Mechanics 36, 281–314. doi:10.1146/annurev.fluid.36.050802.122121.

Yamazaki, H., Osborn, T., 1990. Dissipation estimates for stratified turbulence. Journal of Geophysical Research 95, 9739–9744.

ANNEXE A

CALCUL DU TAUX DE DISSIPATION DE L'ÉNERGIE CINÉTIQUE TURBULENTE À PARTIR DU CISAILLEMENT

Au cours du doctorat, une bibliothèque de fonctions MATLAB permettant d'obtenir les profils de diverses variables pertinentes à nos recherches à partir des données brutes du VMP a été développée. La bibliothèque est disponible sur un dépôt *SVN* à accès restreint situé à l'adresse: http://demeter.uqar.ca/svn/VMP_library/ISMER. Les fonctions principales qui permettent le passage des données brutes du VMP vers les données physiques portent le préfixe *vmp*:

- vmp_dewey_opti.m
- vmp_p2mat.m
- vmp_p2profiles.m
- vmp_shear2epsilon.m
- vmp_shear_analysis.m
- vmp_shear_preanalysis.m
- vmp_spectral_integration.m
- vmp_splitProfiles.m

L'obtention des profils du taux de dissipation de l'énergie cinétique turbulente (ϵ) à partir du cisaillement s'effectue avec la fonction *vmp_shear2epsilon.m*. Le calcul pour chaque profil

s'effectue lors de l'appel des fonctions sous-imbriquées *vmp_shear_analysis.m* → *vmp_spectral_integration.m* → *vmp_dewey_opti.m*. Cette annexe explique la procédure d'intégration spectrale qui permet d'obtenir ϵ à partir d'un spectre du cisaillement.

Quelques éléments de théorie

Bien que la turbulence soit un phénomène en trois dimensions, il est possible de démontrer qu'en conditions isotropiques le taux de dissipation de l'énergie cinétique turbulente (ϵ) se calcule uniquement à partir de la composante verticale du cisaillement ($\frac{\partial u}{\partial z}$, voir démonstration en annexe II):

$$\epsilon = \frac{15\nu}{2}\overline{\left(\frac{\partial u}{\partial z}\right)^2}. \tag{4.1}$$

Ici $\nu = f(T)$ est la viscosité cinématique moléculaire de l'eau de mer (en $m^2\,s^{-1}$) calculée en fonction de la température, et $\overline{\left(\frac{\partial u}{\partial z}\right)^2}$ représente la variance du cisaillement vertical mesuré par le VMP. Au sens propre, la ligne de surlignement indique une *moyenne d'ensemble* sur plusieurs mesures indépendantes du cisaillement. Pour des raisons pratiques et étant donné l'évolution rapide de la turbulence, il est impossible de reproduire plusieurs fois le même échantillonnage. Deux hypothèses nous permettent de subsituer la moyenne d'ensemble par une moyenne spatiale sur des *bins* veticaux. Tout d'abord, nous supposons que sur une certaine portion de la colonne d'eau, de l'épaisseur des bins verticaux choisis, la turbulence est spatialement homogène, c'est-à-dire, la distribution statistique des tourbillons demeure la même. De plus, nous supposons que la turbulence est "gelée" pendant le temps que prend le profileur pour traverser ces bins verticaux. En anglais, cette hypothèse est connu sous le nom de *Taylor's frozen turbulence hypothesis* (Taylor, 1938). Ces deux hypothèses permettent de supposer que l'échantillonnage s'effectue instantanément sur une portion homogène de la colonne d'eau, ce qui est équivalent à obtenir un ensemble de plusieurs échantillons de

la *même* turbulence.

Bien que l'équation 4.1 soit exacte, elle pose un problème pratique puisque la variance du signal mesuré par la sonde est contaminé en partie par le "bruit" aléatoire de l'appareil, c'est-à-dire, les vibrations induites par la descente de l'appareil dans la colonne d'eau. En traitement de signal, l'identité de Parseval est généralement utilisée afin d'éliminer ce problème (Emery and Thomson, 2001). Cette identité nous dit que la variance d'un signal est équivalente à l'intégrale de la densité spectrale de ce signal. Dans le cas présent, ceci se résume à l'équation suivante:

$$\overline{\left(\frac{\partial u}{\partial z}\right)^2} = \int_0^\infty \phi(k)dk, \tag{4.2}$$

où $\phi(k)$ est la densité spectrale (*power spectral density*) du signal $\frac{\partial u}{\partial z}$ et k le nombre d'onde vertical exprimé en m^{-1} (ou en *cycle par mètre*, cpm).

Les profileurs de turbulence sont conçus afin de repousser le bruit aléatoire vers les grands nombres d'onde (fines longueur d'onde) afin de minimiser le bruit dans la portion *révélatrice* du signal. Il est donc possible de se débarasser de ce bruit en intégrant le signal entre deux nombres d'onde k_1 et k_2 correspondant aux bornes du signal que l'on veut extraire:

$$\overline{\left(\frac{\partial u}{\partial z}\right)^2} \simeq \int_{k_1}^{k_2} \phi(k)dk. \tag{4.3}$$

Pour comprendre comment cela est possible, il faut savoir que la distribution de l'énergie entre les différentes échelles de la turbulence tri-dimensionnelle s'effectue selon un spectre de forme unique. Ce résultat fut proposé par Kolmogorov (1941). Ce dernier suggéra une cascade d'énergie où les plus gros tourbillons transfèrent leur énergie aux plus petits et ainsi de suite jusqu'à une échelle assez petite pour que la viscosité de l'eau de mer dissipe l'énergie sous forme de chaleur. L'échelle où la viscosité devient importante s'appelle l'échelle de Kol-

mogorov $l_K = \left(\frac{\nu^3}{\epsilon}\right)^{1/4}$ (en m). Une forme empirique de ces spectres fut suggérée par Nasmyth (1970). Selon ce modèle, l'augmentation de ϵ, pour une viscosité constante, se traduit par une translation de la courbe du spectre dans le domaine spectral de sorte que la puissance associée augmente tout en décalant la variance vers les plus petites échelles spatiale (voir la série de spectres noir sur la figure 44). Autrement dit, plus le taux de dissipation augmente, plus l'échelle à laquelle la viscosité de l'eau de mer peut dissiper l'énergie sous forme de chaleur est petite (plus grand nombre d'onde).

Cette information sur le spectre empirique en fonction de la valeur de ϵ que l'on cherche à déterminer est donc utile pour permettre de déterminer les limites d'intégration. La prochaine section présente l'algorithme qui permet d'identifier k_1 et k_2, les nombres d'onde entre lesquels le signal est intégré.

Algorithme de calcul pour l'intégration spectrale

L'algorithme utilisé pour identifier les limites d'intégration et corriger ϵ pour la perte de variance provenant de la troncation du spectre provient d'une fonction MATLAB (originalement *epsilon_vmp.m*) écrite par Richard K. Dewey et généreusement fournie à Daniel Bourgault pour le traitement des profils du VMP. Cette fonction a été complètement réécrite et adaptée à nos besoins, et seulement la portion itérative qui permet d'identifier les limites d'intégrations à été conservée dans une nouvelle fonction (*vmp_dewey_opti.m*).

Une fois les données de cisaillement nettoyées et corrigées pour les vibrations du profileur et pour la réponse spatiale des sondes de cisaillement (Macoun and Lueck, 2004), un spectre du cisaillement est calculé pour chaque bin vertical à l'intérieur de la fonction *vmp_spectral_integration.m*. Pour chaque spectre, la fonction *vmp_dewey_opti.m* retourne la meilleure estimation de ϵ.

À cause de la grosseur des sondes de cisaillement utilisées (de l'ordre du centimètre), on

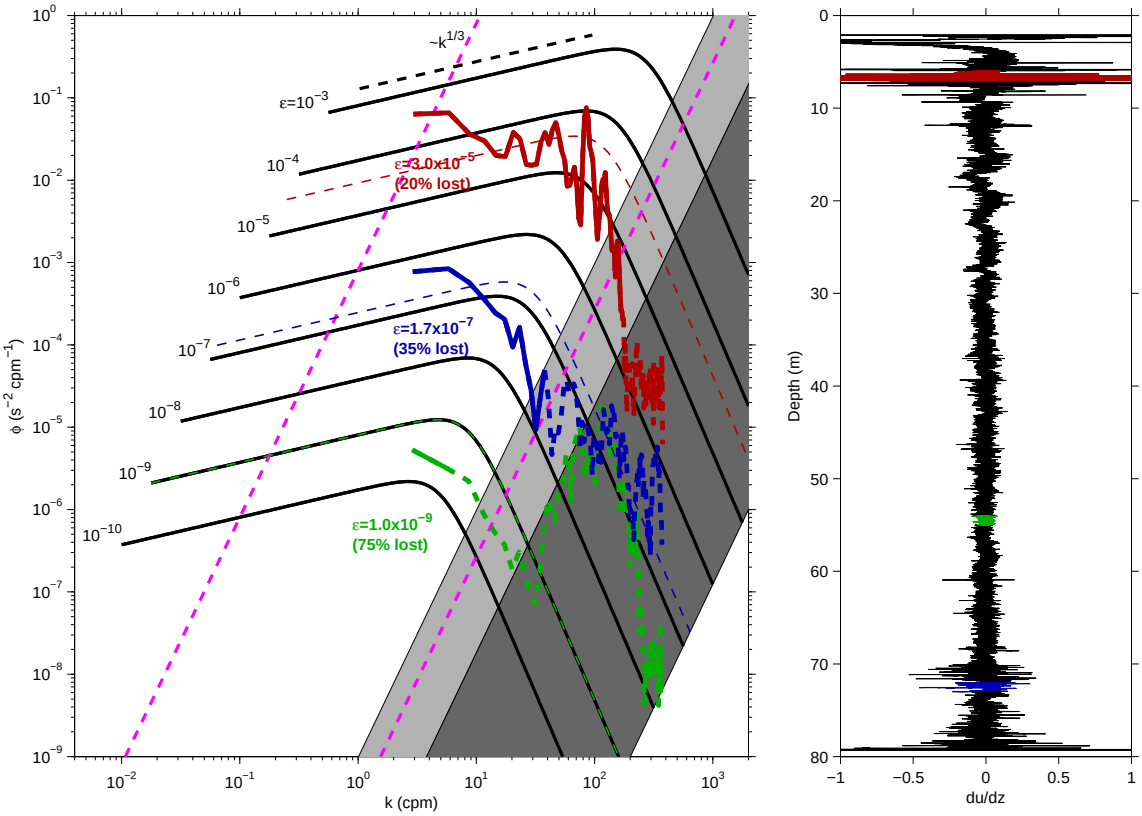

Figure 44: Domaine spectrale du cisaillement. (à gauche) Spectres empiriques de Nasmyth (1970) (en noir) pour différentes valeur du taux de dissipation ($\epsilon \in [10^{-10}, 10^{-3}]\,\mathrm{W\,kg^{-1}}$). Ces spectres sont calculés selon une fonction analytique présentée en annexe de Wolk et al. (2002). La ligne noire tiretée montre la portion du spectre qui croit proportionellement à $k^{1/3}$ selon la théorie de Kolmogorov (1941). La portion ombragée foncée contient les échelles où se produit la dissipation visqueuse, c-à-d, les nombres d'onde plus grands que le nombre d'onde de Kolmogorov (k_s). La portion qui n'est pas ombragée correspond à la portion des spectres qui contiennent 90% de la variance en dehors de le dissipation visqueuse. Les lignes tiretées majenta délimitent l'intervalle $10^{-3} \leq \frac{k}{k_s} \leq 10^{-1}$. Les spectres du cisaillement pour trois bins verticaux choisis pour un profil datant du 22 septembre 2011 à 14h54 sont aussi présentés. Les intervalles verticaux choisis pour ces bins sont respectivement 6-7 m, 54-55 m et 72-73 m pour les spectres rouge, vert et bleu (voir profil du cisaillement sur le panneau de droite). La portion de ces spectres en traits pleins indique la portion sur laquelle chaque spectre a été intégré. La valeur de epsilon calculée et le pourcentage de la variance perdue (entre parenthèses) sont indiqués sous chacun de ces spectres. Les spectres de Nasmyth correspondant aux trois valeurs de epsilon calculées sont montrés en traits tiretés fins de couleur correspondante aux spectres bruts. Le panneau de gauche est largement inspiré de la figure 13 de Wolk et al. (2002).

ne peut généralement pas résoudre le spectre du cisaillement jusqu'à l'échelle de Kolmogorov (de l'ordre du millimètre). Dépendamment du taux de dissipation, la plus petite échelle que nous pouvons espérer résoudre est de l'ordre de 5 à 10 fois l_K (Thorpe, 2005). De l'autre côté du spectre, on peut penser qu'à partir d'une certaine grosseur des tourbillons qui composent la turbulence, le profileur en chute libre peut être entrainé par ceux-ci. La dimension physique du profileur (de l'ordre du mètre) place donc une limitation sur les plus grandes échelles pouvant être résolues, c'est-à-dire, une centaine de fois l'échelle de Kolmogorov. Ces limitations posent donc les extremums de l'intervalle sur lequelle les limites d'intégration du spectre doivent être cherchée. Par commodité et à cause de la façon dont le spectre est calculé (le facteur 2π provient du calcul du spectre), l'algorithme recherche les limites d'intégration pour les nombres d'onde k à l'intérieur de l'intervalle $2\pi \times 10^{-3} \leq \frac{k}{k_s} \leq 2\pi \times 10^{-1}$, ou en terme de longueur: $1.6 l_k \leq \frac{1}{k} \leq 160 l_k$. Si k est exprimé en cpm, le nombre d'onde de Kolmogorov est égal à $k_s = \frac{1}{2\pi}\left(\frac{\epsilon}{\nu^3}\right)^{\frac{1}{4}}$ (en cpm). L'intervalle pour la recherche des limites d'intégration est délimité par les lignes majenta pointillées sur la figure 44.

Lorsque la dissipation est forte, la puissance du spectre est généralement au dessus du bruit. Il arrive cependant, lorsque la dissipation est faible, que le signal soit plus faible que le bruit de l'appareil. Une comparaison entre les profils rouge et vert de la figure 44 illustre ceci: à $k \sim 10^2$ cpm, le bruit semble atteindre $\phi \sim 10^{-5}\,\mathrm{s}^{-2}\,\mathrm{cpm}^{-1}$, c'est-à-dire, au dessus du signal en vert, mais bien en dessous du signal en rouge. Pour cette raison, l'algorithme resserre l'intervalle de recherche autour de la crète du spectre pour les plus faibles dissipations et cet intervalle s'élargit lorsque la dissipation augmente. La recherche incrémentale s'effectue comme suit (notons que pour simplifier l'écriture, $\tilde{k}_s = \frac{k_s}{2\pi}$):

Boucle 1: On suppose au départ que $\epsilon_0 = 10^{-9}\,\mathrm{W\,kg}^{-1}$ et que 25% de la variance est résolue ($lost = \frac{1}{25\%} = 4$)

1. Choix des limites d'intégration selon ϵ_0:

$$\begin{aligned}
\epsilon_0 < 10^{-9} &\rightarrow k_1 = 1.5 \times 10^{-2}\tilde{k}_s \text{ et } k_2 = 3 \times 10^{-2}\tilde{k}_s \\
10^{-9} \leq \epsilon_0 \leq 10^{-8} &\rightarrow k_1 = 1.5 \times 10^{-2}\tilde{k}_s \text{ et } k_2 = 5 \times 10^{-2}\tilde{k}_s \\
10^{-8} \leq \epsilon_0 \leq 10^{-7} &\rightarrow k_1 = 8 \times 10^{-3}\tilde{k}_s \text{ et } k_2 = 7 \times 10^{-2}\tilde{k}_s \\
10^{-7} \leq \epsilon_0 \leq 10^{-6} &\rightarrow k_1 = 3 \times 10^{-3}\tilde{k}_s \text{ et } k_2 = 9 \times 10^{-2}\tilde{k}_s \\
\epsilon_0 > 10^{-6} &\rightarrow k_1 = 1 \times 10^{-3}\tilde{k}_s \text{ et } k_2 = 1 \times 10^{-1}\tilde{k}_s
\end{aligned}$$

2. **Boucle 2:**
   2.1. Calcul de k_s en fonction de ϵ_0
   2.2. Détermination de k_1 et k_2 selon le point 1
   2.3. Calcul de $\epsilon_1 = \frac{15\nu}{2} \int_{k_1}^{k_2} \phi(k)dk$ (équations 4.1 et 4.3)
   2.4. Correction pour la variance perdue: $\epsilon_2 = \epsilon_1 \times lost$
   2.5. **Boucle 3:**
      2.5.1. Génération d'un spectre de Nasmyth à partir de ϵ_2
      2.5.2. Mise à jour de la variance perdue provenant de la troncation du spectre en calculant la variance du spectre de Nasmyth qui est présente entre k_1 et k_2
      2.5.3. Mise à jour de $\epsilon_2 = \epsilon_1 \times lost$ avec la nouvelle estimation de la variance perdue obtenue en 2.5.2
      2.5.4. Fin boucle 3
   2.6. Mise à jour de $\epsilon_2 = \epsilon_1 \times lost$ avec la nouvelle estimation de la variance perdue obtenue en 2.5.2
   2.7. Mise à jour de la meilleure estimation de la dissipation: $\epsilon_0 = \epsilon_2$
   2.8. Fin boucle 2
3. Fin boucle 1: ϵ_0 est la meilleure estimation de la dissipation.

Les boucles 1 et 2 sont exécutées quatres fois chacune et la boucle 3 est itérée deux fois. Habituellement, la valeur de ϵ après deux itérations de la boucle 1 est très près de l'estimé final. Il serait possible d'inclure un critère d'arrêt pour économiser du temps de calcul, mais cela n'a pas été fait pendant la thèse.

La progression au travers des étapes décrites ci-dessus est illustrée par les figures 45 et 46. Celles-ci montrent les spectres rouge et vert de la figure 44 et la convergence vers leur valeur de dissipation calculée par l'algorithme.

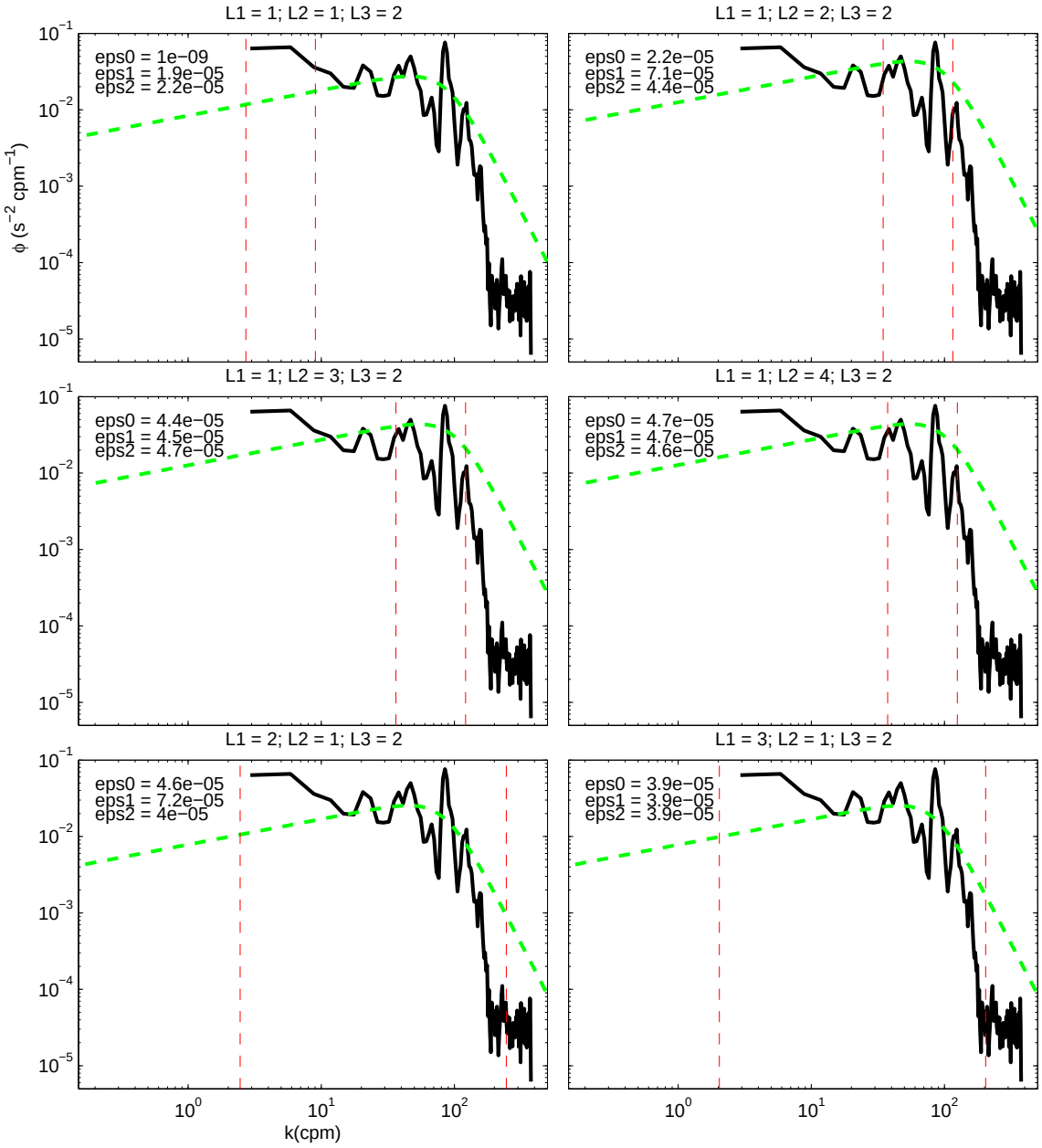

Figure 45: Illustration de l'algorithme itératif permettant d'obtenir ϵ par intégration spectrale. En noir: le spectre du cisaillement correspondant à celui en rouge de la figure 44. En rouge: les limites d'intégrations obtenues au points 2.2 de l'algorithme présenté ci-dessus. En vert, le spectre de Nasmyth correspondant à ϵ_2 et calculé en 2.5.2. Les valeurs ϵ_0, ϵ_1 et ϵ_2 après la mise à jour du point 2.6 sont présentées sur chaque panneau. Chaque panneau correspond à une itération identifiée dans le titre (ex: L1=1; L2=1 et L3=2 signifie première itération des boucles 1 et 2 et deuxième itération de la boucle 3). Seulement les deuxièmes itérations de la boucle 3 sont présentées. Les quatres premiers panneaux proviennent de la première itération de la boucle 1 alors qu'un seul panneau pour les itérations deux et trois de cette boucle est présenté ensuite (aucun panneau n'est présenté pour la quatrième itération de la boucle 1, l'algorithme ayant déjà convergé).

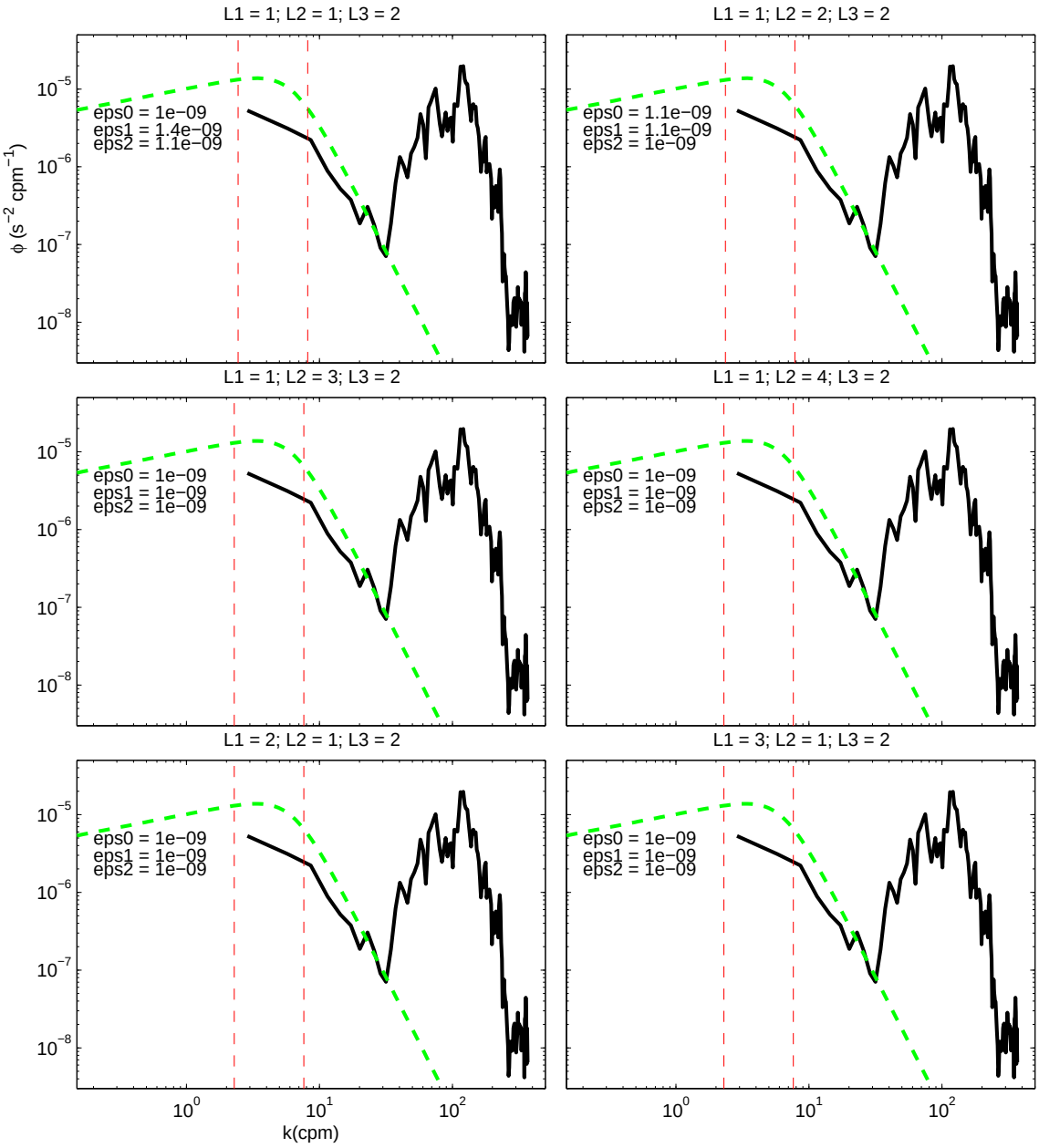

Figure 46: Similaire à la figure 45, mais pour le spectre en vert de la figure 44.

ANNEXE B

EXPRESSION DU TAUX DE DISSIPATION DE L'ÉNERGIE CINÉTIQUE TURBULENTE EN CONDITIONS ISOTROPIQUES

Dans cette annexe, il est démontré un résultat fondamental de la turbulence en conditions isotropiques, c'est-à-dire, que le taux de dissipation de l'énergie cinétique turbulente peut être exprimé seulement en fonction du cisaillement vertical des vitesses horizontales ($\frac{\partial u}{\partial z}$):

$$\epsilon = \frac{15\nu}{2}\overline{\left(\frac{\partial u}{\partial z}\right)^2}, \tag{5.1}$$

où ν est la viscosité cinématique de l'eau de mer. Cette démonstration faisait partie de quelques exercices (préparatoires!) suggérés par Daniel Bourgault au début du doctorat pour me familiariser avec la turbulence. Bien que ce résultat soit bien connu et accepté dans la littérature, une démonstration *claire* est pratiquement impossible à trouver. Parmi les références souvent citées pour cette démonstration, notons Hinze (1959, 1975) et Yamazaki and Osborn (1990), mais plusieurs étapes de la démonstration sont omises dans ces travaux et il est souvent très difficile de comprendre les étapes qui mènent à ce résultat. Il faut remonter à Taylor (1935) pour trouver la première démonstration *complète* de ce résultat. Cette annexe reprend donc la démonstration de Taylor (1935), tout en modifiant quelque peu la façon de faire afin de tenter de rendre la démonstration plus accessible.

Taux de dissipation de l'énergie cinétique turbulente

Pour ce faire, partons de l'équation générale du taux de dissipation de l'énergie cinétique turbulence (ϵ, ci-après appelé la *dissipation*) qui apparait dans l'équation de l'énergie cinétique des fluctuations turbulentes après la décomposition de Reynolds (p. ex., Kundu and Cohen, 2007, équations 13.34 et 13.37):

$$\epsilon = 2\nu\overline{e_{ij}e_{ij}}. \tag{5.2}$$

Ici la notation tensorielle est utilisée avec $e_{ij} = \frac{1}{2}\left(\frac{\partial u_i}{\partial x_j} + \frac{\partial u_j}{\partial x_i}\right)$ le tenseur des contraintes. Les variables u_i et u_j sont donc respectivement les fluctuations de vitesse en trois dimensions ($i, j = [1, 2, 3]$). Plus explicitement, le développement de cette notation donne la double sommation suivante:

$$\epsilon = \sum_{i=1}^{3}\sum_{j=1}^{3}\frac{\nu}{2}\overline{\left(\frac{\partial u_i}{\partial x_j} + \frac{\partial u_j}{\partial x_i}\right)\left(\frac{\partial u_i}{\partial x_j} + \frac{\partial u_j}{\partial x_i}\right)} = \sum_{i=1}^{3}\sum_{j=1}^{3}\frac{\nu}{2}\overline{\left(\frac{\partial u_i}{\partial x_j} + \frac{\partial u_j}{\partial x_i}\right)^2}. \tag{5.3}$$

L'expansion de la dernière expression donne en réalité 9 termes au carré. Pour une meilleure lecture des termes, la notation usuelle en x, y, z est utilisée:

$$\begin{aligned}
\epsilon \;=\; & \frac{\nu}{2}\Bigg[\overline{\left(\frac{\partial u}{\partial x} + \frac{\partial u}{\partial x}\right)^2} + \overline{\left(\frac{\partial u}{\partial y} + \frac{\partial v}{\partial x}\right)^2} + \overline{\left(\frac{\partial u}{\partial z} + \frac{\partial w}{\partial x}\right)^2} \\
& + \overline{\left(\frac{\partial v}{\partial x} + \frac{\partial u}{\partial y}\right)^2} + \overline{\left(\frac{\partial v}{\partial y} + \frac{\partial v}{\partial y}\right)^2} + \overline{\left(\frac{\partial v}{\partial z} + \frac{\partial w}{\partial y}\right)^2} \\
& + \overline{\left(\frac{\partial w}{\partial x} + \frac{\partial u}{\partial z}\right)^2} + \overline{\left(\frac{\partial w}{\partial y} + \frac{\partial v}{\partial z}\right)^2} + \overline{\left(\frac{\partial w}{\partial z} + \frac{\partial w}{\partial z}\right)^2}\Bigg].
\end{aligned}$$

Une fois les carrés développés, l'équation comporte 27 termes qu'il faudra symplifier:

$$
\begin{aligned}
\epsilon &= \frac{\nu}{2}\Bigg[4\overline{\left(\frac{\partial u}{\partial x}\right)^2} \\
&+ \overline{\left(\frac{\partial u}{\partial y}\right)^2} + 2\overline{\frac{\partial u}{\partial y}\frac{\partial v}{\partial x}} + \overline{\left(\frac{\partial v}{\partial x}\right)^2} \\
&+ \overline{\left(\frac{\partial u}{\partial z}\right)^2} + 2\overline{\frac{\partial u}{\partial z}\frac{\partial w}{\partial x}} + \overline{\left(\frac{\partial w}{\partial x}\right)^2} \\
&+ \overline{\left(\frac{\partial v}{\partial x}\right)^2} + 2\overline{\frac{\partial v}{\partial x}\frac{\partial u}{\partial y}} + \overline{\left(\frac{\partial u}{\partial y}\right)^2} \\
&+ \overline{4\left(\frac{\partial v}{\partial y}\right)^2} \\
&+ \overline{\left(\frac{\partial v}{\partial z}\right)^2} + 2\overline{\frac{\partial v}{\partial z}\frac{\partial w}{\partial y}} + \overline{\left(\frac{\partial w}{\partial y}\right)^2} \\
&+ \overline{\left(\frac{\partial w}{\partial x}\right)^2} + 2\overline{\frac{\partial w}{\partial x}\frac{\partial u}{\partial z}} + \overline{\left(\frac{\partial u}{\partial z}\right)^2} \\
&+ \overline{\left(\frac{\partial w}{\partial y}\right)^2} + 2\overline{\frac{\partial w}{\partial y}\frac{\partial v}{\partial z}} + \overline{\left(\frac{\partial v}{\partial z}\right)^2} \\
&+ \overline{4\left(\frac{\partial w}{\partial z}\right)^2}\Bigg].
\end{aligned}
$$

Dans cette équation, déjà certains termes se répètent, et en les regroupant on peut réécrire l'équation:

$$
\begin{aligned}
\epsilon = \nu\Bigg[&2\overline{\left(\frac{\partial u}{\partial x}\right)^2} + 2\overline{\left(\frac{\partial v}{\partial y}\right)^2} + 2\overline{\left(\frac{\partial w}{\partial z}\right)^2} \\
&+ \overline{\left(\frac{\partial u}{\partial y}\right)^2} + \overline{\left(\frac{\partial v}{\partial x}\right)^2} + \overline{\left(\frac{\partial u}{\partial z}\right)^2} + \overline{\left(\frac{\partial w}{\partial x}\right)^2} + \overline{\left(\frac{\partial v}{\partial z}\right)^2} + \overline{\left(\frac{\partial w}{\partial y}\right)^2} \\
&+ 2\overline{\frac{\partial u}{\partial y}\frac{\partial v}{\partial x}} + 2\overline{\frac{\partial u}{\partial z}\frac{\partial w}{\partial x}} + 2\overline{\frac{\partial v}{\partial z}\frac{\partial w}{\partial y}}\Bigg].
\end{aligned}
\tag{5.4}
$$

Considérations pour l'isotropie

Avant d'entrer plus en détails dans le développement de l'équation précédente, voici quelques considérations importantes à faire dans le cas de l'isotropie. Tout d'abord, l'isotropie pour la turbulence signifie que celle-ci n'a pas d'axe de développement préférentiel. Autrement dit, la turbulence est symétrique et invariante peu importe le système d'axe utilisé. Cette hypothèse pour la turbulence océanique tri-dimensionnelle est généralement valable lorsque celle-ci est dite *pleinement développée*. Par contre, lorsque la turbulence est faible, ou la stratification forte, cette hypothèse peut être faussée. Il est généralement admis que turbulence est isotropique lorsque le critère $\frac{\epsilon}{\nu N^2} \geq 200$ est respecté (Gargett et al., 1984; Thorpe, 2005). Dans la dernière équation, $N^2 = \frac{-g}{\rho}\frac{\partial \rho}{\partial z}$ est la fréquence de flottabilité au carré, ρ la densité de l'eau de mer et g l'accélératiopn gravitationelle.

Dans cette section, quelques propriétés du système d'axe en isotropie seront développées. Ces propriétés serviront par la suite à simplifier l'équation 5.4.

Symétrie de la turbulence isotropique

Comme il a été mentionné précédemment, la turbulence isotropique est symétrique. Cela signifie que les taux de déformation des contraintes normales (éq. 5.5), de cisaillement (éq. 5.6) et transversales (éq. 5.7) doivent d'être égales dans toutes les directions:

$$\overline{\left(\frac{\partial u}{\partial x}\right)^2} = \overline{\left(\frac{\partial v}{\partial y}\right)^2} = \overline{\left(\frac{\partial w}{\partial z}\right)^2} \tag{5.5}$$

$$\overline{\left(\frac{\partial u}{\partial y}\right)^2} = \overline{\left(\frac{\partial u}{\partial z}\right)^2} = \overline{\left(\frac{\partial v}{\partial x}\right)^2} = \overline{\left(\frac{\partial v}{\partial z}\right)^2} = \overline{\left(\frac{\partial w}{\partial x}\right)^2} = \overline{\left(\frac{\partial w}{\partial y}\right)^2} \tag{5.6}$$

$$\overline{\frac{\partial u}{\partial y}\frac{\partial v}{\partial x}} = \overline{\frac{\partial u}{\partial z}\frac{\partial w}{\partial x}} = \overline{\frac{\partial u}{\partial z}\frac{\partial w}{\partial x}} \tag{5.7}$$

Ces équations simplifient déjà grandement l'équation 5.4, mais nous y reviendrons (pour un aperçu, voir l'équation 5.22). Obtenons tout d'abord, d'autres relations pour l'isotropie.

Rotation du référentiel

Comme il a été aussi mentionné précédemment, la turbulence isotropique est invariante peu importe le système d'axe utilisé. Utilisons maintenant cette propriété pour chercher de l'information quant aux liens qui unissent les différents termes de l'équation 5.4.

Tout d'abord, considérons un système d'axes xyz auquel une rotation dans le sens antihoraire de 45° autour de l'axe z est effectué. Le nouveau système d'axes sera appelé $x'y'z'$. Puisqu'une rotation de 45° fait apparaître un facteur $\frac{1}{\sqrt{2}}$, on peut exprimer les nouveaux axes ainsi que les fluctuations de vitesses à l'aide de l'ancien référentiel:

$$\begin{aligned}
x' &= \frac{x+y}{\sqrt{2}} \\
y' &= \frac{-x+y}{\sqrt{2}} \\
z' &= z \\
u' &= \frac{u+v}{\sqrt{2}} \\
v' &= \frac{-u+v}{\sqrt{2}} \\
w' &= w
\end{aligned}$$

En recombinant les termes pour obtenir (u, v, x, y) en fonction de (u', v', x', y'), on obtient par exemple $u = \frac{u'-v'}{\sqrt{2}}$ et $x = \frac{x'-y'}{\sqrt{2}}$. À l'aide de ces termes, il est possible d'exprimer, par exemple,

la dérivé de u selon x exprimée dans le nouveau référentiel:

$$\begin{aligned}
\frac{\partial u}{\partial x} &= \frac{1}{\sqrt{2}}\left(\frac{\partial u'}{\partial x} - \frac{\partial v'}{\partial x}\right) \\
&= \frac{1}{\sqrt{2}}\left(\frac{\partial u'}{\partial x'}\frac{\partial x'}{\partial x} + \frac{\partial u'}{\partial y'}\frac{\partial y'}{\partial x} - \frac{\partial v'}{\partial x'}\frac{\partial x'}{\partial x} - \frac{\partial v'}{\partial y'}\frac{\partial y'}{\partial x}\right) \\
&= \frac{1}{\sqrt{2}}\left(\frac{\partial u'}{\partial x'}\frac{1}{\sqrt{2}} - \frac{\partial u'}{\partial y'}\frac{1}{\sqrt{2}} - \frac{\partial v'}{\partial x'}\frac{1}{\sqrt{2}} + \frac{\partial v'}{\partial y'}\frac{1}{\sqrt{2}}\right) \\
&= \frac{1}{2}\left(\frac{\partial u'}{\partial x'} - \frac{\partial v'}{\partial x'} - \frac{\partial u'}{\partial y'} + \frac{\partial v'}{\partial y'}\right)
\end{aligned}$$

En utilisant les mêmes arguments, il est également possible de réécrire les dérivées de fluctuations des vitesses pour les 3 autres termes ($\frac{\partial v}{\partial y}$, $\frac{\partial u}{\partial y}$ et $\frac{\partial v}{\partial x}$) pour obtenir le système suivant:

$$\frac{\partial u}{\partial x} = \frac{1}{2}\left(\frac{\partial u'}{\partial x'} - \frac{\partial v'}{\partial x'} - \frac{\partial u'}{\partial y'} + \frac{\partial v'}{\partial y'}\right) \tag{5.8}$$

$$\frac{\partial v}{\partial y} = \frac{1}{2}\left(\frac{\partial u'}{\partial x'} + \frac{\partial v'}{\partial x'} + \frac{\partial u'}{\partial y'} + \frac{\partial v'}{\partial y'}\right) \tag{5.9}$$

$$\frac{\partial u}{\partial y} = \frac{1}{2}\left(\frac{\partial u'}{\partial x'} - \frac{\partial v'}{\partial x'} + \frac{\partial u'}{\partial y'} - \frac{\partial v'}{\partial y'}\right) \tag{5.10}$$

$$\frac{\partial v}{\partial x} = \frac{1}{2}\left(\frac{\partial u'}{\partial x'} + \frac{\partial v'}{\partial x'} - \frac{\partial u'}{\partial y'} - \frac{\partial v'}{\partial y'}\right) \tag{5.11}$$

Il est utile de remarquer que les quatres équations ci-dessus sont constituées des mêmes termes dans le membre de droite, seulement le signe devant ceux-ci change. Mettons maintenant l'équation 5.8 au carré et moyennons:

$$\begin{aligned}\underbrace{\overline{\left(\frac{\partial u}{\partial x}\right)^2}}_{a_1} =& \frac{1}{2}\Bigg[\underbrace{\overline{\left(\frac{\partial u'}{\partial x'}\right)^2}}_{a_1} + \underbrace{\overline{\left(\frac{\partial v'}{\partial x'}\right)^2}}_{a_3} - \underbrace{\overline{\frac{\partial u'}{\partial x'}\frac{\partial v'}{\partial x'}}}_{a_5} - \underbrace{\overline{\frac{\partial u'}{\partial x'}\frac{\partial u'}{\partial y'}}}_{a_2} \\ &+ \underbrace{\overline{\frac{\partial u'}{\partial x'}\frac{\partial v'}{\partial y'}}}_{a_6} + \underbrace{\overline{\frac{\partial v'}{\partial x'}\frac{\partial u'}{\partial y'}}}_{a_8} - \underbrace{\overline{\frac{\partial v'}{\partial x'}\frac{\partial v'}{\partial y'}}}_{a_2} - \underbrace{\overline{\frac{\partial u'}{\partial y'}\frac{\partial v'}{\partial y'}}}_{a_5}\Bigg].\end{aligned} \tag{5.12}$$

Pour obtenir cette dernière équation, il est à noter que la symétrie de l'isotropie a été utilisée pour simplifer l'équation en posant $\overline{\left(\frac{\partial u'}{\partial x'}\right)^2} = \overline{\left(\frac{\partial v'}{\partial y'}\right)^2}$ et $\overline{\left(\frac{\partial v'}{\partial x'}\right)^2} = \overline{\left(\frac{\partial u'}{\partial y'}\right)^2}$. Notons aussi que puisque la turbulence isotropique est invariante malgré la rotation du système d'axe, $\overline{\left(\frac{\partial u}{\partial x}\right)^2} = \overline{\left(\frac{\partial u'}{\partial x'}\right)^2}$. Réécrivons l'équation 5.12 en tenant compte des relations ci-dessus et en utilisant une notation simplifiée où chaque terme est remplacé par un terme en a_i (voir éq. 5.12) correspondant à ceux définis dans la table 1 de l'article de Taylor (1935):

$$\overline{\left(\frac{\partial u}{\partial x}\right)^2} = a_1 = \frac{1}{2}\left(a_1 + a_3 - a_5 - a_2 + a_6 + a_8 - a_2 - a_5\right). \tag{5.13}$$

Effectuons maintenant le même travail (mettre au carré et moyenner) sur les équations 5.9, 5.10 et 5.11. Toujours avec la notation en a_i, ceci donne:

$$\overline{\left(\frac{\partial v}{\partial y}\right)^2} = a_1 = \frac{1}{2}\left(a_1 + a_3 + a_5 + a_2 + a_6 + a_8 + a_2 + a_5\right), \tag{5.14}$$

$$\overline{\left(\frac{\partial u}{\partial y}\right)^2} = a_3 = \frac{1}{2}\left(a_1 + a_3 - a_5 + a_2 - a_6 - a_8 + a_2 - a_5\right), \tag{5.15}$$

$$\overline{\left(\frac{\partial v}{\partial x}\right)^2} = a_3 = \frac{1}{2}\left(a_1 + a_3 + a_5 - a_2 - a_6 - a_8 - a_2 + a_5\right). \tag{5.16}$$

En soustrayant les équations (5.13) − (5.14) et (5.15) − (5.16) on obtient:

$$a_2 = a_5 = 0. \tag{5.17}$$

En introduisant $a_2 = 0$ et $a_5 = 0$ dans les équations et en effectuant (5.13) − (5.15), il en résulte la relation:

$$a_1 - a_3 - a_6 - a_8 = 0. \tag{5.18}$$

Un autre lien unissant les différentes dérivées dans le cas isotropique a été trouvé avec la rotation du référentiel. Réécris en terme de dérivées, cette relation est:

$$\overline{\left(\frac{\partial u}{\partial x}\right)^2} - \overline{\left(\frac{\partial u}{\partial y}\right)^2} - \overline{\frac{\partial u}{\partial x}\frac{\partial v}{\partial y}} - \overline{\frac{\partial u}{\partial y}\frac{\partial v}{\partial x}} = 0. \tag{5.19}$$

Relation faisant intervenir l'équation de continuité

Une autre relation qui permet de simplifier l'équation 5.4 provient de l'équation de continuité, qui stipule que pour un fluide incompressible, $\frac{\partial u}{\partial x} + \frac{\partial v}{\partial y} + \frac{\partial w}{\partial z} = 0$. Pour obtenir une nouvelle relation, il s'agit de mettre la continuité au carré et d'utiliser les considération de symétrie dans le cas isotropique (éq. 5.5,5.6 et 5.7).

$$\begin{aligned}\left(\frac{\partial u}{\partial x} + \frac{\partial v}{\partial y} + \frac{\partial w}{\partial z}\right)^2 = &\left(\frac{\partial u}{\partial x}\right)^2 + \left(\frac{\partial v}{\partial y}\right)^2 + \left(\frac{\partial w}{\partial z}\right)^2 \\ &+ \frac{\partial u}{\partial x}\frac{\partial v}{\partial y} + \frac{\partial u}{\partial x}\frac{\partial w}{\partial z} + \frac{\partial v}{\partial y}\frac{\partial w}{\partial z} \\ &+ \frac{\partial v}{\partial y}\frac{\partial u}{\partial x} + \frac{\partial w}{\partial z}\frac{\partial u}{\partial x} + \frac{\partial w}{\partial z}\frac{\partial v}{\partial y} = 0\end{aligned} \tag{5.20}$$

Avec l'hypothèse d'isotropie et par symétrie, les 3 premiers termes du membre de droite ainsi que les 6 derniers sont égaux entre eux. Avec cette considération et après avoir moyenné le résultat, on obtient une autre relation importante pour la suite de la simplification de l'équation 5.4:

$$\overline{\left(\frac{\partial u}{\partial x}\right)^2} = -2\overline{\frac{\partial u}{\partial x}\frac{\partial v}{\partial y}}. \tag{5.21}$$

La dissipation exprimée en fonction des contraintes normales

Diverses relations liant les termes de l'équation 5.4 en isotropie ont été obtenues à la section précédente. Celles-ci sont maintenant utilisées afin de simplifier les termes qui la compose. Tout d'abord, en utilisant les relation 5.5 à 5.7, l'équation 5.4 se simplifie grandement et se résume à:

$$\epsilon = \frac{\nu}{2}\left(12\overline{\frac{\partial u}{\partial x}^2} + 12\overline{\frac{\partial u}{\partial y}^2} + 12\overline{\frac{\partial u}{\partial y}\frac{\partial v}{\partial x}}\right). \tag{5.22}$$

Ensuite, en introduisant la relation 5.21 dans 5.19, on obtient:

$$\overline{\left(\frac{\partial u}{\partial y}\right)^2} + \overline{\frac{\partial u}{\partial y}\frac{\partial v}{\partial x}} = -3\overline{\frac{\partial u}{\partial x}\frac{\partial v}{\partial y}}. \tag{5.23}$$

En introduisant maintenant cette dernière équation dans 5.22, on obtient:

$$\epsilon = 6\nu\left(\overline{\left(\frac{\partial u}{\partial x}\right)^2} - 3\overline{\frac{\partial u}{\partial x}\frac{\partial v}{\partial y}}\right). \tag{5.24}$$

Finalement, en utilisant la relation provenant de l'équation de continuité (éq. 5.21) on obtient:

$$\epsilon = 15\nu\overline{\left(\frac{\partial u}{\partial x}\right)^2}. \tag{5.25}$$

Dissipation exprimée en fonction du cisaillement

L'équation 5.25 représente la dissipation de l'énergie cinétique turbulente en fonction du taux de variation des contraintes normales. Pour obtenir la relation que l'on cherche (éq. 5.1), il faut montrer que $2\left(\frac{\partial u}{\partial x}\right)^2 = \left(\frac{\partial u}{\partial z}\right)^2$. Comme il sera vu dans les prochaines lignes, cette démonstration est plutôt longue et fait intervenir de nombreux concepts. Cette partie de la démonstration est aussi présente dans l'article de Taylor, mais celui-ci la résume en quelques lignes en référant à une démonstration qu'il dit *bien connue* provenant de Lamb (1895). Tentons ici de clarifier le raisonnement qui mène à l'expression désirée.

Rappel sur la vorticité

Une partie de cette démonstration consiste à montrer que le taux de dissipation de l'énergie cinétique turbulente s'exprime aussi en fonction de la vorticité. Afin de permettre au lecteur de mieux suivre la suite du raisonnement, voici un petit rappel sur la vorticité qui est définie par le rotationnel du champ de vitesse:

$$\begin{aligned}
\vec{\nabla} \times \vec{U} &= \begin{vmatrix} \vec{i} & \vec{j} & \vec{k} \\ \frac{\partial}{\partial x} & \frac{\partial}{\partial y} & \frac{\partial}{\partial z} \\ u & v & w \end{vmatrix} \\
&= \vec{i}\left(\frac{\partial w}{\partial y} - \frac{\partial v}{\partial z}\right) + \vec{j}\left(\frac{\partial u}{\partial z} - \frac{\partial w}{\partial x}\right) + \vec{k}\left(\frac{\partial v}{\partial x} - \frac{\partial u}{\partial y}\right) \\
&= \vec{i}\omega_1 + \vec{j}\omega_2 + \vec{k}\omega_3 \\
&\equiv \vec{\omega}
\end{aligned} \tag{5.26}$$

Dans cette dernière expression, $\vec{\omega}$ est la vorticié et ω_1, ω_2 et ω_3 ses composantes. Dans d'autres ouvrages, ces composantes sont aussi appelées ξ, η et ζ.

Démonstration pour l'expression de la dissipation en fonction du cisaillement

L'idée de la démonstration est d'exprimer la dissipation turbulente de deux façons différentes et de montrer, après comparaison entre ces deux méthodes, qu'il existe des liens entre les différents termes de l'équation. Pour cette démonstration, oublions tout d'abord, pour plus de généralité, l'hypothèse d'isotropie. La première expression à comparer provient d'un réarangement des termes de l'équation 5.4, où les 9 derniers termes du membre de droite ont été regroupés trois par trois sous un carré. Notons que pour faciliter l'écriture, la moyenne de l'équation n'est pas considérée:

$$\begin{aligned}\epsilon = \nu\Bigg[&2\left(\frac{\partial u}{\partial x}\right)^2 + 2\left(\frac{\partial v}{\partial y}\right)^2 + 2\left(\frac{\partial w}{\partial z}\right)^2 \\ &+ \left(\frac{\partial v}{\partial x} + \frac{\partial u}{\partial y}\right)^2 + \left(\frac{\partial w}{\partial y} + \frac{\partial v}{\partial z}\right)^2 + \left(\frac{\partial u}{\partial z} + \frac{\partial w}{\partial x}\right)^2\Bigg].\end{aligned} \tag{5.27}$$

Cette équation, qui sera réutilisée plus loin, est la première expression à comparer. Pour obtenir la seconde expression à comparer, il faut soustraire à l'équation 5.27 le double de la relation de continuité au carré et réordonner les termes. Rien n'a donc été ajouté à l'équation initiale, puisque la relation de continuité est nulle.

$$\begin{aligned}\epsilon = \nu\Bigg[&2\left(\frac{\partial u}{\partial x}\right)^2 + 2\left(\frac{\partial v}{\partial y}\right)^2 + 2\left(\frac{\partial w}{\partial z}\right)^2 \\ &+ \left(\frac{\partial v}{\partial x} + \frac{\partial u}{\partial y}\right)^2 + \left(\frac{\partial w}{\partial y} + \frac{\partial v}{\partial z}\right)^2 + \left(\frac{\partial u}{\partial z} + \frac{\partial w}{\partial x}\right)^2 \\ &- 2\left(\frac{\partial u}{\partial x} + \frac{\partial v}{\partial y} + \frac{\partial w}{\partial z}\right)^2\Bigg].\end{aligned} \tag{5.28}$$

Cette équation peut se réécrire:

$$\begin{aligned}\epsilon = \nu\Bigg[&\left(\frac{\partial v}{\partial x} - \frac{\partial u}{\partial y}\right)^2 + \left(\frac{\partial w}{\partial y} - \frac{\partial v}{\partial z}\right)^2 + \left(\frac{\partial u}{\partial z} - \frac{\partial w}{\partial x}\right)^2 \\ &- 4\left(\frac{\partial v}{\partial y}\frac{\partial w}{\partial z} - \frac{\partial v}{\partial z}\frac{\partial w}{\partial y} + \frac{\partial w}{\partial z}\frac{\partial u}{\partial x} - \frac{\partial w}{\partial x}\frac{\partial u}{\partial z} + \frac{\partial u}{\partial x}\frac{\partial v}{\partial y} - \frac{\partial u}{\partial y}\frac{\partial v}{\partial x}\right)\Bigg].\end{aligned} \tag{5.29}$$

Les trois premiers termes de l'équation 5.29 sont maintenant familiers. Ce sont en effet les composantes au carré de la vorticité que l'on a présenté à l'équation 5.26.

La prochaine étape de la démonstration consiste à intégrer sur un volume les équations 5.27 et 5.29. Mais tout d'abord, il faut montrer que l'équation 5.29 peut s'écrire sous une forme faisant intervenir la vorticité au carré (les 3 premiers termes du membre de droite) et la divergence de deux termes:

$$\epsilon = \nu\left(\omega^2 - 2\vec{\nabla}\cdot\left(\vec{U}\times\vec{\omega} - \frac{\vec{\nabla}\vec{U}^2}{2}\right)\right). \tag{5.30}$$

Pour montrer que les 6 derniers termes de l'équation 5.29 sont équivalents aux 2 derniers termes de 5.30, développons ces derniers avec l'aide des propriétés des opérateurs scalaires et vectoriels:

$$
\begin{aligned}
2\vec{\nabla}\cdot\left(\vec{U}\times\vec{\omega}-\nabla\frac{\vec{U}^2}{2}\right) &= 2\vec{\nabla}\cdot\left(\vec{U}\times\vec{\omega}\right)-2\nabla^2\frac{U^2}{2} \\
&= 2\vec{\omega}\cdot\left(\vec{\nabla}\times\vec{U}\right)-2\vec{U}\cdot\left(\vec{\nabla}\times\vec{\omega}\right)-\nabla^2U^2 \\
&= 2\vec{\omega}\cdot\vec{\omega}-2\vec{U}\cdot\left(\vec{\nabla}\times\vec{\omega}\right)-\nabla^2U^2.
\end{aligned}
$$

Remplaçons maintenant chacun des termes par sa définition:

$$
\begin{aligned}
&2\vec{\omega}\cdot\vec{\omega}-2\vec{U}\cdot\left(\vec{\nabla}\times\vec{\omega}\right)-\nabla^2U^2 = \\
&\quad 2\left[\left(\frac{\partial v}{\partial x}\right)^2+\left(\frac{\partial w}{\partial x}\right)^2+\left(\frac{\partial u}{\partial y}\right)^2+\left(\frac{\partial w}{\partial y}\right)^2+\left(\frac{\partial u}{\partial z}\right)^2+\left(\frac{\partial v}{\partial z}\right)^2\right] \\
&\quad -4\left[\frac{\partial u}{\partial y}\frac{\partial v}{\partial x}+\frac{\partial v}{\partial z}\frac{\partial w}{\partial y}+\frac{\partial w}{\partial x}\frac{\partial v}{\partial z}\right] \\
&\quad +2u\left(\frac{\partial\omega_2}{\partial z}-\frac{\partial\omega_3}{\partial y}\right)+2v\left(\frac{\partial\omega_3}{\partial x}-\frac{\partial\omega_1}{\partial z}\right)+2w\left(\frac{\partial\omega_1}{\partial y}-\frac{\partial\omega_2}{\partial x}\right) \\
&\quad -\left[\frac{\partial^2u^2}{\partial x^2}+\frac{\partial^2v^2}{\partial x^2}+\frac{\partial^2w^2}{\partial x^2}+\frac{\partial^2u^2}{\partial y^2}+\frac{\partial^2v^2}{\partial y^2}+\frac{\partial^2w^2}{\partial y^2}+\right. \\
&\quad \left.\frac{\partial^2u^2}{\partial z^2}+\frac{\partial^2v^2}{\partial z^2}+\frac{\partial^2w^2}{\partial z^2}\right].
\end{aligned}
$$

Notons qu'il est possible de développer le dernier terme de l'équation précédente ($-[\frac{\partial^2u^2}{\partial x^2}+...]$) en considérant que, par exemple, $\frac{\partial^2u^2}{\partial x^2} = \frac{\partial}{\partial x}\left(\frac{\partial}{\partial x}(uu)\right) = \frac{\partial}{\partial x}\left(u\frac{\partial u}{\partial x}+u\frac{\partial u}{\partial x}\right) = 2\left(u\frac{\partial^2u}{\partial x^2}+\left(\frac{\partial u}{\partial x}\right)^2\right)$. En effectuant ceci pour chacune des dérivées secondes de l'équation, celle-ci peut s'écrire:

$$
\begin{aligned}
&2\vec{\omega}\cdot\vec{\omega} - 2\vec{U}\cdot\left(\vec{\nabla}\times\vec{\omega}\right) - \nabla^2 U^2 = \\
&\quad 2\left[\left(\frac{\partial v}{\partial x}\right)^2 + \left(\frac{\partial w}{\partial x}\right)^2 + \left(\frac{\partial u}{\partial y}\right)^2 + \left(\frac{\partial w}{\partial y}\right)^2 + \left(\frac{\partial u}{\partial z}\right)^2 + \left(\frac{\partial v}{\partial z}\right)^2\right] \\
&\quad - 4\left[\frac{\partial u}{\partial y}\frac{\partial v}{\partial x} + \frac{\partial v}{\partial z}\frac{\partial w}{\partial y} + \frac{\partial w}{\partial x}\frac{\partial v}{\partial z}\right] \\
&\quad + 2u\left(\frac{\partial \omega_2}{\partial z} - \frac{\partial \omega_3}{\partial y}\right) + 2v\left(\frac{\partial \omega_3}{\partial x} - \frac{\partial \omega_1}{\partial z}\right) + 2w\left(\frac{\partial \omega_1}{\partial y} - \frac{\partial \omega_2}{\partial x}\right) \\
&\quad - 2\left[\left(\frac{\partial u}{\partial x}\right)^2 + u\frac{\partial^2 u^2}{\partial x^2} + \left(\frac{\partial v}{\partial x}\right)^2 + v\frac{\partial^2 v^2}{\partial x^2} + \right. \\
&\quad \left(\frac{\partial w}{\partial x}\right)^2 + w\frac{\partial^2 w^2}{\partial x^2} + \left(\frac{\partial u}{\partial y}\right)^2 + u\frac{\partial^2 u^2}{\partial y^2} + \\
&\quad \left(\frac{\partial v}{\partial y}\right)^2 + v\frac{\partial^2 v^2}{\partial y^2} + \left(\frac{\partial w}{\partial y}\right)^2 + w\frac{\partial^2 w^2}{\partial y^2} + \\
&\quad \left(\frac{\partial u}{\partial z}\right)^2 + u\frac{\partial^2 u^2}{\partial z^2} + \left(\frac{\partial v}{\partial z}\right)^2 + v\frac{\partial^2 v^2}{\partial z^2} + \\
&\quad \left.\left(\frac{\partial w}{\partial z}\right)^2 + w\frac{\partial^2 w^2}{\partial z^2}\right].
\end{aligned}
$$

En effectuant les simplifications (c.-à-d., la première ligne disparait avec certains termes que nous venons de développer), cette expression peut s'écrire:

$$
\begin{aligned}
2\vec{\omega}\cdot\vec{\omega} - 2\vec{U}\cdot\left(\vec{\nabla}\times\vec{\omega}\right) - \nabla^2 U^2 = \\
&4\left[\frac{\partial u}{\partial y}\frac{\partial v}{\partial x} + \frac{\partial v}{\partial z}\frac{\partial w}{\partial y} + \frac{\partial w}{\partial x}\frac{\partial v}{\partial z}\right] \\
&+ 2u\left(\frac{\partial \omega_2}{\partial z} - \frac{\partial \omega_3}{\partial y}\right) + 2v\left(\frac{\partial \omega_3}{\partial x} - \frac{\partial \omega_1}{\partial z}\right) + 2w\left(\frac{\partial \omega_1}{\partial y} - \frac{\partial \omega_2}{\partial x}\right) \\
&- 2u\left(\frac{\partial^2 u^2}{\partial x^2} + \frac{\partial^2 u^2}{\partial y^2} + \frac{\partial^2 u^2}{\partial z^2}\right) \\
&- 2v\left(\frac{\partial^2 v^2}{\partial x^2} + \frac{\partial^2 v^2}{\partial y^2} + \frac{\partial^2 v^2}{\partial z^2}\right) \\
&- 2w\left(\frac{\partial^2 w^2}{\partial x^2} + \frac{\partial^2 w^2}{\partial y^2} + \frac{\partial^2 w^2}{\partial z^2}\right) \\
&- 2\left[\left(\frac{\partial u}{\partial x}\right)^2 + \left(\frac{\partial v}{\partial y}\right)^2 + \left(\frac{\partial w}{\partial z}\right)^2\right]
\end{aligned}
$$

En introduisant une dérivée de la relation de continuité dans les lignes 3, 4 et 5, nous remarquons que celles-ci s'annulent avec la ligne 2. Par exemple, la continuité nous donne:

$$\frac{\partial}{\partial x}\left(\frac{\partial u}{\partial x} + \frac{\partial v}{\partial y} + \frac{\partial w}{\partial z}\right) = 0$$

d'où

$$\frac{\partial^2 u}{\partial x^2} = -\frac{\partial^2 v}{\partial x \partial y} - \frac{\partial^2 w}{\partial x \partial z} \tag{5.31}$$

Et en introduisant 5.31 dans la troisième ligne de la grande expression ci-dessus, $-2u\left(\frac{\partial^2 u^2}{\partial x^2} + \frac{\partial^2 u^2}{\partial y^2} + \frac{\partial^2 u^2}{\partial z^2}\right)$ devient $-2u\Big(-\frac{\partial^2 v}{\partial x \partial y} - \frac{\partial^2 w}{\partial x \partial z} + \frac{\partial^2 u^2}{\partial y^2} + \frac{\partial^2 u^2}{\partial z^2}\Big)$, ce qui est égal (au signe près) au premier terme de la deuxième ligne de l'expression considérée, c'est-à-dire, $2u\left(\frac{\partial \omega_2}{\partial z} - \frac{\partial \omega_3}{\partial y}\right)$. Donc le premier terme de la ligne 2 s'annule avec la ligne 3, et ainsi de suite pour les lignes 4 et 5. L'expression restante est:

$$
\begin{aligned}
2\vec{\omega}\cdot\vec{\omega} - 2\vec{U}\cdot\left(\vec{\nabla}\times\vec{\omega}\right) - \nabla^2 U^2 &= -4\left[\frac{\partial u}{\partial y}\frac{\partial v}{\partial x} + \frac{\partial v}{\partial z}\frac{\partial w}{\partial y} + \frac{\partial w}{\partial x}\frac{\partial v}{\partial z}\right] \\
&- 2\left[\left(\frac{\partial u}{\partial x}\right)^2 + \left(\frac{\partial v}{\partial y}\right)^2 + \left(\frac{\partial w}{\partial z}\right)^2\right]
\end{aligned}
$$

Utilisons maintenant une dernière fois la relation de continuité au carré que nous additionnons deux fois à la relation précédente afin de faire disparaître le deuxième terme du membre de droite. Il en résulte:

$$
\begin{aligned}
&2\vec{\omega}\cdot\vec{\omega} - 2\vec{U}\cdot\left(\vec{\nabla}\times\vec{\omega}\right) - \nabla^2 U^2 = \\
&\qquad 4\left(\frac{\partial v}{\partial y}\frac{\partial w}{\partial z} - \frac{\partial v}{\partial z}\frac{\partial w}{\partial y} + \frac{\partial w}{\partial z}\frac{\partial u}{\partial x} - \frac{\partial w}{\partial z}\frac{\partial u}{\partial x} + \frac{\partial u}{\partial x}\frac{\partial v}{\partial y} - \frac{\partial u}{\partial y}\frac{\partial v}{\partial x}\right).
\end{aligned} \tag{5.32}
$$

Ce terme, qui se retrouve dans l'équation 5.29 est celui que nous cherchions a obtenir. Nous venons donc de montrer que l'équation 5.29 s'exprime selon l'équation 5.30.

À ce moment-ci, il est important de rappeler que l'idée de la démonstration est d'exprimer la dissipation turbulente de deux façons (équations 5.27 et 5.29). Comme ces deux termes sont égaux, on peut poser:

$$
\iiint_V (\text{eq. 5.27})\; dV = \iiint_V (\text{eq. 5.29})\; dV. \tag{5.33}
$$

Comme nous venons de le montrer, ceci est équivalent à:

$$
\iiint_V (\text{eq. 5.27})\; dV = \iiint_V (\text{eq. 5.30})\; dV. \tag{5.34}
$$

Attardons-nous maintenant à simplifier le membre de droite de cette équation en utilisant certaines propriétés. La première étape est d'utiliser le théorème de Gauss ($\iiint_V \vec{\nabla} \cdot \vec{A}\, dV = \iint_S \vec{A}\, dS$) afin de transformer l'intégrale sur le volume du second terme par une intégrale sur la surface délimitant ce volume. L'utilisation de ce théorème mène à :

$$\iiint_V \omega^2 - 2\vec{\nabla} \cdot \left(\vec{U} \times \vec{\omega} - \nabla \frac{\vec{U}^2}{2} \right) dV = \iiint_V \omega^2\, dV - 2 \iint_S \left(\vec{U} \times \vec{\omega} - \nabla \frac{\vec{U}^2}{2} \right) dS. \tag{5.35}$$

Dans sa démonstration, Taylor (1935) suggère qu'en sélectionnant le volume d'intégration de sorte que la surface d'intégration soit grande par rapport à l'échelle de la turbulence, l'intégrale de surface disparait. Ceci s'explique par la nature chaotique de la turbulence qui rend l'intégration des fluctuations turbulentes sur la surface négligeable par rapport à l'intégrale sur le volume (alors que les termes dans l'intégrale de surface peuvent être positifs ou négatifs et s'annuler dans une large mesure, le terme dans l'intégrale volumique ne peut être que positif). En d'autres termes, l'équation 5.35 devient:

$$\iiint_V \omega^2 - 2\vec{\nabla} \cdot \left(\vec{U} \times \vec{\omega} - \nabla \frac{\vec{U}^2}{2} \right) dV = \iiint_V \omega^2\, dV. \tag{5.36}$$

Rappelons que l'équation 5.36 provient du membre de droite de l'égalité 5.33. Nous faisons maintenant disparaitre l'intégrale volumique en normalisant par le volume (moyenne volumique). En faisant réaparaitre la moyenne temporelle, et en gardant à l'esprit que ce résultant est valable pour un volume assez grand par rapport à l'échelle de la turbulence, il est possible d'affirmer que:

$$\overline{(\text{eq. } 5.27)} = \overline{\nu\omega^2}. \tag{5.37}$$

En réintroduisant explicitement les termes composant cette égalité et en distribuant la moyenne de l'équation, on obtient:

$$\begin{aligned} 2\overline{\left(\frac{\partial u}{\partial x}\right)^2} + 2\overline{\left(\frac{\partial v}{\partial y}\right)^2} + 2\overline{\left(\frac{\partial w}{\partial z}\right)^2} + \overline{\left(\frac{\partial v}{\partial x} + \frac{\partial u}{\partial y}\right)^2} + \overline{\left(\frac{\partial w}{\partial y} + \frac{\partial v}{\partial z}\right)^2} \\ + \overline{\left(\frac{\partial u}{\partial z} + \frac{\partial w}{\partial x}\right)^2} \\ = \overline{\left(\frac{\partial v}{\partial x} - \frac{\partial u}{\partial y}\right)^2} + \overline{\left(\frac{\partial w}{\partial y} - \frac{\partial v}{\partial z}\right)^2} + \overline{\left(\frac{\partial u}{\partial z} - \frac{\partial w}{\partial x}\right)^2}. \end{aligned} \tag{5.38}$$

En introduisant maintenant les hyptohèses d'isotropie (équations 5.5,5.6 et 5.7), on obtient:

$$\begin{aligned} 6\overline{\left(\frac{\partial u}{\partial x}\right)^2} + 6\overline{\left(\frac{\partial u}{\partial y}\right)^2} + 6\overline{\frac{\partial u}{\partial y}\frac{\partial v}{\partial x}} = 6\overline{\left(\frac{\partial u}{\partial y}\right)^2} - 6\overline{\frac{\partial u}{\partial y}\frac{\partial v}{\partial x}} \\ \overline{\left(\frac{\partial u}{\partial x}\right)^2} = -2\overline{\frac{\partial u}{\partial y}\frac{\partial v}{\partial x}}. \end{aligned} \tag{5.39}$$

L'équation 5.39 est une nouvelle relation entre les dérivées pour la turbulence isotropique (notez bien que le terme croisé est différent de celui de la relation 5.21 trouvée précédemment). En utilisant les relations déjà démontrées (éq. 5.19 et 5.21), on obtient la relation qui associe les déformations normales aux déformations en cisaillement en turbulence isotropique:

$$2\overline{\left(\frac{\partial u}{\partial x}\right)^2} = \overline{\left(\frac{\partial u}{\partial y}\right)^2} = \overline{\left(\frac{\partial u}{\partial z}\right)^2}. \tag{5.40}$$

Finalement, en introduisant cette dernière relation moyennée dans le résultat de la section précédente (éq.5.25), on obtient l'équation qui relie le cisaillement des vitesses à la dissipation de l'énergie cinétique turbulente:

$$\epsilon = \frac{15\nu}{2}\overline{\left(\frac{\partial u}{\partial z}\right)^2}. \tag{5.41}$$